

**COUPLED NONLINEAR AEROELASTICITY AND FLIGHT DYNAMICS OF
FULLY FLEXIBLE AIRCRAFT**

by

Weihua Su

A dissertation submitted in partial fulfillment
of the requirements for the degree of
Doctor of Philosophy
(Aerospace Engineering)
in The University of Michigan
2008

Doctoral Committee:

Associate Professor Carlos E. S. Cesnik, Chair
Professor Peretz P. Friedmann
Professor Anthony M. Waas
Associate Professor Bogdan Epureanu

学如逆水行舟，不进则退。

Learning is like rowing upstream: not to advance is to drop back.

– A Chinese Proverb

© Weihua Su 2008
All Rights Reserved

To my family

ACKNOWLEDGEMENTS

I would like to acknowledge my advisor, Dr. Carlos E. S. Cesnik for his invaluable support, encouragement, and guidance throughout my Ph.D. studies at the University of Michigan. His brilliant insight always inspires me on the road of research. I really feel honored and enjoy the opportunity to work with Carlos. I am also grateful to my Ph.D. committee members: Dr. Peretz P. Friedmann, Dr. Anthony M. Waas, and Dr. Bogdan Epureanu. Many thanks are given to their suggestions during the review of this dissertation.

I appreciate the help from Dr. Eric Brown, who guided me into the numerical code of NAST. Special thanks go to Drs. Christopher Shearer and Rafael Palacios for their valuable suggestions and help. I am also thankful to my colleagues and friends in A²SRL and the Department of Aerospace Engineering: Dr. Sang-Joon Shin, Dr. Ajay Raghavan, Mr. Smith Thepvongs, Ms. Jiwon Mok, Mr. Satish Chimakurthi, Mr. Ken Salas, Mr. Devesh Kumar, Mr. Benjamin Friedland, Dr. De Xie, Dr. Li Liu, Dr. Ce Sun, Dr. Shunjun Song, Dr. Quanhua Sun, Dr. Yongxian Gu, and Dr. Li Qiao. I really enjoyed the discussion, the challenge, and the cooperation with each other.

To my parents, Chengpan and Jihong, I feel I am indebted to them. They gave me life, taught me the first classes, such as “1+1=2”, and always encourage me to be perseverant from the early stages of my childhood.

To my lovely wife, Ying, I am forever thankful for her unconditional support over the years. Without her love, understanding, and support, I would not be able to make any achievements.

Sponsorships of this work came from the Air Force Office of Scientific Research (under grant F49620-02-1-0425, monitored by Dr. Clark Allred), the NASA Dryden

Flight Research Center (under contract NND05AC19P, monitored by Mr. Martin Brenner), and the Air Force Research Laboratory (under grant FA8650-06-2-3625, monitored by Dr. Greg Brooks). I appreciate these supports that allow me to conduct research and finish my Ph.D. degree.

TABLE OF CONTENTS

DEDICATION	ii
ACKNOWLEDGEMENTS	iii
LIST OF FIGURES	ix
LIST OF TABLES	xviii
LIST OF APPENDICES	xix
LIST OF SYMBOLS	xx
ABSTRACT	xxvi
CHAPTER	
I. Introduction	1
1.1 Motivation	1
1.2 Literature Review of Previous Work	4
1.2.1 Nonlinear Modeling and Analysis of HALE Aircraft	5
1.2.2 Joined-Wing Configurations	6
1.2.3 Flying-Wing Configurations	9
1.2.4 Simulation of Gust Responses	13
1.2.5 Nonlinear Aeroelastic Simulation Environment	14
1.3 Outline of this Dissertation	16
II. Theoretical Formulation	19
2.1 Overview: Modeling of Fully Highly Flexible Aircraft	19
2.2 Elastic System Equations of Motion	23
2.2.1 Fundamental Descriptions	23

2.2.2 Internal Virtual Work	27
2.2.3 External Virtual Work	37
2.2.4 Elastic Equations of Motion	39
2.2.5 Skin Wrinkling: Stiffness Nonlinearity	40
2.3 Kinematics.....	42
2.3.1 Single Beam System.....	44
2.3.2 Split Beam System	45
2.4 Additional Nodal Displacement Constraints.....	46
2.4.1 Absolute Constraints	47
2.4.2 Relative Constraints.....	48
2.4.3 Elastic Equations of Motion with Constraints.....	51
2.4.4 Special Treatment Regarding the Constraints	51
2.5 Body Frame Propagation Equations.....	53
2.6 Unsteady Aerodynamics	54
2.7 Simplified Stall Models.....	56
2.8 Discrete Gust Formulation	57
2.9 Coupled Aeroelastic and Flight Dynamic Equations of Motion	59
2.10 Stability Analysis: Frequency Domain Solution	59
2.10.1 Linearization of Nonlinear System Equations.....	59
2.10.2 Solution of Stability Boundary	62
III. Introduction to the Numerical Analysis Framework.....	64
3.1 Development of the Numerical Framework	64
3.2 Architecture of the Numerical Framework	67
3.3 Introduction to Main Function Modules	67
3.3.1 Model Initialization	67
3.3.2 Modal Analysis.....	69
3.3.3 Geometric Nonlinear Static Solver.....	70

3.3.4 Trim Module.....	71
3.3.5 Time Domain Simulation	71
3.3.6 Stability Analysis.....	73
3.3.7 Visualization.....	74
IV. Numerical Verification of Formulation	75
4.1 Cantilever Beam Configuration	76
4.1.1 Cantilever Beam with Static Tip Forces.....	77
4.1.2 Time Simulation of Cantilever Beam with Tip Force	78
4.2 Split Beam Configuration.....	79
4.2.1 Split Beam with Multi-Axial Static Tip Forces.....	80
4.2.2 Time Simulation of Split Beam with Single Tip Force	81
4.3 Beam Configuration with Absolute Displacement Constraints	83
4.3.1 Fixed-Pinned Beam with Static Tip Force	84
4.3.2 Time Simulation of Fixed-Pinned Beam with Tip Force	84
4.4 Beam Configuration with Relative Displacement Constraints	86
4.4.1 Joined-Beam with Multi-Axial Static Force.....	86
4.4.2 Time Simulation of Joined-Beam with Tip Force	87
4.5 Follower Loading Case	89
4.5.1 Cantilever Beam with Static Follower Loads.....	89
4.5.2 Time Simulation of Cantilever Beam with Follower Tip Load	89
4.6 Aeroelastic Formulation: Prediction of Flutter Boundary.....	91
4.6.1 Highly Flexible Wing with Cantilevered Root.....	91
4.6.2 Flutter of Free Flight Aircraft.....	95
V. Numerical Studies	102
5.1 Introduction	102
5.2 Representative Aircraft Models	104
5.2.1 Single-Wing Configuration	104

5.2.2 Joined-Wing Configuration	107
5.2.3 Blended-Wing-Body Configuration	112
5.2.4 Flying-Wing Configuration	114
5.3 Static Stability	117
5.4 Dynamic Stability.....	123
5.4.1 Flutter Boundary of Constrained Vehicle: Single-Wing	123
5.4.2 Flutter Boundary of Free Flight Vehicle: Single-Wing.....	126
5.4.3 Flutter Boundary of Free Flight Vehicle: Blended-Wing-Body.....	128
5.4.4 Flight Stability: Flying-Wing	133
5.5 Roll Response.....	134
5.5.1 Linearized and Fully Nonlinear Approaches.....	135
5.5.2 Roll Response of Single-Wing Models	137
5.5.3 Roll Response of Joined-Wing Models.....	139
5.6 Flight Response with Flap Perturbation	142
5.7 Gust Response	147
5.7.1 Effects of Different Gust Durations	147
5.7.2 Effects of Stall	156
5.7.3 Effects of Gust Amplitudes	162
5.7.4 Effects of Skin Wrinkling.....	165
VI. Conclusions and Recommendations	169
6.1 Summary of the Theoretical Formulation Developments	169
6.2 Conclusion from Numerical Studies	171
6.3 Key Contributions of this Dissertation.....	173
6.4 Recommendations for Future Work.....	174
APPENDICES	177
BIBLIOGRAPHY	228

LIST OF FIGURES

Figure 1.1: Three basic ISR SensorCraft concepts	2
Figure 1.2: Pathfinder-Plus and Helios as samples of highly flexible Flying-Wings (photo courtesy of NASA Dryden Flight Research Center)	10
Figure 2.1: Modeling scheme of a highly flexible vehicle	20
Figure 2.2: Example of a Joined-Wing aircraft	20
Figure 2.3: Aircraft with beam reference line representations	21
Figure 2.4: Rigid engine unit attached to elastic wing.....	22
Figure 2.5: Closeup of the Helios prototype showing the wing structure (photo courtesy of NASA Dryden Flight Research Center).....	22
Figure 2.6: Global and Body reference frames.....	24
Figure 2.7: Basic beam reference frames.....	25
Figure 2.8: Deformations of constant-strain elements	26
Figure 2.9: Rigid fuselage reference frames	28
Figure 2.10: Reference frame for rigid bodies attached to elastic members	33
Figure 2.11: Bilinear characteristics of the wing torsional stiffness.....	41
Figure 2.12: Switching of system properties during time integration	41
Figure 2.13: Single beam system (one member consisting of three elements).....	44
Figure 2.14: Split beam system (three members each consisting of one element).....	45
Figure 2.15: Cantilever beam with absolute nodal displacement constraint	46
Figure 2.16: Beam configuration and reference frames with relative nodal displacement constraint	49
Figure 2.17: Airfoil coordinate systems and velocity components.....	54
Figure 2.18: Variation of lift and moment coefficients for Stall Model 1	56

Figure 2.19: Variation of lift and moment coefficients for Stall Model 2	56
Figure 2.20: Example of gust spatial distribution for $n_E = 1$, $n_N = 2$, $A_c = 10$ m/s.....	58
Figure 2.21: Time variation of gust speed	58
Figure 2.22: Scheme of searching for the stability boundary	63
Figure 3.1: Block diagram showing functions of UM/NAST.....	66
Figure 3.2: Sketch of a Joined-Wing configuration.....	68
Figure 3.3: Bottom-up structural relationships for the sample Joined-Wing configuration	69
Figure 4.1: Model description of a cantilever beam	76
Figure 4.2: A cantilever beam with concentrated tip load	77
Figure 4.3: Change of vertical tip displacement with different tip loads (normalized with respect to the beam span)	77
Figure 4.4: Change of axial tip displacement with different tip loads (normalized with respect to the beam span)	78
Figure 4.5: Tip displacement of the cantilever beam under vertical tip load (normalized with respect to the beam span)	79
Figure 4.6: Model description of a split beam system	80
Figure 4.7: A split beam system under multi-axial tip loads	80
Figure 4.8: Three-dimensional deformation of the split beam system under multi-axial loads (normalized with respect to the beam span).....	81
Figure 4.9: A split beam system under single tip load.....	81
Figure 4.10: Displacement of the front tip of the split beam system under single tip load (normalized with respect to the beam span)	82
Figure 4.11: Displacement of the rear tip of the split beam system under single tip load (normalized with respect to the beam span)	82
Figure 4.12: A cantilever beam with pinned mid point and concentrated tip force.....	83
Figure 4.13: Deformation of the constrained beam under vertical tip load (normalized with respect to the beam span)	83
Figure 4.14: Tip displacement of the constrained beam under vertical tip load (normalized with respect to the beam span)	84

Figure 4.15: Displacement of the constrained node in UM/NAST model (normalized with respect to the beam span)	85
Figure 4.16: Model description of a joined-beam system.....	85
Figure 4.17: Three-dimensional deformation of the joined-bema system under multi-axial loads (normalized with respect to the beam span).....	86
Figure 4.18: Lateral and vertical displacements of the joined-beam system under multi-axial loads (normalized with respect to the beam span).....	87
Figure 4.19: Tip displacement of the joined-beam system under vertical tip load (normalized with respect to the beam span)	88
Figure 4.20: UM/NAST displacement results for the Two Tips of the joined-beam system under vertical tip load (normalized with respect to the beam span).....	88
Figure 4.21: A cantilever beam subject to concentrated follower loads.....	89
Figure 4.22: Three-dimensional deformation of the cantilever beam under follower tip loads (normalized with respect to the beam span).....	90
Figure 4.23: Lateral and vertical displacement of the cantilever beam under follower tip loads (normalized with respect to the beam span).....	90
Figure 4.24: Tip displacement of the cantilever beam under follower tip loads (normalized with respect to the beam span)	91
Figure 4.25: Root locus with changing velocity of the cantilevered highly flexible wing, speed from 0 m/s (triangle) to 30 m/s (square).....	93
Figure 4.26: Tip displacement of the pre-flutter case for the cantilevered highly flexible wing	94
Figure 4.27: Tip displacement of the post-flutter case for the cantilevered highly flexible wing	95
Figure 4.28: Model description of a sample Blended-Wing-Body model.....	96
Figure 4.29: Mode shape of flutter in free flight condition of the sample Blended-Wing-Body model	97
Figure 4.30: Root locus with changing velocity of the sample Blended-Wing-Body model, speed from 94.83 m/s (triangle) to 140 m/s (square).....	98
Figure 4.31: Deflection of elevator angle as a perturbation for the sample Blended-Wing-Body model	99
Figure 4.32: Tip displacement of the pre-flutter case for the sample Blended-Wing-Body model, speed 120 m/s	99

Figure 4.33: Pitching angle of the pre-flutter case for the sample Blended-Wing-Body model, speed 120 m/s	100
Figure 4.34: Tip displacement of the post-flutter case for the sample Blended-Wing-Body model, speed 125 m/s	100
Figure 4.35: Pitching angle of the post-flutter case for the sample Blended-Wing-Body model, speed 125 m/s	101
Figure 5.1: Mission profile for SensorCraft.....	103
Figure 5.2: Baseline Single-Wing configuration (arrow indicates the direction of thrust force in undeformed vehicle configuration)	104
Figure 5.3: Trim results for the Single-Wing configuration (Model 5).....	107
Figure 5.4: Baseline Joined-Wing configuration (arrow indicates the direction of thrust force in undeformed vehicle configuration)	108
Figure 5.5: Trim results for the Joined-Wing configuration (Model 5).....	111
Figure 5.6: Baseline Blended-Wing-Body configuration (arrow indicates the direction of thrust force in undeformed vehicle configuration)	111
Figure 5.7: Trim results for the Blended-Wing-Body configuration.....	113
Figure 5.8: Baseline Flying-Wing configuration (after Ref. [51]).....	113
Figure 5.9: Trim results for the Flying-Wing configuration.....	115
Figure 5.10: Trimmed light model with respect to undeformed shape – nearly identical ($U=12.2$ m/s, at sea level).....	116
Figure 5.11: Trimmed heavy model with respect to undeformed shape ($U=12.2$ m/s, at sea level).....	116
Figure 5.12: Lift distribution on the vehicle as the critical speed is approached, (a) undeformed; (b) $U=61.21$ m/s; (c) $U = 80$ m/s; (d) $U = 81.1$ m/s (sea level, fully fueled, no rigid body degrees of freedom).....	117
Figure 5.13: Wing shape for varying load factors (Model 5, level flight at sea level)...	118
Figure 5.14: Wing bending deflections for varying load factors (Model 5, level flight at sea level)	119
Figure 5.15: Changes in tip deflection as function of the flight speed of the vehicle (Model 5, level flight at sea level).....	119
Figure 5.16: Changes in tip deflection as function of the lift generation capability (load factor) of the vehicle (Model 5, level flight at sea level)	120

Figure 5.17: Nonlinear growth of maximum longitudinal strain due to loss of stiffness on the aft wing with increasing load factor (Model 5, level flight at sea level)	120
Figure 5.18: Nonlinear growth of maximum transverse strain due to loss of stiffness on the aft wing with increasing load factor (Model 5, level flight at sea level)	121
Figure 5.19: Nonlinear growth of maximum shear strain due to loss of stiffness on the aft wing with increasing load factor (Model 5, level flight at sea level)	121
Figure 5.20: Load fact with respect to flight speeds for different models of the Joined-Wing configuration (level flight at sea level)	122
Figure 5.21: Nonlinear flutter speed at each flight index for different models of the Single-Wing configuration (no rigid body motions, no retrim)	124
Figure 5.22: Anti-symmetric flutter mode of Single-Wing configuration (Model 3, Index 2)	124
Figure 5.23: Symmetric flutter mode of Single-Wing configuration (Model 3, Index 3)	125
Figure 5.24: Symmetric flutter mode of Single-Wing configuration (Model 5, Index 3)	125
Figure 5.25: Symmetric flutter mode of Single-Wing configuration (Model 5, Index 5)	125
Figure 5.26: Flutter speed of Single-Wing configuration with constrained rigid body DOF and in free flight condition (Model 5, no retrim)	126
Figure 5.27: Frequency of flutter modes of Single-Wing configuration with constrained rigid body DOF and in free flight condition (Model 5, no retrim)	127
Figure 5.28: Flutter mode of Single-Wing configuration in free flight condition (Model 5, Index 3, no retrim)	127
Figure 5.29: Flutter mode of Single-Wing configuration in free flight condition (Model 5, Index 7, no retrim)	128
Figure 5.30: Change of flutter boundaries of the Blended-Wing-Body configuration with respect to out-of-plane bending stiffness	129
Figure 5.31: Change of flutter frequency of the Blended-Wing-Body configuration with respect to out-of-plane bending stiffness	130
Figure 5.32: Flutter mode shape of the nominal Blended-Wing-Body configuration with all rigid body motions constrained	130

Figure 5.33: Flutter mode shape of the nominal Blended-Wing-Body configuration in free flight condition	131
Figure 5.34: Change of flutter boundaries of the Blended-Wing-Body configuration with respect to in-plane bending stiffness	131
Figure 5.35: Change of flutter frequency of the Blended-Wing-Body configuration with respect to in-plane bending stiffness	132
Figure 5.36: Change of flutter boundaries of the Blended-Wing-Body configuration with respect to torsional stiffness	132
Figure 5.37: Change of flutter frequency of the Blended-Wing-Body configuration with respect to torsional stiffness	133
Figure 5.38: Root locus for phugoid mode of the Flying-Wing configuration (left: flexible vehicle, right: rigid vehicle)	134
Figure 5.39: Aileron deflection for the Joined-Wing and Single-Wing configurations .	135
Figure 5.40: Comparison of nonlinear and linearized roll rate of the Single-Wing configuration (Model 5)	136
Figure 5.41: Comparison of nonlinear and linearized roll angle of the Single-Wing configuration (Model 5)	136
Figure 5.42: Linearized roll rate for the Single-Wing configurations	137
Figure 5.43: Linearized roll angle for the Single-Wing configurations.....	138
Figure 5.44: Nonlinear roll rate for the Single-Wing configurations	138
Figure 5.45: Nonlinear roll angle for the Single-Wing configurations.....	139
Figure 5.46: Linearized roll rate for the Joined-Wing configurations	140
Figure 5.47: Linearized roll angle for the Joined-Wing configurations	140
Figure 5.48: Nonlinear roll rate for the Joined-Wing configurations	141
Figure 5.49: Nonlinear roll angle for the Joined-Wing configurations	141
Figure 5.50: Flap deflection for the Flying-Wing configuration	142
Figure 5.51: Stall effects on the airspeed of flight with initial flap angle perturbation..	144
Figure 5.52: Stall effects on the altitude of flight with initial flap angle perturbation ...	144
Figure 5.53: Stall effects on the angle of attack of flight with initial flap angle perturbation.....	145

Figure 5.54: Bending curvature at the mid span location of flight with initial flap angle perturbation.....	145
Figure 5.55: Variation of body velocities with initial flap angle perturbation	146
Figure 5.56: Initial vehicle position with respect to the gust region and intended flight path if in calm air.....	146
Figure 5.57: Effects of gust duration on body position – North	148
Figure 5.58: Effects of gust duration on body position – West (zoomed for initial times at the bottom).....	149
Figure 5.59: Effects of gust duration on body position – Altitude	150
Figure 5.60: Effects of gust duration on Euler angle – Yaw (zoomed for initial times at the bottom).....	151
Figure 5.61: Effects of gust duration on Euler angle – Pitch.....	152
Figure 5.62: Effects of gust duration on Euler angle – Roll	152
Figure 5.63: Effects of gust duration on bending curvature at the mid span location	153
Figure 5.64: Vehicle deformation at 30 seconds with 8-s gust (golden: 30s with 8-s gust; green: trimmed steady state; frame: undefomed)	154
Figure 5.65: Flight path of the Flying-Wing with 2-s gust duration.....	154
Figure 5.66: Flight path of the Flying-Wing with 4-s gust duration.....	155
Figure 5.67: Flight path of the Flying-Wing with 8-s gust duration.....	155
Figure 5.68: Lift distribution on the wings from 25 to 35 seconds with stall effects	157
Figure 5.69: Lift distribution on the wings from 25 to 35 seconds without stall effects	157
Figure 5.70: Stall effects on bending curvature at the mid span location when vehicle is subjected to 10-m/s center amplitude and 4-s duration gust	158
Figure 5.71: Stall effects on body position (west) when vehicle is subjected to 10-m/s center amplitude and 4-s duration gust.....	158
Figure 5.72: Stall effects on body position (north) when vehicle is subjected to 10-m/s center amplitude and 4-s duration gust.....	159
Figure 5.73: Stall effects on body position (altitude) when vehicle is subjected to 10-m/s center amplitude and 4-s duration gust.....	159
Figure 5.74: Stall effects on body Euler angle (yaw) when vehicle is subjected to 10-m/s center amplitude and 4-s duration gust.....	160

Figure 5.75: Stall effects on body Euler angle (pitch) when vehicle is subjected to 10-m/s center amplitude and 4-s duration gust.....	160
Figure 5.76: Stall effects on body Euler angle (roll) when vehicle is subjected to 10-m/s center amplitude and 4-s duration gust.....	161
Figure 5.77: Effects of gust amplitude on bending curvature at the mid span location .	161
Figure 5.78: Effects of gust amplitude on body position (West).....	162
Figure 5.79: Effects of gust amplitude on body position (North).....	163
Figure 5.80: Effects of gust amplitude on body position (Altitude)	163
Figure 5.81: Effects of gust amplitude on body Euler angle (Yaw)	164
Figure 5.82: Effects of gust amplitude on body Euler angle (Pitch)	164
Figure 5.83: Effects of gust amplitude on body Euler angle (Roll).....	165
Figure 5.84: Effects of skin wrinkling on bending curvature at wing root when vehicle is subjected to 5-m/s center amplitude and 4-s duration gust	166
Figure 5.85: Effects of skin wrinkling on twist curvature at wing root when vehicle is subjected to 5-m/s center amplitude and 4-s duration gust	166
Figure 5.86: Effects of skin wrinkling on body position (west) when vehicle is subjected to 5-m/s center amplitude and 4-s duration gust	167
Figure 5.87: Effects of skin wrinkling on body Euler angle (yaw) when vehicle is subjected to 5-m/s center amplitude and 4-s duration gust	168
Figure 5.88: Effects of skin wrinkling on body Euler angle (roll) when vehicle is subjected to 5-m/s center amplitude and 4-s duration gust	168
Figure A.1: Rotation of aerodynamic loads.....	179
Figure A.2: Relation between strain and aerodynamic loads	187
Figure A.3: Relation between strain rate and aerodynamic loads	188
Figure A.4: Relation between strain acceleration and aerodynamic loads	188
Figure A.5: Relation between body velocity and aerodynamic loads	188
Figure A.6: Relation between body acceleration and aerodynamic loads	189
Figure C.1: Member and group definitions for the Single-Wing configuration (arrows indicate the kinematics marching direction and element progression as presented below).....	199

Figure C.2: Member and group definitions for the Joined-Wing configuration (arrows indicate the kinematics marching direction and element progression as presented below)	210
Figure C.3: Member and group definitions for the Blended-Wing-Body configuration (arrows indicate the kinematics marching direction and element progression as presented below)	223

LIST OF TABLES

Table 3.1: Inputs and outputs of the static solver	70
Table 3.2: Inputs and outputs of the trim module	71
Table 3.3: Inputs of the time domain simulation	72
Table 3.4: Outputs of the time domain simulation and stability analysis.....	73
Table 4.1: Properties of the reference beam	76
Table 4.2: Properties of a highly flexible wing (after Ref. [88])	92
Table 4.3: Natural frequencies of the highly flexible wing	92
Table 4.4: Flutter results of the highly flexible wing.....	93
Table 4.5: Body properties of the Blended-Wing-Body model	96
Table 4.6: Wing properties of the Blended-Wing-Body model.....	97
Table 5.1: Geometric parameters of the Single-Wing configuration.....	105
Table 5.2: Vehicle mass distribution for the Single-Wing configuration.....	105
Table 5.3: Models with different flexibility levels of the Single-Wing configuration ...	106
Table 5.4: Geometric parameters of the Joined-Wing configuration	109
Table 5.5: Vehicle mass distribution for the Joined-Wing configuration.....	109
Table 5.6: Models with different flexibility levels of the Joined-Wing configuration...	110
Table 5.7: Vehicle mass distribution for the Blended-Wing-Body configuration.....	112
Table 5.8: Cross-sectional properties of the Flying-Wing configuration (after Ref. [51])	114
Table 5.9: Trim results for light and heavy models of the Flying-Wing configuration..	115
Table 5.10: Phugoid and short-period modes for light and heavy models	134
Table C.1: Material properties of S-glass	221

LIST OF APPENDICES

Appendix A. Derivatives of Aerodynamic Loads.....	178
A.1 Rotation of Aerodynamic Forces and Moments	178
A.2 Derivatives in the Local Aerodynamic Frame	180
A.3 Derivatives in the Body Frame	185
A.4 Block Diagrams Showing Aerodynamic Derivative Relationships	187
Appendix B. Linearization of System Equations of Motion.....	190
B.1 Generic Nonlinear Equation	190
B.2 Nonlinear Aeroelastic Equations of Motion.....	191
Appendix C. Properties of the Numerical Models.....	198
C.1 Single-Wing Configuration	199
C.2 Joined-Wing Configuration	210
C.3 Blended-Wing-Body Configuration	223

LIST OF SYMBOLS

Reference Frames and Rotation Matrices

G	Global (inertial) reference frame
B	Body reference frame
w	Local beam reference frame defined at each node along beam reference line
b	Local auxiliary reference frame defined at each node along beam reference line
a_0	Local aerodynamic frame, with a_{0y} axis aligned with the zero lift line of airfoil
a_l	Local aerodynamic frame, with a_{ly} axis aligned with airfoil motion velocity
C^{GB}	Rotation matrix from B frame to G frame
C^{Bw}	Rotation matrix from w frame to B frame
C^{Bb}	Rotation matrix from b frame to B frame
C^{wa_0}	Rotation matrix from a_0 frame to w frame
$C^{a_0a_l}$	Rotation matrix from a_l frame to a_0 frame
C^{Ba_0}	Rotation matrix from a_0 frame to B frame
C^{Ba_l}	Rotation matrix from a_l frame to B frame

Variables and Functions

b (p_B , θ_B)	Position and orientation components of body reference frame (B), resolved in B frame itself
b	Semichord of airfoil
P_B	Inertial position of B frame, resolved in G frame

β (v_B , ω_B)	Body velocities, resolved in body reference frame (B), with its translational and angular components
ε ($[\varepsilon_x \quad \kappa_x \quad \kappa_y \quad \kappa_z]$)	Strain vector defined at each element, with its components: extension, twist curvature, bending curvatures about w_y and w_z axis, respectively
ε^0	Initial (prescribed) strain vector
q	Independent variables of the Equations of Motion
\mathbf{p}_w	Relative position of w frame with respect to B frame, resolved in B frame
\mathbf{p}_b	Relative position of b frame with respect to B frame, resolved in B frame
\mathbf{p}_{cm}	Inertial position of rigid fuselage's center of mass
$\mathbf{p}_{r_{cm}}$	Position of the rigid fuselage's center of mass with respect to B frame
\mathbf{v}_{cm}	Inertial velocity of rigid fuselage's center of mass
\mathbf{a}_{cm}	Inertial acceleration of rigid fuselage's center of mass
\mathbf{a}_B	Inertial acceleration of origin of B frame
\mathbf{p}_a	Inertial position of an arbitrary point on beam cross-section
\mathbf{p}_r	Position of an arbitrary point on beam cross-section with respect to B frame
\mathbf{v}_a	Inertial velocity of an arbitrary point on beam cross-section
\mathbf{a}_a	Inertial acceleration of an arbitrary point on beam cross-section
h	Column matrix defining absolute positions and rotations of nodes along beam reference line. Rotations are represented through w frame base vectors
h_r	Column matrix defining relative positions and rotations of nodes along beam reference line with respect to B frame. Rotations are represented through w frame base vectors
h_{r0}	Column matrix defining relative positions and rotations of the boundary node of a beam member

h^b	Column matrix defining absolute positions and rotations of nodes along beam reference line. Rotations are represented through b frame base vectors
h_r^b	Column matrix defining relative positions and rotations of nodes along beam reference line with respect to B frame. Rotations are represented through b frame base vectors
D^{bw}	Matrix consisting of direction cosines, which transforms h_r to h_r^b
D^{nm} ($m, n = 1, 2, 3, \dots$)	Matrix consisting of direction cosines, accounting for the break of beam reference line
$J_{h\varepsilon}$	Jacobians relating nodal positions/rotations and element strains
$J_{p\varepsilon}$	Jacobians relating nodal positions and element strains
$J_{\theta\varepsilon}$	Jacobians relating nodal rotations and element strains
J_{hb}	Jacobians relating nodal positions/rotations and B frame motions
J_{pb}	Jacobians relating nodal positions and B frame motions
$J_{\theta b}$	Jacobians relating nodal rotations and B frame motions
H_{hb}	Matrix consisting of influence from the Jacobian J_{hb} and body angular velocities ω_B
m_B	Mass of rigid fuselage
\mathbf{I}_B	Rigid fuselage's moment of inertia tensor about the origin point of B frame
\mathbf{I}_{cm}	Rigid fuselage's moment of inertia tensor about its center of mass
M_{RB}	Mass matrix of rigid fuselage
C_{RB}	Damping matrix of rigid fuselage
R_{RB}^{ext} ($\mathbf{F}_{RB}^{ext}, \mathbf{M}_{RB}^{ext}$)	External load vector applied on rigid fuselage
s	Beam coordinate
$m(s)$	Beam cross-sectional mass per unit span
ρ	Local density at an arbitrary point within beam cross-section

$M(s)$	Beam cross-sectional mass matrix
$A(s)$	Beam cross-section area
r_i ($i = x, y, z$)	Position of cross-sectional center of mass in local w frame
I_{ij} ($i, j = x, y, z$)	Beam cross-sectional mass moment of inertia
m_{rb}	Mass of rigid body attached to wings
M_{rb}	Discrete mass matrix of rigid body attached to wings
cg_i ($i = x, y, z$)	Position of rigid body's center of mass in local b frame
$I_{ij_{cg}}$ ($i, j = x, y, z$)	mass moment of inertia of rigid body, about its c.g. point
α	Stiffness-proportional damping coefficient
\mathbf{g}	Gravity acceleration vector
$c(s), k(s)$	Beam cross-sectional damping and stiffness matrices
K_e, C_e, M_e	Discrete element stiffness, damping, and mass matrices
$M_{FF}, M_{FB}, M_{BF}, M_{BB}$	Components of generalized mass matrix
$C_{FF}, C_{FB}, C_{BF}, C_{BB}$	Components of generalized damping matrix
K_{FF}	Components of generalized stiffness matrix
R_F, R_B	Components of generalized load vector
N, B_F, B_M	Influence matrices for gravity force, distributed forces and moments, respectively
F^{dist}, M^{dist}	Distributed forces and moments
F^{pt}, M^{pt}	Point forces and moments
$\bar{M}_{FF}, \bar{M}_{FB}, \bar{M}_{BF}, \bar{M}_{BB}$	Components of mass matrix of linearized system
$\bar{C}_{FF}, \bar{C}_{FB}, \bar{C}_{BF}, \bar{C}_{BB}$	Components of damping matrix of linearized system
\bar{K}_{FF}	Components of stiffness matrix of linearized system
Π	Energy functional of the system
Π^*	Modified energy functional with displacement constraints introduced through Lagrange Multipliers
$\lambda_{ca}, \lambda_{cr}$	Lagrange Multipliers for absolute and relative displacement constraints, respectively
λ_c	Total Lagrange Multipliers vector

K_{ca}, K_{cr}	Generalized stiffness matrices for absolute and relative displacement constraints, respectively
K_c	Total generalized stiffness matrix due to additional displacement constraints
R_{ca}, R_{cr}	Generalized load vector for absolute and relative displacement constraints, respectively
R_c	Total generalized load vector due to additional displacement constraints
ζ	Quaternions defining orientation of B reference frame
$\Omega(\beta)$	Coefficient matrix of the quaternion equations, which is a function of body (angular) velocities
ra	Location of beam reference axis within airfoil
d	The distance of mid-chord in front if the reference axis
δ	Flap deflection
\dot{y}, \dot{z}	Airfoil translational vecocity components resolved in a_0 frame
\ddot{y}, \ddot{z}	Airfoil translational acceleration components resolved in a_0 frame
$\dot{\alpha}$	Airfoil angular vecocity about a_{0x} axis
$\ddot{\alpha}$	Airfoil angular acceleration about a_{0x} axis
e_i ($i = 1, 2, 3$)	Unit vectors along local reference frame
λ_0	Inflow velocities
λ	Inflow states
l_{mc}, m_{mc}, d_{mc}	Nodal aerodynamic loads in a_l frame, evaluated at the mid-chord
l_{ac}, m_{ac}, d_{ac}	Nodal aerodynamic loads in a_l frame, evaluated at the aero-dynamic center
$c_{l\alpha}$	Lift curve slope
$c_{l\delta}, c_{m\delta}$	Lift and moment slopes due to flap defelction
c_{m0}, c_{d0}	Moment and drag coefficients
F^{aero}, M^{aero}	Aerodynamics loads that are rotated into B frame

F_1, F_2, F_3	Influence matrices in inflow equations
R_F^{aero}, R_B^{aero}	Flexible and rigid body components of generalized aero-dynamic loads
R_F^{grav}, R_B^{grav}	Flexible and rigid body components of generalized gravity loads
Q_1, Q_2, A	Matrices of the system equations in state-space form
ε_{sw}	Strain vector when (flat) bending curvature reaches the threshold value
t_{sw}	Time when the threshold bending curvature is reached
x_{sw}	System variables at the time when the threshold bending curvature is reached
r, η	Polar coordinates that determine the location of a point within the gust region
r_0	Radius of the gust region
t_g	Gust duration
$A(r, \eta, t)$	Function that determines the temporal- and spatial-distribution of gust amplitude
A_c	Gust amplitude at the center of region
n_E, n_N	Tuning parameters that determine the spatial-distribution of gust amplitude

Operators

$\mathbf{a} \cdot \mathbf{b}$	Dot product of vectors \mathbf{a} and \mathbf{b}
$\mathbf{a} \times \mathbf{b}$	Cross product of vectors \mathbf{a} and \mathbf{b}
$\langle \mathbf{a}, \mathbf{b} \rangle$	Inner product of vectors \mathbf{a} and \mathbf{b} (same as dot product)
$\mathbf{a} \otimes \mathbf{b}$	Outer product of vectors \mathbf{a} and \mathbf{b}
$(\cdot)_{/x_0}$	$\frac{d(\cdot)}{dx}\Big _{x_0}$ or $\frac{\partial(\cdot)}{\partial x}\Big _{x_0}$ for different variables

ABSTRACT

COUPLED NONLINEAR AEROELASTICITY AND FLIGHT DYNAMICS OF FULLY FLEXIBLE AIRCRAFT

by

Weihua Su

Chair: Carlos E. S. Cesnik

This dissertation introduces an approach to effectively model and analyze the coupled nonlinear aeroelasticity and flight dynamics of highly flexible aircraft. A reduced-order, nonlinear, strain-based finite element framework is used, which is capable of assessing the fundamental impact of structural nonlinear effects in preliminary vehicle design and control synthesis. The cross-sectional stiffness and inertia properties of the wings are calculated along the wing span, and then incorporated into the one-dimensional nonlinear beam formulation. Finite-state unsteady subsonic aerodynamics is used to compute airloads along lifting surfaces. Flight dynamic equations are then introduced to complete the aeroelastic/flight dynamic system equations of motion.

Instead of merely considering the flexibility of the wings, the current work allows all members of the vehicle to be flexible. Due to their characteristics of being slender structures, the wings, tail, and fuselage of highly flexible aircraft can be modeled as beams undergoing three dimensional displacements and rotations. New kinematic

relationships are developed to handle the split beam systems, such that fully flexible vehicles can be effectively modeled within the existing framework. Different aircraft configurations are modeled and studied, including Single-Wing, Joined-Wing, Blended-Wing-Body, and Flying-Wing configurations. The Lagrange Multiplier Method is applied to model the nodal displacement constraints at the joint locations.

Based on the proposed models, roll response and stability studies are conducted on fully flexible and rigidized models. The impacts of the flexibility of different vehicle members on flutter with rigid body motion constraints, flutter in free flight condition, and roll maneuver performance are presented. Also, the static stability of the compressive member of the Joined-Wing configuration is studied.

A spatially-distributed discrete gust model is incorporated into the time simulation of the framework. Gust responses of the Flying-Wing configuration subject to stall effects are investigated. A bilinear torsional stiffness model is introduced to study the skin wrinkling due to large bending curvature of the Flying-Wing.

The numerical studies illustrate the improvements of the existing reduced-order formulation with new capabilities of both structural modeling and coupled aeroelastic and flight dynamic analysis of fully flexible aircraft.

CHAPTER I

Introduction

1.1 Motivation

Flight has been a dream of humankind. Myths and legends about flight can be found in many ancient eastern and western cultures. Historically, many people made efforts to realize the dream. However, it was not until December 17th, 1903 that the first powered heavier-than-air flight took place. The vehicle built by the Wright brothers traveled one hundred and twenty feet in twelve seconds. Since then, aviation technologies have undergone vast improvements, and airplanes are widely used for civilian and military applications.

The vehicle in the first powered flight was structurally flexible. The pilot did not face aeroelastic problems due to the very low flight speed at that time. Since then, aircraft designs have developed with much stiffer wings, to meet higher performance requirements. Modern commercial transport and military fight aircraft feature high speed and even supersonic flight, which makes it necessary for the wings to be stiff to provide sufficient structural integrity, aeroelastic stability, and maneuverability. At the same time, stiffened wings bring the cost of increased structural weight.

Early human flight involved flexible aircraft to emulate birds, since birds can fly with little effort with their flexible wings. However, the modern stiff wing designs seem to have “betrayed” this thinking. An exception is the High-Altitude Long-Endurance

(HALE) vehicles, which feature light wings with a high-aspect ratio, in contrast to the common aircraft with stiff wings. HALE concepts are being developed for multiple applications, including environmental sensing, telecom relay, and military reconnaissance. The long and slender wings, by their inherent nature, can maximize lift to drag ratio. On the other hand, these wings may undergo large deformations under normal operating loads, exhibiting geometrically nonlinear behaviors.

In the last several years, the U.S. Air Force has been working on a new generation of the Intelligence, Surveillance, and Reconnaissance (ISR) platform, which is called “SensorCraft”. These are large HALE aircraft with a wing span of approximately sixty meters. At this moment, three basic platform shapes are being considered^[1]: Single-Wing, Joined-Wing, and Blended-Wing-Body configurations, as illustrated in Fig. 1.1.

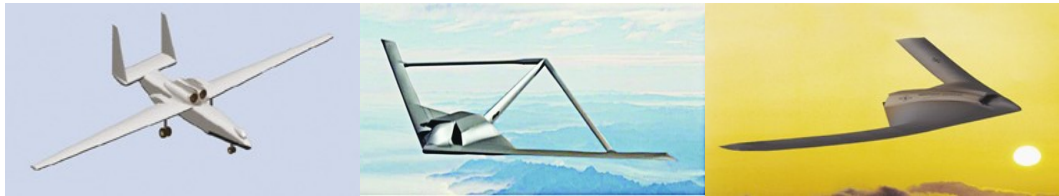


Figure 1.1: Three basic ISR SensorCraft concepts

The large overall vehicle size associated with the SensorCraft configurations may lead to a very flexible aircraft overall. In fact, long and slender fuselage and tail surfaces result in elastic coupling with the lifting surfaces. This directly impacts the trim of the vehicle, and the couplings between roll, yaw, and pitch require the use of nonlinear aeroelastic and flight dynamics analyses to predict vehicle response, design of control laws, and its overall guidance. Flexibility effects may make the response of the vehicle very different from rigid or linearized models would predict.

Furthermore, the long and slender wings of these configurations feature low natural frequencies, which can cause their oscillation to be coupled with the periodic plunging, pitching, or roll motion of the vehicle. The aeroelastic responses of the wings are therefore coupled with the rigid body motions. In addition, the flutter boundary of the wing structures in isolation cannot reflect the stability of the whole vehicle. Therefore,

flutter boundaries predicted in the free flight condition is more accurate when evaluating the stability of these vehicles.

Among the three SensorCraft concepts, the Joined-Wing configuration is the most unconventional one. From the elicitation of previous research, deformation of the structure of the Joined-Wing configuration at a certain location may produce large changes in angle of attack at other locations due to their complex structural coupling. Efforts to minimize structural weight may create aeroelastic instabilities that are not encountered in conventional aircraft designs. For Joined-Wing aircraft, the first sign of failure may be associated with the loss of elastic stability of the compressively loaded members as the structure is softened. Flutter and divergence may also become a problem in these members due to the reduction in effective stiffness as they go into compression. As the aircraft becomes more flexible, the geometric structural nonlinearities become more important and the lift distribution on the aircraft may be adversely affected.

Flying-Wings, including all-wing and tailless aircraft, belong to the concept of All Lifting Vehicles (ALV). The Blended-Wing-Body is this type of vehicle. Another type of Flying-Wing has been developed by AeroVironment for atmosphere research, such as Pathfinder and Helios vehicles. In contrast to the Blended-Wing-Body, these are highly flexible vehicles, which feature significantly different deformations when their payload is changed. The aeroelastic response of these vehicles is inherently nonlinear, due to the structural nonlinearity and the aerodynamic nonlinearity. An important event that should be mentioned is the accident of Helios prototype (HP3) on June 26th, 2003. The vehicle crashed due to gust disturbance. The number one recommendation from the investigation panel^[2] on this accident was an appropriate time-domain analysis method for this type of highly flexible vehicles considering multidisciplines.

In regard to the above reasons, it is necessary to develop a new approach for the modeling of the complex nonlinear structural system of fully flexible aircraft. With the fully flexible aircraft models, different nonlinear characteristics of the HALE vehicles can be studied and assessed. This dissertation will address some of these aspects, including the effects of induced flexibility of fuselage and tail on stability and roll performance of fully flexible aircraft, the characteristics of flutter boundary of highly

flexible aircraft considering coupled 6 rigid body degrees of freedom and fully flexible aircraft, and the time-domain dynamic response of the highly flexible vehicle subject to different nonlinear effects

1.2 Literature Review of Previous Work

This dissertation focuses on nonlinear aeroelastic and flight dynamic analysis of HALE aircraft, including some unconventional configurations. There is much ongoing research and literature in this area. This section will summarize some important and relevant studies.

A comprehensive overview about aero-servo-elasticity (ASE) was given by Friedmann^[3]. Therein, Friedmann emphasized the importance of aeroelasticity, especially nonlinear aeroelasticity, on understanding the characteristics of different types of aircraft. Challenges on HALE vehicles, including unconventional configurations were predicted as well.

Recently, Livne and Weishaar^[4] gave a detailed overview of the interactions between the unconventional aircraft concepts and the development of the aeroelastic technologies. Therein, they point out that the area of unmanned aerial vehicles (UAVs) is the most likely to develop unconventional aircraft designs, due to the lack of constraints on pilots. One characteristic of the UAVs operating at high altitude and long endurance is the local transonic aerodynamic effects, despite overall low operating speed. Another key aeroelastic lesson learned from the past is the coupling between the low-frequency rigid body motions and the high-aspect-ratio, low-bending-frequency wings. Livne^[5] also surveyed some emerging technologies and challenges in the area of aeroelasticity of fixed-wing aircraft.

In addition, Dowell, Edwards, and Strganac^[6] identified several physical mechanisms, including aerodynamic, structural, and store-induced sources, that may lead to nonlinear aeroelastic response of an aeroelastic system with different configurations. They suggested that studies of nonlinear aeroelasticity must sometimes consider a full

aircraft configuration. It was also suggested that the finite amplitude oscillation led by nonlinear flutter could be potentially exploited in a well designed system, to improve the performance and safety of aircraft.

1.2.1 Nonlinear Modeling and Analysis of HALE Aircraft

Nonlinear techniques for analysis of HALE aircraft have been previously studied by several aeroelasticians. van Schoor, Zerweckh and von Flotow^[7] have studied aeroelastic characteristics and control of highly flexible aircraft. They used linearized modes, including rigid body modes to predict the stability of the aircraft under different flight conditions. Their results indicate that unsteady aerodynamics and flexibility of the aircraft should be considered to correctly model the dynamic system.

Drela^[8] has modeled a complete flexible aircraft as an assemblage of joined nonlinear beams. In his work, the aerodynamic model was a vortex/source-lattice with wind-aligned trailing vorticity and Prandtl-Glauert compressibility correction. The nonlinear equation was solved by using a full Newton method. Through simplifications of the model, the computational size was reduced for iterative preliminary design.

Patil, Hodges, and Cesnik^[9, 10] have studied the aeroelasticity and flight dynamics of HALE aircraft. The results indicate that the large wing deformations due to the high-aspect-ratio structure may change the aerodynamic load distributions comparing to the initial shape. This brings significant changes to the aeroelastic and flight dynamic behaviors of the wings and overall aircraft. Therefore, the analysis results obtained through linear analysis based on the undeformed shape may not be valid in this case, since those effects can only be caught through nonlinear analysis. The vehicle should be first solved in its nonlinear steady state. Analysis can be carried out by linearizing the system about this state. The importance of geometric nonlinearity has also been studied in Refs. [11, 12, 13].

Chang, Hodges, and Patil^[14] have studied the flight dynamics of highly flexible aircraft. A nonlinear methodology was used for analyzing flight dynamics and aeroelastic stability of aircraft with slender structures. In this work, studies were carried out to

explore the effects of the large deformation due to the payloads and the parameters of fuselage and horizontal tails on the flight dynamic characteristics of a highly flexible aircraft. In addition, high sensitivity of some aeroelastic characteristics to the configuration parameters was also addressed. This high sensitivity was identified to be the result of strong coupling between the highly flexible structure and the aerodynamics.

More recently, Shearer^[15] has studied the nonlinear trajectory control of a highly flexible vehicle. In this work, flight dynamics were coupled with fully nonlinear aeroelastic equations. The coupling between the low frequency rigid body motions and wing structural oscillations was considered when developing the controller.

To summarize, for the highly flexible vehicles, the coupled effects between the large deflection due to vehicle flexibility and flight dynamics (*e.g.*, roll controllability) and other aeroelastic effects (*e.g.*, gust response, flutter instability) must be properly accounted for in a nonlinear aeroelastic formulation. A more complete analysis should be developed although previous work has made achievements towards accounting for these effects.

1.2.2 Joined-Wing Configurations

Among the SensorCraft concepts, the Joined-Wing configuration is of more interests to the researchers due to its potential advantages. It was first proposed by Wolkovitch^[16], who suggested that this new design would lead to possible weight savings and some aeroelastic benefits. However, the effects of structural deformation on the aerodynamic and aeroelastic responses are difficult to predict.

Livne^[17] presented a comprehensive survey on the design challenges of Joined-Wing aircraft. Therein, he presented a review of past works in Joined-Wing aeroelasticity and gave a qualitative discussion of their behavior in a multidisciplinary context. Much of the discussion in the paper dealt with structural and aeroelastic issues relating to the aft wing/tail. The in-plane loads due to structural deformation and changes in geometric stiffness may lead to non-intuitive aeroelastic behavior. Bending and twisting couplings of the entire structure cause natural frequencies and mode shapes to shift. The tendency

for buckling and divergence in the aft member is of major concern when trying to reduce weight. The finding of rear wing divergence to be more critical than flutter is counterintuitive, since the aft wing is supported at the joint. This phenomenon seems associated with a reduction in effective structural stiffness due to the in-plane compressive loads in the rear members. The geometry of the joint between forward and aft wings is also of importance because it plays a major role in how in-plane, bending, and torsion loads are transferred. For instance, a pinned joint may allow upward buckling of the aft wing, while a fixed rigid joint may allow the aft wing to buckle downward, since bending moments are transferred across the joint. Lin, Jhou and Stearman^[18] have studied the influence of joint fixity on the aeroelastic characteristics of the Joined-Wing. Their results show that the fixed joint provides the best characteristics.

Weight estimation studies of Joined-Wing aircraft have been done previously. The structural weight of a Joined-Wing and that of a Boeing 727 were compared by Samuels^[19]. His conclusion is that the Joined-Wing's structural weight is 12-22% lighter than that of a conventional configuration, while in Ref. [20], Gallman and Kroo conclude that the structural weight increases by 13% when including the buckling constraint of the aft wing. Therefore, Joined-Wing configurations are not guaranteed to be lighter than conventional ones. Research by Miura, Shyu, and Wolkovitch^[21] shows that the structural weight of a Joined-Wing strongly depends on the geometry and the structural arrangement of the wing. Blair and Canfield^[22] have described an integrated design process for generating high fidelity analytical weight estimates of Joined-Wing configurations. They suggest an integrated design process that can combine different software package, such as Nastran, PanAir, and integrate them through the Air Vehicles Technology Integration Environment (AVTIE), so that structures, aerodynamics and aeroelastic analysis are incorporated.

Structural optimization for Joined-Wing aircraft has been done by Kroo, Gallman and Smith^[20, 23, 24]. The wings were modeled as boxed-beams to study the effects of several parameters on the trimmed performance of Joined-Wing aircraft. In Ref. [23], the results show that the wings with similar aspect ratio joining at 60-75% of the front wing span are optimal for the given condition. Asymmetric material distribution leads to more

drag reduction than symmetric distribution. They also suggest using a fully stressed design method since it is computationally cheaper even though it produces a result that is slightly heavier and is with more direct operation cost (DOC). Roberts, Canfield and Blair^[25] have performed the structural optimization for a Joined-Wing SensorCraft. They identified some critical points in a flight index and optimized the SensorCraft with respect to these critical points. Their results indicate the necessity of nonlinear structural analysis. More recently, Rasmussen, Canfield and Blair^[26] have performed an optimum design for Joined-Wing aircraft that utilizes both structural and aerodynamic analysis. The Response Surface Method was employed within their scheme of design optimization.

Different technologies, in addition to the traditional ailerons, have been included in structural design of Joined-Wing SensorCraft to improve their performance. Active aeroelastic wing (AAW)^[27] technology has been applied in a Joined-Wing SensorCraft for the purpose of minimizing deformations of the antenna embedded in the wing skins, in addition to generating maneuver loads for the SensorCraft.

Cesnik and Brown^[28] have studied some aeroelastic characteristics of a Joined-Wing aircraft with active warping actuation for maneuver load generation. The active warping concept has its advantage over traditional ailerons in terms of structural integration. However, according to the studies of Ref. [28], the wing-warping design, which is based on the current anisotropic piezoelectric actuators (APA) technology, presents a terminal roll rate that is three times smaller than the aileron concept due to limited actuator authority.

Cesnik and Su^[29] have extended the above work by considering the flexibility of the fuselage and vertical tails. Stability and roll maneuverability (using traditional aileron only) were compared for models with different flexibility levels. The results have shown that the structural coupling between the vertical tails and wings may bring significant complexity and changes to the aeroelastic performances.

Meanwhile, Demasi and Livne^[30] studied the effects of structural nonlinearity on the divergence and linearized flutter predictions of a Joined-Wing configuration. In this work, a nonlinear updated Lagrange formulation for the structures was used, which was

coupled with a linear aerodynamic model. The researchers continued their work by using a structural modal order reduction method to simplify the nonlinear structural problem for the Joined-Wing configuration^[31]. Challenges in capturing the nonlinear deformation and internal stresses have been found when using the modal reduction. However, the attractive aspect of this method lies in the widespread use of modally based generalized aerodynamic matrices generated by established aerodynamic codes. In Ref. [32], Demasi and Livne presented analysis of a Joined-Wing configuration through coupled full-order (rather than modal-based) linear unsteady aerodynamics and full-order geometrically nonlinear structures. Static divergence, linear and nonlinear flutter speed, and time domain simulations were performed through this method. Effects of the rigidity of the joint and wings were discussed.

Weishaar and Lee^[33] have also studied a high aspect ratio Joined-Wing vehicle. Their research shows the importance of weight and c.g. location on the effect of body freedom flutter. In Ref. [34], a comprehensive parametric study has been carried out for exploring the characteristic of flutter boundaries of a Joined-Wing configuration with constrained and free rigid body motions. A design optimization scheme for the Joined-Wing configuration was also discussed in this work.

1.2.3 Flying-Wing Configurations

As a tailless configuration, the Flying-Wing is also an unconventional aircraft. Northrop made important contributions^[35] to the development of Flying-Wings in the United States. Northrop's first Flying-Wing model, N-1M, took flight in 1940. After that, Northrop made more than 10 innovative designs, and the B-2 is the more recent example of a Flying-Wing vehicle. Other Flying-Wing concepts have been developed, such as AeroVironment's Pathfinder and Helios (for atmosphere research, see Fig. 1.2), and Boeing/NASA's Blended-Wing-Body (for transportation). The Blended-Wing-Body configuration has been proposed as a solution for commercial transport planes^[36]. The advantage results from a double deck cabin that extends spanwise, providing structural and aerodynamic overlap with the wing. This reduces the total wetted area of the airplane

and allows a long wing span to be achieved, since the deep and stiff center body provides efficient structural wingspan.



Figure 1.2: Pathfinder-Plus and Helios as samples of highly flexible Flying-Wings (photo courtesy of NASA Dryden Flight Research Center)

Many researchers have addressed particular issues on the analysis and design of Flying-Wings. Weisshaar and Ashley^[37] have studied the static aeroelasticity of Flying-Wings, including instabilities such as divergence and large twist and bending that may lead to loss of control effectiveness.

Fremaux, Vairo and Whipple^[38] identified some of the parameters that cause a Flying-Wing configuration to be capable of sustaining a tumbling motion through the use of dynamically scaled generic models. In their work, effects due to the change of mass distribution and wing sweep angle were presented.

Esteban^[39] and his coworkers have performed the static and dynamic analysis of a Flying-Wing. They conclude that by selecting the correct winglet parameters, such as leading edge sweep, taper ratio, winglet area, effective moment arm, and vertical coordinate of the mean aerodynamic center of the winglet, a Flying-Wing vehicle can be constructed so that the desired lateral stability characteristics can be achieved.

Mialon *et al.*^[40] have performed aerodynamic optimization of subsonic Flying-Wing configurations. In their work, CFD codes developed at ONERA were used for the analysis. Manual modifications and numerical optimization were both used during their design process. They also designed a new family of airfoils, which was better suited for their specific Flying-Wing vehicle. The importance of geometric parameters, such as the sweep angle at the leading edge, the aspect ratio or shape of the generated airfoils was investigated as well.

Sevant, Bloor and Wilson^[41] have also performed the design of a subsonic Flying-Wing, aiming at maximum lift. The Response Surface Method was applied to solve the problem caused by the local minima, since the optimization problem was quite complex.

Love *et al.*^[42] have studied the body freedom flutter of a high aspect ratio Flying-Wing model. Their results indicate that the body freedom flutter is an issue over lower altitude portions of the flight envelop and that active flutter suppression should be considered.

Research about Blended-Wing-Body aircraft has been conducted with various focuses. Liebeck^[43] discussed some challenging issues in terms of the design of Blended-Wing-Body concepts, including the size and application commonality, design cruise Mach number, and flight mechanics.

Mukhopadhyay^[44] have studied structural design of a Blended-Wing-Body fuselage for weight reduction. In his work, he designed and analyzed different efficient structural concepts for pressurized fuselage design of Blended-Wing-Body type flight vehicles. His results indicate that efficient design of non-cylindrical pressurized structure is vital for non-conventional vehicles. Due to penalty of structural weight, advanced geometric configurations for stress balancing and composite materials are essential.

Wakayama^[45, 46] used Boeing Company's Wing Multidisciplinary Optimization Design (WingMOD) code to perform Blended-Wing-Body designs. He also identified some challenges and promises of Blended-Wing-Body optimization^[47].

Ko et al.^[48] performed multidiscipline design optimization of a Blended-Wing-Body transport aircraft with distributed propulsion. In their model, a small number of large engines were replaced with a moderate number of small engines and part of the engine exhaust was ducted to exit out along the trailing edge of the wing. They also integrated the model describing the effects of this distributed propulsion concept into an MDO formulation, and exhaust designs that could increase propulsive efficiency were studied.

For the SensorCraft applications, Beran *et al.*^[49] performed static nonlinear aeroelastic analysis of a Blended-Wing-Body. They used a high-fidelity computational process to assess the contributions of aerodynamic nonlinearities to the transonic air loads sustained by a Blended-Wing-Body with different static aeroelastic deflections. The structural deflections prescribed in the nonlinear analysis were obtained from linear methodology. Recently, Northrop Grumman created a wind tunnel model^[50] under the U.S. Air Force's High Lift over Drag Active (HiLDA) Wing program to study the aeroelastic characteristics of Blended Wing Body for a potential SensorCraft concept.

In 1994, NASA and members from industry initiated the Environmental Research Aircraft and Sensor Technology (ERAST) program aimed at developing UAV capabilities for long duration and very high altitude flights. AeroVironment's Helios aircraft, which was a type of very flexible Flying-Wing aircraft, was one of the several UAVs developed under the NASA ERAST program. The accident of the Helios prototype^[2] indicated that these long, slender Flying-Wing vehicles can be very sensitive to disturbance.

In recent years, flight dynamic and aeroelastic analysis of highly flexible (Helios-like) Flying-Wings have received special attention from researchers. It is well established that the deformation of these vehicles is dependent on both the mission profile and operating conditions. Under certain operating conditions, the aircraft's deformed shape can be significantly different from its undeformed one. In this case, the aeroelastic analysis must be based on the actual trimmed conditions. The large local angle of attack and dihedral angle associated with the large deformations may cause vehicle instability

under disturbances or gust loads. Therefore, the dynamic response of highly flexible Flying-Wing vehicles considering different nonlinear effects is still an open problem.

Patil and Hodges^[51] have studied the flight dynamics of a Flying-Wing. Due to the high flexibility of the configuration, the vehicle undergoes large deformation at its trimmed condition when fully loaded. According to their study, the flight dynamic characteristics of the deformed vehicle under heavy payload conditions presents unstable phugoid mode. The classical short-period mode does not exist. In this work, the nonlinear time-marching simulation was performed with no stall effects, and no other simulation other than the response to aileron perturbation was presented.

Su and Cesnik^[52] have considered stall effects through simplified static behavior of lift and pitching moment after some critical angle of attack. An asymmetric distributed gust model was applied to the time domain simulations to learn the behaviors of the Flying-Wing configuration under such perturbations. Bilinear torsional stiffness changes due to wrinkling of the skin were addressed as well.

From the other point of view, analysis of linear gust responses for a Flying-Wing vehicle has been presented by Patil and Taylor^[53], where the responses with continuous gust were solved in frequency domain. Continuing with this work, Patil^[54] has also studied the nonlinear gust responses of the Flying-Wing vehicle in the time domain.

Wang *et al.*^[55] have studied a Flying-Wing using a geometrically exact beam model coupled with an unsteady vortex lattice aerodynamic model. Critical instabilities were identified under some flow conditions.

1.2.4 Simulation of Gust Responses

Gusts are random in nature. They can affect different aspects of the aircraft's operation, such as its dynamic loads, flight stability and safety, and controls^[56]. In a high-fidelity analysis, a random gust is represented by a continuous model. However, discrete gust models are also used due to their simplicity (also mandated by FAR). The main difference between the continuous and discrete gust analysis is that the former is

statistical while the latter is deterministic^[57]. The simplest gust model is based on one single discrete gust, such as “one-minus-cosine” gust speed profile disturbing the airplane’s plunging motion. Statistical discrete gust (SDG) was developed more recently. For example, Lee and Lan^[58] used experimental nonlinear unsteady aerodynamics to determine the maximum aircraft response to random gusts. In their investigation, the gust model is characterized by von Karman’s power spectral density (PSD) function. They also used linear aerodynamic loads, for the purpose of comparison. The results show that the more realistic nonlinear unsteady aerodynamic model produces at least 50-60% higher maximum lift response than the linear model.

1.2.5 Nonlinear Aeroelastic Simulation Environment

From the previous review, it is evident that a geometrically nonlinear beam formulation is required for the structural modeling of HALE vehicles. In practice, geometric nonlinearity has become one focus of investigations of slender structures, and many kinematic relationships for nonlinear beams have been developed. Moreover, to accurately model the nonlinear effects of HALE vehicles, one may need a framework with nonlinear beam formulation coupled with aerodynamics.

In the process of analyzing a three-dimensional beam, a one-dimensional analysis is used along with a two-dimensional analysis that determines the cross-sectional properties. One can find many theories that address the two-dimensional cross-sectional analysis. Successive contributions can be found, including prismatic beams^[59], beams with initial curvature and twist^[60], beams with non-perpendicular cross-sectional planes^[61], beams with arbitrary deformation modes^[62], beams with transverse shear effects^[63, 64], and more recently, thin-walled beams^[65], general beams^[66] and active materials embedded in beams^[67], where Ref. [67] is the implementation of the Variational-Asymptotic Beam Sectional (VABS) analysis method discussed in Ref. [68].

In one-dimensional beam analysis, MSC.Nastran^[69], which is a displacement-based commercial finite element solver, has been enhanced to model the nonlinearities of the structures, including geometric nonlinearities, material nonlinearities, and contact

problems. For beams undergoing large rotations, such that nonlinear terms in curvature expressions are no longer negligible, the updated Lagrange formulation is employed.

A nonlinear intrinsic formulation for the dynamics of beams with initial curvatures has been presented by Hodges^[70], and implemented in Ref. [71]. This beam theory is characterized by mixed-form formulations, where displacements and strains are both considered as independent variables. Ref. [72] has applied this formulation for the time-domain analysis of slender rotors. In Ref. [73], computational schemes for the dynamics of a nonlinear elastic system have been presented. This scheme is based on time-discontinuous Galerkin approximations. High-frequency numerical dissipation is also obtained in this scheme.

More recently, Patil *et al.*^[9, 10] have developed a formulation for the complete modeling of a HALE type vehicle. As discussed before, nonlinear wing deformation has been identified as the driving reason that brings significant change in flight dynamic and aeroelastic characteristics of the wing and the whole vehicle.

Palacios and Cesnik^[67, 74, 75, 76, 77] have developed an analysis framework based on mixed-form beam theory, which can model slender beams with embedded piezoelectric materials. The low-order formulation can provide high accuracy for the modeling, design, and analysis of active slender structures.

Displacement-based or mixed-form beam theories may be used for different applications with different emphasis. One aspect that should be considered during the structural analysis is the compatibility of the selected formulation. Currently, analysis always includes multiple disciplines, including structures, control, and aerodynamics. It will be more convenient if the theory selected for structural modeling and analysis may facilitate the analysis of controls and aerodynamics. It is natural that a strain-based formulation is preferred since strains are the variable that can be measured by the strain gauges in control study. In addition to this advantage, a strain-based formulation will show great computational efficiency, since the degrees of freedom are reduced compared to the displacement-based or mixed-form formulations. In view of the above, a low-order,

strained based beam theory is necessary to be developed to model the nonlinear behavior of slender structures and facilitate control studies.

A strain-based beam formulation was originally developed by Cesnik and Brown^[28, 78, 79] for the modeling of highly flexible aircraft with embedded active materials. In those works, the aircraft's high-aspect-ratio wings were modeled as slender beams, whereas the fuselage was treated as a rigid body. The two-dimensional finite state inflow theory from Peters *et al.*^[80, 81] was used for unsteady aerodynamic modeling. An explicit integration method was implemented for the time marching solutions.

Following the initial contribution on the strain-based framework, Cesnik and Su^[29, 82] have introduced flexibility of fuselage and vertical tails to the analysis. A split beam formulation was developed, to gain the capability of required modeling and analysis. Stability and maneuverability characteristics were studied for the fully flexible vehicles. Su and Cesnik^[52] have also studied the dynamic responses of a highly flexible Flying-Wing by incorporating a discrete gust model. Shearer and Cesnik^[15, 83, 84] completed the flight dynamic equations and updated the integration scheme with an implicit modified Newmark Method, which can provide long term numerical integration stability, compared to the previous explicit method. Nonlinear trajectory control schemes were developed for trajectory control of highly flexible aircraft.

1.3 Outline of this Dissertation

This dissertation will present the completed theoretical development in the strain-based aeroelastic analysis framework. Improvement to the modeling and analyzing capability of the framework will be demonstrated with numerical studies. Nonlinear aeroelastic and flight dynamic characteristics will be explored and discussed for different highly flexible aircraft configurations.

Chapter II introduces the nonlinear differential equations for the coupled aeroelastic and flight dynamic systems. The three-dimensional beam deformations are represented by strain-based beam elements. Two-dimensional finite state inflow unsteady

aerodynamics couples with nonlinear beams. More general kinematic relationships are developed to model the split beam system as well as the single beam system. To handle the absolute and relative nodal displacement constraints, a formulation is developed utilizing the variation of energy functional, where the constraints are introduced into the functional through Lagrange Multipliers. The system's partial differential equations are then augmented with a set of algebraic equations. Formulations for modeling some other nonlinear aspects are also developed, such as follower loading cases and bilinear stiffness. After that, a discrete gust model is introduced for simulation of gust response.

Chapter III gives the overview of the implemented numerical analysis framework – The University of Michigan’s Nonlinear Aeroelastic Simulation Toolbox (UM/NAST). Contributions from different researchers are summarized. A block diagram is presented to exemplify the main functions of the framework. Details on model initialization, static and dynamic simulations, and stability analysis are introduced. This chapter will be able to provide a break-in point for the user to understand and use the code.

Chapter IV presents the numerical verification of the newly developed structural and aeroelastic formulations. The enhanced structural modeling capabilities are first evaluated for accuracy. In doing so, different beam configurations are created and tested with static and dynamic loading cases. Comparisons are made between current results and those from the commercial finite element software MSC.Nastran. As for the aerodynamic formulations, the current linear flutter analysis implementation is first compared with the previous published results, to verify the consistency between the current and previous UM/NAST implementations. The new implementation of nonlinear flutter formulations for both constrained and free flight vehicles are then verified through the time domain simulation within UM/NAST.

Chapter V presents the numerical analysis results. Four baseline aircraft models are introduced. The numerical studies are carried out in both time and frequency domains. Stability analysis, roll responses, and gust responses of different types of vehicles are presented.

Finally, Chapter VI presents the concluding remarks from the numerical studies and the key contributions of this work. Recommendations for the future work are made in terms of structural and aerodynamic modeling capability, analysis capability, and computational efficiency and accuracy of the strain-based aeroelastic analysis framework.

CHAPTER II

Theoretical Formulation

This chapter begins with a brief review of the aircraft modeling in previous work and brings out the new requirements of fully flexible aircraft. The strain-based beam formulation used in the previous work is introduced and then enhanced to meet the requirements. The elastic equations of motion are derived by applying the energy methods (the Principle of Virtual Work and variation of energy functional). A distributed beam system, used for representing the fully flexible aircraft, is modeled by introducing new kinematic relationships. The Lagrange Multiplier Method is applied for modeling of additional nodal displacement constraints. The large three-dimensional deformations of slender beams are then governed by a set of differential-algebraic equations. With this formulation, arbitrary fully flexible vehicles can be modeled. Quaternions are used to represent the spatial orientation of the vehicle. The equations of aerodynamics are introduced to complete the aeroelastic equations of motion for the vehicle. The nonlinear equations of motion are linearized to facilitate the stability analysis. Lastly, formulations for bilinear stiffness, simplified stall models, and discrete gust models are introduced.

2.1 Overview: Modeling of Fully Highly Flexible Aircraft

In previous work, complete vehicles have been modeled such that various nonlinear aeroelastic analyses, including the effects of large wing deformations, the impact of wing flexibility on the vehicle stability, and nonlinear control studies could be

performed. In those studies, the long, slender wings and horizontal tails were modeled as nonlinear beams, which may have dihedral, sweep, and prescribed deformations. A finite state unsteady aerodynamic model is incorporated to complete the aeroelastic system equations, which can represent the aerodynamic forces and moments on those lifting surfaces undergoing large deformations. Figure 2.1 describes a typical modeling scheme of a highly flexible vehicle.

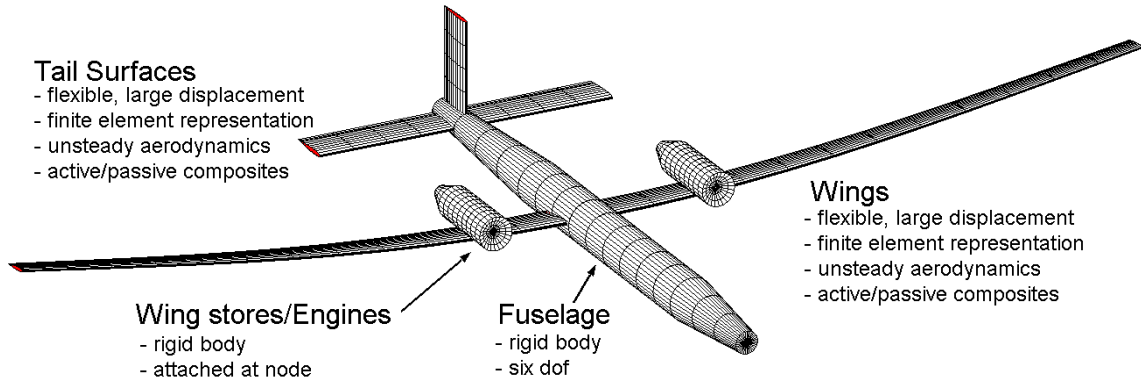


Figure 2.1: Modeling scheme of a highly flexible vehicle

The above representation neglects the impacts of flexibility of the fuselage and vertical tail, which is acceptable for most types of vehicles. However, this is not the case for the Joined-Wing configuration, whose front and aft wings are structurally coupled with the vertical tail and fuselage, as described in Fig. 2.2.

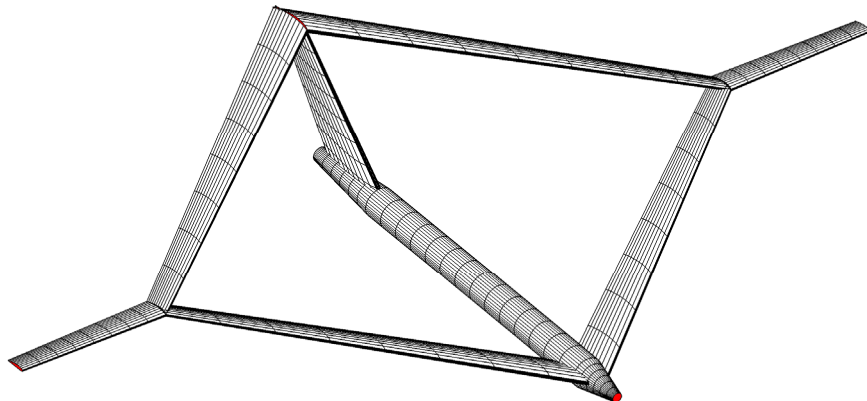


Figure 2.2: Example of a Joined-Wing aircraft

To model a fully flexible aircraft, the fuselage and the vertical tail are both modeled as slender beams, similar to the wings. Assume the beam reference line starts from one reference point on the fuselage, as shown in Fig. 2.3, it will split at the root of the wings and go to the different directions following the wing span. Therefore, it is necessary to build such a split beam system that may model the connection at the roots of the wings to the fuselage and similar situations. This modeling capability is achieved by modifying the kinematic relationships as will be described in details below.

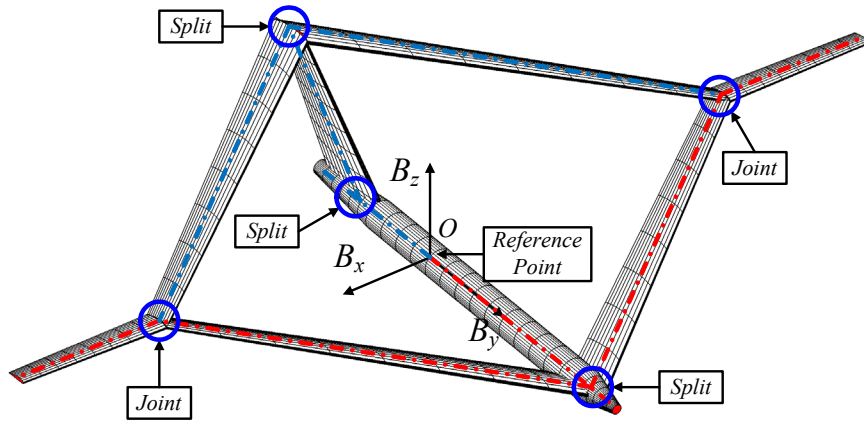


Figure 2.3: Aircraft with beam reference line representations

For Joined-Wing configurations, the connections between front and aft wings also need some special treatment. As will be detailed later, the finite element formulations are strain-based, where the beam extension strain and bending/twist curvatures are independent degrees of freedom. Therefore, at the joint location, an approach is necessary to impose translational and rotational displacement constraints that are compatible with the strain formulations. In previous work^[79], this problem was solved by using the Penalty Method. However, the introducing of a large penalty number makes the system matrices ill-conditioned, which may result in numerical instability and difficulty in solving eigenvalue problems. In current work, the Lagrange Multiplier Method will be applied to model the additional constraints, which gives quite good modeling capability and numerical stability.

Engine thrust is required to balance drag forces. Assume engines are rigidly mounted to one point on beam structures (wings or fuselage), the engine loads may keep

their relative direction unchanged with respect to the mounting point. Due to their flexibility, the wings or fuselage may undergo large deformations at operating conditions. Therefore, the engine loads are essentially follower loads, instead of dead loads. This type of nonlinear loading is appropriately modeled in the current work.

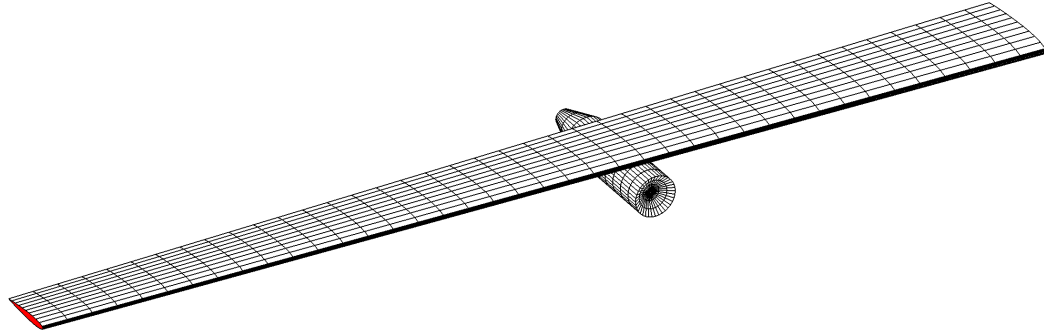


Figure 2.4: Rigid engine unit attached to elastic wing



Figure 2.5: Closeup of the Helios prototype showing the wing structure (photo courtesy of NASA Dryden Flight Research Center)

One particular aspect that can potentially bring some interesting nonlinear effects is associated with the wrinkling of the wing skin for highly flexible Flying-Wings (*e.g.*,

the Helios Prototype). As shown in Fig. 2.5, to achieve very light constructions, typical wing structure of such vehicles is composed of a main (circular) spar with ribs attached to it along specific span stations. A very light and thin film is used to close the airfoil and provide the desired airfoil shape. The resulting structure can be represented by a closed cell beam section. Significant torsional stiffness comes from the presence of the skin. However, during large bending deformations, the skin may be un-stretched and wrinkle. The local torsional stiffness will drop as a result of the skin wrinkling. Once the bending curvature is reduced, the skin is stretched again and the original configuration may be recovered. This additional nonlinear effect can alter the vehicle aeroelastic response during flight. A bilinear stiffness model is introduced for this analysis.

2.2 Elastic System Equations of Motion

The equations of motion for the highly flexible beams are derived through energy methods: the Principle of Virtual Work and variation of energy functional. Rigid body equations are coupled with the elastic equations. Due to the nature of the objectives of this formulation, the modeling and analysis of a three-dimensional beam structure is decomposed as a combination of two-dimensional cross-sectional analysis and one-dimensional beam analysis. The discussion of cross-sectional analysis is not included in this dissertation. It can be accomplished through any cross-sectional analysis code package, such as VABS^[68]. The results from two-dimensional analysis – cross-sectional inertias and rigidities – are fed into the one-dimensional beam analysis. With the formulation, the structures are modeled with fully coupled three-dimensional extensional, twisting, and bending deformations.

2.2.1 Fundamental Descriptions

As shown in Fig. 2.6, a global (inertial) frame G is defined, which is fixed on the ground. A body frame B is built in the global frame to describe the vehicle position and orientation, with B_x pointing to the right wing, B_y pointing forward, and B_z being cross product of B_x and B_y . The position and orientation of the B frame can be defined as

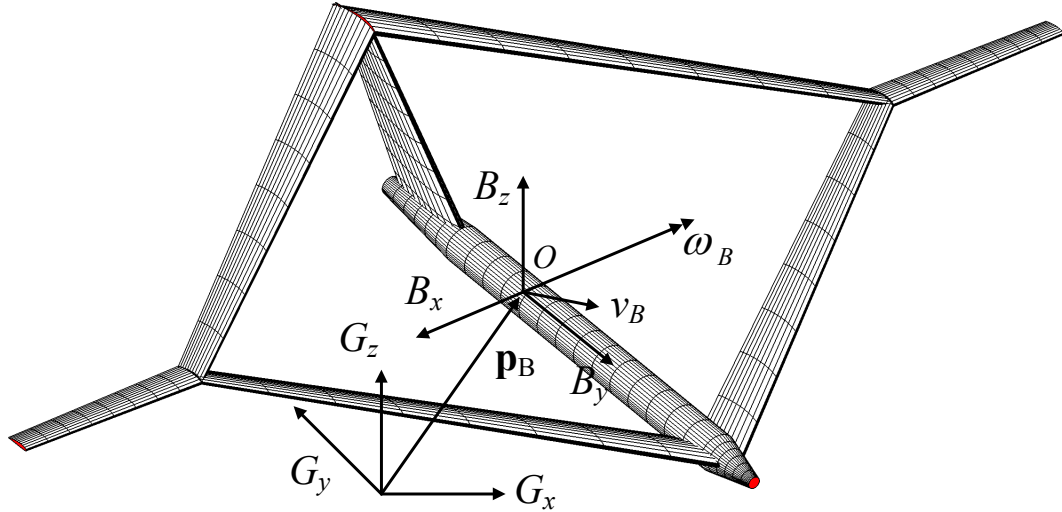


Figure 2.6: Global and Body reference frames

$$b = \begin{bmatrix} p_B \\ \theta_B \end{bmatrix} \quad (2.1)$$

where p_B and θ_B are body position and orientation, both resolved in the body frame. The corresponding body velocity and acceleration are given as

$$\begin{aligned} \dot{b} &= \beta = \begin{bmatrix} \dot{p}_B \\ \dot{\theta}_B \end{bmatrix} = \begin{bmatrix} v_B \\ \omega_B \end{bmatrix} \\ \ddot{b} &= \dot{\beta} = \begin{bmatrix} \ddot{p}_B \\ \ddot{\theta}_B \end{bmatrix} = \begin{bmatrix} \dot{v}_B \\ \dot{\omega}_B \end{bmatrix} \end{aligned} \quad (2.2)$$

Note that the origin of the body frame does not have to be the location of the vehicle's center of gravity.

As described in Fig. 2.7, a local beam frame (w) is built within the body frame, which is used to define the position and orientation of each node along the beam reference line. \mathbf{w}_x , \mathbf{w}_y , and \mathbf{w}_z are base vectors of the beam frame, whose directions are pointing along the beam reference axis, toward the leading edge, and normal to the beam surface, respectively, resolved in the body frame.

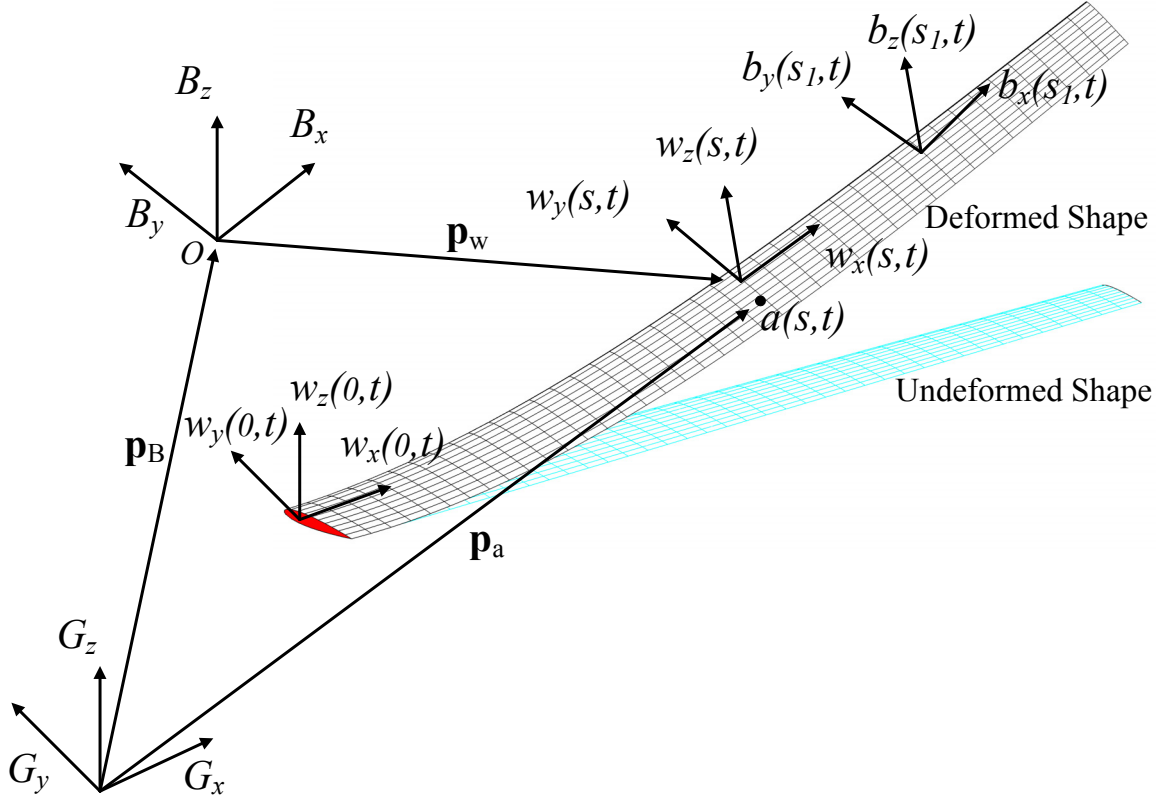


Figure 2.7: Basic beam reference frames

To facilitate the modeling process, another auxiliary reference frame (b) is also defined at each node. This frame is aligned with the body frame upon initialization. However, it may undergo both translational and rotational displacements due to beam deformations and rigid body motions. The b frame is useful for modeling rigid units attached to elastic members and relative nodal displacement constraints, which will be discussed in following sections.

To model the elastic deformation of slender beams, a new nonlinear beam element is developed. Each of the elements has three nodes and four degrees of freedom, which are extension, twist, and two bending strains of the beam reference line. This beam formulation described in this current work is named as strain-based formulation. Figure 2.8 exemplifies the deformations of constant-strain elements.

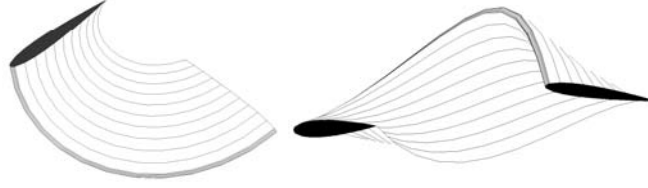


Figure 2.8: Deformations of constant-strain elements

The strain vector of an element can be denoted as ε , with the component of

$$\varepsilon = [\varepsilon_x \quad \kappa_x \quad \kappa_y \quad \kappa_z]^T \quad (2.3)$$

where ε_x is the extensional strain. κ_x , κ_y , and κ_z are twist of the beam reference line, bending about local w_y axis, and bending about local w_z axis, respectively.

The absolute position of a beam reference node is obtained by the following vector summation (refer to Fig. 2.7)

$$\mathbf{p}(s) = \mathbf{p}_B + \mathbf{p}_w(s) \quad (2.4)$$

where \mathbf{p}_B is the vector representing the position of the body frame as introduced in Eq. (2.1), \mathbf{p}_w is the vector representing the position of the local beam frame with respect to the body frame, which is a function of the beam coordinate s .

The absolute position and orientation of a beam node can be determined by a 12-by-1 matrix.

$$h^T(s) = [p^T(s) \quad w_x^T(s) \quad w_y^T(s) \quad w_z^T(s)] \quad (2.5)$$

In some cases, the nodal position and orientation information within the body frame is also necessary, which is

$$h_r^T(s) = [p_w^T(s) \quad w_x^T(s) \quad w_y^T(s) \quad w_z^T(s)] \quad (2.6)$$

It is easy to see that h_r is the displacement vector due to wing deformations, while h differs h_r with the position of the body reference frame.

Due to the nature of the strain-based formulation, the governing equations to be derived will solve for the curvatures of the beam reference line (ε) directly. The positions and rotations (h and h_r) are dependent variables, which can be recovered from curvatures through kinematic relationships (see Section 2.3).

With the elastic and rigid body degrees of freedom defined, the complete independent variables of the strain-based formulation are as follows

$$\begin{aligned} q = \begin{bmatrix} \varepsilon \\ p_B \\ b \\ \theta_B \end{bmatrix} &= \begin{bmatrix} \varepsilon \\ p_B \\ b \\ \theta_B \end{bmatrix}, & \dot{q} = \begin{bmatrix} \dot{\varepsilon} \\ \dot{p}_B \\ \dot{b} \\ \dot{\theta}_B \end{bmatrix} &= \begin{bmatrix} \dot{\varepsilon} \\ v_B \\ \dot{b} \\ \omega_B \end{bmatrix}, & \ddot{q} = \begin{bmatrix} \ddot{\varepsilon} \\ \ddot{p}_B \\ \ddot{b} \\ \ddot{\theta}_B \end{bmatrix} &= \begin{bmatrix} \ddot{\varepsilon} \\ \dot{v}_B \\ \ddot{b} \\ \dot{\omega}_B \end{bmatrix} \end{aligned} \quad (2.7)$$

The derivative and variation dependent variable h and h_r are related with those of the independent ones.

$$\delta h = J_{h\varepsilon} \delta \varepsilon + J_{hb} \delta b \quad \delta h_r = J_{h\varepsilon} \delta \varepsilon \quad (2.8)$$

$$dh = J_{h\varepsilon} d\varepsilon + J_{hb} db \quad dh_r = J_{h\varepsilon} d\varepsilon \quad (2.9)$$

$$\dot{h} = J_{h\varepsilon} \dot{\varepsilon} + J_{hb} \dot{b} = J_{h\varepsilon} \dot{\varepsilon} + J_{hb} \beta \quad \dot{h}_r = J_{h\varepsilon} \dot{\varepsilon} \quad (2.10)$$

$$\ddot{h} = J_{h\varepsilon} \ddot{\varepsilon} + J_{h\varepsilon} \dot{\varepsilon} + J_{hb} \dot{\beta} + J_{hb} \beta \quad \ddot{h}_r = J_{h\varepsilon} \ddot{\varepsilon} + J_{h\varepsilon} \dot{\varepsilon} \quad (2.11)$$

where

$$J_{h\varepsilon} = \frac{\partial h}{\partial \varepsilon} \quad J_{hb} = \frac{\partial h}{\partial b} \quad (2.12)$$

which are Jacobians obtained from kinematics^[15, 79].

2.2.2 Internal Virtual Work

Internal virtual work includes the contributions of inertia forces, internal strains and strain rates. For a complete vehicle, it may consist of both elastic members and rigid bodies (rigid fuselage and rigid non-structural inertia units attached to the elastic

members). The corresponding inertial virtual work is derived individually. All the above virtual work will need to be summated to represent the total internal virtual work of a complete vehicle.

Rigid Fuselage

As described in Fig. 2.9, the position of the rigid fuselage's center of mass point is given as

$$\mathbf{p}_{cm} = \mathbf{p}_B + \mathbf{p}_{r_{cm}} \quad (2.13)$$

Note that \mathbf{p}_B and $\mathbf{p}_{r_{cm}}$ are both resolved within the body frame (B). With the above definition, the velocity and acceleration of the center of mass are

$$\begin{aligned} \mathbf{v}_{cm} &= \mathbf{v}_B + \boldsymbol{\omega}_B \times \mathbf{p}_{r_{cm}} \\ \mathbf{a}_{cm} &= \dot{\mathbf{v}}_B + \dot{\boldsymbol{\omega}}_B \times \mathbf{p}_{r_{cm}} + \boldsymbol{\omega}_B \times (\mathbf{v}_B + \boldsymbol{\omega}_B \times \mathbf{p}_{r_{cm}}) \end{aligned} \quad (2.14)$$

The acceleration of origin point of the B frame is obtained by letting $\mathbf{p}_{r_{cm}}$ to be zero.

$$\mathbf{a}_B = \dot{\mathbf{v}}_B + \boldsymbol{\omega}_B \times \mathbf{v}_B \quad (2.15)$$

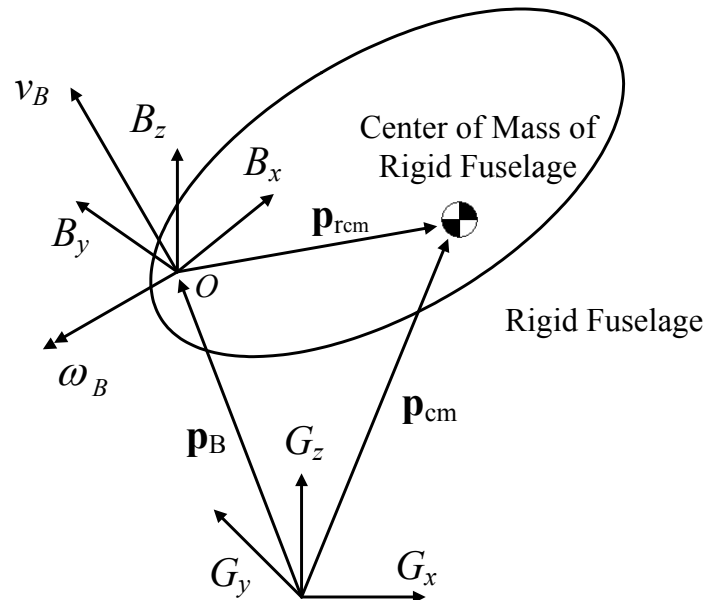


Figure 2.9: Rigid fuselage reference frames

Therefore, the virtual work applied on the rigid fuselage is

$$\begin{aligned}\delta W_{RB}^F &= \delta \mathbf{p}_B \cdot (-m_B \mathbf{a}_{cm} + \mathbf{F}_{RB}^{ext}) \\ \delta W_{RB}^M &= \delta \boldsymbol{\theta}_B \cdot \left[-\frac{d}{dt} (\mathbf{I}_B \cdot \boldsymbol{\omega}_B) - \mathbf{p}_{r_{cm}} \times (m_B \mathbf{a}_B) + \mathbf{M}_{RB}^{ext} \right]\end{aligned}\quad (2.16)$$

where \mathbf{F}_{RB}^{ext} and \mathbf{M}_{RB}^{ext} are external forces and moments about the origin point of the B frame. \mathbf{I}_B is the moment of inertia tensor about the origin point of the B frame, which can be derived from the moment of inertia about the center of mass.

$$\mathbf{I}_B = \mathbf{I}_{cm} + m_B \left[(\mathbf{p}_{r_{cm}} \cdot \mathbf{p}_{r_{cm}}) \mathbf{I} - \mathbf{p}_{r_{cm}} \otimes \mathbf{p}_{r_{cm}} \right] \quad (2.17)$$

Substitute Eqs. (2.14) and (2.15) into (2.16), it yields

$$\begin{aligned}\delta W_{RB}^F &= \delta \mathbf{p}_B \cdot \left[-m_B \dot{\mathbf{v}}_B - m_B \dot{\boldsymbol{\omega}}_B \times \mathbf{p}_{r_{cm}} - m_B \boldsymbol{\omega}_B \times (\mathbf{v}_B + \boldsymbol{\omega}_B \times \mathbf{p}_{r_{cm}}) + \mathbf{F}_{RB}^{ext} \right] \\ \delta W_{RB}^M &= \delta \boldsymbol{\theta}_B \cdot \left[-\mathbf{I}_B \cdot \dot{\boldsymbol{\omega}}_B - \boldsymbol{\omega}_B \times (\mathbf{I}_B \cdot \boldsymbol{\omega}_B) - \mathbf{p}_{r_{cm}} \times m_B (\dot{\mathbf{v}}_B + \boldsymbol{\omega}_B \times \mathbf{v}_B) + \mathbf{M}_{RB}^{ext} \right]\end{aligned}\quad (2.18)$$

For two vectors defined in three-dimensional space, one can rewrite a cross product between those two vectors in terms of pure matrix multiplication as the product of a skew-symmetric matrix and a vector:

$$\begin{aligned}\mathbf{m} \times \mathbf{n} &= [\tilde{m}] \{n\} = \begin{bmatrix} 0 & -m_3 & m_2 \\ m_3 & 0 & -m_1 \\ -m_2 & m_1 & 0 \end{bmatrix} \begin{bmatrix} n_1 \\ n_2 \\ n_3 \end{bmatrix} \\ &= [\tilde{n}]^T \{m\} = \begin{bmatrix} 0 & -n_3 & n_2 \\ n_3 & 0 & -n_1 \\ -n_2 & n_1 & 0 \end{bmatrix}^T \begin{bmatrix} m_1 \\ m_2 \\ m_3 \end{bmatrix}\end{aligned}\quad (2.19)$$

where

$$[\tilde{m}] \equiv \begin{bmatrix} 0 & -m_3 & m_2 \\ m_3 & 0 & -m_1 \\ -m_2 & m_1 & 0 \end{bmatrix}, \quad \{n\} \equiv \begin{bmatrix} n_1 \\ n_2 \\ n_3 \end{bmatrix} \quad (2.20)$$

With the above notations, Eq. (2.18) can be written into matrix form

$$\begin{aligned}\delta W_{RB} &= \begin{bmatrix} \delta p_B^T & \delta \theta_B^T \end{bmatrix} \left\{ -M_{RB} \begin{bmatrix} \dot{\nu}_B \\ \dot{\omega}_B \end{bmatrix} - C_{RB} \begin{bmatrix} \nu_B \\ \omega_B \end{bmatrix} + \begin{bmatrix} F_{RB}^{ext} \\ M_{RB}^{ext} \end{bmatrix} \right\} \\ &= \delta b^T (-M_{RB} \dot{\beta} - C_{RB} \beta + R_{RB}^{ext})\end{aligned}\quad (2.21)$$

where

$$M_{RB} = \begin{bmatrix} m_B I & m_B \tilde{p}_{r_{cm}}^T \\ m_B \tilde{p}_{r_{cm}} & I_B \end{bmatrix}, \quad C_{RB} = \begin{bmatrix} m_B \tilde{\omega}_B & m_B \tilde{\omega}_B \tilde{p}_{r_{cm}}^T \\ m_B \tilde{p}_{r_{cm}} \tilde{\omega}_B & I_B \tilde{\omega}_B \end{bmatrix}, \quad R_{RB}^{ext} = \begin{bmatrix} F_{RB}^{ext} \\ M_{RB}^{ext} \end{bmatrix} \quad (2.22)$$

Elastic Members

Refer to Fig. 2.7, the location of an arbitrary point (*a*) on the beam cross-section can be written as:

$$\mathbf{p}_a = \mathbf{p}_B + \mathbf{p}_w + x\mathbf{w}_x + y\mathbf{w}_y + z\mathbf{w}_z \quad (2.23)$$

where constant $[x \ y \ z]$ is the position of the point in the local beam frame (*w*). Note that the wing cross-section is assumed to maintain its shape while undergoing translations and rotations. \mathbf{p}_a may also be written as offsets from either the *B* frame or the *w* frame, which becomes

$$\mathbf{p}_a = \mathbf{p}_B + \mathbf{p}_r = \mathbf{p} + x\mathbf{w}_x + y\mathbf{w}_y + z\mathbf{w}_z \quad (2.24)$$

where

$$\mathbf{p}_r = \mathbf{p}_w + x\mathbf{w}_x + y\mathbf{w}_y + z\mathbf{w}_z, \quad \mathbf{p} = \mathbf{p}_B + \mathbf{p}_w \quad (2.25)$$

With the above relationships, the velocity and acceleration of the arbitrary point can be written as follows

$$\begin{aligned}\mathbf{v}_a &= \dot{\mathbf{p}}_B + \dot{\mathbf{p}}_r + \boldsymbol{\omega}_B \times \mathbf{p}_r \\ \mathbf{a}_a &= \ddot{\mathbf{p}}_B + \ddot{\mathbf{p}}_r + \dot{\boldsymbol{\omega}}_B \times \mathbf{p}_r + \boldsymbol{\omega}_B \times \dot{\mathbf{p}}_r + \boldsymbol{\omega}_B \times (\dot{\mathbf{p}}_B + \dot{\mathbf{p}}_r + \boldsymbol{\omega}_B \times \mathbf{p}_r) \\ &= \ddot{\mathbf{p}} + \dot{\boldsymbol{\omega}}_B \times \mathbf{p}_r + \boldsymbol{\omega}_B \times \dot{\mathbf{p}}_r + \boldsymbol{\omega}_B \times (\dot{\mathbf{p}}_B + \dot{\mathbf{p}}_r + \boldsymbol{\omega}_B \times \mathbf{p}_r)\end{aligned}\quad (2.26)$$

Substitute Eqs. (2.23) to (2.25) into Eq. (2.26), the velocity and acceleration become

$$\begin{aligned}
\mathbf{v}_a &= \dot{\mathbf{p}} + x\dot{\mathbf{w}}_x + y\dot{\mathbf{w}}_y + z\dot{\mathbf{w}}_z + \boldsymbol{\omega}_B \times (\mathbf{p}_w + x\mathbf{w}_x + y\mathbf{w}_y + z\mathbf{w}_z) \\
\mathbf{a}_a &= \ddot{\mathbf{p}} + x\ddot{\mathbf{w}}_x + y\ddot{\mathbf{w}}_y + z\ddot{\mathbf{w}}_z + \dot{\boldsymbol{\omega}}_B \times (\mathbf{p}_w + x\mathbf{w}_x + y\mathbf{w}_y + z\mathbf{w}_z) \\
&\quad + \boldsymbol{\omega}_B \times [\dot{\mathbf{p}}_B + \boldsymbol{\omega}_B \times (\mathbf{p}_w + x\mathbf{w}_x + y\mathbf{w}_y + z\mathbf{w}_z)] \\
&\quad + 2\boldsymbol{\omega}_B \times (\dot{\mathbf{p}}_w + x\dot{\mathbf{w}}_x + y\dot{\mathbf{w}}_y + z\dot{\mathbf{w}}_z)
\end{aligned} \tag{2.27}$$

Note that the last term in the acceleration equation reflects the Coriolis effect. The infinitesimal virtual work applied on a unit volume is

$$\delta W_a = \delta \mathbf{p}_a \cdot (-\mathbf{a}_a \rho dA ds) \tag{2.28}$$

where

$$\delta \mathbf{p}_a = \delta \mathbf{p} + x\delta \mathbf{w}_x + y\delta \mathbf{w}_y + z\delta \mathbf{w}_z \tag{2.29}$$

Substitute Eqs. (2.27) and (2.29) into Eq. (2.28), it yields

$$\begin{aligned}
\delta W_a &= -(\delta \mathbf{p} + x\delta \mathbf{w}_x + y\delta \mathbf{w}_y + z\delta \mathbf{w}_z) \cdot \\
&\quad \left\{ \ddot{\mathbf{p}} + x\ddot{\mathbf{w}}_x + y\ddot{\mathbf{w}}_y + z\ddot{\mathbf{w}}_z + \dot{\boldsymbol{\omega}}_B \times (\mathbf{p}_w + x\mathbf{w}_x + y\mathbf{w}_y + z\mathbf{w}_z) \right. \\
&\quad + \boldsymbol{\omega}_B \times [\dot{\mathbf{p}}_B + \boldsymbol{\omega}_B \times (\mathbf{p}_w + x\mathbf{w}_x + y\mathbf{w}_y + z\mathbf{w}_z)] \\
&\quad \left. + 2\boldsymbol{\omega}_B \times (\dot{\mathbf{p}}_w + x\dot{\mathbf{w}}_x + y\dot{\mathbf{w}}_y + z\dot{\mathbf{w}}_z) \right\} \rho dA ds
\end{aligned} \tag{2.30}$$

The virtual work done by the inertia force along the beam coordinate s can be obtained by integrating Eq. (2.30) over each cross-section, which yields

$$\begin{aligned}
\delta W^{int}(s) &= -\delta h^T(s) \left\{ M(s) \begin{bmatrix} \ddot{p}_w(s) \\ \ddot{w}_x(s) \\ \ddot{w}_y(s) \\ \ddot{w}_z(s) \end{bmatrix} + M(s) \begin{bmatrix} I & \tilde{p}_w^T(s) \\ 0 & \tilde{w}_x^T(s) \\ 0 & \tilde{w}_y^T(s) \\ 0 & \tilde{w}_z^T(s) \end{bmatrix} \dot{\beta} \right. \\
&\quad \left. + M(s) \begin{bmatrix} \tilde{\omega}_B & 0 & 0 & 0 \\ 0 & \tilde{\omega}_B & 0 & 0 \\ 0 & 0 & \tilde{\omega}_B & 0 \\ 0 & 0 & 0 & \tilde{\omega}_B \end{bmatrix} \begin{bmatrix} I & \tilde{p}_w^T(s) \\ 0 & \tilde{w}_x^T(s) \\ 0 & \tilde{w}_y^T(s) \\ 0 & \tilde{w}_z^T(s) \end{bmatrix} \beta + 2M(s) \begin{bmatrix} 0 & \dot{\tilde{p}}_w^T(s) \\ 0 & \dot{\tilde{w}}_x^T(s) \\ 0 & \dot{\tilde{w}}_y^T(s) \\ 0 & \dot{\tilde{w}}_z^T(s) \end{bmatrix} \beta \right\}
\end{aligned} \tag{2.31}$$

where

$$\begin{aligned}
M(s) &= \int_{A(s)} \rho \begin{bmatrix} 1 & x & y & z \\ x & x^2 & xy & xz \\ y & yx & y^2 & yz \\ z & zx & zy & z^2 \end{bmatrix} dA \\
&= \begin{bmatrix} m & mr_x & mr_y & mr_z \\ mr_x & \frac{(I_{yy} + I_{zz} - I_{xx})}{2} & I_{xy} & I_{xz} \\ mr_y & I_{yx} & \frac{(I_{zz} + I_{xx} - I_{yy})}{2} & I_{yz} \\ mr_z & I_{zx} & I_{zy} & \frac{(I_{xx} + I_{yy} - I_{zz})}{2} \end{bmatrix} \quad (2.32)
\end{aligned}$$

m is the mass per unit span at each cross-section. $[r_x \ r_y \ r_z]$ is the position of the center of mass of the cross-section in the w frame. I_{ij} are cross-sectional inertial properties.

In Eq. (2.31), $[\ddot{p}_w(s) \ \ddot{w}_x(s) \ \ddot{w}_y(s) \ \ddot{w}_z(s)]^T$ is the second time derivative of $h_r(s)$ in Eq (2.6). It can be written in terms of the second time derivative independent variables using Eq. (2.11). In addition, the following relations are defined

$$J_{hb} \equiv \begin{bmatrix} I & \tilde{p}_w^T(s) \\ 0 & \tilde{w}_x^T(s) \\ 0 & \tilde{w}_y^T(s) \\ 0 & \tilde{w}_z^T(s) \end{bmatrix}, \quad \dot{J}_{hb} \equiv \begin{bmatrix} 0 & \dot{\tilde{p}}_w^T(s) \\ 0 & \dot{\tilde{w}}_x^T(s) \\ 0 & \dot{\tilde{w}}_y^T(s) \\ 0 & \dot{\tilde{w}}_z^T(s) \end{bmatrix}, \quad H_{hb} \equiv \begin{bmatrix} \tilde{\omega}_B & 0 & 0 & 0 \\ 0 & \tilde{\omega}_B & 0 & 0 \\ 0 & 0 & \tilde{\omega}_B & 0 \\ 0 & 0 & 0 & \tilde{\omega}_B \end{bmatrix} \begin{bmatrix} I & \tilde{p}_w^T(s) \\ 0 & \tilde{w}_x^T(s) \\ 0 & \tilde{w}_y^T(s) \\ 0 & \tilde{w}_z^T(s) \end{bmatrix} \quad (2.33)$$

With the above definitions, Eq. (2.31) can be simplified to

$$\begin{aligned}
\delta W^{int}(s) &= - \begin{bmatrix} \delta \varepsilon^T(s) & \delta b^T \end{bmatrix} \begin{bmatrix} J_{he}^T M(s) J_{he} & J_{he}^T M(s) J_{hb} \\ J_{hb}^T M(s) J_{he} & J_{hb}^T M(s) J_{hb} \end{bmatrix} \begin{bmatrix} \ddot{\varepsilon}(s) \\ \dot{\beta} \end{bmatrix} \\
&\quad + \begin{bmatrix} J_{he}^T M(s) \dot{J}_{he} & 0 \\ J_{hb}^T M(s) \dot{J}_{he} & 0 \end{bmatrix} \begin{bmatrix} \dot{\varepsilon}(s) \\ \beta \end{bmatrix} + \begin{bmatrix} 0 & J_{he}^T M(s) H_{hb} \\ 0 & J_{hb}^T M(s) H_{hb} \end{bmatrix} \begin{bmatrix} \dot{\varepsilon}(s) \\ \beta \end{bmatrix} \\
&\quad + \begin{bmatrix} 0 & 2 J_{he}^T M(s) \dot{J}_{hb} \\ 0 & 2 J_{hb}^T M(s) \dot{J}_{hb} \end{bmatrix} \begin{bmatrix} \dot{\varepsilon}(s) \\ \beta \end{bmatrix} \quad (2.34)
\end{aligned}$$

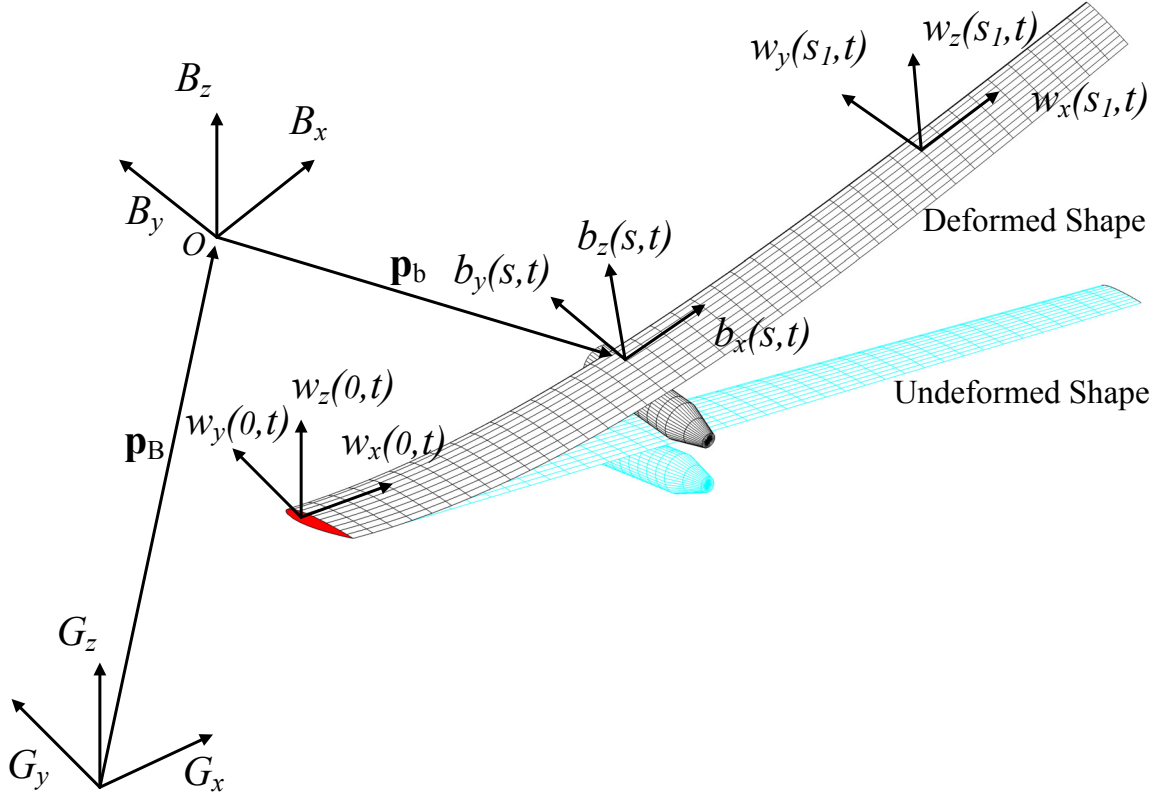


Figure 2.10: Reference frame for rigid bodies attached to elastic members

Rigid Units Attached to Elastic Members

The rigid units discussed here refer to engines or any other nonstructural masses attached to elastic members. Those units undergo only rigid body motions due to elastic member's deformation and vehicle's rigid body motion. For the case of engines, the modeling of a rigid unit consists of both inertias and thrust forces. This section only discusses the modeling of inertias. The modeling of engine loads is to be introduced in Section 2.2.3.

The derivation of the virtual work on discrete rigid units is quite similar to the process described for the elastic members, while the reference frame is b (see Fig. 2.10), instead of w . The virtual work done by inertia forces on each discrete rigid unit is derived as

$$\begin{aligned} \delta W_{rb}^{int} = & -\delta(h^b)^T \left\{ M_{rb} \begin{bmatrix} \ddot{p}_b \\ \ddot{b}_x \\ \ddot{b}_y \\ \ddot{b}_z \end{bmatrix} + M_{rb} \begin{bmatrix} I & \tilde{p}_b^T \\ 0 & \tilde{b}_x^T \\ 0 & \tilde{b}_y^T \\ 0 & \tilde{b}_z^T \end{bmatrix} \dot{\beta} \right. \\ & \left. + M_{rb} \begin{bmatrix} \tilde{\omega}_B & 0 & 0 & 0 \\ 0 & \tilde{\omega}_B & 0 & 0 \\ 0 & 0 & \tilde{\omega}_B & 0 \\ 0 & 0 & 0 & \tilde{\omega}_B \end{bmatrix} \begin{bmatrix} I & \tilde{p}_b^T \\ 0 & \tilde{b}_x^T \\ 0 & \tilde{b}_y^T \\ 0 & \tilde{b}_z^T \end{bmatrix} \beta + 2M_{rb} \begin{bmatrix} 0 & \dot{\tilde{p}}_b^T \\ 0 & \dot{\tilde{b}}_x^T \\ 0 & \dot{\tilde{b}}_y^T \\ 0 & \dot{\tilde{b}}_z^T \end{bmatrix} \dot{\beta} \right\} \quad (2.35) \end{aligned}$$

where

$$(h^b)^T = [p^T \quad b_x^T \quad b_y^T \quad b_z^T] \quad (2.36)$$

$$M_{rb} = \begin{bmatrix} m_{rb} & m_{rb}cg_x & m_{rb}cg_y & m_{rb}cg_z \\ m_{rb}cg_x & I_{xx_{cg}} + m_{rb}cg_x^2 & I_{xy_{cg}} + m_{rb}cg_xcg_y & I_{xz_{cg}} + m_{rb}cg_xcg_z \\ m_{rb}cg_y & I_{yx_{cg}} + m_{rb}cg_ycg_x & I_{yy_{cg}} + m_{rb}cg_y^2 & I_{yz_{cg}} + m_{rb}cg_ycg_z \\ m_{rb}cg_z & I_{zx_{cg}} + m_{rb}cg_zcg_x & I_{zy_{cg}} + m_{rb}cg_zcg_y & I_{zz_{cg}} + m_{rb}cg_z^2 \end{bmatrix} \quad (2.37)$$

m_{rb} is the mass of discrete rigid body units. $[cg_x \quad cg_y \quad cg_z]$ is the position of the center of mass of the rigid body unit in the b frame.

The displacements resolved in the b frames can be transformed to the w frame through the transformation matrix

$$h^b = D^{bw}h \quad (2.38)$$

and

$$\begin{bmatrix} \ddot{p}_b \\ \ddot{b}_x \\ \ddot{b}_y \\ \ddot{b}_z \end{bmatrix} = D^{bw} \begin{bmatrix} \ddot{p}_w \\ \ddot{w}_x \\ \ddot{w}_y \\ \ddot{w}_z \end{bmatrix}, \quad \begin{bmatrix} I & \tilde{p}_b^T \\ 0 & \tilde{b}_x^T \\ 0 & \tilde{b}_y^T \\ 0 & \tilde{b}_z^T \end{bmatrix} = D^{bw} \begin{bmatrix} I & \tilde{p}_w^T \\ 0 & \tilde{w}_x^T \\ 0 & \tilde{w}_y^T \\ 0 & \tilde{w}_z^T \end{bmatrix}, \quad \begin{bmatrix} 0 & \dot{\tilde{p}}_b^T \\ 0 & \dot{\tilde{b}}_x^T \\ 0 & \dot{\tilde{b}}_y^T \\ 0 & \dot{\tilde{b}}_z^T \end{bmatrix} = D^{bw} \begin{bmatrix} 0 & \dot{\tilde{p}}_w^T \\ 0 & \dot{\tilde{w}}_x^T \\ 0 & \dot{\tilde{w}}_y^T \\ 0 & \dot{\tilde{w}}_z^T \end{bmatrix} \quad (2.39)$$

where D^{bw} contains direction cosines at each node. Following the same procedure when dealing with the inertia virtual work of elastic members, Eq (2.35) can be written as

$$\begin{aligned} \delta W_{rb}^{int} = & -\begin{bmatrix} \delta \varepsilon^T & \delta b^T \end{bmatrix} \left\{ \begin{bmatrix} J_{he}^T (D^{bw})^T M_{rb} D^{bw} J_{he} & J_{he}^T (D^{bw})^T M_{rb} D^{bw} J_{hb} \\ J_{hb}^T (D^{bw})^T M_{rb} D^{bw} J_{he} & J_{hb}^T (D^{bw})^T M_{rb} D^{bw} J_{hb} \end{bmatrix} \begin{bmatrix} \ddot{\varepsilon} \\ \dot{\beta} \end{bmatrix} \right. \\ & + \begin{bmatrix} J_{he}^T (D^{bw})^T M_{rb} D^{bw} \dot{J}_{he} & 0 \\ J_{hb}^T (D^{bw})^T M_{rb} D^{bw} \dot{J}_{he} & 0 \end{bmatrix} \begin{bmatrix} \dot{\varepsilon} \\ \beta \end{bmatrix} + \begin{bmatrix} 0 & J_{he}^T (D^{bw})^T M_{rb} D^{bw} H_{hb} \\ 0 & J_{hb}^T (D^{bw})^T M_{rb} D^{bw} H_{hb} \end{bmatrix} \begin{bmatrix} \dot{\varepsilon} \\ \beta \end{bmatrix} \quad (2.40) \\ & \left. + \begin{bmatrix} 0 & 2J_{he}^T (D^{bw})^T M_{rb} D^{bw} \dot{J}_{hb} \\ 0 & 2J_{hb}^T (D^{bw})^T M_{rb} D^{bw} \dot{J}_{hb} \end{bmatrix} \begin{bmatrix} \dot{\varepsilon} \\ \beta \end{bmatrix} \right\} \end{aligned}$$

Eq. (2.40) has a very similar form as Eq. (2.34), except that $M(s)$ in Eq. (2.34) is replaced with $(D^{bw})^T M_{rb} D^{bw}$. However, Eq. (2.40) is no longer a continuous function of beam reference coordinate s , since it has only discrete values at locations where rigid masses are attached.

Internal Strain and Strain Rate

The virtual work due to the internal strain is

$$\delta W^{int}(s) = -\delta \varepsilon(s)^T k(s) (\varepsilon(s) - \varepsilon^0(s)) \quad (2.41)$$

where $\varepsilon^{ini}(s)$ is the initial strain upon beam initialization.

Internal damping is added to the formulation to accurately model the actual behavior of the beams. A stiffness proportional damping is used in current formulation

$$c(s) = \alpha k(s) \quad (2.42)$$

Thus, the virtual work due to strain rate is

$$\delta W^{int}(s) = -\delta \varepsilon(s)^T c(s) \dot{\varepsilon}(s) \quad (2.43)$$

Internal Virtual Work on Elements

To obtain the total internal virtual on an element, one needs firstly to summarize Eqs. (2.34), (2.40), (2.41), and (2.43), and then integrate the summation over the length of each element. In practice, the integration is performed numerically.

As mentioned before, a three-node element is used in the current implementation. It is assumed that the strain over an element is constant. Some of the properties, such as inertias and displacements, are assumed to vary linearly between the nodes of an element. However, the cross-section stiffness and damping ($k(s)$ and $c(s)$) are evaluated at the middle of each element, and are assumed to be constant over the length of the elements. Using these assumptions, an element internal virtual work can be written as

$$\begin{aligned} \delta W_e^{int} = & - \begin{bmatrix} \delta \varepsilon_e^T & \delta b^T \end{bmatrix} \left\{ \begin{bmatrix} J_{he}^T M_e J_{he} & J_{he}^T M_e J_{hb} \\ J_{hb}^T M_e J_{he} & J_{hb}^T M_e J_{hb} \end{bmatrix} \begin{bmatrix} \ddot{\varepsilon}_e \\ \dot{\beta} \end{bmatrix} \right. \\ & + \begin{bmatrix} J_{he}^T M_e \dot{J}_{he} & 0 \\ J_{hb}^T M_e \dot{J}_{he} & 0 \end{bmatrix} \begin{bmatrix} \dot{\varepsilon}_e \\ \beta \end{bmatrix} + \begin{bmatrix} 0 & J_{he}^T M_e H_{hb} \\ 0 & J_{hb}^T M_e H_{hb} \end{bmatrix} \begin{bmatrix} \dot{\varepsilon}_e \\ \beta \end{bmatrix} + \begin{bmatrix} 0 & 2J_{he}^T M_e \dot{J}_{hb} \\ 0 & 2J_{hb}^T M_e \dot{J}_{hb} \end{bmatrix} \begin{bmatrix} \dot{\varepsilon}_e \\ \beta \end{bmatrix} \\ & \left. + \begin{bmatrix} C_e & 0 \\ 0 & 0 \end{bmatrix} \begin{bmatrix} \dot{\varepsilon}_e \\ \beta \end{bmatrix} + \begin{bmatrix} K_e & 0 \\ 0 & 0 \end{bmatrix} \begin{bmatrix} \varepsilon_e \\ b \end{bmatrix} - \begin{bmatrix} K_e \varepsilon_e^0 \\ 0 \end{bmatrix} \right\} \quad (2.44) \end{aligned}$$

where

$$\begin{aligned} K_e &= k \Delta s \\ C_e &= c \Delta s \\ M_e &= \frac{1}{2} \Delta s \begin{bmatrix} \frac{1}{4} M_1 + \frac{1}{12} M_2 & \frac{1}{12} M_1 + \frac{1}{12} M_2 & 0 \\ \frac{1}{12} M_1 + \frac{1}{12} M_2 & \frac{1}{12} M_1 + \frac{1}{2} M_2 + \frac{1}{12} M_3 & \frac{1}{12} M_2 + \frac{1}{12} M_3 \\ 0 & \frac{1}{12} M_2 + \frac{1}{12} M_3 & \frac{1}{12} M_2 + \frac{1}{4} M_3 \end{bmatrix} \quad (2.45) \end{aligned}$$

M_i in the above equation are cross-sectional inertia properties at each node of an element, which consists of both Eqs. (2.32) and (2.37), in case rigid body masses is modeled.

2.2.3 External Virtual Work

In general, the external virtual work applied on a differential volume can be written as

$$\delta W^{ext} = \int_V \delta \mathbf{u}(x, y, z) \cdot \mathbf{f}(x, y, z) dV \quad (2.46)$$

where $\mathbf{f}(x, y, z)$ represents generalized forces acting on a differential volume, which may include gravity forces, external distributed forces and moments, external point forces and moments, etc. $\delta \mathbf{u}(x, y, z)$ is the corresponding virtual displacement. When beam cross-sectional properties are known, the integration of Eq. (2.46) over the volume is simplified as integration over the beam coordinate. The detailed derivation of the external work is listed in Ref [79]. The equations are listed here for reference purpose.

Gravity

Following the similar approach as obtaining the virtual work of inertial forces, the virtual work of gravity force acting on a differential volume is given as

$$\delta W_2 = \delta \mathbf{p}_a \cdot \mathbf{g} \rho dA ds \quad (2.47)$$

where \mathbf{g} is the gravity acceleration vector, resolved in the B frame. Integrate this equation over the cross-section, and it yields the virtual work on a differential beam section due to gravity force

$$\delta W^{ext}(s) = \delta h^T(s) N(s) g ds \quad (2.48)$$

$N(s)$ is related with the mass moment of inertia of the cross section, given as

$$N(s) = \int_{A(s)} \rho \begin{bmatrix} 1 \\ x \\ y \\ z \end{bmatrix} dA \quad (2.49)$$

The total virtual work due to gravity force on an element is obtained by integrating Eq. (2.48) over the element length, and given by

$$\delta W_e^{ext} = \delta h^T N g = \begin{bmatrix} \delta \varepsilon_e^T & \delta b^T \end{bmatrix} \begin{bmatrix} J_{he}^T \\ J_{hb}^T \end{bmatrix} N_e g \quad (2.50)$$

where

$$N_e = \begin{bmatrix} \frac{1}{3} N_1 + \frac{1}{6} N_2 \\ \frac{1}{6} N_1 + \frac{2}{3} N_2 + \frac{1}{6} N_3 \\ \frac{1}{6} N_2 + \frac{1}{3} N_3 \end{bmatrix} \quad (2.51)$$

Distributed Force

$$\delta W_e^{ext} = \int_{\Delta s} \delta \mathbf{p}(s) \cdot \mathbf{F}^{dist}(s) ds = \begin{bmatrix} \delta \varepsilon_e^T & \delta b^T \end{bmatrix} \begin{bmatrix} J_{pe}^T \\ J_{pb}^T \end{bmatrix} B_e^F F^{dist} \quad (2.52)$$

Distributed Moment

$$\delta W_e^{ext} = \int_{\Delta s} \delta \boldsymbol{\theta}(s) \cdot \mathbf{M}^{dist}(s) ds = \begin{bmatrix} \delta \varepsilon_e^T & \delta b^T \end{bmatrix} \begin{bmatrix} J_{\theta e}^T \\ J_{\theta b}^T \end{bmatrix} B_e^M M^{dist} \quad (2.53)$$

Point Force

$$\delta W_e^{ext} = \sum_{i=1}^3 \delta \mathbf{p}_i \cdot \mathbf{F}_i^{pt} = \begin{bmatrix} \delta \varepsilon_e^T & \delta b^T \end{bmatrix} \begin{bmatrix} J_{pe}^T \\ J_{pb}^T \end{bmatrix} F^{pt} \quad (2.54)$$

Point Moment

$$\delta W_e^{ext} = \sum_{i=1}^3 \delta \boldsymbol{\theta}_i \cdot \mathbf{M}_i^{pt} = \begin{bmatrix} \delta \varepsilon_e^T & \delta b^T \end{bmatrix} \begin{bmatrix} J_{\theta e}^T \\ J_{\theta b}^T \end{bmatrix} M^{pt} \quad (2.55)$$

In the above equations, N_e , B_e^F , and B_e^M are influence matrices, coming from numerical integrations. J_{he} , J_{pe} , $J_{\theta e}$, J_{hb} , J_{pb} , and $J_{\theta b}$ are Jacobians relating the

fundamental displacements and rotations (h , p , and θ) to the independent variables (ε and b).

To model the engine thrust, the loads are defined within the b frame. Since the b frame may undergo three-dimensional displacements and rotations with the wing deformations, the loads defined in this frame are follower loads. There is necessity to rotate the loads from their local frames to the B frame, which is written as

$$\mathbf{F}^B = C^{Bb}\mathbf{F}^b \quad (2.56)$$

where

$$C^{Bb} = \begin{bmatrix} b_x & b_y & b_z \end{bmatrix} \quad (2.57)$$

which should be updated at each solution iteration according to the current deformation. This formulation is not limited to thrust loads, since it is applicable for any follower distributed and concentrated loads. However, one may note that no dynamic effects, such as gyroscopic effects, are considered in the current formulation.

2.2.4 Elastic Equations of Motion

The total virtual work on the system is obtained by summation of all elements' internal and external work, and the contribution from rigid fuselage, if exists.

$$\begin{aligned} \delta W &= \delta W_{RB} + \sum (\delta W_e^{int} + \delta W_e^{ext}) \\ &= \begin{bmatrix} \delta\varepsilon^T & \delta b^T \end{bmatrix} \left\{ - \begin{bmatrix} J_{he}^T MJ_{he} & J_{he}^T MJ_{hb} \\ J_{hb}^T MJ_{he} & J_{hb}^T MJ_{hb} \end{bmatrix} \begin{bmatrix} \ddot{\varepsilon} \\ \dot{\beta} \end{bmatrix} - \begin{bmatrix} 0 & 0 \\ 0 & M_{RB} \end{bmatrix} \begin{bmatrix} \ddot{\varepsilon} \\ \dot{\beta} \end{bmatrix} \right. \\ &\quad - \begin{bmatrix} J_{he}^T M\dot{J}_{he} & 0 \\ J_{hb}^T M\dot{J}_{he} & 0 \end{bmatrix} \begin{bmatrix} \dot{\varepsilon} \\ \beta \end{bmatrix} - \begin{bmatrix} 0 & J_{he}^T MH_{hb} \\ 0 & J_{hb}^T MH_{hb} \end{bmatrix} \begin{bmatrix} \dot{\varepsilon} \\ \beta \end{bmatrix} - \begin{bmatrix} 0 & 2J_{he}^T M\dot{J}_{hb} \\ 0 & 2J_{hb}^T M\dot{J}_{hb} \end{bmatrix} \begin{bmatrix} \dot{\varepsilon} \\ \beta \end{bmatrix} \\ &\quad - \begin{bmatrix} C & 0 \\ 0 & 0 \end{bmatrix} \begin{bmatrix} \dot{\varepsilon} \\ \beta \end{bmatrix} - \begin{bmatrix} 0 & 0 \\ 0 & C_{RB} \end{bmatrix} \begin{bmatrix} \dot{\varepsilon} \\ \beta \end{bmatrix} - \begin{bmatrix} K & 0 \\ 0 & 0 \end{bmatrix} \begin{bmatrix} \varepsilon \\ b \end{bmatrix} + \begin{bmatrix} K\varepsilon^0 \\ R_{RB}^{ext} \end{bmatrix} \\ &\quad \left. + \begin{bmatrix} J_{he}^T \\ J_{hb}^T \end{bmatrix} Ng + \begin{bmatrix} J_{pe}^T \\ J_{pb}^T \end{bmatrix} B^F F^{dist} + \begin{bmatrix} J_{\theta e}^T \\ J_{\theta b}^T \end{bmatrix} B^M M^{dist} + \begin{bmatrix} J_{pe}^T \\ J_{pb}^T \end{bmatrix} F^{pt} + \begin{bmatrix} J_{\theta e}^T \\ J_{\theta b}^T \end{bmatrix} M^{pt} \right\} \end{aligned} \quad (2.58)$$

The equations of motion can be obtained by letting the total virtual work to be zero. Since the variation $[\delta\boldsymbol{\varepsilon} \quad \delta\boldsymbol{b}]$ is arbitrary, the elastic system equations of motion are derived as.

$$\begin{bmatrix} M_{FF} & M_{FB} \\ M_{BF} & M_{BB} \end{bmatrix} \begin{bmatrix} \ddot{\boldsymbol{\varepsilon}} \\ \dot{\boldsymbol{\beta}} \end{bmatrix} + \begin{bmatrix} C_{FF} & C_{FB} \\ C_{BF} & C_{BB} \end{bmatrix} \begin{bmatrix} \dot{\boldsymbol{\varepsilon}} \\ \boldsymbol{\beta} \end{bmatrix} + \begin{bmatrix} K_{FF} & 0 \\ 0 & 0 \end{bmatrix} \begin{bmatrix} \boldsymbol{\varepsilon} \\ \boldsymbol{b} \end{bmatrix} = \begin{bmatrix} R_F \\ R_B \end{bmatrix} \quad (2.59)$$

where

$$\begin{aligned} M_{FF}(\boldsymbol{\varepsilon}) &= J_{he}^T M J_{he} & M_{FB}(\boldsymbol{\varepsilon}) &= J_{he}^T M J_{hb} \\ M_{BF}(\boldsymbol{\varepsilon}) &= J_{hb}^T M J_{he} & M_{BB}(\boldsymbol{\varepsilon}) &= J_{hb}^T M J_{hb} + M_{RB} \\ C_{FF}(\boldsymbol{\varepsilon}, \dot{\boldsymbol{\varepsilon}}, \boldsymbol{\beta}) &= C + J_{he}^T M \dot{J}_{he} & C_{FB}(\boldsymbol{\varepsilon}, \dot{\boldsymbol{\varepsilon}}, \boldsymbol{\beta}) &= J_{he}^T M H_{hb} + 2J_{he}^T M \dot{J}_{hb} \\ C_{BF}(\boldsymbol{\varepsilon}, \dot{\boldsymbol{\varepsilon}}, \boldsymbol{\beta}) &= J_{hb}^T M \dot{J}_{he} & C_{BB}(\boldsymbol{\varepsilon}, \dot{\boldsymbol{\varepsilon}}, \boldsymbol{\beta}) &= J_{hb}^T M H_{hb} + 2J_{hb}^T M \dot{J}_{hb} + C_{RB} \\ K_{FF} &= K \\ \begin{bmatrix} R_F \\ R_B \end{bmatrix} &= \begin{bmatrix} K_{FF} \boldsymbol{\varepsilon}^0 \\ R_{RB}^{ext} \end{bmatrix} + \begin{bmatrix} J_{he}^T \\ J_{hb}^T \end{bmatrix} N g + \begin{bmatrix} J_{pe}^T \\ J_{pb}^T \end{bmatrix} B_F F^{dist} + \begin{bmatrix} J_{\theta e}^T \\ J_{\theta b}^T \end{bmatrix} B_M M^{dist} + \begin{bmatrix} J_{pe}^T \\ J_{pb}^T \end{bmatrix} F^{pt} + \begin{bmatrix} J_{\theta e}^T \\ J_{\theta b}^T \end{bmatrix} M^{pt} \end{aligned} \quad (2.60)$$

2.2.5 Skin Wrinkling: Stiffness Nonlinearity

As discussed, for a typical highly flexible Flying-Wing construction, significant torsional stiffness comes from the presence of the stretched thin skin (Fig. 2.5). During large bending deformations the skin may wrinkle. The unstretched skin causes the local torsional stiffness to drop. However, when the bending deformation is reduced and the wing skin is stretched again, the torsional stiffness is recovered. This effect is represented with a bilinear response as shown in Fig. 2.11. To model it, a switch is set up such that once the bending curvature increases to a predefined threshold value, the torsional stiffness is reduced. However, this reduction is not permanent. When the bending curvature falls back to being smaller than that threshold, the original torsional stiffness is recovered.

The most important issue for the modeling of this bilinear stiffness is to search for the time when the state (bending curvature) reaches the critical value (threshold value), which is denoted in Fig. 2.12 as t_{sw} . Hénon^[85] proposed a method to determine the exact time when the threshold is reached and the corresponding value of all states at that point.

It has been used in previous work^[86] successfully. However, its implementation within the current work was shown to be difficult. Although the threshold strain could be determined accurately, threshold strain rates had unreasonable estimates.

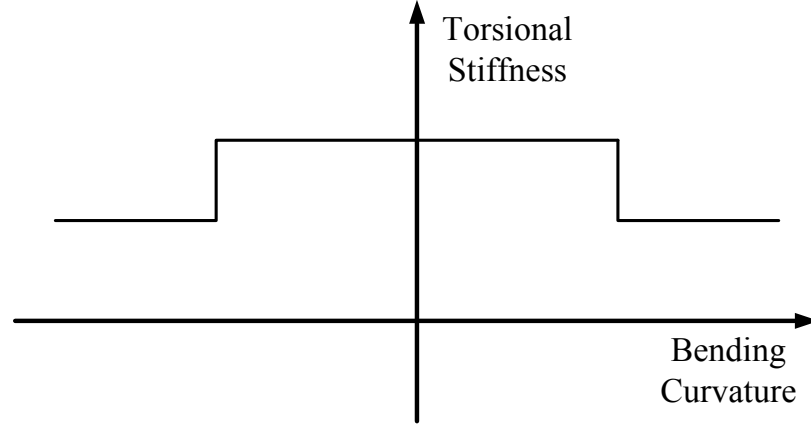


Figure 2.11: Bilinear characteristics of the wing torsional stiffness

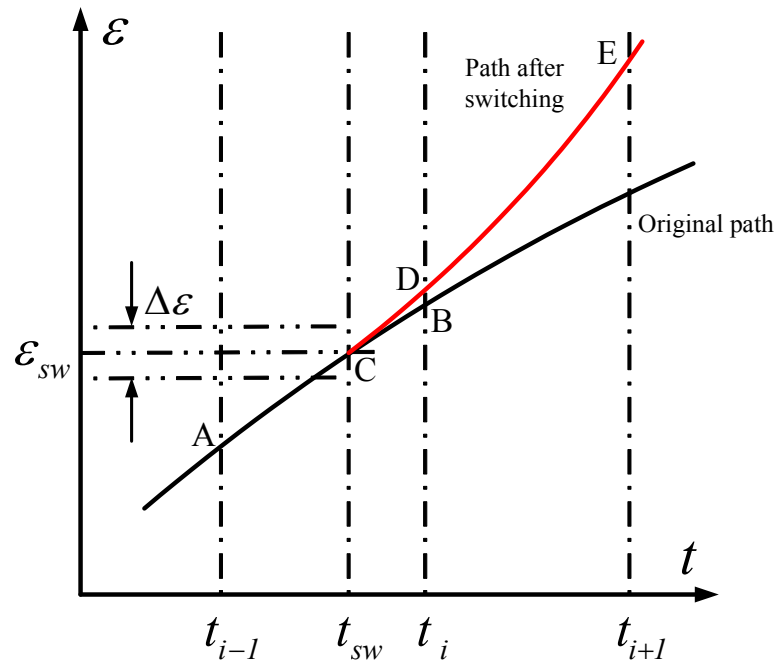


Figure 2.12: Switching of system properties during time integration

An alternate approach adopted for the current study is based on linear interpolation. Suppose the threshold happens between t_{i-1} and t_i . The switching time can be estimated by using following equations

$$t_{sw} = \frac{\varepsilon_{sw} - \varepsilon_{i-1}}{\frac{1}{2}(\dot{\varepsilon}_{i-1} + \dot{\varepsilon}_i)} \quad (2.61)$$

$$x_{sw} = x_{i-1} + \frac{t_{sw} - t_{i-1}}{t_i - t_{i-1}} (x_i - x_{i-1}) \quad (2.62)$$

Equations (2.61) and (2.62) give good approximation as long as the time step for integration is small enough. In practice, t_{sw} can be approximated by looking for the time point when the strain falls into a band of tolerance $\Delta\varepsilon$. However, this would give no information on the accuracy of the approximation of t_{sw} , since the states obtained at t_{sw} are all based on linear interpolation. To solve this problem, instead of using Eq. (2.62) directly, one more step of integration from t_{i-1} to t_{sw} can be performed to obtain the real states at t_{sw} and to ensure the approximation falls into an acceptable tolerance band.

2.3 Kinematics

As discussed before, the system equations solve for the independent variables (ε and b) directly. Displacements and rotations of each node are recovered from those variables through kinematic relationships. The kinematic relationships are obtained from the following differential equations

$$\begin{aligned} \frac{\partial p_w(s)}{\partial s} &= [1 + \varepsilon_x(s)] w_x(s) \\ \frac{\partial w_x(s)}{\partial s} &= \kappa_z(s) w_y(s) - \kappa_y(s) w_z(s) \\ \frac{\partial w_y(s)}{\partial s} &= \kappa_x(s) w_z(s) - \kappa_z(s) w_x(s) \\ \frac{\partial w_z(s)}{\partial s} &= \kappa_y(s) w_x(s) - \kappa_x(s) w_y(s) \end{aligned} \quad (2.63)$$

with the compact form of

$$\frac{\partial h_r(s)}{\partial s} = A(s) h_r(s) \quad (2.64)$$

where

$$A(s) = \begin{bmatrix} 0 & 1 + \varepsilon_x(s) & 0 & 0 \\ 0 & 0 & \kappa_z(s) & -\kappa_y(s) \\ 0 & -\kappa_z(s) & 0 & \kappa_x(s) \\ 0 & \kappa_y(s) & -\kappa_x(s) & 0 \end{bmatrix} \quad (2.65)$$

The solution of Eq. (2.64) is given as

$$h_r(s) = e^{A(s-s_0)} h_{r0} = e^{G(s)} h_{r0} \quad (2.66)$$

where h_{r0} is the position and rotation of the boundary node.

It can be noticed that the above solution is also true when solving for h , since Eq. (2.64) does not contain any body degrees of freedom. In fact, one may use Eq. (2.66) to recover h or h_r from strains, depending on different boundary conditions applied. For the cases where h is being recovered, one needs to provide the position of the body frame (p_B), which can be derived from the body frame propagation equations (See Section 2.5). After all, it is not necessary to distinguish h and h_r in Eq. (2.66). A general variable \bar{h} is used to denote both of them.

For elements with constant strain assumed, Eq. (2.65) is also constant over each element length. Therefore, the solution can be performed by using the discrete form.

$$\bar{h}_{n1} = D^{nm} \bar{h}_{m3} \quad \bar{h}_{n2} = e^{\frac{1}{2} A_n \Delta s} \bar{h}_{n1} = e^{G_n} \bar{h}_{n1} \quad \bar{h}_{n3} = e^{\frac{1}{2} A_n \Delta s} \bar{h}_{n2} = e^{G_n} \bar{h}_{n2} \quad (2.67)$$

where element n is the current element with the length of Δs , and element m is the one that element n is attached to. \bar{h}_{ni} is the displacement of the i th node of element n . D^{nm} is the rotation matrix that accounts for the discontinuities of the beam reference line between elements m and n .

Due to different connection relations, single beam and split beam systems (shown in Figs. 2.13 and 2.14) have different marching process when solving for the displacement.

2.3.1 Single Beam System

For a single beam system shown in Fig. 2.13, kinematics for a member is obtained by marching elemental kinematics from boundary node to end node. Following Eq. (2.67), the marching procedure can be written as the equations below.

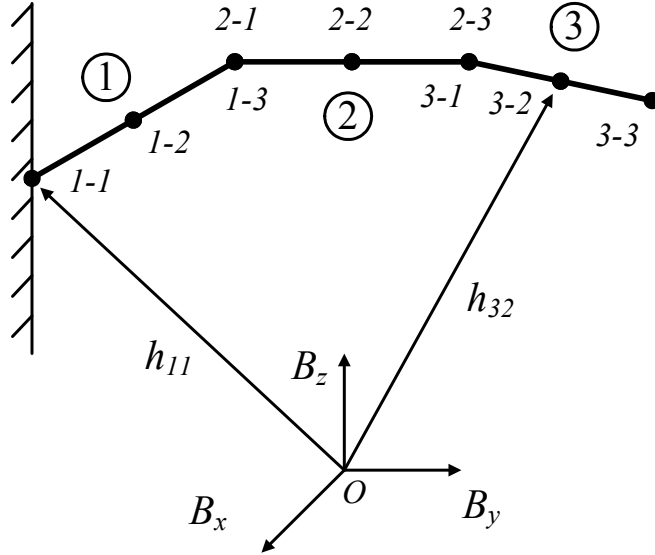


Figure 2.13: Single beam system (one member consisting of three elements)

$$\begin{aligned}\bar{h}_{11} &= \bar{h}_0 & \bar{h}_{21} &= D_{21}\bar{h}_{13} & \bar{h}_{31} &= D_{32}\bar{h}_{23} \\ \bar{h}_{12} &= e^{G_1}\bar{h}_{11} & \bar{h}_{22} &= e^{G_2}\bar{h}_{21} & \bar{h}_{32} &= e^{G_3}\bar{h}_{31} \\ \bar{h}_{13} &= e^{G_1}\bar{h}_{12} & \bar{h}_{23} &= e^{G_2}\bar{h}_{22} & \bar{h}_{33} &= e^{G_3}\bar{h}_{32}\end{aligned}\quad (2.68)$$

These can be written into matrix form as

$$\left[\begin{array}{cccccc} I & & & & & \\ -e^{G_1} & I & & & & \\ & -e^{G_1} & I & & & \\ & & -D_{21} & I & & \\ & & & -e^{G_2} & I & \\ & & & & -e^{G_2} & I \\ & & & & & -D_{32} \\ & & & & & & I \\ & & & & & & -e^{G_3} \\ & & & & & & & I \\ & & & & & & & -e^{G_3} \end{array} \right] \begin{bmatrix} \bar{h}_{11} \\ \bar{h}_{12} \\ \bar{h}_{13} \\ \bar{h}_{21} \\ \bar{h}_{22} \\ \bar{h}_{23} \\ \bar{h}_{31} \\ \bar{h}_{32} \\ \bar{h}_{33} \end{bmatrix} = \begin{bmatrix} \bar{h}_0 \\ 0 \\ 0 \\ 0 \\ 0 \\ 0 \\ 0 \\ 0 \\ 0 \end{bmatrix} \quad (2.69)$$

where \bar{h}_0 is the position and rotation of boundary node. The solution of Eq. (2.69) yields the displacements of a single beam system from strains.

2.3.2 Split Beam System

Kinematics for members of a split beam system (see Fig. 2.14) is still obtained by marching element kinematics from boundary node to each of the end nodes. However, the marching procedure is a little bit different, because of the existence of the split point.

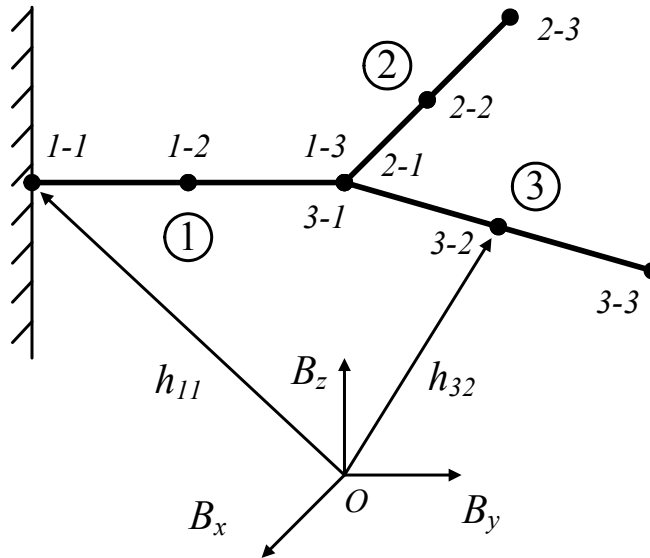


Figure 2.14: Split beam system (three members each consisting of one element)

In the connections shown in Fig. 2.14, the first nodes of elements 2 and 3 (\bar{h}_{21} and \bar{h}_{31}) are both connected with the last node of element 1 (\bar{h}_{13}). Therefore, \bar{h}_{21} and \bar{h}_{31} are both related with \bar{h}_{13} , with different direction cosines, as seen in the equations below.

$$\begin{array}{lll} \bar{h}_{11} = \bar{h}_0 & \bar{h}_{21} = D_{21}\bar{h}_{13} & \bar{h}_{31} = D_{31}\bar{h}_{13} \\ \bar{h}_{12} = e^{G_1}\bar{h}_{11} & \bar{h}_{22} = e^{G_2}\bar{h}_{21} & \bar{h}_{32} = e^{G_3}\bar{h}_{31} \\ \bar{h}_{13} = e^{G_1}\bar{h}_{12} & \bar{h}_{23} = e^{G_2}\bar{h}_{22} & \bar{h}_{33} = e^{G_3}\bar{h}_{32} \end{array} \quad (2.70)$$

which can be written into matrix form as

$$\begin{bmatrix} I & & & & \\ -e^{G_1} & I & & & \\ & -e^{G_1} & I & & \\ & & -D_{21} & I & \\ & & & -e^{G_2} & I \\ & & & & -e^{G_2} & I \\ & & -D_{31} & & I & \\ & & & & -e^{G_3} & I \\ & & & & & -e^{G_3} & I \end{bmatrix} \begin{bmatrix} \bar{h}_{11} \\ \bar{h}_{12} \\ \bar{h}_{13} \\ \bar{h}_{21} \\ \bar{h}_{22} \\ \bar{h}_{23} \\ \bar{h}_{31} \\ \bar{h}_{32} \\ \bar{h}_{33} \end{bmatrix} = \begin{bmatrix} \bar{h}_0 \\ 0 \\ 0 \\ 0 \\ 0 \\ 0 \\ 0 \\ 0 \\ 0 \end{bmatrix} \quad (2.71)$$

The solution of Eq. (2.71) yields the displacements of a split beam system from strains.

2.4 Additional Nodal Displacement Constraints

Since the present beam formulation is strain-based, only one displacement boundary condition can be directly imposed for each beam member. The additional displacement constraints are introduced by using the Lagrange Multiplier Method. The derivation starts from the energy functional. With the other terms omitted, the energy functional of a nonlinear beam in current formulation is written as

$$\Pi = \frac{1}{2} \int_L k(s) \varepsilon^2 ds - R\varepsilon \quad (2.72)$$

where $k(s)$ is cross-sectional stiffness. L is the beam length. R is generalized load. The constraint formulation will be different, depending on different types of constraints.

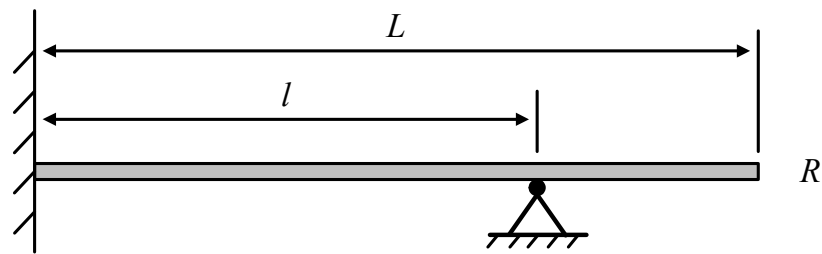


Figure 2.15: Cantilever beam with absolute nodal displacement constraint

2.4.1 Absolute Constraints

Suppose a cantilever beam with an arbitrary point constrained (see Fig. 2.15), the additional constraint can be introduced into the energy functional by applying a Lagrange multiplier.

$$\Pi^* = \frac{1}{2} \int_L k(s) \varepsilon^2 ds - R\varepsilon + \lambda_{ca} [h(l) - h^0(l)] \quad (2.73)$$

where λ_{ca} is the Lagrange Multiplier, $h(l)$ is the displacement (position and/or rotations) of the constrained point, and $h^0(l)$ is the initial displacement of the constrained point. The variation of the functional is

$$\delta\Pi^* = \int_L k(s) \varepsilon \delta\varepsilon ds - R\delta\varepsilon + \lambda_{ca} \delta h(l) + \delta\lambda_{ca} [h(l) - h^0(l)] \quad (2.74)$$

The above equation can be written into matrix form upon discretization, which is

$$\delta\Pi^* = \delta\varepsilon^T K_{FF} \varepsilon - \delta\varepsilon^T R + \delta\varepsilon^T J_{h\varepsilon}^T(l) \lambda_{ca} + \delta\lambda_{ca}^T [h(l) - h^0(l)] \quad (2.75)$$

where $J_{h\varepsilon}(l)$ is the Jacobian matrix evaluated at the constrained point.

The variation of the functional is zero, which yields the equilibrium equation of the system with additional absolute displacement constraints. However, it is still necessary to handle the variable of $h(l)$, which is a function of the independent variable ε . The solution is performed with an iterative procedure. Assume the independent variable, ε , and the dependent variable, $h(l)$, have been solved at step i , which are ε_i and $h_i(l)$, respectively, the variation of energy functional at step $i+1$ can be written as

$$\delta\varepsilon_{i+1}^T K_{FF} \varepsilon_{i+1} + \delta\varepsilon_{i+1}^T [J_{h\varepsilon}(l)]_i^T (\lambda_{ca})_{i+1} + \delta(\lambda_{ca})_{i+1}^T [h_{i+1}(l) - h^0(l)] = \delta\varepsilon_{i+1}^T R_i \quad (2.76)$$

The displacement can be written into incremental form.

$$\begin{aligned} h_{i+1}(l) &= h_i(l) + \delta h_{i+1}(l) \\ &= h_i(l) + [J_{h\varepsilon}(l)]_i (\varepsilon_{i+1} - \varepsilon_i) \end{aligned} \quad (2.77)$$

Substitute Eq. (2.77) into Eq. (2.76), which yields

$$\begin{aligned} & \delta \varepsilon_{i+1}^T K_{FF} \varepsilon_{i+1} + \delta \varepsilon_{i+1}^T [J_{he}(l)]_i^T (\lambda_{ca})_{i+1} + \delta (\lambda_{ca})_{i+1}^T [J_{he}(l)]_i \varepsilon_{i+1} \\ &= \delta \varepsilon_{i+1}^T R_i + \delta (\lambda_{ca})_{i+1}^T [J_{he}(l)]_i \varepsilon_i - \delta (\lambda_{ca})_{i+1}^T [h_i(l) - h^0(l)] \end{aligned} \quad (2.78)$$

which can be simplified as

$$\begin{aligned} & \begin{bmatrix} \delta \varepsilon_{i+1}^T & \delta (\lambda_{ca})_{i+1}^T \end{bmatrix} \begin{bmatrix} K_{FF} & (K_{ca})_i^T \\ (K_{ca})_i & 0 \end{bmatrix} \begin{bmatrix} \varepsilon_{i+1} \\ (\lambda_{ca})_{i+1} \end{bmatrix} \\ &= \begin{bmatrix} \delta \varepsilon_{i+1}^T & \delta (\lambda_{ca})_{i+1}^T \end{bmatrix} \begin{bmatrix} R_i \\ (R_{ca})_i \end{bmatrix} \end{aligned} \quad (2.79)$$

where

$$\begin{aligned} (K_{ca})_i &= [J_{he}(l)]_i \\ (R_{ca})_i &= (K_{ca})_i \varepsilon_i - [h_i(l) - h^0(l)] \end{aligned} \quad (2.80)$$

Therefore, the equilibrium equation of the system is given as a generalized form.

$$\begin{bmatrix} K_{FF} & (K_{ca})_i^T \\ (K_{ca})_i & 0 \end{bmatrix} \begin{bmatrix} \varepsilon_{i+1} \\ (\lambda_{ca})_{i+1} \end{bmatrix} = \begin{bmatrix} R_i \\ (R_{ca})_i \end{bmatrix} \quad (2.81)$$

Note that the Jacobian $[J_{he}(l)]_i$ and its transpose are both updated at each solution step.

2.4.2 Relative Constraints

For some beam configurations with two or more members joining at a common point (see Fig. 2.16), these members should be considered together and inter-member displacement constraints should be imposed. Let the uth node of member m be coincident with the vth node of member n upon initialization. The positions and orientations of the two nodes are always constrained to be the same. This relation can be written as,

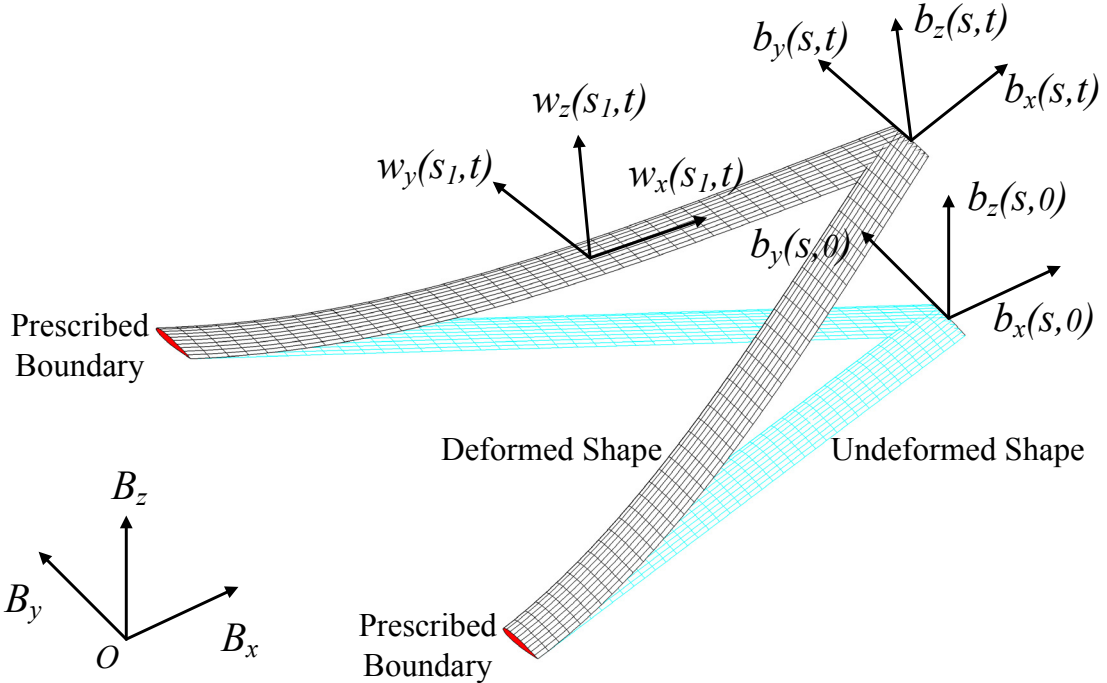


Figure 2.16: Beam configuration and reference frames with relative nodal displacement constraint

$$\left(h_r^b \right)_{mu} = \left(h_r^b \right)_{nv} \quad (2.82)$$

where h_r^b is the position and orientation vector with respect to the body frame (B). The rotations are expressed using using b frame unit vectors. Eq. (2.82) can be transformed into the local beam frame (w) by applying the individual rotation matrix

$$D_{mu}^{bw} \left(h_r \right)_{mu} - D_{nv}^{bw} \left(h_r \right)_{nv} = 0 \quad (2.83)$$

Therefore, the corresponding constrained energy functional and its variation are

$$\Pi^* = \frac{1}{2} \int_L k(s) \varepsilon^2 ds - R\varepsilon + \lambda_{cr} \left(D_{mu}^{bw} h_{mu} - D_{nv}^{bw} h_{nv} \right) \quad (2.84)$$

and

$$\delta\Pi^* = \int_L k(s) \varepsilon \delta\varepsilon ds - R\delta\varepsilon + \lambda_{cr} \delta \left(D_{mu}^{bw} h_{mu} - D_{nv}^{bw} h_{nv} \right) + \delta\lambda_{cr} \left(D_{mu}^{bw} h_{mu} - D_{nv}^{bw} h_{nv} \right) \quad (2.85)$$

Note that the subscript r is omitted in the equations following in this section. The discrete form of the above equation can be written as

$$\begin{aligned}\delta\Pi^* = & \delta\boldsymbol{\varepsilon}^T K_{FF} \boldsymbol{\varepsilon} - \delta\boldsymbol{\varepsilon}^T R \\ & + \delta\boldsymbol{\varepsilon}^T (J_{he}(mu))^T (D_{mu}^{bw})^T \lambda_{cr} - \delta\boldsymbol{\varepsilon}^T (J_{he}(nv))^T (D_{nv}^{bw})^T \lambda_{cr} \\ & + \delta\lambda_{cr}^T D_{mu}^{bw} h_{mu} - \delta\lambda_{cr}^T D_{nv}^{bw} h_{nv}\end{aligned}\quad (2.86)$$

where $J_{he}(mu)$ and $J_{he}(nv)$ are the Jacobian matrices evaluated at the constrained points, respectively.

The variation of the functional is zero, which yields the equations of motion. Following the same procedure as described in the previous section, the variation is written into iterative form that facilitates the implementation.

$$\begin{aligned}& \delta\boldsymbol{\varepsilon}_{i+1}^T K_{FF} \boldsymbol{\varepsilon}_{i+1} + \delta\boldsymbol{\varepsilon}_{i+1}^T \left[(J_{he}(mu))_i^T (D_{mu}^{bw})^T - (J_{he}(nv))_i^T (D_{nv}^{bw})^T \right] (\lambda_{cr})_{i+1} \\ & + \delta(\lambda_{cr})_{i+1}^T \left[D_{mu}^{bw} (h_{mu})_{i+1} - D_{nv}^{bw} (h_{nv})_{i+1} \right] \\ & = \delta\boldsymbol{\varepsilon}_{i+1}^T R_i\end{aligned}\quad (2.87)$$

where

$$\begin{aligned}(h_{mu})_{i+1} &= (h_{mu})_i + \delta(h_{mu})_{i+1} \\ &= (h_{mu})_i + (J_{he}(nu))_i (\boldsymbol{\varepsilon}_{i+1} - \boldsymbol{\varepsilon}_i) \\ (h_{nv})_{i+1} &= (h_{nv})_i + \delta(h_{nv})_{i+1} \\ &= (h_{nv})_i + (J_{he}(nv))_i (\boldsymbol{\varepsilon}_{i+1} - \boldsymbol{\varepsilon}_i)\end{aligned}\quad (2.88)$$

Substitute Eq. (2.88) into Eq. (2.87), which yields,

$$\begin{aligned}& \delta\boldsymbol{\varepsilon}_{i+1}^T K_{FF} \boldsymbol{\varepsilon}_{i+1} + \delta\boldsymbol{\varepsilon}_{i+1}^T \left[(J_{he}(mu))_i^T (D_{mu}^{bw})^T - (J_{he}(nv))_i^T (D_{nv}^{bw})^T \right] (\lambda_{cr})_{i+1} \\ & + \delta(\lambda_{cr})_{i+1}^T \left[D_{mu}^{bw} (J_{he}(mu))_i - D_{nv}^{bw} (J_{he}(nv))_i \right] \boldsymbol{\varepsilon}_{i+1} \\ & = \delta\boldsymbol{\varepsilon}_{i+1}^T R_i + \delta(\lambda_{cr})_{i+1}^T \left[D_{mu}^{bw} (J_{he}(mu))_i - D_{nv}^{bw} (J_{he}(nv))_i \right] \boldsymbol{\varepsilon}_i \\ & - \delta(\lambda_{cr})_{i+1}^T \left[D_{mu}^{bw} (h_{mu})_i - D_{nv}^{bw} (h_{nv})_i \right]\end{aligned}\quad (2.89)$$

which can be written into matrix form as Eq. (2.90),

$$\begin{bmatrix} \delta\varepsilon_{i+1}^T & \delta(\lambda_{cr})_{i+1}^T \end{bmatrix} \begin{bmatrix} K_{FF} & (K_{cr})_i^T \\ (K_{cr})_i & 0 \end{bmatrix} \begin{bmatrix} \varepsilon_{i+1} \\ (\lambda_{cr})_{i+1} \end{bmatrix} = \begin{bmatrix} \delta\varepsilon_{i+1}^T & \delta(\lambda_{cr})_{i+1}^T \end{bmatrix} \begin{bmatrix} R_i \\ (R_{cr})_i \end{bmatrix} \quad (2.90)$$

where

$$\begin{aligned} (K_{cr})_i &= D_{mu}^{bw}(J_{he}(mu))_i - D_{nv}^{bw}(J_{he}(nv))_i \\ (R_{cr})_i &= (K_{cr})_i \varepsilon_i - [D_{mu}^{bw}(h_{mu})_i - D_{nv}^{bw}(h_{nv})_i] \end{aligned} \quad (2.91)$$

Therefore, the equilibrium equation of the system is given as

$$\begin{bmatrix} K_{FF} & (K_{cr})_i^T \\ (K_{cr})_i & 0 \end{bmatrix} \begin{bmatrix} \varepsilon_{i+1} \\ (\lambda_{cr})_{i+1} \end{bmatrix} = \begin{bmatrix} R_i \\ (R_{cr})_i \end{bmatrix} \quad (2.92)$$

Note that the Jacobian $(J_{he})_i$ and its transpose should be updated at each solution step.

2.4.3 Elastic Equations of Motion with Constraints

For a general beam configuration that consists of both absolute and relative displacement constraints, one may define the total constraint matrices as

$$\lambda_c = \begin{bmatrix} \lambda_{ca} \\ \lambda_{cr} \end{bmatrix}, \quad K_c = \begin{bmatrix} K_{ca} \\ K_{cr} \end{bmatrix}, \quad R_c = \begin{bmatrix} R_{ca} \\ R_{cr} \end{bmatrix} \quad (2.93)$$

Therefore, the complete system equations of motion with constraints can be given as a set of differential-algebraic equations.

$$\begin{bmatrix} M_{FF} & M_{FB} & 0 \\ M_{BF} & M_{BB} & 0 \\ 0 & 0 & 0 \end{bmatrix} \begin{bmatrix} \ddot{\varepsilon} \\ \dot{\beta} \\ \ddot{\lambda}_c \end{bmatrix} + \begin{bmatrix} C_{FF} & C_{FB} & 0 \\ C_{BF} & C_{BB} & 0 \\ 0 & 0 & 0 \end{bmatrix} \begin{bmatrix} \dot{\varepsilon} \\ \beta \\ \dot{\lambda}_c \end{bmatrix} + \begin{bmatrix} K_{FF} & 0 & K_c^T \\ 0 & 0 & 0 \\ K_c & 0 & 0 \end{bmatrix} \begin{bmatrix} \varepsilon \\ b \\ \lambda_c \end{bmatrix} = \begin{bmatrix} R_F \\ R_B \\ R_c \end{bmatrix} \quad (2.94)$$

2.4.4 Special Treatment Regarding the Constraints

The figure above is the coordinate system of current beam formulation. As discussed before, the displacement vector can be written as:

$$h_r(s) = \begin{bmatrix} p_w(s)^T & w_x(s)^T & w_y(s)^T & w_z(s)^T \end{bmatrix}^T \quad (2.95)$$

where s is the beam coordinate. The full list of its component is,

$$h_r = \begin{bmatrix} p_{wx} & p_{wy} & p_{wz} & w_{xx} & w_{xy} & w_{xz} & w_{yx} & w_{yy} & w_{yz} & w_{zx} & w_{zy} & w_{zz} \end{bmatrix}^T \quad (2.96)$$

The displacement is a 12 by 1 vector. However, not all of its components are linearly independent. This property can also be observed from the block of K_{ca} in Eq. (2.81) and K_{cr} in Eq. (2.92). The rows in these matrices are not linearly independent, which makes the generalized stiffness matrices in Eqs. (2.81) and (2.92) rank defective. Therefore, the generalized stiffness matrices are not invertible, which may bring trouble in solutions.

From above analysis, additional treatment should be performed when the displacement vector is required to be constrained. Take a fully constraint condition as an example. To determine the position of a node, the 3 by 1 position vector ($\begin{bmatrix} p_{wx} & p_{wy} & p_{wz} \end{bmatrix}^T$) is required. Therefore, the corresponding rows in K_{ca} and K_{cr} are linearly independent. The directions of a node should be considered carefully. The local beam frame (w) is defined such that

$$\begin{aligned} w_{xx}^2 + w_{xy}^2 + w_{xz}^2 &= 1 \\ w_{yx}^2 + w_{yy}^2 + w_{yz}^2 &= 1 \\ w_{zx}^2 + w_{zy}^2 + w_{zz}^2 &= 1 \\ \langle \mathbf{w}_x, \mathbf{w}_y \rangle &= 0 \\ \langle \mathbf{w}_y, \mathbf{w}_z \rangle &= 0 \\ \langle \mathbf{w}_z, \mathbf{w}_x \rangle &= 0 \end{aligned} \quad (2.97)$$

The above six equations should always be satisfied. Therefore, only three components of the vector $\begin{bmatrix} w_{xx} & w_{xy} & w_{xz} & w_{yx} & w_{yy} & w_{yz} & w_{zx} & w_{zy} & w_{zz} \end{bmatrix}^T$ are linearly independent. Therefore, only three of the remaining rows of K_{ca} and K_{cr} are linearly independent. To obtain a full-ranked generalized stiffness matrices, it is necessary to determine linearly

independent rows from K_{ea} and K_{cr} . This could be accomplished by either the code's dynamic searching or a predefinition of a linearly independent set. The approach of predefinition is preferred, since the linearly independent set could vary due to dynamic searching. Note that only the fully constrained condition is discussed here. If the rotations are partially constrained, it can be treated through a similar approach.

2.5 Body Frame Propagation Equations

The body frame (B) propagation equations have been introduced in Refs. [15] and [87]. Quaternions ζ are used for determining the orientation of the B frame, which is given by the following equation.

$$\begin{bmatrix} \dot{\zeta}_0 \\ \dot{\zeta}_1 \\ \dot{\zeta}_2 \\ \dot{\zeta}_3 \end{bmatrix} = -\frac{1}{2} \begin{bmatrix} 0 & \omega_{B_1} & \omega_{B_2} & \omega_{B_3} \\ -\omega_{B_1} & 0 & -\omega_{B_3} & \omega_{B_2} \\ -\omega_{B_2} & \omega_{B_3} & 0 & -\omega_{B_1} \\ -\omega_{B_3} & -\omega_{B_2} & \omega_{B_1} & 0 \end{bmatrix} \begin{bmatrix} \zeta_0 \\ \zeta_1 \\ \zeta_2 \\ \zeta_3 \end{bmatrix} = -\frac{1}{2} \Omega_\zeta(\beta) \zeta \quad (2.98)$$

where ω_B is body angular velocity. The position of the B frame resolved in the inertia (G) frame is governed by the following differential equation.

$$\dot{P}_B = C^{GB} v_B = \begin{bmatrix} C^{GB} & 0 \end{bmatrix} \beta \quad (2.99)$$

Note that P_B describes the same vector as p_B in Eq. (2.1). However, p_B is resolved in the body (B) frame. C^{GB} is the rotation matrix that transforms a vector from the B frame to the G frame, which is composed of quaternions.

$$\begin{aligned} C^{GB} &= \begin{bmatrix} B_x & B_y & B_z \end{bmatrix} \\ &= \begin{bmatrix} \zeta_0^2 + \zeta_1^2 - \zeta_2^2 - \zeta_3^2 & 2(\zeta_1\zeta_2 - \zeta_0\zeta_3) & 2(\zeta_1\zeta_3 + \zeta_0\zeta_2) \\ 2(\zeta_1\zeta_2 + \zeta_0\zeta_3) & \zeta_0^2 - \zeta_1^2 + \zeta_2^2 - \zeta_3^2 & 2(\zeta_2\zeta_3 - \zeta_0\zeta_1) \\ 2(\zeta_1\zeta_3 - \zeta_0\zeta_2) & 2(\zeta_2\zeta_3 + \zeta_0\zeta_1) & \zeta_0^2 - \zeta_1^2 - \zeta_2^2 + \zeta_3^2 \end{bmatrix} \end{aligned} \quad (2.100)$$

2.6 Unsteady Aerodynamics

The unsteady aerodynamic loads used in current work are based on the 2-D finite inflow theory, provided by Ref. [80]. The theory calculates aerodynamic loads on a thin airfoil section undergoing large motions in an incompressible flow. Prandtl-Glauert correction is then applied to account for the subsonic compressibility effects. The different velocity components are shown in Fig. 2.17. The aerodynamic loads calculated at middle chord are given as Eq. (2.101).

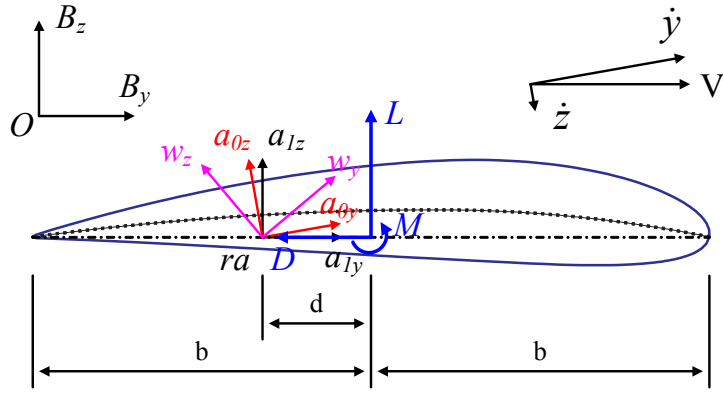


Figure 2.17: Airfoil coordinate systems and velocity components

$$\begin{aligned}
 l_{mc} &= \pi\rho b^2 (-\dot{z} + \dot{y}\dot{\alpha} - d\ddot{\alpha}) + 2\pi\rho b \dot{y}^2 \left[-\frac{\dot{z}}{\dot{y}} + \left(\frac{1}{2}b - d \right) \frac{\dot{\alpha}}{\dot{y}} - \frac{\lambda_0}{\dot{y}} \right] + 2\pi\rho b c_l \dot{y}^2 \delta \\
 m_{mc} &= 2\pi\rho b^2 \left(-\frac{1}{2}\dot{y}\dot{z} - \frac{1}{2}d\dot{y}\dot{\alpha} - \frac{1}{2}\dot{y}\lambda_0 - \frac{1}{16}b^2\ddot{\alpha} \right) + 2\pi\rho b^2 c_s \dot{y}^2 \delta \\
 d_{mc} &= -2\pi\rho b \left(\dot{z}^2 + d^2\dot{\alpha}^2 + \lambda_0^2 + 2d\dot{\alpha}\dot{z} + 2\lambda_0\dot{z} + 2d\dot{\alpha}\lambda_0 \right) \\
 &\quad - 2\pi\rho b \left[c_l \dot{y}\dot{z}\delta + (dc_l + bg_2) \dot{y}\dot{\alpha}\delta + c_l \dot{y}\lambda_0\delta + \frac{1}{2}bg_2\ddot{z}\delta + \left(\frac{1}{2}bdg_2 - \frac{1}{4}b^2g_3 \right) \ddot{\alpha}\delta \right]
 \end{aligned} \tag{2.101}$$

where δ is the trailing-edge flap deflection angle, b is the semichord, d is the distance of the mid-chord in front of the reference axis. $-\dot{z} / \dot{y}$ is the angle of attack that consists of the contribution from both the steady state angle of attack and the unsteady plunging motion of the airfoil. The coefficients c_i through g_i are based upon geometry and complete details are provided in Refs. [79] and [80]. λ_0 is the inflow parameter,

accounting for induced flow due to free vorticity, which is the summation of the inflow states λ as described in Ref. [80] and given by

$$\begin{aligned}\dot{\lambda} &= F_1 \ddot{q} + F_2 \dot{q} + F_3 \lambda \\ &= F_1 \begin{bmatrix} \ddot{\varepsilon} \\ \dot{\beta} \end{bmatrix} + F_2 \begin{bmatrix} \dot{\varepsilon} \\ \beta \end{bmatrix} + F_3 \lambda\end{aligned}\quad (2.102)$$

The above equations are based upon thin airfoil theory, where no cambered airfoil is considered and aerodynamic moment coefficient c_{m0} is assumed to be zero. To model the aerodynamic loads of a cambered airfoil with aerodynamic coefficients supplied, the lift, moment, and drag about the aerodynamic center are given as

$$\begin{aligned}l_{ac} &= \pi \rho b^2 (-\ddot{z} + \dot{y} \dot{\alpha} - d \ddot{\alpha}) + c_{l\alpha} \rho b \dot{y}^2 \left[-\frac{\dot{z}}{\dot{y}} + \left(\frac{1}{2} b - d \right) \frac{\dot{\alpha}}{\dot{y}} - \frac{\lambda_0}{\dot{y}} \right] + \rho b \dot{y}^2 c_{l\delta} \delta \\ m_{ac} &= \pi \rho b^3 \left[\frac{1}{2} \ddot{z} - \dot{y} \dot{\alpha} - \left(\frac{1}{8} b - \frac{1}{2} d \right) \ddot{\alpha} \right] + 2 \rho b^2 \dot{y}^2 (c_{m0} + c_{m\delta} \delta) \\ d_{ac} &= -\rho b \dot{y}^2 c_{d0}\end{aligned}\quad (2.103)$$

where $c_{l\alpha}$ is the lift curve slope, $c_{l\delta}$ and $c_{m\delta}$ are the lift and moment slopes due to flap deflection, respectively. Furthermore, c_{d0} and c_{m0} are the drag and moment coefficients for zero angle of attack, respectively.

To transfer the loads from the middle chord or the aerodynamic center to the wing reference axis, one may use

$$\begin{aligned}l_{ra} &= l_{mc} & l_{ra} &= l_{ac} \\ m_{ra} &= m_{mc} + d l_{mc} & \text{or} & m_{ra} = m_{ac} + \left(\frac{1}{2} b + d \right) l_{ac} \\ d_{ra} &= d_{mc} & d_{ra} &= d_{ac}\end{aligned}\quad (2.104)$$

Furthermore, the loads are rotated to the body coordinate system, which yields

$$F^{aero} = C^{Ba_I} \begin{bmatrix} 0 \\ d_{ra} \\ l_{ra} \end{bmatrix}, \quad M^{aero} = C^{Ba_I} \begin{bmatrix} m_{ra} \\ 0 \\ 0 \end{bmatrix} \quad (2.105)$$

2.7 Simplified Stall Models

There are two different simplified stall models considered in the current work. For Stall Model 1, the lift coefficient, c_l , is kept constant and equal to c_{lmax} once the angle of attack goes beyond the stall angle, and the moment coefficient (c_{m0}) remains the same as before stall. Stall Model 2 is similar to Stall Model 1 with the only difference that now the moment coefficient is dropped to changes to $c_{m0stall}$.

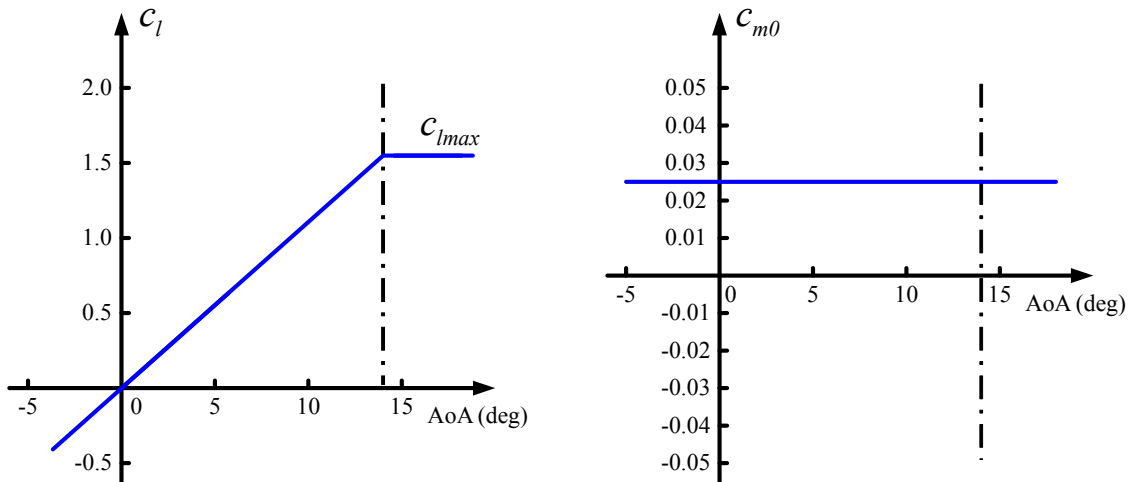


Figure 2.18: Variation of lift and moment coefficients for Stall Model 1

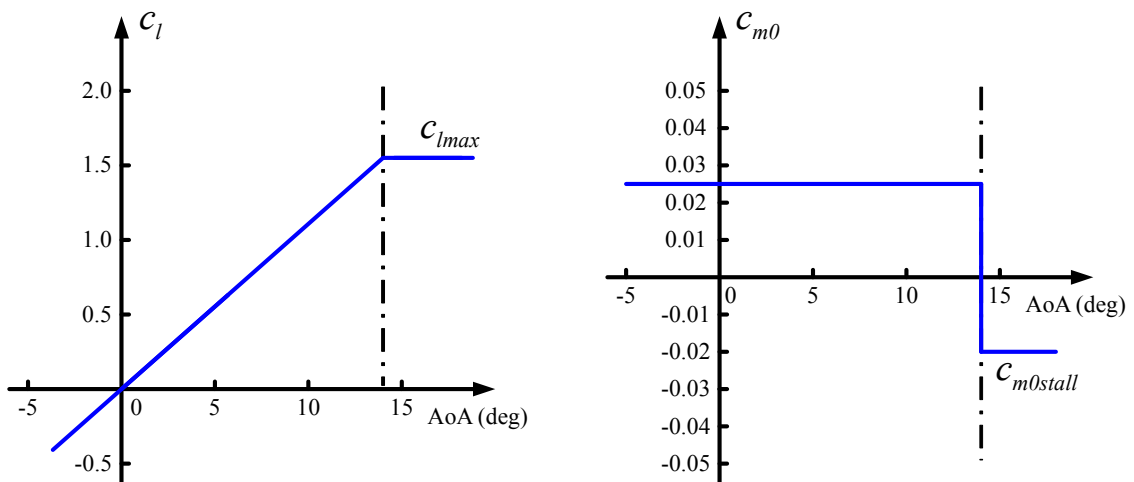


Figure 2.19: Variation of lift and moment coefficients for Stall Model 2

2.8 Discrete Gust Formulation

In general, gust disturbance is stochastic. In current work, the gust model is simplified as an elliptical region with only vertical disturbance. However, this gust model is both space- and time-dependent. The gust region is located on the flight path of the vehicle. The amplitude of gust speed reaches a maximum at the center and reduces to zero at the boundaries. Figure 2.20 shows the amplitude distribution of the gust model. For this particular example, the gust region has a maximum outer radius of 40 m, and the maximum gust speed center amplitude of 10 m/s. Note that the amplitude distribution along the North and East directions maybe different. At each location within the gust region, the amplitudes follow the same one-minus-cosine characteristic. Figure 2.21 shows a sample of the time variation of the amplitude at the gust center. Different time variations can be applied for numerical studies. The basic equations governing the gust model are

$$A(r, \eta, t) = \frac{1}{2} A_c \left\{ 1 - \cos \left[2\pi \left(\frac{t}{t_g} \right) \right] \right\} \sqrt{(A_E \cos \eta)^2 + (A_N \sin \eta)^2} \quad (2.106)$$

$$\begin{aligned} A_E(r) &= \sin \left\{ \frac{\pi}{2} \left[1 - \left(\frac{r}{r_0} \right)^{n_E} \right] \right\} \\ A_N(r) &= \sin \left\{ \frac{\pi}{2} \left[1 - \left(\frac{r}{r_0} \right)^{n_N} \right] \right\} \end{aligned} \quad 0 < r \leq r_0 \quad (2.107)$$

where footnotes E and N stand for East and North directions, respectively. r_0 is the outer radius of the gust region. r is the distance from one point within the gust region to the gust center. η is the orientation angle of the point with respect to East direction. n_E and n_N are parameters used for adjusting the gust spatial distribution along East and North directions, respectively. By choosing different n_E and n_N , the spatial variation of gust amplitudes in East and North directions will be different. It also satisfies the requirement that the amplitude at the gust center is the maximum and decreased down to zero at the boundary. The spatial distribution is then combined with the “one-minus-

“cosine” time distribution, leading to the gust model represented by Eq. (2.106). Finally, t_g is the gust duration.

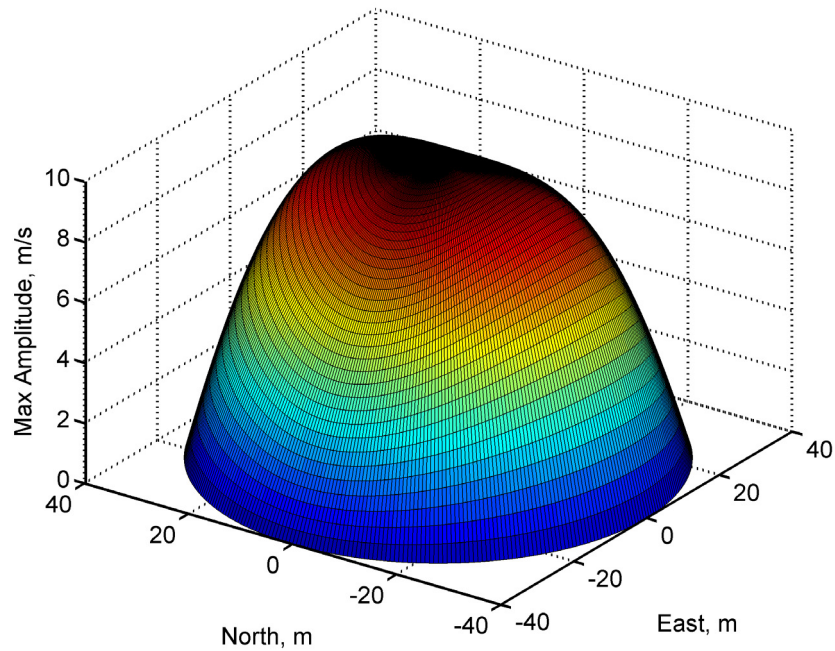


Figure 2.20: Example of gust spatial distribution for $n_E = 1$, $n_N = 2$, $A_c = 10$ m/s

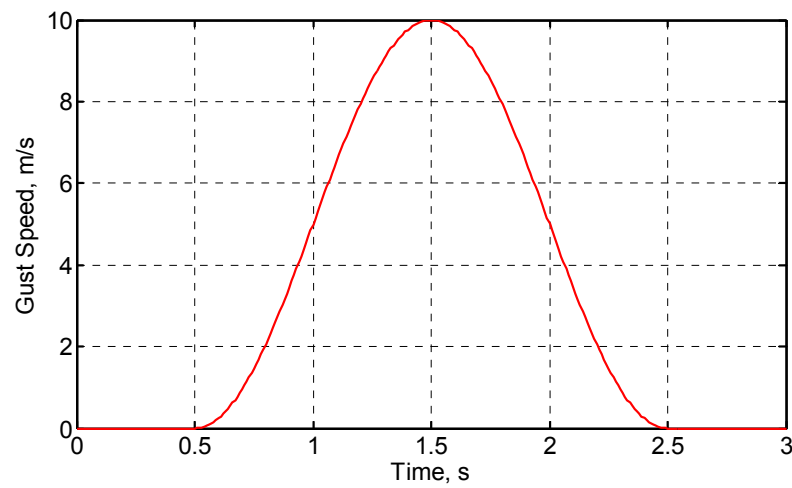


Figure 2.21: Time variation of gust speed

2.9 Coupled Aeroelastic and Flight Dynamic Equations of Motion

The coupled flight dynamic and aeroelastic system equations of motion can be obtained by combining the elastic equations, Eq. (2.94), the B frame propagation equations, Eqs. (2.98), (2.99), and the unsteady aerodynamic equations, Eq. (2.102). They are given as the following differential-algebraic equations.

$$\begin{aligned}
 M_{FF}\ddot{\varepsilon} + M_{FB}\dot{\beta} + C_{FF}\dot{\varepsilon} + C_{FB}\beta + K_{FF}\varepsilon + K_c^T\lambda_c &= R_F \\
 M_{BF}\ddot{\varepsilon} + M_{BB}\dot{\beta} + C_{BF}\dot{\varepsilon} + C_{BB}\beta &= R_B \\
 \dot{\zeta} &= -\frac{1}{2}\Omega_\zeta\zeta \\
 \dot{P}_B &= \begin{bmatrix} C^{GB} & 0 \end{bmatrix}\beta \\
 \dot{\lambda} &= F_1 \begin{bmatrix} \ddot{\varepsilon} \\ \dot{\beta} \end{bmatrix} + F_2 \begin{bmatrix} \dot{\varepsilon} \\ \beta \end{bmatrix} + F_3\lambda \\
 K_c\varepsilon &= R_c
 \end{aligned} \tag{2.108}$$

The definition of each variable in the above equations can be found in the previous sections. The aerodynamic forces and moments contribute to the generalized loads (R_F and R_B) as distributed forces and moments.

2.10 Stability Analysis: Frequency Domain Solution

2.10.1 Linearization of Nonlinear System Equations

For cases of free flight, only aerodynamic and gravity loads are applied to the system. Therefore, the system equations of motion (without additional displacement constraints) can be written as

$$\begin{aligned}
& M_{FF}(\varepsilon)\ddot{\varepsilon} + M_{FB}(\varepsilon)\dot{\beta} + C_{FF}(\dot{\varepsilon}, \varepsilon, \beta)\dot{\varepsilon} + C_{FB}(\dot{\varepsilon}, \varepsilon, \beta)\beta + K_{FF}\varepsilon \\
& = R_F^{aero}(\ddot{\varepsilon}, \dot{\varepsilon}, \varepsilon, \dot{\beta}, \beta, \lambda) + R_F^{grav}(\zeta) \\
& M_{BF}(\varepsilon)\ddot{\varepsilon} + M_{BB}(\varepsilon)\dot{\beta} + C_{BF}(\dot{\varepsilon}, \varepsilon, \beta)\dot{\varepsilon} + C_{BB}(\dot{\varepsilon}, \varepsilon, \beta)\beta \\
& = R_B^{aero}(\ddot{\varepsilon}, \dot{\varepsilon}, \varepsilon, \dot{\beta}, \beta, \lambda) + R_B^{grav}(\zeta) \\
& \dot{\zeta} = -\frac{1}{2}\Omega_\zeta(\beta)\zeta \\
& \dot{P}_B = \begin{bmatrix} C^{BG}(\zeta) & 0 \end{bmatrix}\beta \\
& \dot{\lambda} = F_1 \begin{bmatrix} \ddot{\varepsilon} \\ \dot{\beta} \end{bmatrix} + F_2 \begin{bmatrix} \dot{\varepsilon} \\ \beta \end{bmatrix} + F_3\lambda
\end{aligned} \tag{2.109}$$

R_F^{grav} and R_B^{grav} are flexible and rigid body components of generalized gravity loads, respectively. As discussed in Eq. (2.47), the gravitational acceleration vector is resolved in the body frame, which is rotated from the constant gravitational acceleration vector resolved in the global frame. The rotation matrix between the two frames (C^{BG}) is a function of quaternions (ζ), as given in Eq. (2.100).

Linearization of Eq. (2.109) can be performed about a certain time (t_0), with the variables being $\begin{bmatrix} \ddot{\varepsilon}_0 & \dot{\varepsilon}_0 & \varepsilon_0 & \dot{\beta}_0 & \beta_0 & \zeta_0 & P_{B_0} & \lambda_0 \end{bmatrix}^T$. The detailed process can be found in Appendix B. The linearized equations are given as follows.

$$\begin{aligned}
& M_{FF}\ddot{\varepsilon} + M_{FB}\dot{\beta} + \left(C_{FF} + C_{FF/\dot{\varepsilon}_0}\dot{\varepsilon}_0 + C_{FB/\dot{\varepsilon}_0}\beta_0 \right)\dot{\varepsilon} \\
& + \left(C_{FB} + C_{FF/\beta_0}\dot{\varepsilon}_0 + C_{FB/\beta_0}\beta_0 \right)\beta + K_{FF}\varepsilon \\
& = R_{F/\dot{\varepsilon}_0}^{aero}\ddot{\varepsilon} + R_{F/\dot{\varepsilon}_0}^{aero}\dot{\varepsilon} + R_{F/\varepsilon_0}^{aero}\varepsilon + R_{F/\dot{\beta}_0}^{aero}\dot{\beta} + R_{F/\beta_0}^{aero}\beta + R_{F/\lambda_0}^{aero}\lambda + R_{F/\zeta_0}^{grav}\zeta \\
& M_{BF}\ddot{\varepsilon} + M_{BB}\dot{\beta} + \left(C_{BF} + C_{BF/\dot{\varepsilon}_0}\dot{\varepsilon}_0 + C_{BB/\dot{\varepsilon}_0}\beta_0 \right)\dot{\varepsilon} + \left(C_{BB} + C_{BF/\beta_0}\dot{\varepsilon}_0 + C_{BB/\beta_0}\beta_0 \right)\beta \\
& = R_{B/\dot{\varepsilon}_0}^{aero}\ddot{\varepsilon} + R_{B/\dot{\varepsilon}_0}^{aero}\dot{\varepsilon} + R_{B/\varepsilon_0}^{aero}\varepsilon + R_{B/\dot{\beta}_0}^{aero}\dot{\beta} + R_{B/\beta_0}^{aero}\beta + R_{B/\lambda_0}^{aero}\lambda + R_{B/\zeta_0}^{grav}\zeta
\end{aligned} \tag{2.110}$$

$$\begin{aligned}
& \dot{\zeta} = -\frac{1}{2}\Omega_\zeta\zeta - \frac{1}{2}\left(\Omega_{\zeta/\beta_0}\beta\right)\zeta_0 \\
& \dot{P}_B = \begin{bmatrix} C^{GB} & 0 \end{bmatrix}\beta + \begin{bmatrix} (C_{/\zeta_0}^{GB})\zeta & 0 \end{bmatrix}\beta_0 \\
& \dot{\lambda} = F_1 \begin{bmatrix} \ddot{\varepsilon} \\ \dot{\beta} \end{bmatrix} + F_2 \begin{bmatrix} \dot{\varepsilon} \\ \beta \end{bmatrix} + F_3\lambda
\end{aligned}$$

where $(\cdot)_{x_0}$ denotes $\frac{d(\cdot)}{dx}\Big|_{x_0}$ or $\frac{\partial(\cdot)}{\partial x}\Big|_{x_0}$ for different variables.

The linearized equations can be put into state-space form, which is

$$\begin{bmatrix} \dot{\varepsilon} & \ddot{\varepsilon} & \dot{\beta} & \dot{\zeta} & \dot{P}_B & \dot{\lambda} \end{bmatrix}^T = Q_I^{-1} Q_2 \begin{bmatrix} \varepsilon & \dot{\varepsilon} & \beta & \zeta & P_B & \lambda \end{bmatrix}^T \\ = A \begin{bmatrix} \varepsilon & \dot{\varepsilon} & \beta & \zeta & P_B & \lambda \end{bmatrix}^T \quad (2.111)$$

where

$$Q_I = \begin{bmatrix} I & 0 & 0 & 0 & 0 & 0 \\ 0 & \bar{M}_{FF} & \bar{M}_{FB} & 0 & 0 & 0 \\ 0 & \bar{M}_{BF} & \bar{M}_{BB} & 0 & 0 & 0 \\ 0 & 0 & 0 & I & 0 & 0 \\ 0 & 0 & 0 & 0 & I & 0 \\ 0 & -F_{IF} & -F_{IB} & 0 & 0 & I \end{bmatrix} \quad (2.112)$$

$$Q_2 = \begin{bmatrix} 0 & I & 0 & 0 & 0 & 0 \\ -\bar{K}_{FF} & -\bar{C}_{FF} & -\bar{C}_{FB} & R_{F/\zeta_0}^{grav} & 0 & R_{F/\lambda_0}^{aero} \\ 0 & -\bar{C}_{BF} & -\bar{C}_{BB} & R_{B/\zeta_0}^{grav} & 0 & R_{B/\lambda_0}^{aero} \\ 0 & 0 & -\frac{1}{2}\Omega_{\zeta/\beta_0}\zeta_0 & -\frac{1}{2}\Omega_\zeta & 0 & 0 \\ 0 & 0 & [C^{GB} & 0] & [C_{/\zeta_0}^{GB} & 0]\beta_0 & 0 & 0 \\ 0 & F_{2F} & F_{2B} & 0 & 0 & F_3 \end{bmatrix}$$

and

$$\begin{aligned} \bar{M}_{FF} &= M_{FF} - R_{F/\dot{\varepsilon}_0}^{aero} & \bar{M}_{FB} &= M_{FB} - R_{F/\dot{\beta}_0}^{aero} \\ \bar{M}_{BF} &= M_{BF} - R_{B/\dot{\varepsilon}_0}^{aero} & \bar{M}_{BB} &= M_{BB} - R_{B/\dot{\beta}_0}^{aero} \\ \bar{C}_{FF} &= C_{FF} + C_{FF/\dot{\varepsilon}_0}\dot{\varepsilon}_0 + C_{FB/\dot{\varepsilon}_0}\beta_0 - R_{F/\dot{\varepsilon}_0}^{aero} & \bar{C}_{FB} &= C_{FB} + C_{FF/\beta_0}\dot{\varepsilon}_0 + C_{FB/\beta_0}\beta_0 - R_{F/\beta_0}^{aero} \\ \bar{C}_{BF} &= C_{BF} + C_{BF/\dot{\varepsilon}_0}\dot{\varepsilon}_0 + C_{BB/\dot{\varepsilon}_0}\beta_0 - R_{B/\dot{\varepsilon}_0}^{aero} & \bar{C}_{BB} &= C_{BB} + C_{BF/\beta_0}\dot{\varepsilon}_0 + C_{BB/\beta_0}\beta_0 - R_{B/\beta_0}^{aero} \\ \bar{K}_{FF} &= K_{FF} - R_{F/\varepsilon_0}^{aero} \end{aligned} \quad (2.113)$$

2.10.2 Solution of Stability Boundary

The nonlinear stability analysis is carried out in an iterative way, which is shown in Fig. 2.22. Starting from a predefined flight condition, the system is brought to the nonlinear steady state and linearized about the condition. Eigenvalue analysis of the resulting system matrix A in Eq. (2.111) is performed. Eigenvalues with positive real parts indicate instability. The process is repeated until the instability is reached. One may use the same system matrix for different solution types of stability analysis, such as flutter of free flight vehicles, flutter of vehicles with constrained rigid body motions, or just the flight dynamic stability. To do so, one needs to choose corresponding subset of the system matrix.

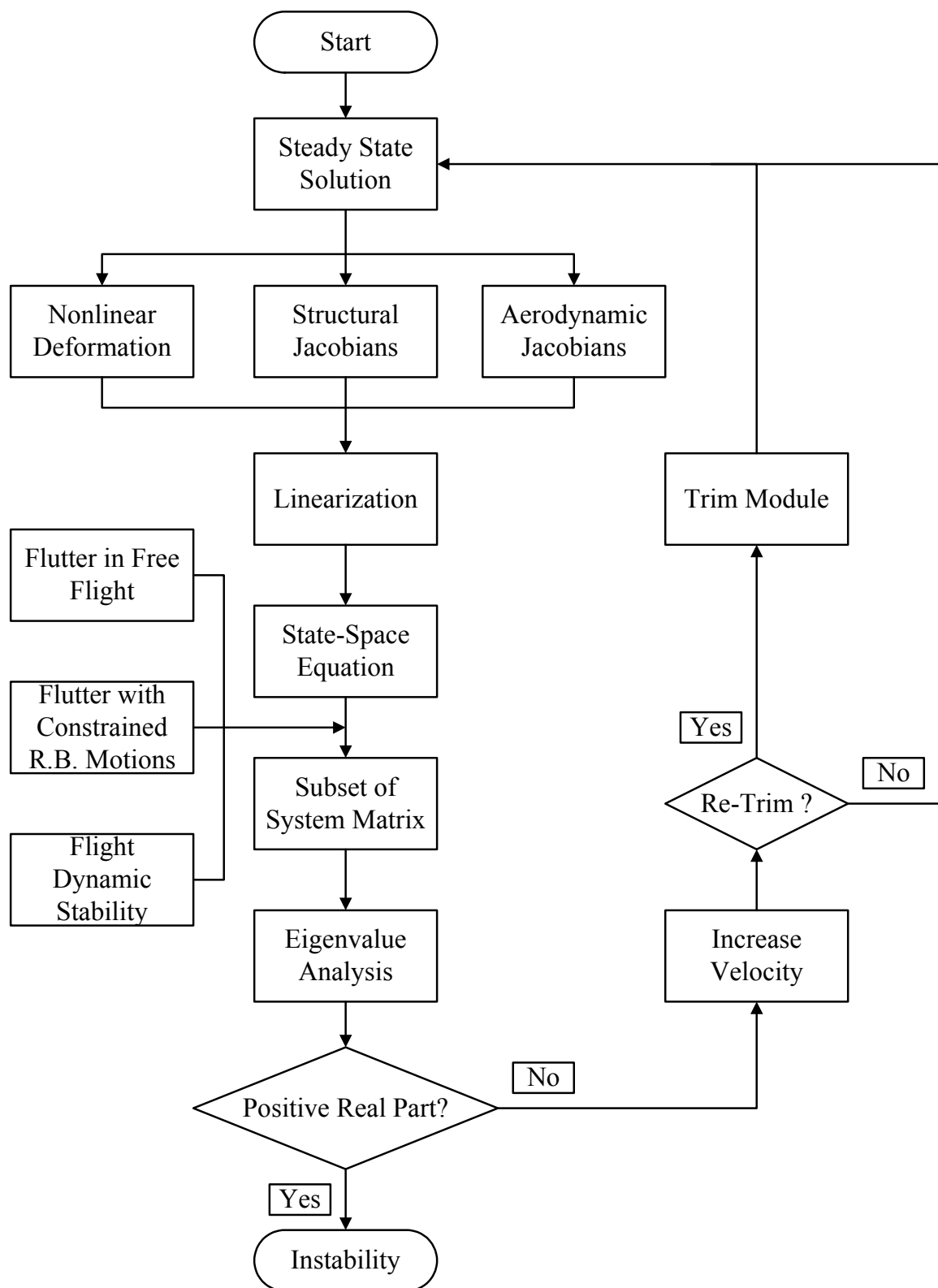


Figure 2.22: Scheme of searching for the stability boundary

CHAPTER III

Introduction to the Numerical Analysis Framework

This chapter presents the overview of the numerical framework – the University of Michigan’s Nonlinear Aeroelastic Simulation Toolbox (UM/NAST). A history of the framework development is also summarized. A block diagram is introduced to demonstrate the framework’s architecture, followed by the explanations of some main function modules. The intent is to provide a break-in point, such that the user may gain a basic idea of the framework, which may facilitate the code usage and future improvements.

3.1 Development of the Numerical Framework

The original numerical analysis framework was developed by Brown^[79], under the guidance of Professor Carlos E. S. Cesnik. A reduced-order, strain-based beam formulation is developed for nonlinear aeroelastic analysis of highly flexible vehicles. The code package is built using Matlab, which provides comprehensive scientific computational capabilities and other valuable toolboxes, facilitating the implementations.

Within the framework, composite beam structures with embedded active piezoelectric materials are modeled. Actuations are used for the roll simulation^[78]. Roll performance under active wing warping control and traditional aileron concept of a Joined-Wing configuration was compared^[28].

Subsequently, still under the guidance of Professor Carlos E. S. Cesnik, the framework was improved and enhanced by two other researchers from the University of Michigan: Shearer^[15, 83, 84] and this author^[29, 52, 82]. The framework is named the University of Michigan's Nonlinear Aeroelastic Simulation Toolbox (UM/NAST). The time line for its development is provided next.

Between 2004 and 2005, this author developed new kinematic relationships for the modeling of split beam systems^[29]. The formulation for searching the nonlinear flutter boundary was developed and flutter analysis was conducted^[82].

In 2005, Shearer corrected and improved the governing differential equations by considering the Coriolis effects^[83], upon which three types of time simulation were performed: rigid body, linearized, and nonlinear. In addition, Shearer also developed closed form solutions to the matrix exponential and closed form solutions to some of the Jacobian matrices.

Also in 2005, this author developed the formulation for the modeling of absolute and relative nodal displacement constraints, by applying the Lagrange Multiplier Method.

In 2006, this author integrated a temporal- and spatial-distributed discrete gust model into the time simulation scheme, for the purpose of modeling the dynamic responses of Flying-Wing vehicles^[52]. In addition, a bilinear stiffness model was implemented to study the changes in torsional stiffness due to skin wrinkling. Modifications to the finite state aerodynamics were made as well.

Simultaneously, Shearer developed a long term stable integration scheme^[84], and enhanced the framework to include open and closed loop simulations^[15].

Recently, this author completed the derivation of aerodynamic Jacobians. A formulation for flutter analysis of a free flight vehicle was developed based on the nonlinear equations of motions.

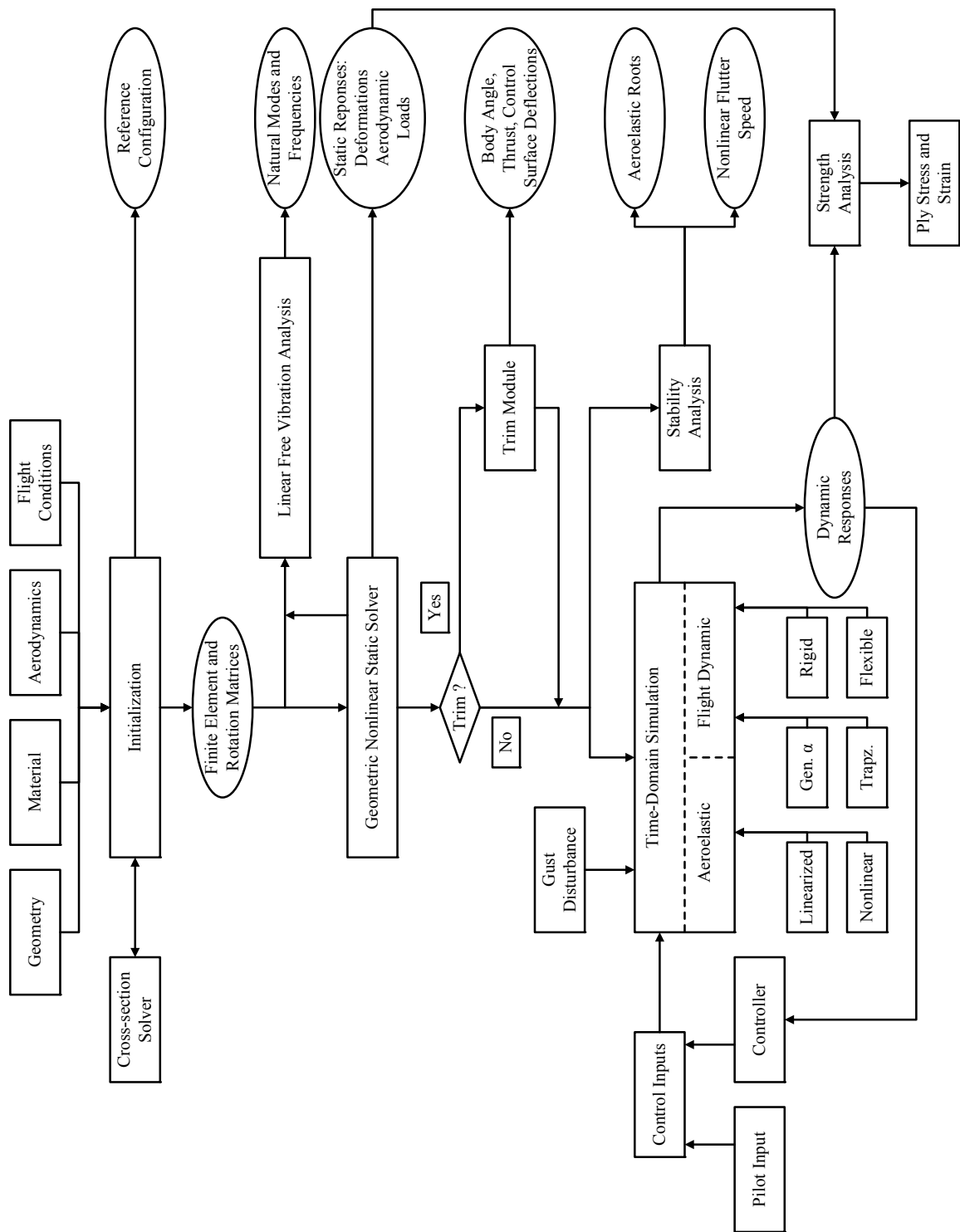


Figure 3.1: Block diagram showing functions of UM/NAST

3.2 Architecture of the Numerical Framework

Figure 3.1 presents an overview of the main function modules of the current implementation of NAST. These modules include: initialization, modal analysis, static solver, trim module, time simulation, and stability analysis. Beyond these, there are other auxiliary modules not listed in the figure, *e.g.*, for visualization.

3.3 Introduction to Main Function Modules

3.3.1 Model Initialization

Two model setup files (*modelnamedriver.m* and *modelname.m*) are used for defining the aircraft properties and initializing other important variables. The first file is relatively flexible for the user to define some fundamental variables used for parametric study. The second one has a relatively fixed structure, where the aircraft geometry, finite element discretization (includes the definition of beam members and groups), aerodynamic settings, fuel storage, rigid bodies, cross-sectional stiffness and inertia properties, nodal displacement constraints, etc. are defined. A cross-sectional solver is embedded with the code^[65], which allows the properties of two-cell, thin-walled composite cross-sections to be computed. However, the beam solver can also accept inputs from other cross-sectional solvers, such as VABS^[68], or even direct inputs from the driver file.

The slender members of an aircraft are modeled as beams. Therefore, a line representation of the aircraft geometry profile is always helpful before making the model initialization files. Figure 3.2 gives an example of the reference lines of a Joined-Wing aircraft. By taking the advantage of symmetry, the starting point of the beam reference lines is always located somewhere on the fuselage. However, it is not necessary for it to be the c.g. point of either the vehicle or the fuselage itself.

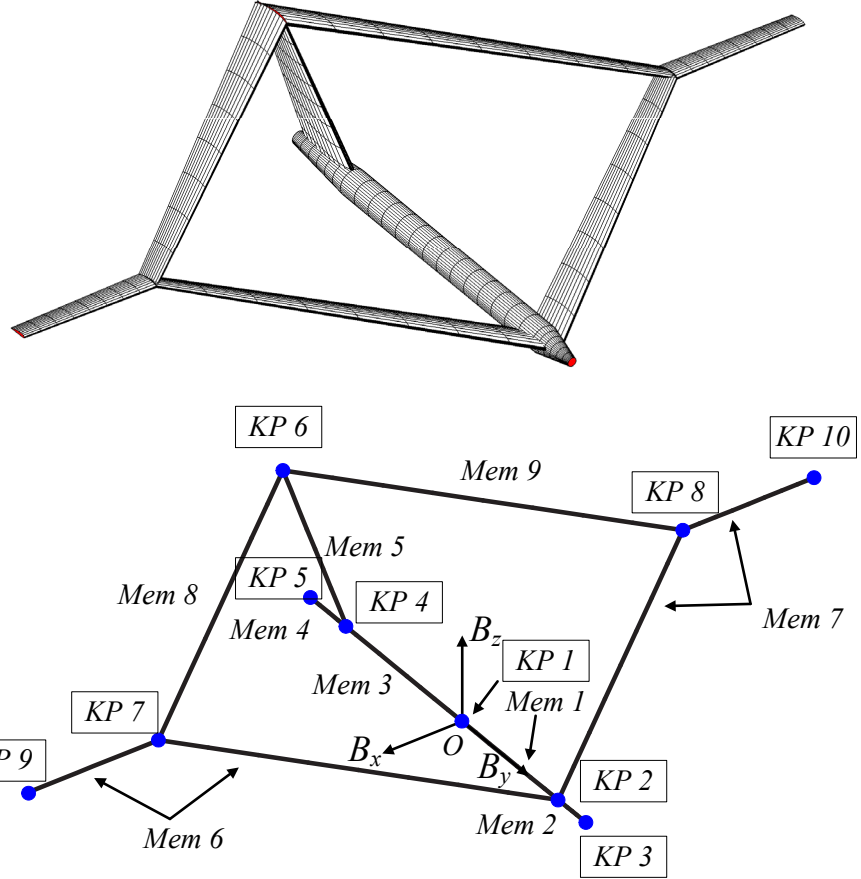


Figure 3.2: Sketch of a Joined-Wing configuration

The process of defining the beam structures follows the levels of “Key Point – Member – Group”, which is exemplified in Fig. 3.3. Two or more key points determine a member, while a group is formed by the set of members that originate from one common member. Key Points 2, 4, and 6 are split points. Member connection relationships should be defined for these points in the model setup file. The kinematics of a member only couples with the ones from the same group.

One clarification should be made here to avoid confusion: the structural coupling between the joined members (*e.g.*, Members 6 and 8, and Members 7 and 9) are modeled through the nodal displacement constraints, as discussed in Chapter II. To define an inter-member constraint, the user should specify the constrained nodes for the joining members, in the model setup file

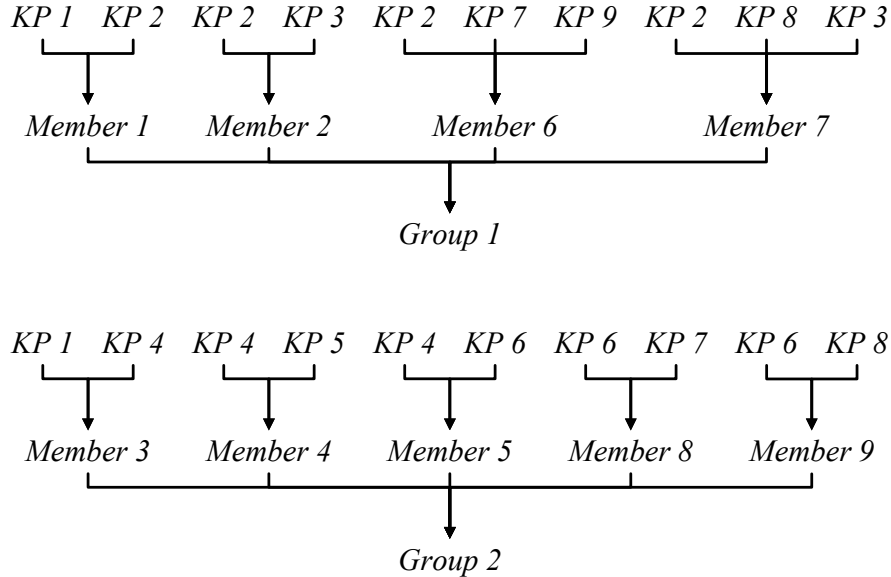


Figure 3.3: Bottom-up structural relationships for the sample Joined-Wing configuration

With the model setup files, a series of subroutines are executed (within the main function *mainF.m*), such that a reference aircraft configuration is obtained, which includes the undeformed shape, fuselage inertia properties (if modeled as a rigid body), finite element mass, damping, and stiffness matrices, aerodynamic inflow matrices, rotation matrices between the reference frames, and structural Jacobians relating the independent variables and dependent variables. Note that the Jacobians and some of the rotation matrices will be updated according to the current deformed shapes.

3.3.2 Modal Analysis

The modal analysis may be carried out in two stages. One is right after the initialization of the aircraft model, which returns the natural modes and frequencies of the structural system. Since the slender structures may significantly deform with operating loads, the modes and frequencies could change at the deformed states. Therefore, the modal analysis may also be carried out after a static solver, which returns the modes and frequencies of small vibrations about the nonlinear steady state.

3.3.3 Geometric Nonlinear Static Solver

This solver returns the static deformation under a given load condition. The rigid body motions of the vehicle are constrained, and the time derivatives and unsteady aerodynamic terms are eliminated from the equations of motion (Eq. 2.108). The solution is performed in an iterative way until a converged nonlinear deformation is reached. Details about this solution can be found in Ref. [79]. The input and output parameters are listed in Table 3.1.

Table 3.1: Inputs and outputs of the static solver

Flight Conditions	Flight Speed
	Altitude
	Body Angle
	Fuel Mass (if modeled)
	Gravity
Control Inputs	Elevator, Rudder, and Aileron Angles
	Actuation Voltage
	Concentrated Mass and/or Moments (<i>e.g.</i> , Engine Thrust)
	Distributed Forces and/or Moments
Solution Setups	Switch for Prandlt-Glauert Correction
	Switch for Follower Structural Loads
	Convergence Criterion
Outputs	Strain Vector
	Nodal Positions and Orientations
	Updated Structural Jacobians and Rotation Matrices
	Nodal Aerodynamics Loads
	Aerodynamic Jacobians
	Vehicle Center of Gravity after Deformation
	Total Lift, Drag, and Moments about Updated c.g. Point
	Ply Stress and Strain Components (if modeled)

The control input is defined in another user-defined file: `get_control_inputs_modelname.m`. The distributed forces and moments are not control inputs. However, they are input to the solver through the control inputs file, in a similar way as the concentrated loads.

The aerodynamic module is executed within the static solver, which returns the distributed nodal aerodynamic force and moment at each solution step, and the corresponding derivatives of the aerodynamic loads. After a converged solution is reached, nodal positions and orientations are recovered from the strain vector through the kinematic relationships. The c.g. point is updated according to the deformed shape.

3.3.4 Trim Module

The trim module provides input date for many other modules, as seen from Fig. 3.1. It returns the vehicle body angle, control surface deflection, and thrust forces at a given flight condition. Currently, there are two trim schemes implemented, one of which calculates the trimmed conditions by minimizing the body accelerations, while the other minimizes the loads about the vehicle's c.g. point. Both of them provide very similar results. The input and output parameters are listed in Table 3.2.

Table 3.2: Inputs and outputs of the trim module

Input	Flight Speed
	Flight Altitude
	Fuel Mass (if modeled)
Output	Body Angle
	Elevator Angle
	Thrust Force

3.3.5 Time Domain Simulation

The time simulation returns the transient responses of the vehicles at a given flight condition. The simulation always begins with a steady state obtained from the static

solver. The user is able to choose the simulation type (nonlinear, linearized, and rigid body) and the numerical integration scheme (Modified Generalized- α ^[15], and Trapezoidal). The control information may come from pilot input or from feedback of a closed-loop controller. Other input and output parameters are listed in Tables 3.3 and 3.4. Note that the direct outputs of the time simulation are no more than the independent variables and their time derivatives. The other information, such as the nodal positions, Euler Angles of the rigid body, and aerodynamic loads at each time step may be obtained after the simulation is finished, through a user defined script. The reason to do this is to save unnecessary post-processing during the time simulation.

Table 3.3: Inputs of the time domain simulation

Flight Conditions	Steady State Input
	Flight Speed
	Altitude
	Body Angle
	Fuel Mass (if modeled)
	Gravity
Control Inputs	Gust Model
	Elevator, Rudder, and Aileron Angles
	Actuation Voltage
	Concentrated Mass and/or Moments (<i>e.g.</i> , Engine Thrust)
Simulation Setups	Distributed Forces and/or Moments
	Time Range
	Size of Time Steps
	Switch for Prandlt-Glauert Correction
	Switch for Follower Structural Loads
	Switch for Constrained or Free Flight Simulation
	Choice of Simulation Type
	Choice of Integration Scheme
	Tuning Parameters for Generalized- α Method
	Convergence Criterion

Table 3.4: Outputs of the time domain simulation and stability analysis

Outputs of the Time Domain Simulation	Strain Vector
	Strain Rate Vector
	Strain Acceleration Vector
	Body Velocity
	Body Acceleration
	Quaternion
	Quaternion Rate
	Body Position
	Body Position Rate
	Inflow States
	Inflow States Rate
	Lagrange Multipliers for Constraints (if exists)
	Lagrange Multiplier Rates for Constraints (if exists)
	Error States (if exists)
	Error States Rate (if exists)
	Convergence Information
Outputs of the Stability Analysis	Eigenvalues (Poles) of the State Space System
	Eigenvectors of the State Space System
	Flutter Speed
	Frequency of the Flutter Mode
	Flutter Mode

3.3.6 Stability Analysis

The block diagram showing the scheme of searching the stability boundary at a level flight condition has already been presented in Chapter II. It is briefly described here. The user first chooses an arbitrary flight speed at the given flight condition, which should be well below the flutter boundary. As the speed is increased, the nonlinear system is linearized at each new steady state and put into state space form. Eigenvalues are then checked for the real parts. Once an eigenvalue with a positive real part is found, the

system instability point is reached. Since the steady state is updated according to each increased flight speed, the flutter boundary found through this scheme is a matched-point flutter speed.

Since the stability is evaluated about a steady state, the inputs for this analysis are almost the same as the static solver, in addition to some constraint information. The outputs are listed in Table 3.4. The user may choose to constrain the rigid body motions of the vehicle or not. The solution then returns flutter boundaries of the constrained vehicle or the vehicle in free flight condition, correspondingly. Flight stability may also be evaluated by only considering the rigid body motions at a given flight condition.

3.3.7 Visualization

The visualization consists of two sub-functions. The first is the output of the mode shapes from the modal analysis or stability analysis. The solver takes the eigenvector from the previous analysis, and adds the corresponding components to the steady state (or undeformed) solution as small perturbations. The new position and the deformed shape of the vehicle can be determined and output based on the perturbed states. The user may need to choose appropriate coefficients to amplify the mode shapes for clearer views.

Another function of visualization is to animate the time domain simulation. The solver recovers deformation, position and orientation of the vehicle from the independent variables at each time step. Individual pictures are generated according to the information. A movie file is then generated by sequencing those pictures in time series.

CHAPTER IV

Numerical Verification of Formulation

Before numerical analysis can be carried out, the newly developed formulation is subject to verification for its accuracy. This is completed in this chapter.

First, various beam configurations are created to test the formulation of the kinematic relationships for split beam systems, the absolute and relative (inter-member) nodal displacement constraints, and the follower loading conditions. For these beam configurations, different types of solutions are performed, including steady-state solution, forced dynamics response, natural modes and frequencies. Results from the current implementation are compared with those generated by using MSC.Nastran^[69]. MSC.Nastran is a widely used commercial finite element software package. It can solve for geometrical nonlinear deformations, both statically (with Sol. 106) and dynamically (with Sol. 129). Therefore, MSC.Nastran is chosen for comparison and verification purpose. Next, the accuracy of the new aeroelastic implementation should be verified. Linear flutter and natural frequency results of a highly flexible, high-aspect-ratio wing are compared with data given in Refs. [79] and [88]. Finally, nonlinear flutter results with both cantilever condition and rigid body motions are validated by using time-domain simulation within the UM/NAST environment as verification. Note that some other formulations, which are used for the numerical studies, such as the gust model, stall model and skin wrinkling model, are straight forward. Therefore, the verification processes are not presented here.

4.1 Cantilever Beam Configuration

A 1-meter long slender cantilever beam is firstly used for the validation, whose geometric and physical properties are listed in Table 4.1. The beam can be modeled as one single beam member or a split beam system with two members connecting at the middle point, as shown in Fig. 4.1. The latter model will apply the kinematics of split beam systems. The whole beam is discretized into 20 elements in both UM/NAST and MSC.Nastran models. CBEAM element is selected in MSC.Nastran for modeling.

Table 4.1: Properties of the reference beam

Length	1.00 m
Extensional Stiffness K_{11}	$1.00 \times 10^6 \text{ Pa}\cdot\text{m}^2$
Torsional Stiffness K_{22}	$8.00 \times 10^1 \text{ N}\cdot\text{m}^2$
Flat Bending Stiffness K_{33}	$5.00 \times 10^1 \text{ N}\cdot\text{m}^2$
In-plane Bending Stiffness K_{44}	$1.25 \times 10^3 \text{ N}\cdot\text{m}^2$
Mass per Unit Span	0.10 kg/m
Rotational Inertia I_{xx}	$1.30 \times 10^{-4} \text{ kg}\cdot\text{m}$
Flat Bending Inertia I_{yy}	$5.00 \times 10^{-6} \text{ kg}\cdot\text{m}$
In-plane Bending Inertia I_{zz}	$1.25 \times 10^{-4} \text{ kg}\cdot\text{m}$

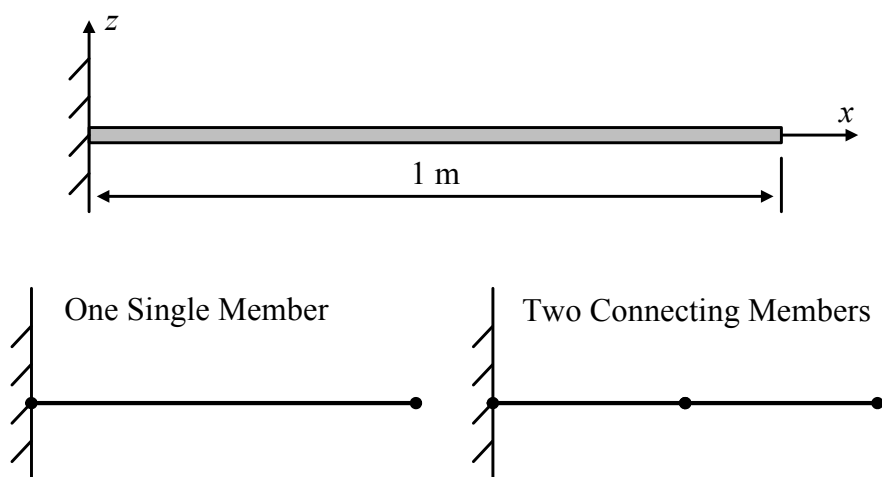


Figure 4.1: Model description of a cantilever beam

4.1.1 Cantilever Beam with Static Tip Forces

The load condition is shown in Fig. 4.2. The point tip force is varied from 0 to 150 (N). The vertical and axial tip displacements versus tip load are plotted in Figs. 4.3 and 4.4. The results show very good agreement with those using MSC.Nastran. As can be observed from the plots, the single member and split beam implementations give nearly identical results.

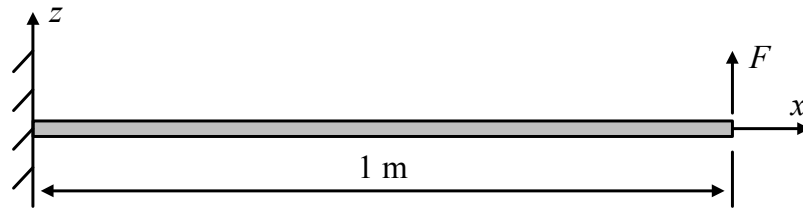


Figure 4.2: A cantilever beam with concentrated tip load

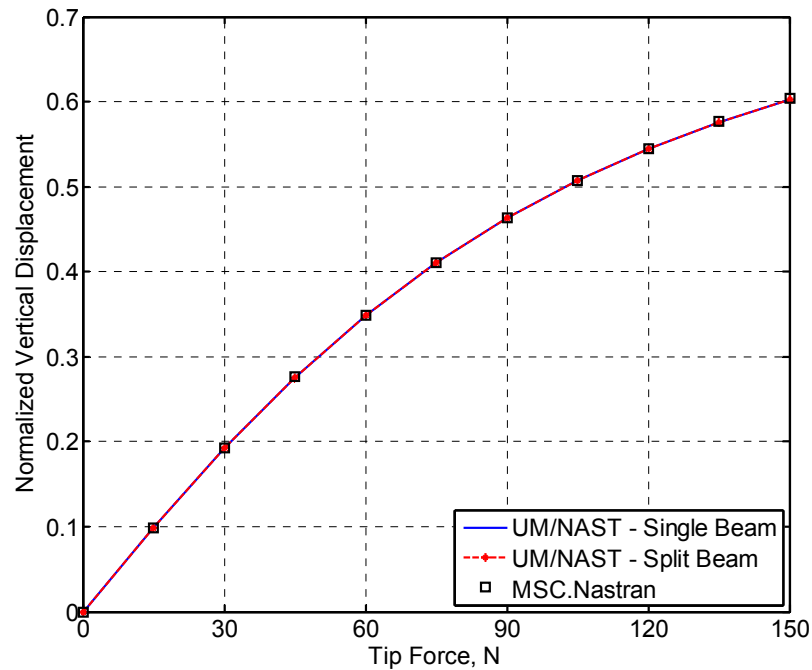


Figure 4.3: Change of vertical tip displacement with different tip loads (normalized with respect to the beam span)

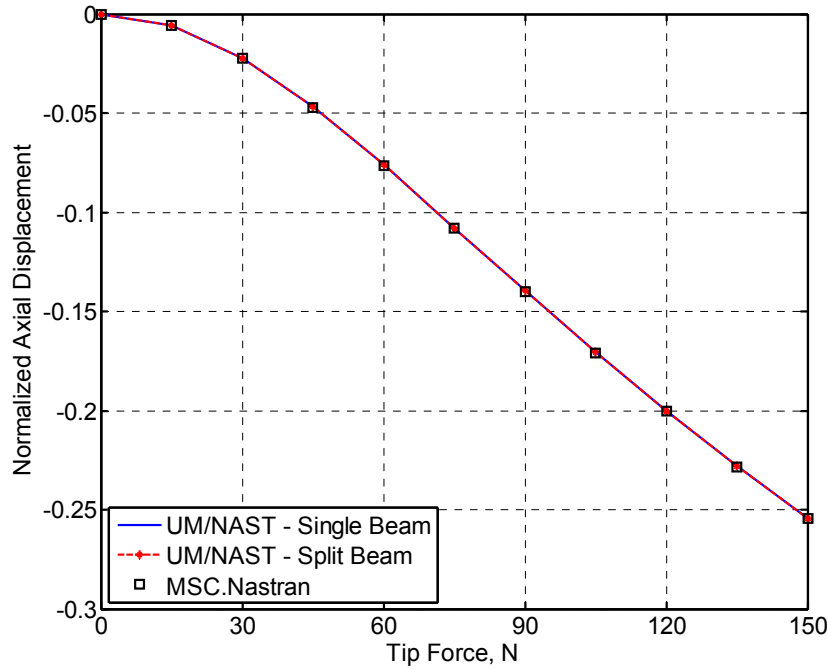


Figure 4.4: Change of axial tip displacement with different tip loads (normalized with respect to the beam span)

4.1.2 Time Simulation of Cantilever Beam with Tip Force

The same beam model is used for this case as for the static test. In this case, the point load is still applied at the tip in the vertical direction, with a sinusoidal function of time: $F = 30\sin 20t$ (N), such that the beam deformation is brought to the nonlinear range. The three-dimensional tip displacements of the cantilever beam are compared with the results from MSC.Nastran and are plotted in Fig. 4.5. The time steps used are 0.0025 s in UM/NAST and 0.002 s in MSC.Nastran. All results are showing good agreement, especially between the single beam and split beam models.

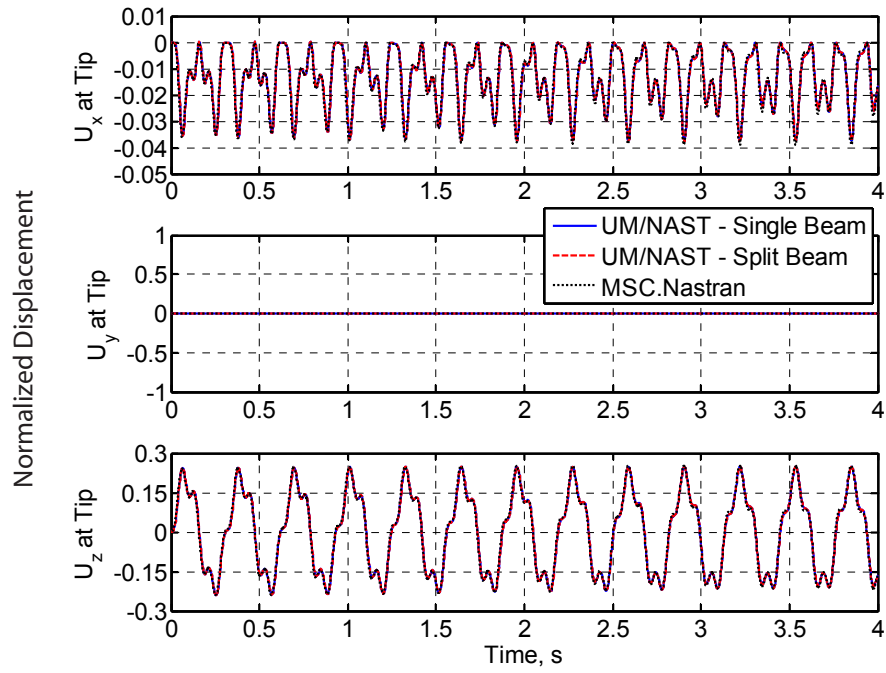


Figure 4.5: Tip displacement of the cantilever beam under vertical tip load (normalized with respect to the beam span)

4.2 Split Beam Configuration

As mentioned in the previous chapter, the kinematics formulation of split beam systems is an important prerequisite for successful modeling of fully flexible vehicles. Therefore, its accuracy should be verified before numerical studies can be performed. The previous testing has verified that a cantilever beam can be modeled as a single beam or a split beam system, both of which generate nearly identical numerical results. To be more complete, it is necessary to test a beam system with two branches splitting from each other, such that the deformation or motion of these branches can be studied. Figure 4.6 exemplifies a split beam system, which has the same cross-sectional properties as the cantilever beam used previously. Each of the branches is discretized into 10 elements in both UM/NAST and MSC.Nastran models.

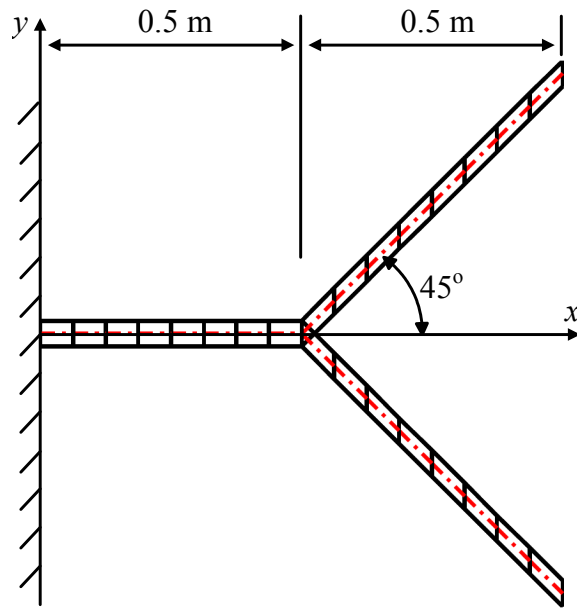


Figure 4.6: Model description of a split beam system

4.2.1 Split Beam with Multi-Axial Static Tip Forces

Accuracy of the current formulation when performing static solutions of the split beam system is assessed in this analysis. A vertical point load of 50 (N) is applied at the front tip of the beam and another vertical point load of -50 (N) is applied at the rear tip (Fig. 4.7). The resulting deformations of the beam are shown in Fig. 4.8. The results show very close correlation.

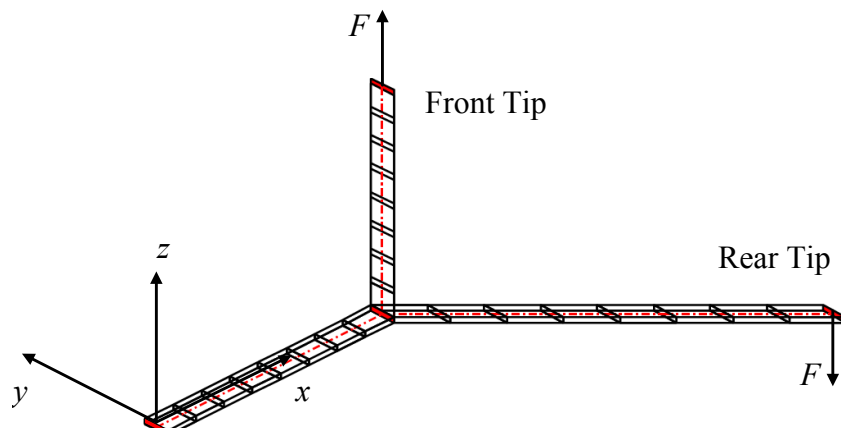


Figure 4.7: A split beam system under multi-axial tip loads

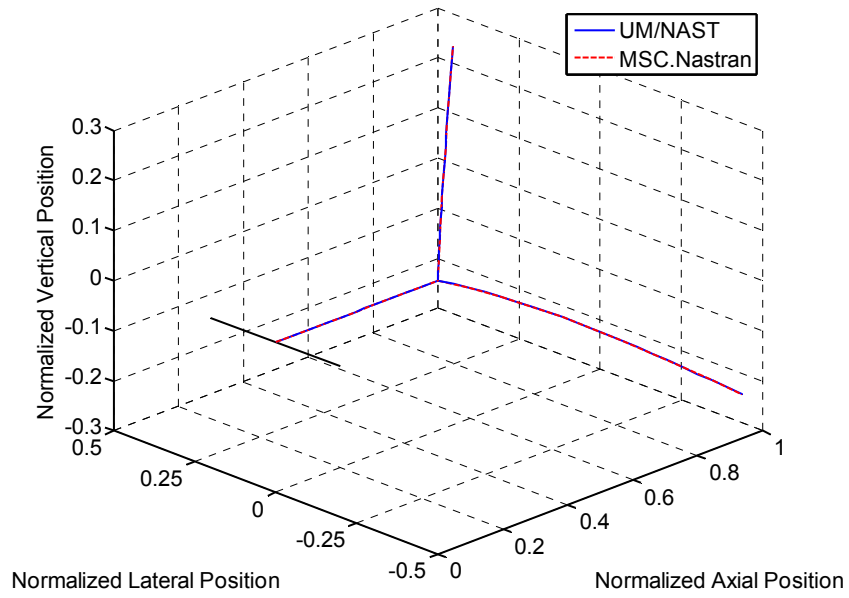


Figure 4.8: Three-dimensional deformation of the split beam system under multi-axial loads (normalized with respect to the beam span)

4.2.2 Time Simulation of Split Beam with Single Tip Force

A sinusoidal load of $F = 30\sin 20t$ (N) is applied at the front tip along z direction as shown in Fig. 4.9. The time responses of both tips are plotted Figs. 4.10 and 4.11, and compared with the results from MSC.Nastran. The time steps used are 0.0025 s in UM/NAST and 0.002 s in MSC.Nastran. Both of the results are very close to each other.

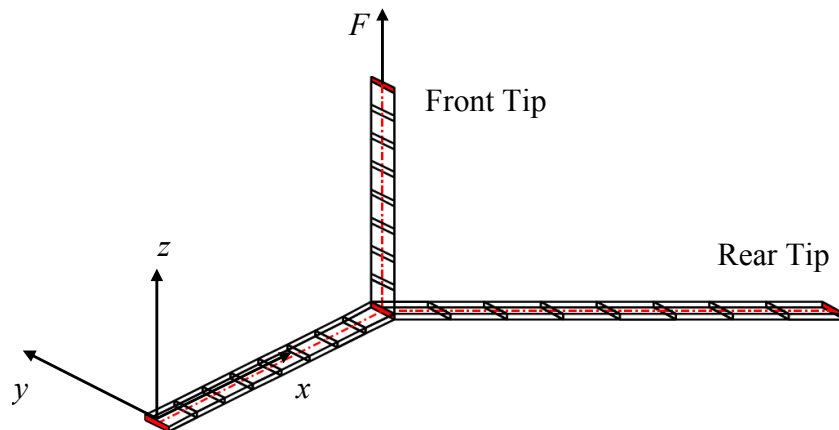


Figure 4.9: A split beam system under single tip load

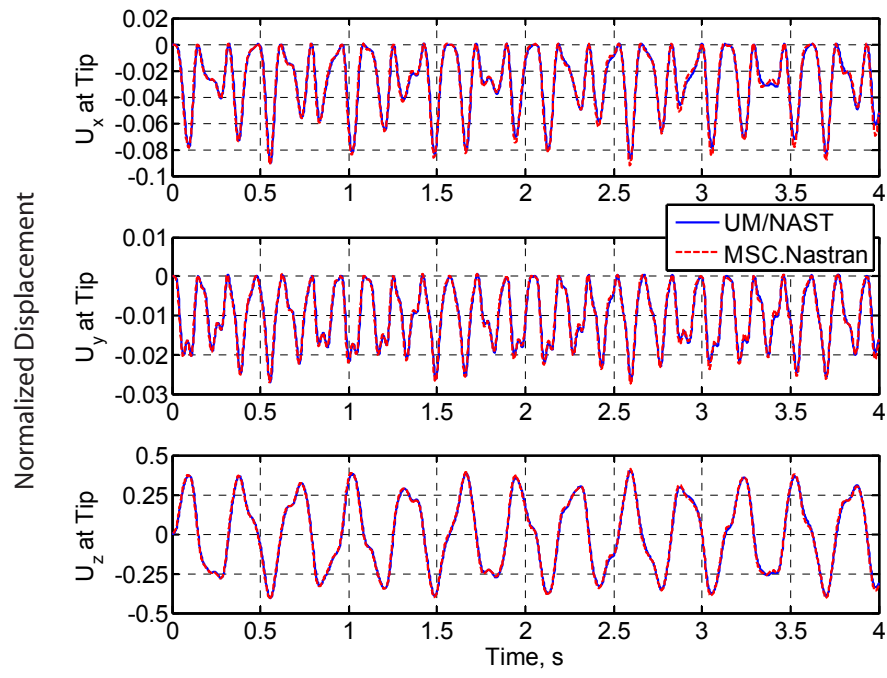


Figure 4.10: Displacement of the front tip of the split beam system under single tip load
(normalized with respect to the beam span)

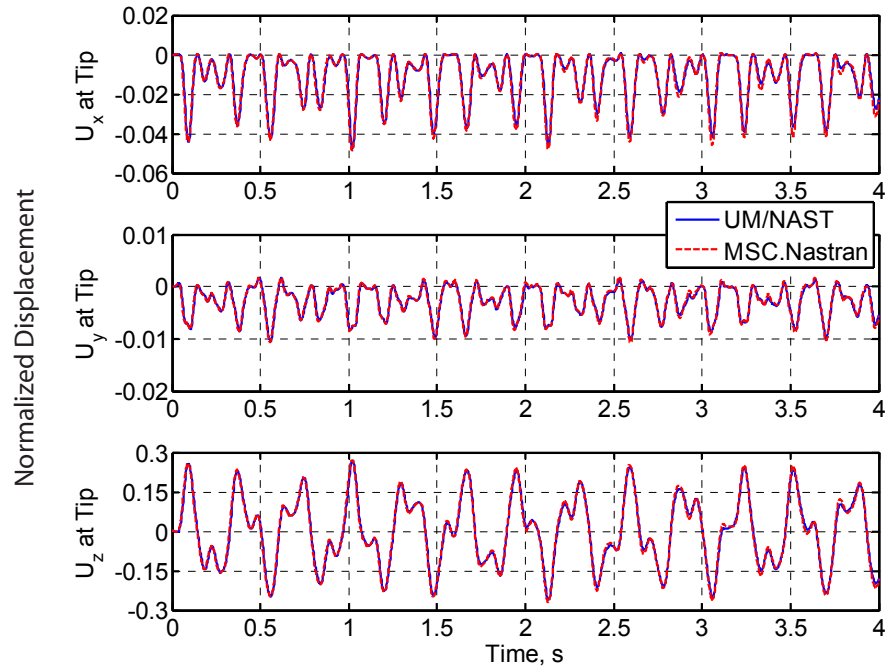


Figure 4.11: Displacement of the rear tip of the split beam system under single tip load
(normalized with respect to the beam span)

4.3 Beam Configuration with Absolute Displacement Constraints

This section is to test the implementation of the Lagrange Multiplier Method for the modeling of absolute displacement constraints. For the models used in this section, the beam is clamped at its root, whose middle point is pinned – only displacements of that node are constrained while the rotations are free (see Fig. 4.12). The properties and discretization of the beam used in this section are the same as the previous cantilever beam.

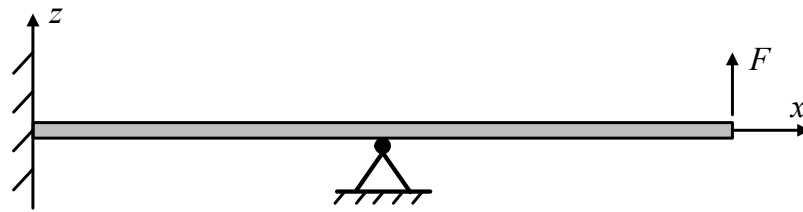


Figure 4.12: A cantilever beam with pinned mid point and concentrated tip force

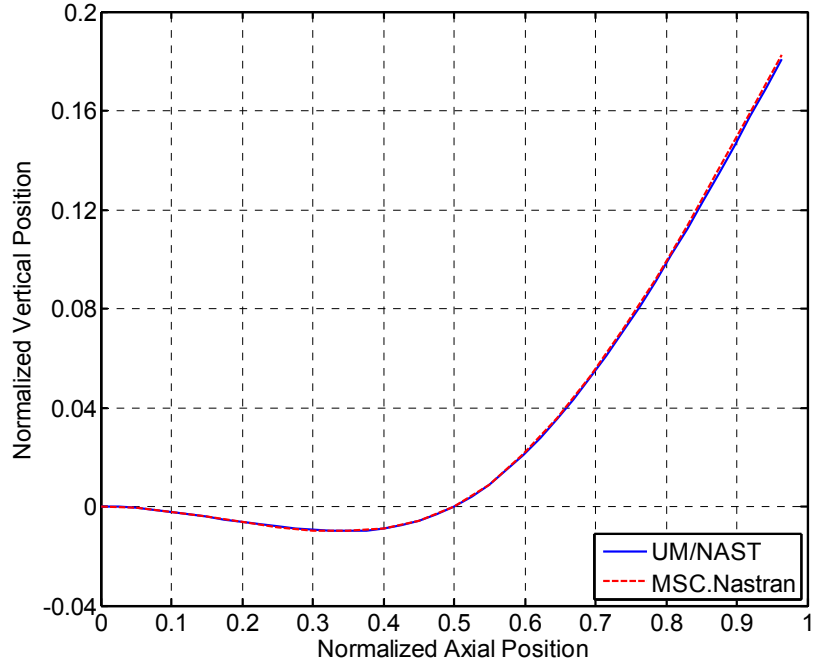


Figure 4.13: Deformation of the constrained beam under vertical tip load (normalized with respect to the beam span)

4.3.1 Fixed-Pinned Beam with Static Tip Force

Consider a tip load of 150 (N) is applied along the z direction. The comparison of current implementation with MSC.Nastran is plotted in Fig. 4.13. Very close correlation between the two sets of results can be observed.

4.3.2 Time Simulation of Fixed-Pinned Beam with Tip Force

A sinusoidal tip force of $F = 150\sin 20t$ (N) is applied at the free end of the fixed-pinned beam model. The responses are compared with MSC.Nastran and plotted in Fig. 4.14. The time steps used are 0.002 s in UM/NAST and 0.0025 s with the adaptive option in MSC.Nastran. From the comparison, one may find UM/NAST catches the low-frequency responses well, but loses some accuracy in high-frequency information.

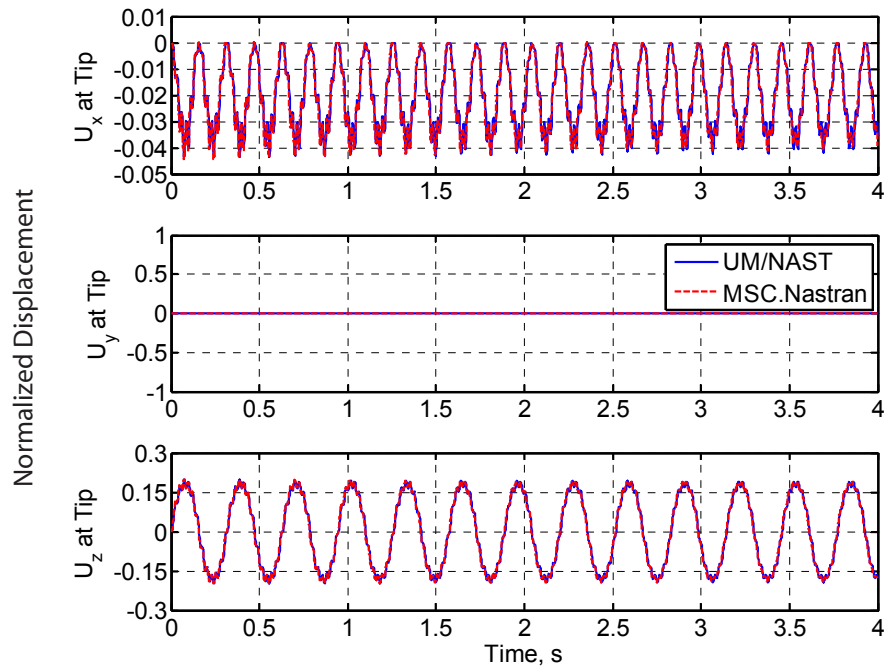


Figure 4.14: Tip displacement of the constrained beam under vertical tip load
(normalized with respect to the beam span)

It is also of interests to explore how accurately the constraints are modeled in this formulation. Figure 4.15 plots the displacements of the constrained node (middle point). It can be observed that the displacement of the node is as low as the order of 10^{-8} (comparing to the total beam length). Therefore, the modeling here is correct.

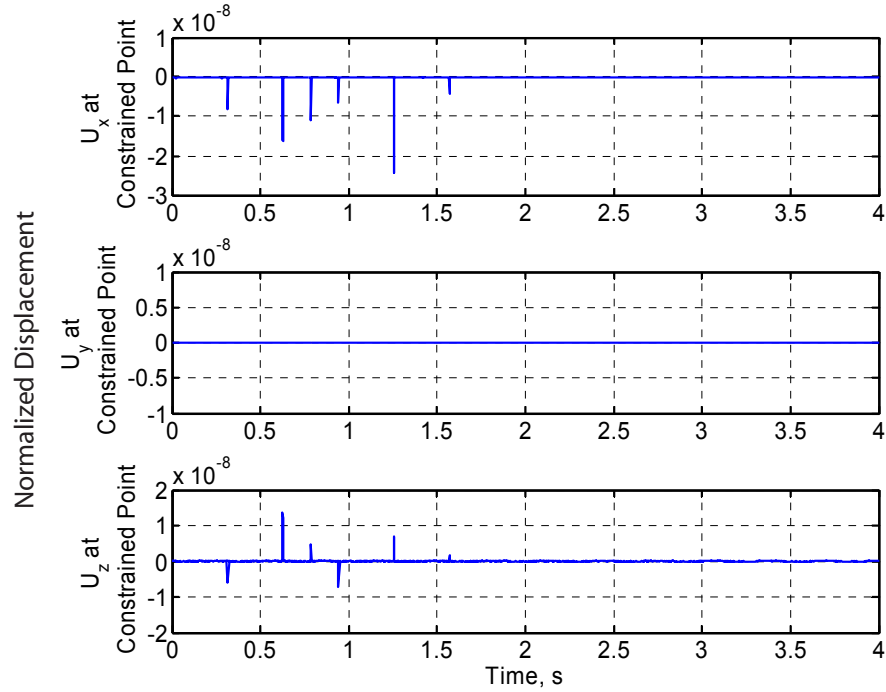


Figure 4.15: Displacement of the constrained node in UM/NAST model (normalized with respect to the beam span)

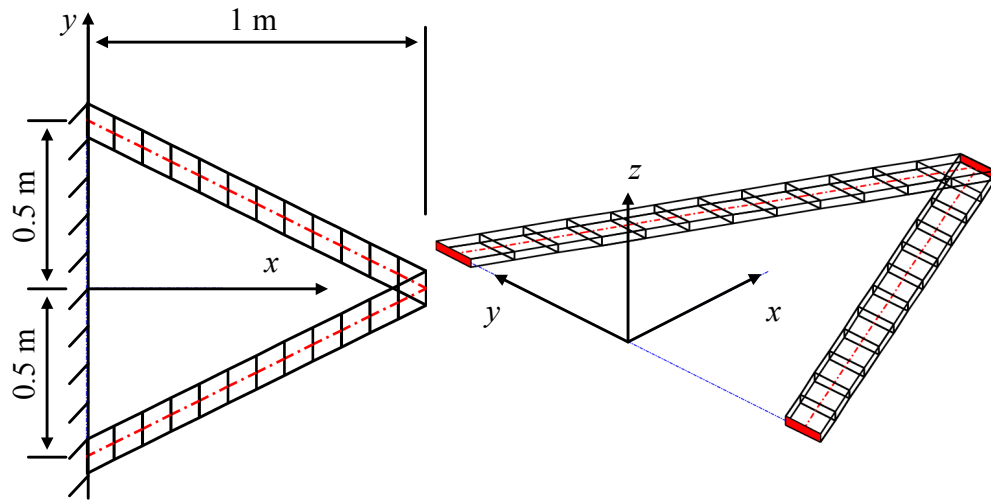


Figure 4.16: Model description of a joined-beam system

4.4 Beam Configuration with Relative Displacement Constraints

The Lagrange Multiplier formulation for relative nodal displacement constraints is also necessary to be verified. For a joined-beam model, the two cantilever beam members meet at their tips. The cross-sectional properties of each beam member are still the same as defined before, with geometries shown in Fig. 4.16. Each beam member is discretized into 20 elements in both UM/NAST and MSC.Nastran.

4.4.1 Joined-Beam with Multi-Axial Static Force

In this analysis, a multi-axial force is applied at the common tip of the two branches. The magnitude of the load is 10 (N) in the z direction, and 1000 (N) in the y direction. Deformed beam shape (Fig. 4.17) and displacements (Fig. 4.18) are compared between UM/NAST and MSC.Nastran. The results show very good agreement.

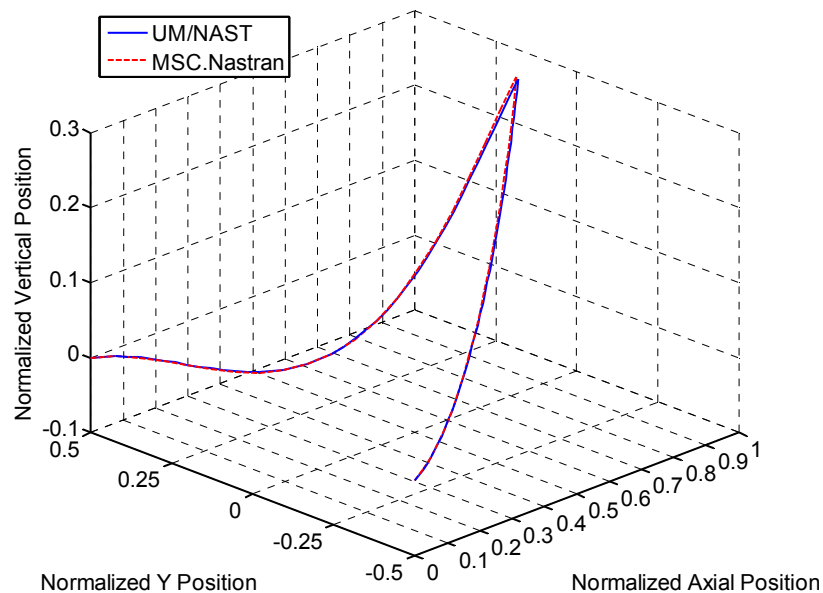


Figure 4.17: Three-dimensional deformation of the joined-beam system under multi-axial loads (normalized with respect to the beam span)

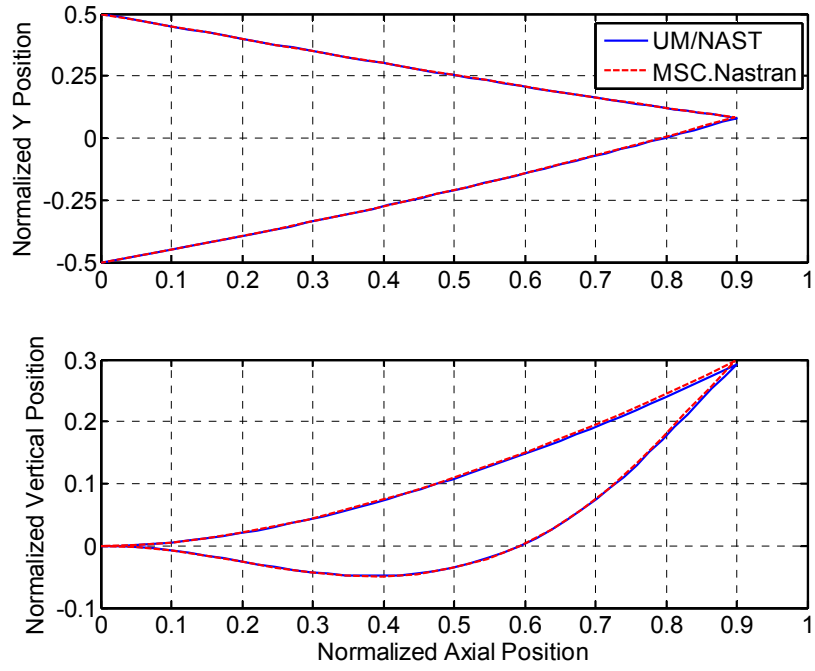


Figure 4.18: Lateral and vertical displacements of the joined-beam system under multi-axial loads (normalized with respect to the beam span)

4.4.2 Time Simulation of Joined-Beam with Tip Force

To test the time simulation for the joined-beam model with relative displacement constraint, a sinusoidal tip force of $F = 60\sin 20t$ (N) is applied at the common tip of the two members. The responses are compared with MSC.Nastran and plotted in Fig. 4.19. The time steps used are 0.002 s in UM/NAST and 0.0016 s in MSC.Nastran. Good agreement of the two sets of results can be observed.

The accuracy of the modeling of the relative nodal displacement constraints may also be examined. Figure 4.20 compares the displacements of two tips of the individual members. It can be seen that the displacements of the two tips are almost identical, while demonstrating numerical differences at a few time steps.

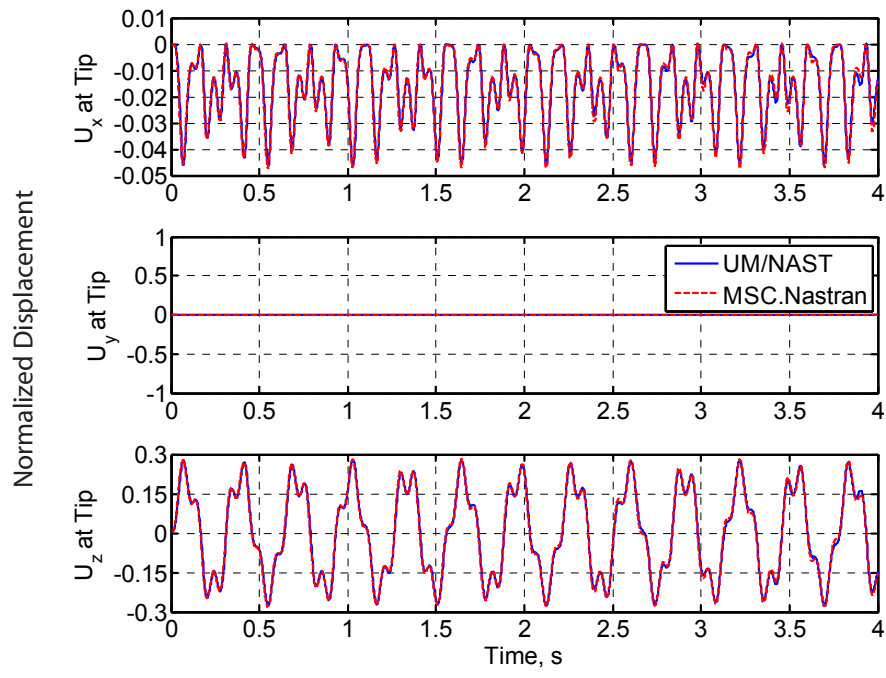


Figure 4.19: Tip displacement of the joined-beam system under vertical tip load (normalized with respect to the beam span)

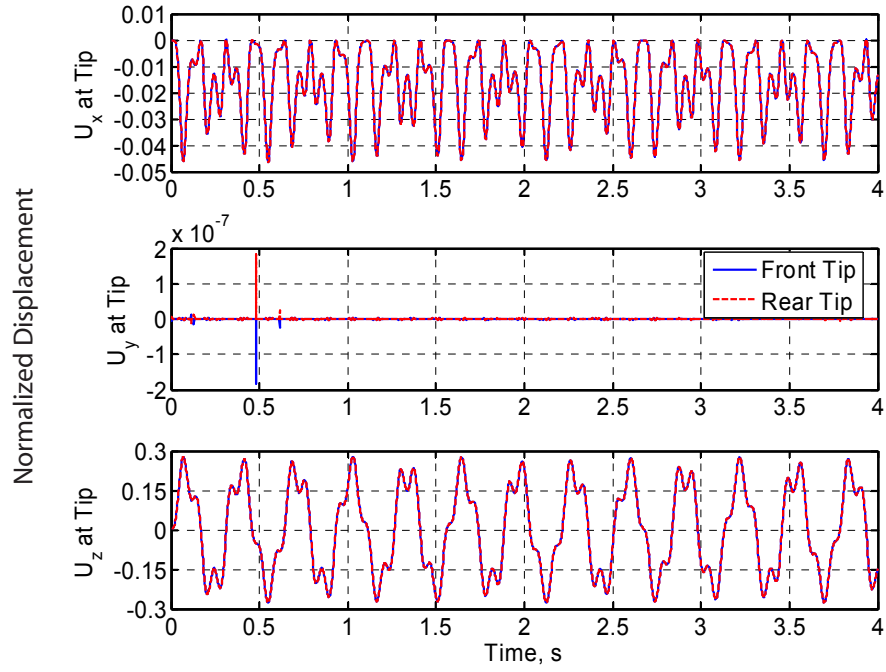


Figure 4.20: UM/NAST displacement results for the Two Tips of the joined-beam system under vertical tip load (normalized with respect to the beam span)

4.5 Follower Loading Case

Follower loads are used for modeling engine thrust forces. In this section, a cantilever beam is tested with follower loads. The beam model is the same as the one used for the previous cantilever test with dead loads.

4.5.1 Cantilever Beam with Static Follower Loads

Nonlinear static solution with follower loads of the cantilever beam is validated in this case. A tip force of 50 (N) and a twist moment of 50 (N·m) are both applied to the cantilever beam (Fig. 4.21). Note that both of them are follower loads. Deformed beam shape (Fig. 4.22) and displacements (Fig. 4.23) are compared between UM/NAST and MSC.Nastran. The results show perfect agreement.

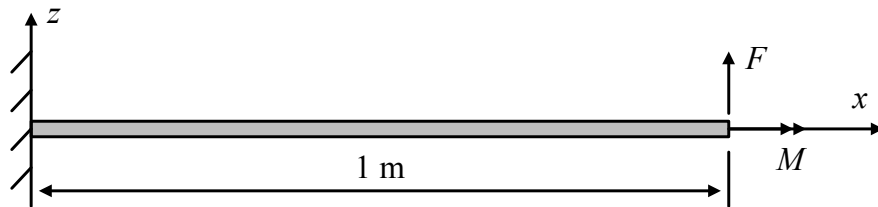


Figure 4.21: A cantilever beam subject to concentrated follower loads

4.5.2 Time Simulation of Cantilever Beam with Follower Tip Load

A sinusoidal tip force of $F = 30\sin 20t$ (N) is applied at the tip of the beam. Note that the direction of the tip load is still following the beam deformation, instead of being fixed. The response are compared with MSC.Nastran and plotted in Fig. 4.24. The time steps used are 0.0025 s in UM/NAST and 0.002 s in MSC.Nastran. Good agreement of the two result sets can be observed.

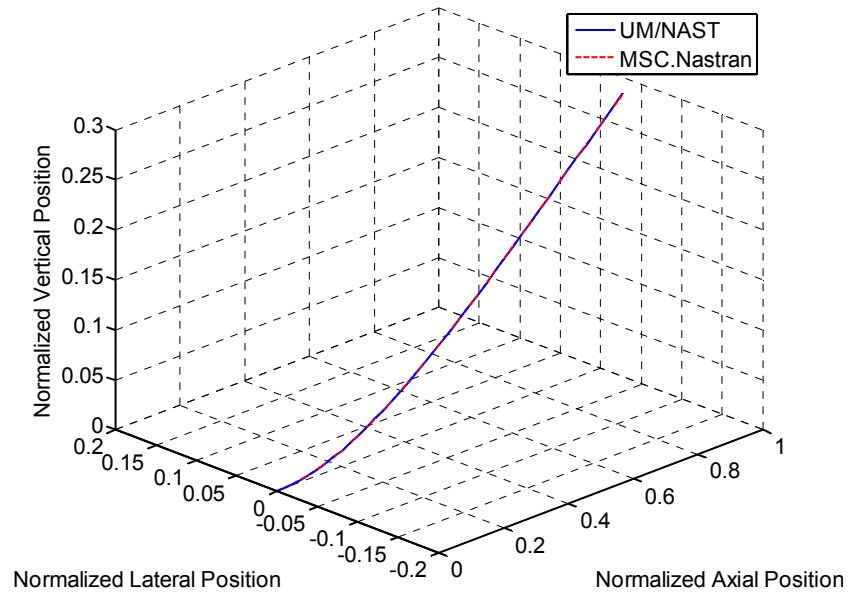


Figure 4.22: Three-dimensional deformation of the cantilever beam under follower tip loads (normalized with respect to the beam span)

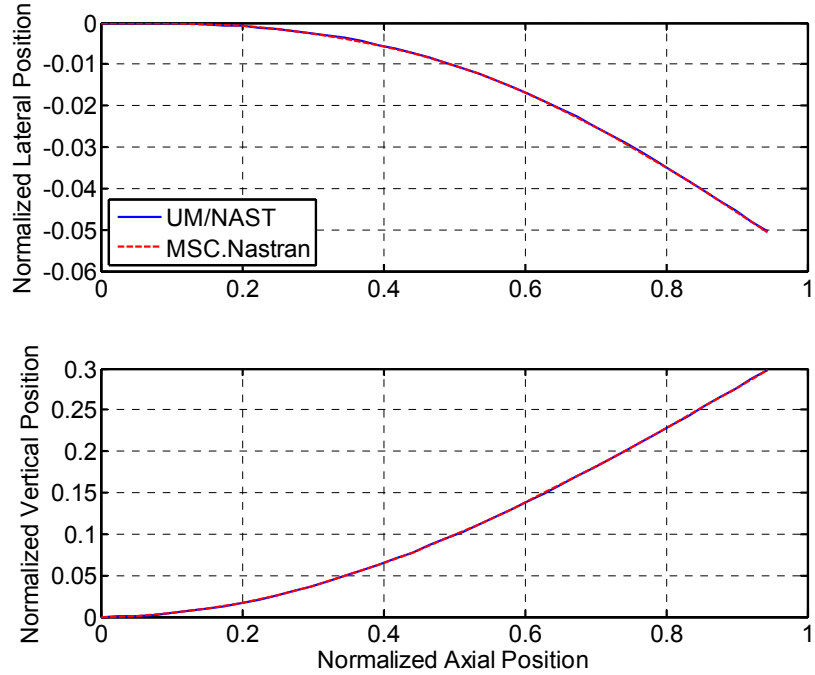


Figure 4.23: Lateral and vertical displacement of the cantilever beam under follower tip loads (normalized with respect to the beam span)

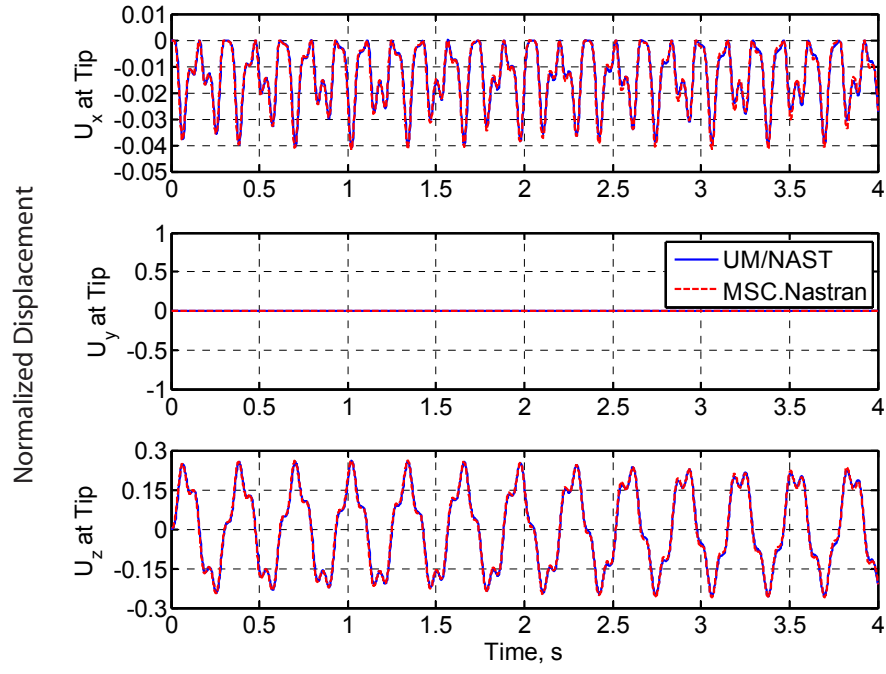


Figure 4.24: Tip displacement of the cantilever beam under follower tip loads (normalized with respect to the beam span)

4.6 Aeroelastic Formulation: Prediction of Flutter Boundary

A comprehensive verification of the aerodynamic formulations was performed in Ref. [79]. This section only validates the newly developed formulation for the stability analysis. To validate this formulation, various cases are tested, including linear flutter of a cantilevered slender wing, nonlinear flutter of the same slender wing, and body freedom flutter of a complete vehicle model. The results are compared with existing results from other solution packages or verified through time-domain simulations within UM/NAST.

4.6.1 Highly Flexible Wing with Cantilevered Root

In Ref. [88], a highly flexible, high-aspect-ratio wing was created for aeroelastic analysis. The physical and geometrical properties of the wing are given in Table 4.2. Natural frequencies and linear flutter speed of this model were calculated in Refs. [88] and [79].

Table 4.2: Properties of a highly flexible wing (after Ref. [88])

Length	16 m
Chord	1 m
Spanwise Ref. Axis Location (From L.E.)	50% of chord
Center of Gravity (From L.E.)	50% of chord
Flat Bending Rigidity	$2 \times 10^4 \text{ N}\cdot\text{m}^2$
Chord Bending Rigidity	$4 \times 10^6 \text{ N}\cdot\text{m}^2$
Torsional Rigidity	$1 \times 10^4 \text{ N}\cdot\text{m}^2$
Mass per Unit Length	0.75 kg/m
Rotational Inertia per Unit Length	0.1 kg·m

Natural modes are calculated for the undeformed beam. The first five natural frequencies are listed in Table 4.3. An 8-element discretization was used in Ref. [88], whereas 10- and 20-element discretizations are employed in the current work for convergence studies. These results are all compared with analytical solutions. As can be observed, the current formulation gives accurate numerical predictions on the fundamental frequencies of the slender beam, when compared to the analytical solutions.

Table 4.3: Natural frequencies of the highly flexible wing

	Ref. [88]	Current (10 Elements)	Current (20 Elements)	Analytical
1st Flat Bend (rad/s)	2.247	2.2468	2.2438	2.2454
2nd Flat Bend (rad/s)	14.606	14.2875	14.1129	14.0335
1st Torsion (rad/s)	31.146	31.0775	31.0536	31.0456
1st Edge Bend (rad/s)	31.739	31.7741	31.7323	31.7543
3rd Flat Bend (rad/s)	44.012	41.0561	39.7703	39.3577

The linear flutter results using the present formulation are compared with those presented in Refs. [88] and [79] (Table 4.4). The results are all identical. Furthermore, it is more accurate and meaningful to evaluate the nonlinear flutter speed of a cantilever

wing or a vehicle, since flutter is always a nonlinear problem for these highly flexible wings when it is demonstrating large deformation. With the current formulation, the nonlinear flutter speed obtained of this model is 23.2 m/s and the corresponding frequency is 10.3 rad/s (1.64 Hz), as listed in Table 4.4. The root locus is plotted in Fig. 4.25, with the flow velocity varying from zero to 30 m/s.

Table 4.4: Flutter results of the highly flexible wing

	Ref. [88]	Ref. [79]	Current / Linear	Current / Nonlinear
Speed (m/s)	32.2	32.2	32.2	23.2
Frequency (rad/s)	22.6	22.6	22.6	10.3

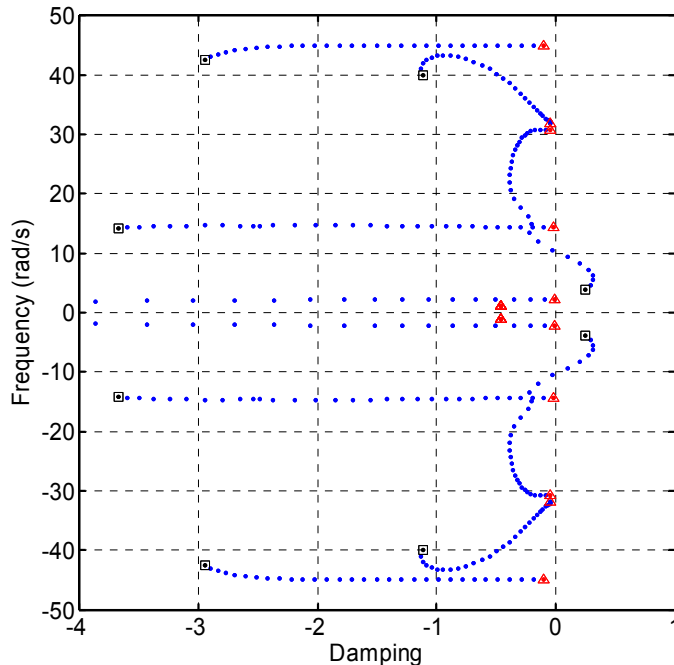


Figure 4.25: Root locus with changing velocity of the cantilevered highly flexible wing, speed from 0 m/s (triangle) to 30 m/s (square)

To verify the nonlinear flutter speed obtained above, two individual time domain simulation are performed. One of the simulations has a flow velocity (23 m/s) under the flutter speed, while the other simulates with a slightly higher flow velocity (24.5 m/s)

than the flutter speed. The time histories of the tip displacements are plotted in Figs. 4.26 and 4.27, respectively. From Fig. 4.26, the wing deformation of the pre-flutter case is stabilized after some initial oscillations. However, the wing oscillation is self-excited for the post-flutter case, as seen from Fig. 4.27. The amplitude of the wing oscillation is increased, until it goes into the limit cycle oscillation. It is also of interests to see that the steady state of the limit cycle oscillation is different from the initial state.

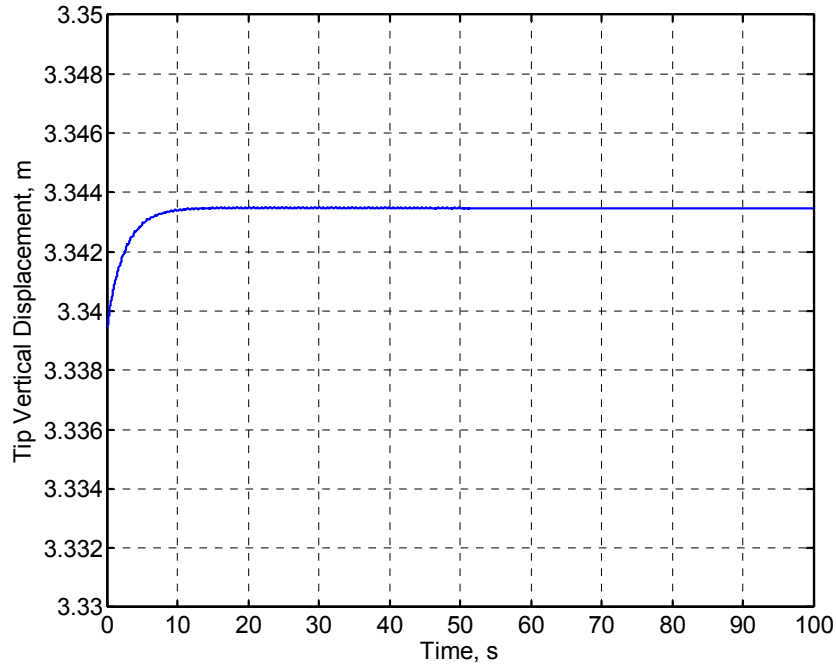


Figure 4.26: Tip displacement of the pre-flutter case for the cantilevered highly flexible wing

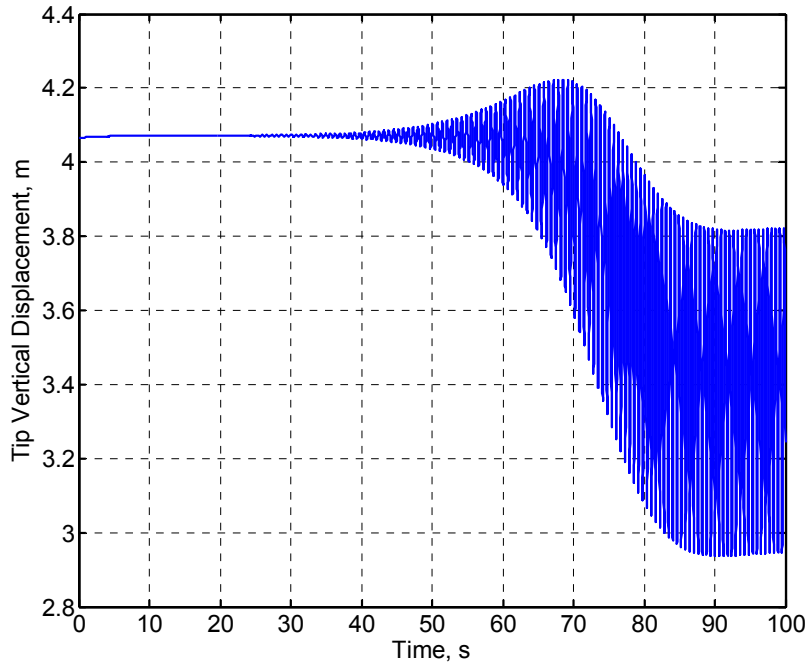


Figure 4.27: Tip displacement of the post-flutter case for the cantilevered highly flexible wing

4.6.2 Flutter of Free Flight Aircraft

A Blended-Wing-Body model is developed for this test. The geometry is shown in Fig. 4.28. Both body and wing are modeled as beams coupled with aerodynamics. The red dash-dot line shows the location of the beam reference axis. The shear center of the beam varies from the body's root (64.38% of the chord) to the wing root (45.60% of the chord), and keeps its relative position unchanged along the wing. Physical parameters of the body and wings are listed in Tables 4.5 and 4.6. One balance weight of 80 kg is positioned at the center of the model, 0.89 m ahead of the reference line. In addition, nine nonstructural masses, each 20 kg, are evenly distributed along the wing from the root to the tip. The wing contains three independent elevators, as indicated in Fig. 4.28. These elevators occupy 25% of the chord from wing root to 75% span of the wing.

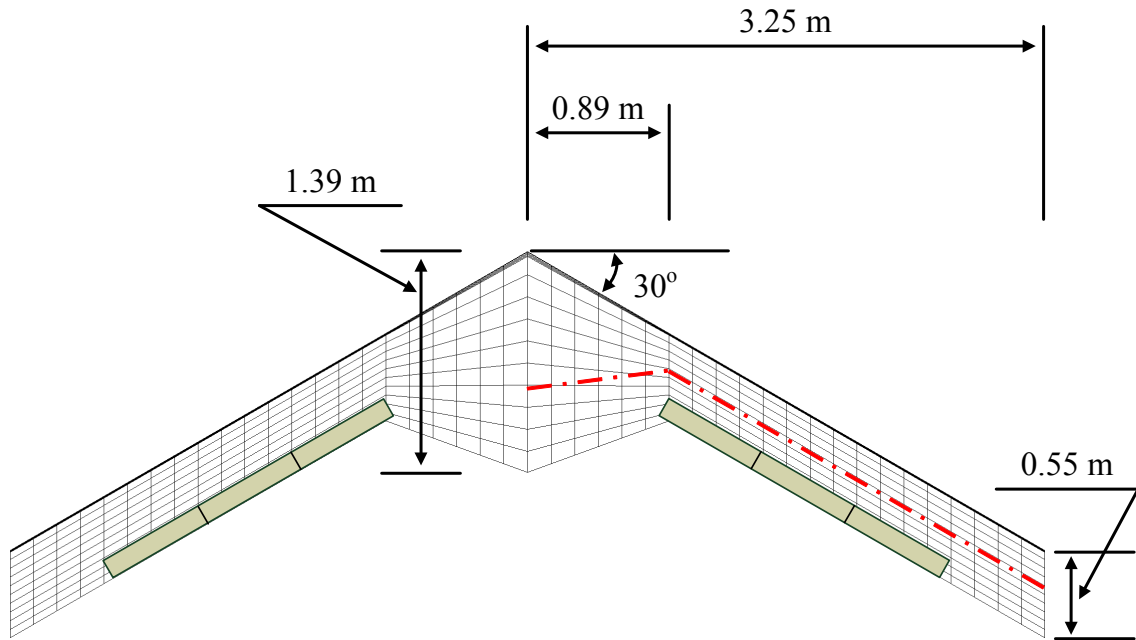


Figure 4.28: Model description of a sample Blended-Wing-Body model

Table 4.5: Body properties of the Blended-Wing-Body model

Ref. Axis Location (Root / Tip) (From L.E.)	64.38% / 45.60% of chord
Center of Gravity (Root / Tip) (From L.E.)	64.38% / 45.60% of chord
Extension Rigidity	1.69×10^8 N
Flat Bending Rigidity	7.50×10^5 N·m ²
Chord Bending Rigidity	3.50×10^7 N·m ²
Torsional Rigidity	2.25×10^6 N·m ²
Mass per Unit Length	50.00 kg/m
Flat Bending Inertia per Unit Length	0.70 kg·m
Edge Bending Inertia per Unit Length	22.0 kg·m
Rotational Inertia per Unit Length	4.50 kg·m

Table 4.6: Wing properties of the Blended-Wing-Body model

Ref. Axis Location (Root / Tip) (From L.E.)	45.60% / 45.60% of chord
Center of Gravity (Root / Tip) (From L.E.)	45.60% / 45.60% of chord
Extension Rigidity	1.55×10^8 N
Flat Bending Rigidity	1.17×10^4 N·m ²
Chord Bending Rigidity	1.30×10^5 N·m ²
Torsional Rigidity	1.10×10^4 N·m ²
Mass per Unit Length	6.20 kg/m
Flat Bending Inertia per Unit Length	5.00×10^{-4} kg·m
Edge Bending Inertia per Unit Length	4.63×10^{-3} kg·m
Rotational Inertia per Unit Length	5.08×10^{-3} kg·m

At a given altitude (6096 m, 20000 ft), the flutter speed of the complete vehicle with rigid body motions is predicted to be 123.36 m/s, with a frequency of 20.92 rad/s (3.33 Hz). The flutter mode shape and root locus with the changing of the flight velocity are plotted in Figs. 4.29 and 4.30. Note that the aircraft model is trimmed at each flight velocity increment when searching for the flutter boundary. The unstable mode is coupled plunging/pitching of the body and the first flat bending of the wing.

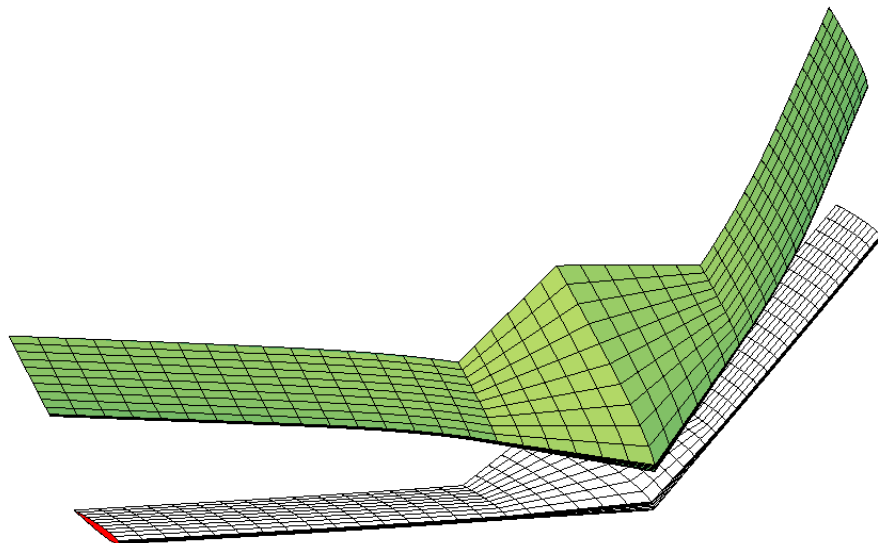


Figure 4.29: Mode shape of flutter in free flight condition of the sample Blended-Wing-Body model

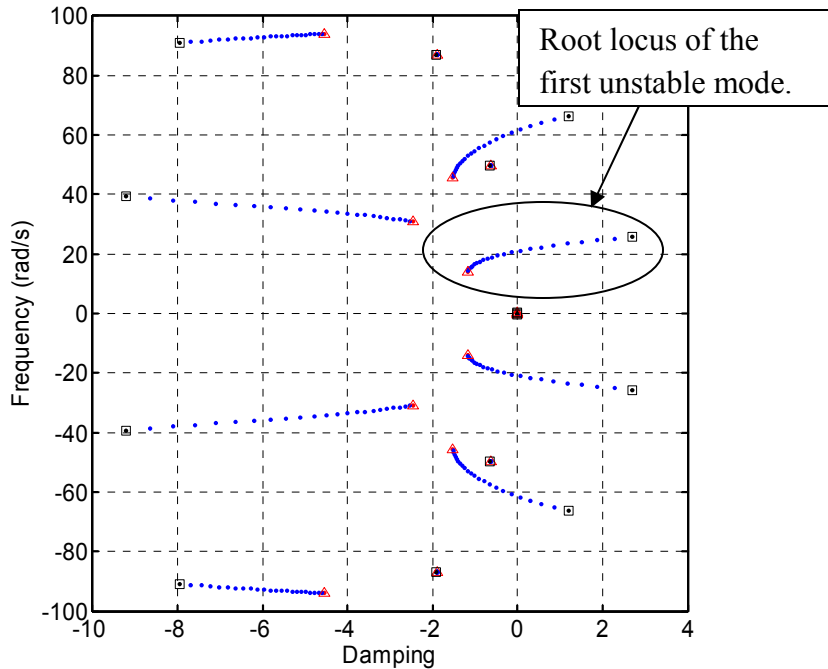


Figure 4.30: Root locus with changing velocity of the sample Blended-Wing-Body model, speed from 94.83 m/s (triangle) to 140 m/s (square)

Following the same procedure as in the previous section, two individual time domain simulations are carried out for verification purposes, one of which simulates the level flight of the model with a flight velocity lower than the flutter speed (120 m/s), while the other flies with a slightly higher velocity (125 m/s) than the flutter speed. A deflection of elevator angle is applied as a perturbation (Fig. 4.31). The time histories of the tip displacements and body pitching angles are plotted in Figs. 4.32 to 4.35. For the pre-flutter case (Figs. 4.32 and 4.33), the responses are converged after initial oscillations. However, the responses of the post-flutter case are diverged, showing instability, as indicated by Figs. 4.34 and 4.35. As one may see from Fig. 4.35, the pitching motion is not stable, which is correctly predicted by the frequency domain flutter calculation. One more observation from the time domain simulation is that the frequency of the unstable oscillation is about 3.33 Hz, which agrees with the frequency domain prediction as well. Overall, the flutter prediction formulation is effective and accurate based upon the verification.

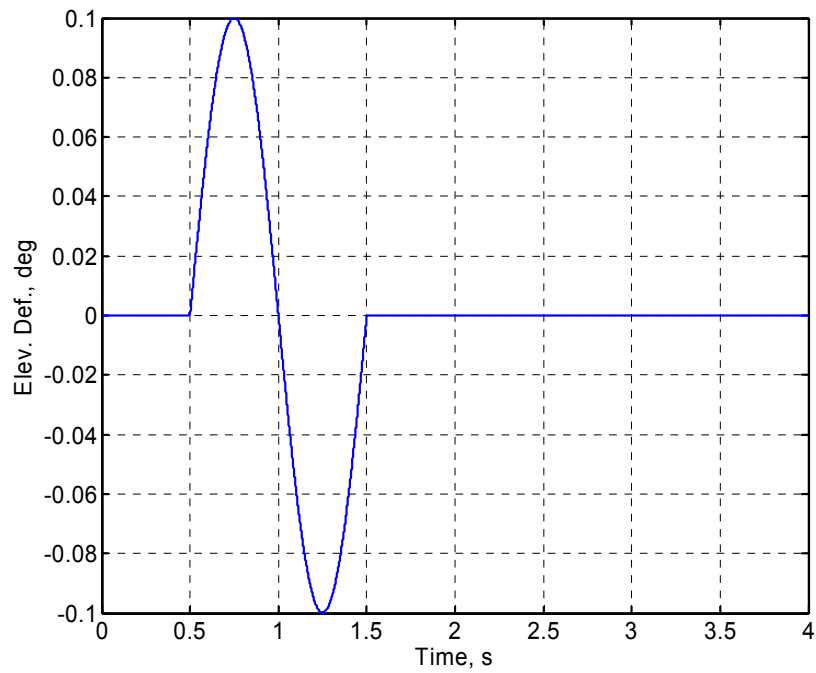


Figure 4.31: Deflection of elevator angle as a perturbation for the sample Blended-Wing-Body model

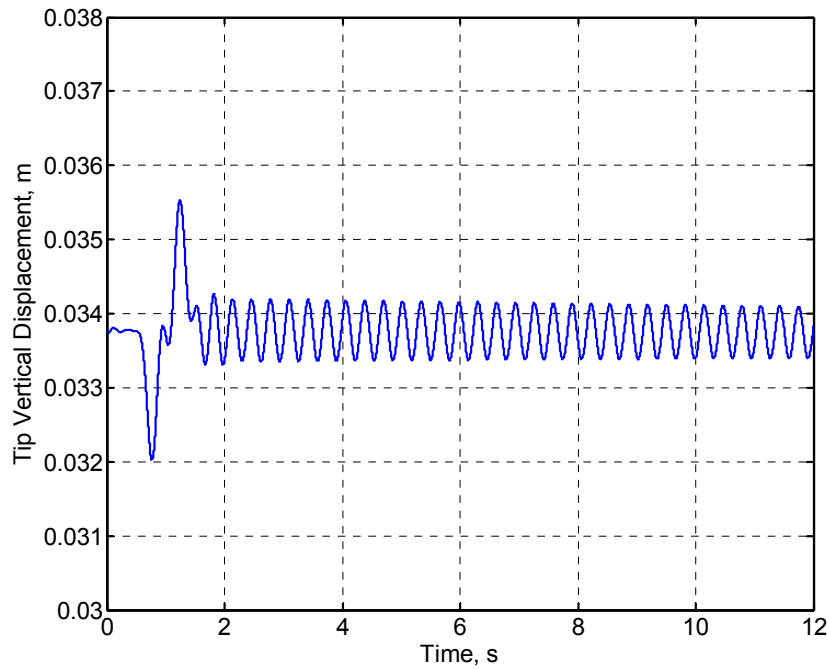


Figure 4.32: Tip displacement of the pre-flutter case for the sample Blended-Wing-Body model, speed 120 m/s

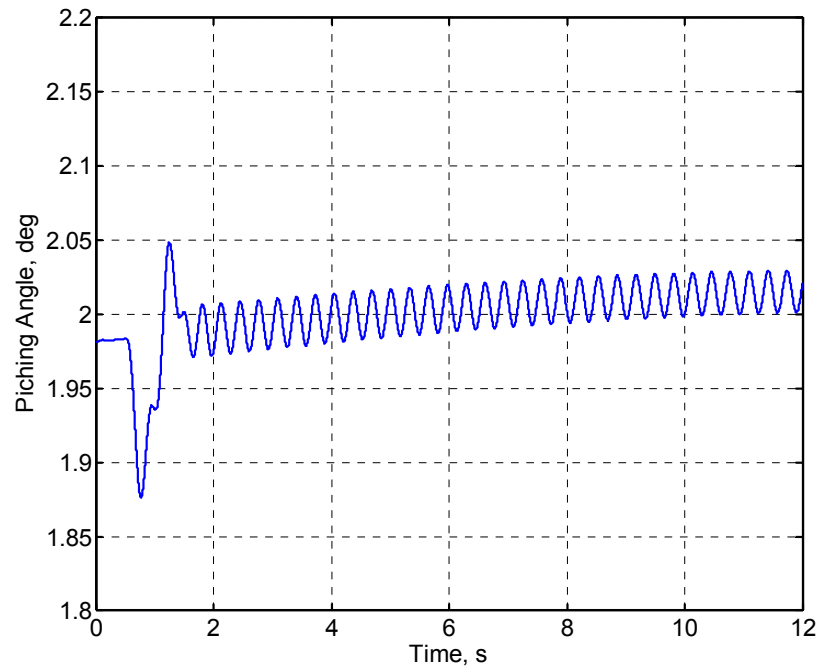


Figure 4.33: Pitching angle of the pre-flutter case for the sample Blended-Wing-Body model, speed 120 m/s

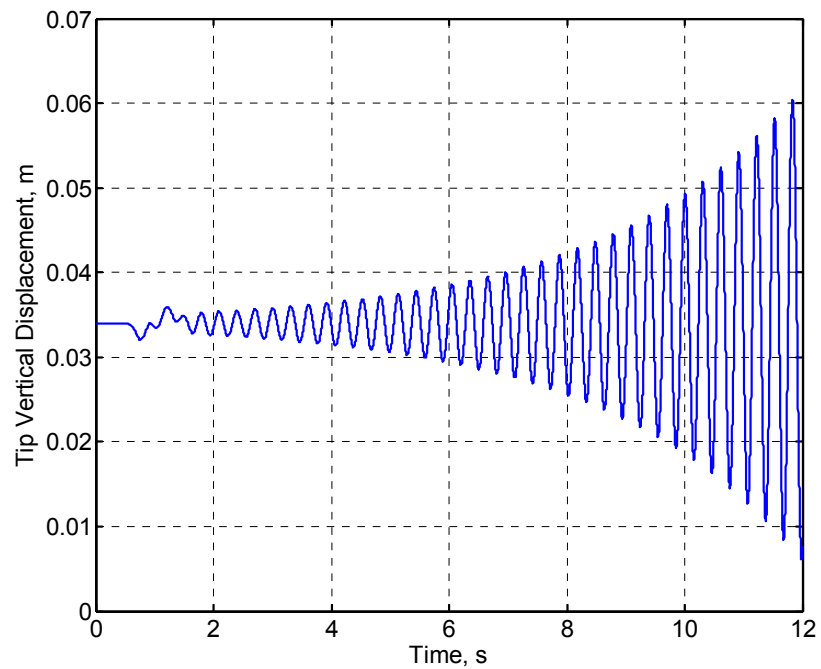


Figure 4.34: Tip displacement of the post-flutter case for the sample Blended-Wing-Body model, speed 125 m/s

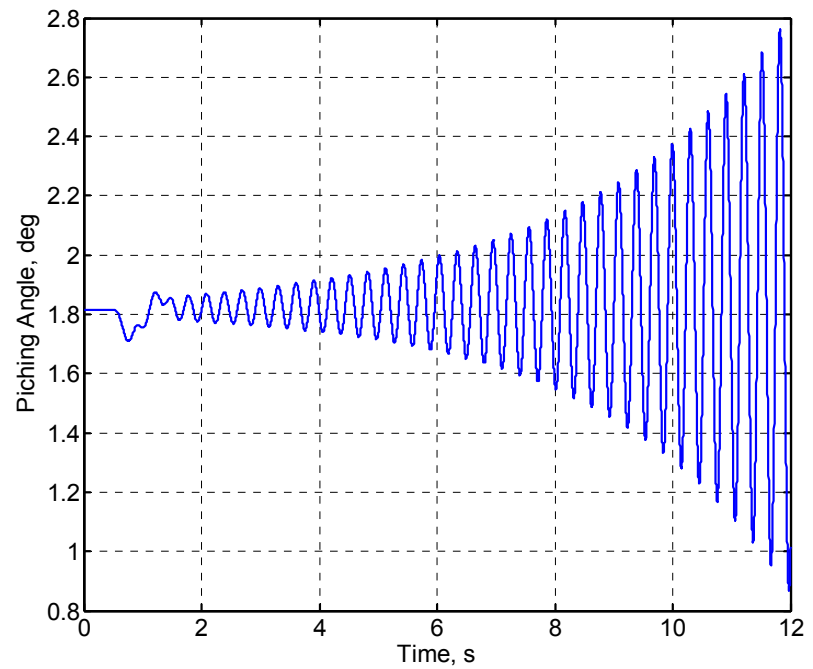


Figure 4.35: Pitching angle of the post-flutter case for the sample Blended-Wing-Body model, speed 125 m/s

CHAPTER V

Numerical Studies

Results from the numerical studies are presented in this chapter. To illustrate the capabilities of the new formulation and study the aeroelastic and flight dynamic characteristics, four different baseline HALE vehicles are modeled in UM/NAST environment. Aeroelastic analysis is then carried out with fully flexible and rigidized models. Stability analysis results are first presented, exploring flutter boundaries (with constraints of rigid body motions or in free flight) and flight dynamic stability for different vehicles. In addition, flight dynamic responses with maneuver inputs or gust perturbations are presented, subject to some nonlinear effects.

5.1 Introduction

Among the four highly flexible vehicles that will be studied, three of them, *i.e.*, Single-Wing, Joined-Wing, and Blended-Wing-Body configurations, are inspired by the ISR SensorCraft concepts^[1]. The design of a SensorCraft itself includes a complex process. The models developed here are far from replicating SensorCraft airplanes. Furthermore, the studies regarding SensorCraft may cover a wide range of fields. This dissertation is limited to nonlinear aeroelastic aspects.

Aircraft are designed according to mission requirements. Seven flight index points are selected to represent the nominal mission profile of the three SensorCraft configurations, as indicated in Fig. 5.1. At each index point, the altitude, fuel mass, and

nominal flight speed are specified. The index points represent: (1) takeoff, (2) climb, (3) cruise ingress, (4) cruise/loiter/cruise, (5) cruise egress, (6) descent, and (7) landing. The fuel burn determines the duration of each flight segment. The nominal flight speed at each index point is based on the cruise speed (input parameter), and it is computed such that the dynamic pressure is constant (constant indicated airspeed). At each flight index point, the vehicle is trimmed for equilibrium in horizontal flight at the corresponding flight speed.

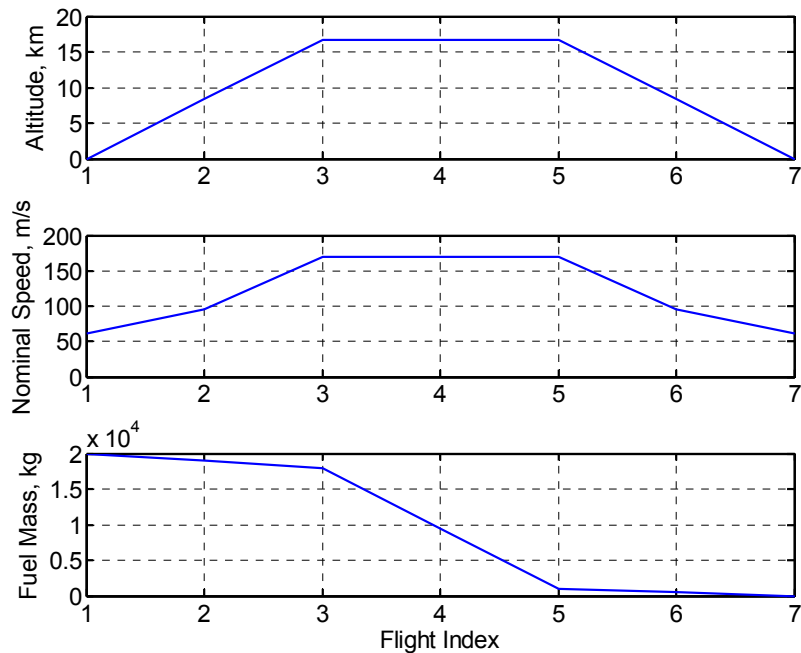


Figure 5.1: Mission profile for SensorCraft

Three sets of constraints were defined to help sizing the baseline designs: strength (based on first-ply failure) at 1.5-g load, strength based on gust loads, and minimum flutter margin. For these vehicles, the 1.5-g load factor was shown to be the critical constraint and the wing structural thickness distribution was sized for a fully-strained design along span. A description of the design process can be found in Ref. [28].

One last class of highly flexible vehicle that will be studied here has a Helios-like configuration. The current study only explores its performance at sea level. The nominal

flight speed is 12.192 m/s (40 ft). However, the payload may be varied, which results in different steady state deformations, as will be demonstrated in a following section.

5.2 Representative Aircraft Models

5.2.1 Single-Wing Configuration

Geometry

Figure 5.2 shows the Single-Wing configuration, whose geometric parameters are listed in Table 5.1. The wings are divided into nine regions, and the horizontal and vertical tail surfaces are both divided into five regions for definition of cross-sectional property distribution. NACA 4415 is chosen as the airfoil and it is kept constant throughout the wing members, while NACA 0012 is chosen as the airfoil for the tails. Three independent ailerons are defined on the wing, which locations are listed in Table 5.1. Elevators and rudders are also defined on horizontal and vertical tails, respectively. For simplicity, these control surfaces occupy 20% of the chord, and are allowed to deflect $\pm 30^\circ$. Engine thrust force is modeled as a point follower load applied at the location of 15 m back from the nose of the aircraft, as shown in Fig. 5.2.

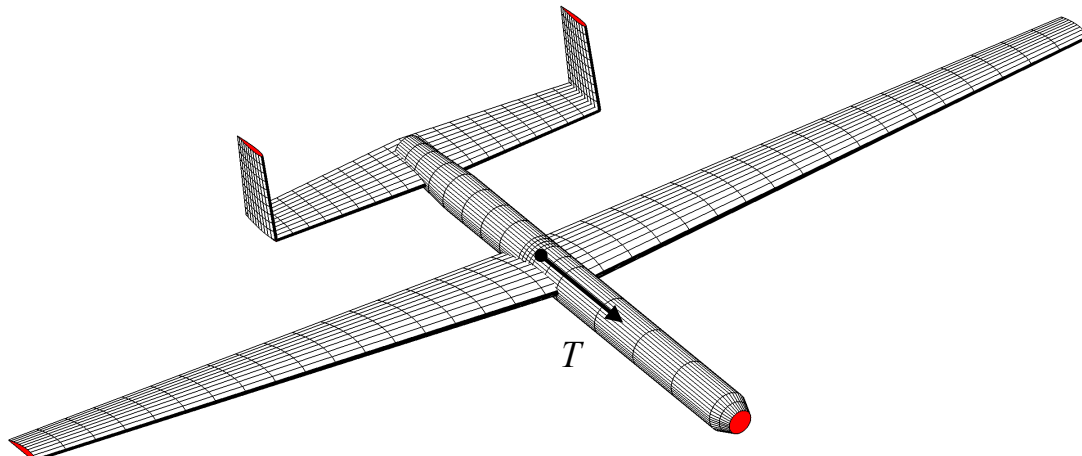


Figure 5.2: Baseline Single-Wing configuration (arrow indicates the direction of thrust force in undeformed vehicle configuration)

Table 5.1: Geometric parameters of the Single-Wing configuration

Fuselage Length	26.4 m
Wing Span	29.3 m
Wing Chord Length (Root/Tip)	4.5 m/2.2 m
Wing Incidence Angle	3°
Wing Swept Angle	0°
Wing Dihedral Angle	3°
Horizontal Tail Span	9 m
Horizontal Tail Chord Length (Root/Tip)	3.5 m/2.45 m
Horizontal Tail Incidence Angle	-4.5°
Vertical Tail Span	4 m
Vertical Tail Chord Length (Root/Tip)	2.45 m/2.0 m
Vertical Tail Swept Angle	14°
Aileron 1 Span Location (on Wing)	6.51 – 13.02 m
Aileron 2 Span Location (on Wing)	13.02 – 22.79 m
Aileron 3 Span Location (on Wing)	22.79 – 29.3 m
Elevator Span Location (on Horizontal Tail)	1.8 – 9.0 m
Rudder Span Location (on Vertical Tail)	0.8 – 3.2 m

Vehicle Mass Breakdown

The vehicle mass breakdown is given in Table 5.2. The fuel is assumed to be distributed up to half span of the wings, independent of the total amount of fuel on board. The fuselage contains no fuel.

Table 5.2: Vehicle mass distribution for the Single-Wing configuration

Fuselage Structure + Payload + Engine Mass	4,000 kg
Fuel Mass	20,000 kg
Vertical Tail Structure Mass	419 kg
Vehicle Total Wing Structure Mass	4,230 kg
Vehicle Gross Take-off Mass	28,649 kg

Cross-sectional Inertia and Stiffness Distributions

The stiffness and inertia properties of each cross-section of the wing, tail and fuselage can be found in Appendix C. Note that a 2400-kg payload is evenly distributed at the nose part of the fuselage, while a 455-kg payload is distributed along the rest of the fuselage, which are modeled as nonstructural masses attached at each node for simplicity.

Rigidity Levels

To assess the effects of the flexibility of different members of the vehicle on their roll response and stability that will be analyzed in the coming sections, models with different flexibility levels are considered for the Single-Wing configuration. They are summarized in Table 5.3.

Table 5.3: Models with different flexibility levels of the Single-Wing configuration

	Fuselage	Tails	Wings
Model 1	Rigid	Rigid	Flexible
Model 2	Rigid	Flexible	Flexible
Model 3	Rigid	8 × Flexible	Flexible
Model 4	Flexible	Rigid	Flexible
Model 5	Flexible	Flexible	Flexible

Trim of the vehicle

The vehicle is trimmed for equal lift and weight, and zero pitching moment about its center of gravity at level flight. The interference between the wings and tails is not accounted for in the trim process. A concentrated thrust is applied in the fuselage longitudinal direction to balance the drag (see Fig. 5.2 for the location and orientation of the thrust). The trim results of the fully flexible model (Model 5) are shown in Fig. 5.3. Note that these results will vary for the different models listed in Table 5.3.

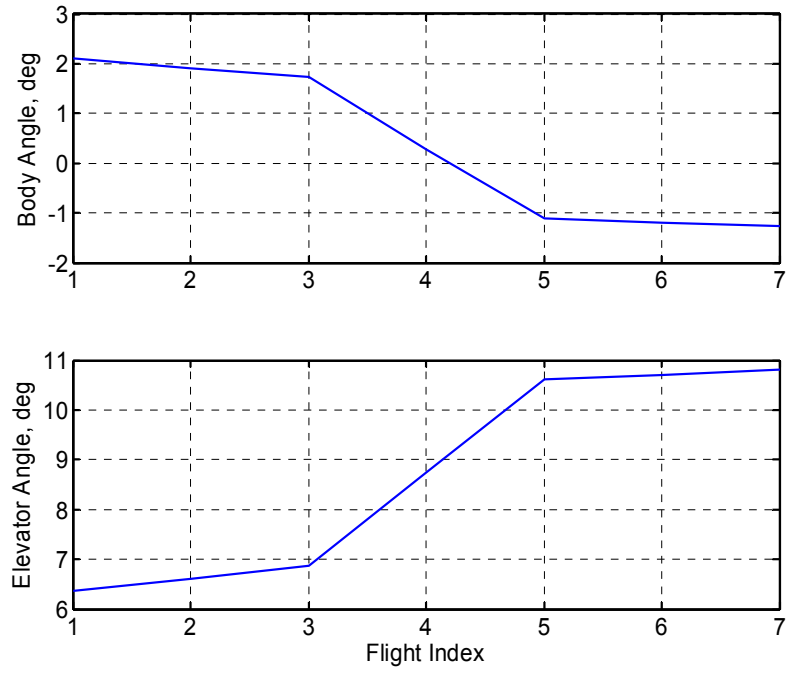


Figure 5.3: Trim results for the Single-Wing configuration (Model 5)

5.2.2 Joined-Wing Configuration

Geometry

Figure 5.4 shows the Joined-Wing configuration, with the geometric parameters listed in Table 5.4. From top view, the vehicle shape is symmetric (although one may want to vary the forward/aft location of the joint). The wings are denoted right front wing (with inner and outer wings), left front wing, right aft wing (with inner-wing only), and left aft wing. Right and left are determined as in Fig. 5.4 (as viewed from top with nose pointing up). The front wings are divided into eight regions while the aft wings are divided into four regions for definition of cross-sectional properties distribution. The members of all inner wings are identical in construction, and the material distribution follows the numbering convention indicated in Fig. 5.4. NACA 4415 is chosen as the airfoil and it is kept constant throughout the wing members. The outer wings contain a

50%-span aileron (regions 6 and 7 as shown in Fig. 5.4) while elevators are defined along the span of the inner wings (regions 1 to 4 as shown in Fig. 5.4). 50%-span rudders are defined on the vertical tail (from 25% to 75% span of it). For simplicity, these control surfaces occupy 20% of the chord, and are allowed to deflect +/-30°. Engine thrust force is modeled as a point follower load applied at the location of 26 m back from the nose of the aircraft, as shown in Fig. 5.4.

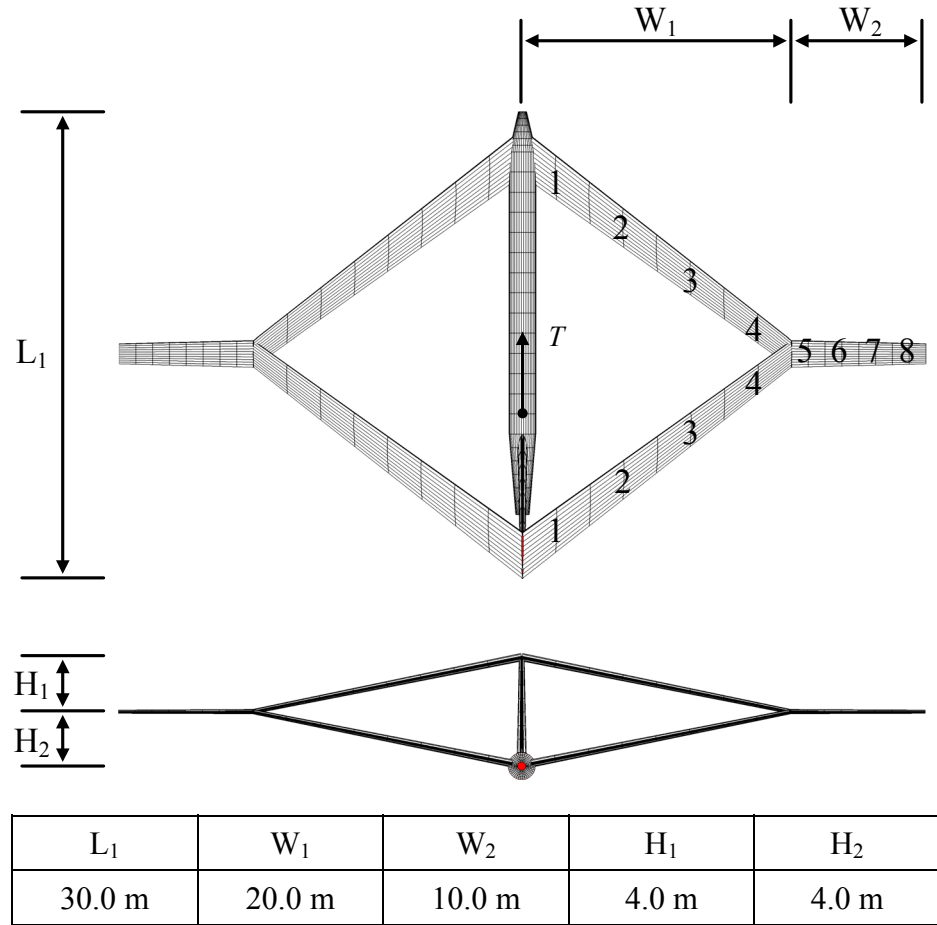


Figure 5.4: Baseline Joined-Wing configuration (arrow indicates the direction of thrust force in undeformed vehicle configuration)

Vehicle Mass Breakdown

The vehicle mass breakdown is given in Table 5.5. The fuel is assumed to be distributed evenly throughout the inner and outer wings, independent of the total amount of fuel on board. The fuselage contains no fuel.

Table 5.4: Geometric parameters of the Joined-Wing configuration

Fuselage Length L_1	30.0 m
Inner Wing Span W_1	20.0 m
Inner Wing Chord Length (Root/Tip)	3.5 m/2.0 m
Inner Wing Incidence Angle	4°
Outer Wing Span W_2	10 m
Outer Wing Chord Length (Root/Tip)	2.0 m/1.5 m
Outer Wing Incidence Angle	4°
Outer Wing Swept Angle	0°
Outer Wing Dihedral Angle	0°
Vertical Tail Span	8 m
Vertical Tail Chord Length (Root/Tip)	6.0 m/3.15 m
Vertical Tail Swept Angle	41°
Aileron Span Location (on Outer Wing)	2.5 – 7.5 m
Elevator Span Location (on Front Inner Wing)	0 – 20.0 m
Rudder Span Location (on Vertical Tail)	2.0 – 6.0 m

Table 5.5: Vehicle mass distribution for the Joined-Wing configuration

Fuselage Structure + Payload + Engine Mass	4,000 kg
Fuel Mass	20,000 kg
Vertical Tail Structure Mass	550 kg
Vehicle Total Wing Structure Mass	3,440 kg
Vehicle Gross Take-off Mass	27,990 kg

Cross-sectional Inertia and Stiffness Distributions

The stiffness and inertia properties of the wing, vertical tail and fuselage can be found in Appendix C. Note that a payload of 2769 kg is evenly distributed along the fuselage, which are modeled as nonstructural masses attached at each node for simplicity.

Rigidity Levels

To assess the effects of the flexibility of different members of the vehicle on their roll response and stability that will be analyzed in the coming sections, models with different flexibility levels are considered for the Joined-Wing configuration. They are summarized in Table 5.6.

Table 5.6: Models with different flexibility levels of the Joined-Wing configuration

	Fuselage	Vertical Tail	Inner Wing	Outer Wing
Model 1	Rigid	Rigid	Rigid	Flexible
Model 2	Rigid	Rigid	Flexible	Flexible
Model 3	Rigid	Flexible	Flexible	Flexible
Model 3m	Rigid	$10 \times$ Flexible	Flexible	Flexible
Model 4	Flexible	Rigid	Flexible	Flexible
Model 4m	$5 \times$ Flexible	Rigid	Flexible	Flexible
Model 5	Flexible	Flexible	Flexible	Flexible
Model 5m	$5 \times$ Flexible	$10 \times$ Flexible	Flexible	Flexible

Trim of the vehicle

The same trim scheme used for the Single-Wing configuration is applied to the Joined-Wing configuration. The interference between the front and aft wings is not accounted for in the trim process. A concentrated thrust is applied in the fuselage longitudinal direction to balance the drag (see Fig. 5.4 for the location and orientation of the thrust). The trim results of the fully flexible model (Model 5) are shown in Fig. 5.5. Note that these results will vary for the different models listed in Table 5.6.

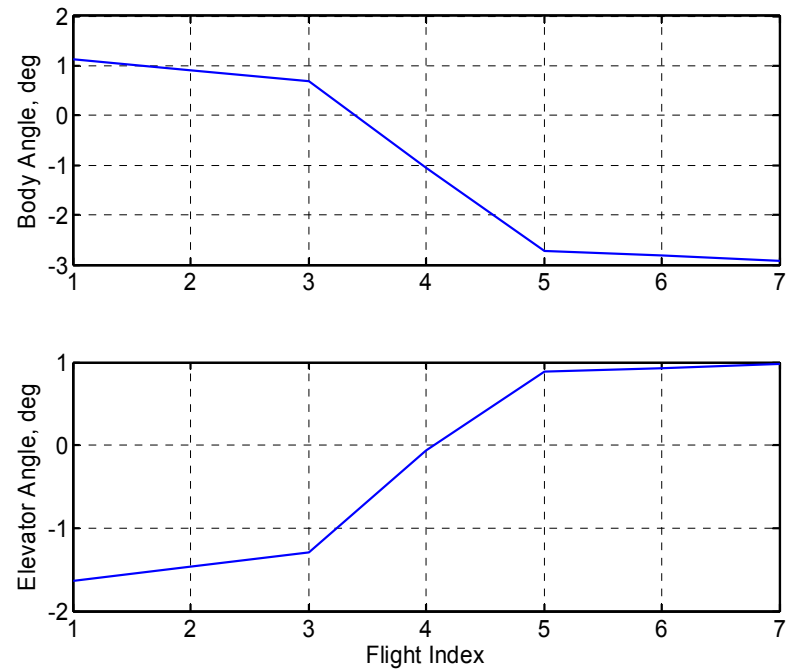


Figure 5.5: Trim results for the Joined-Wing configuration (Model 5)

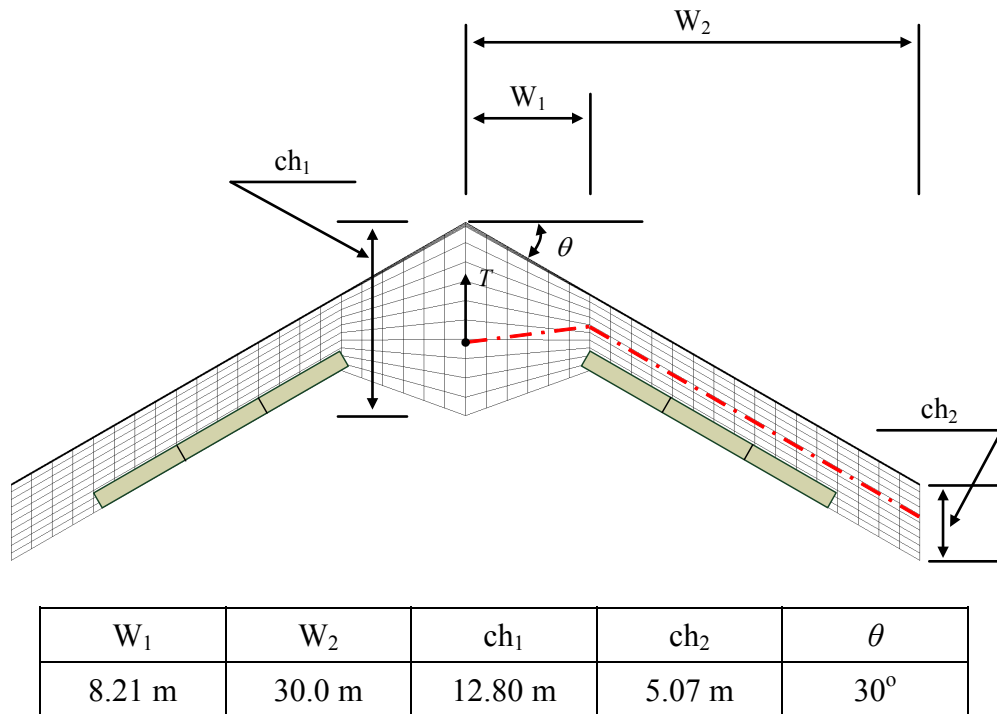


Figure 5.6: Baseline Blended-Wing-Body configuration (arrow indicates the direction of thrust force in undeformed vehicle configuration)

5.2.3 Blended-Wing-Body Configuration

The Blended-Wing-Body configuration is exemplified in Fig. 5.6. The wings are back swept 30°. Three independent elevators are defined from 0 to 75% of wing span, which occupy 25% of the chord. NACA 0012 is chosen as the airfoil and it is kept constant throughout the body and wing members. The physical properties of the body and wings are listed in Appendix C.

Vehicle Mass Breakdown

The vehicle mass breakdown is given in Table 5.7. The fuel is assumed to be distributed only in the wings (outboard of W_1 , as in Fig. 5.6), independent of the total amount of fuel on board. The fuselage contains no fuel.

Table 5.7: Vehicle mass distribution for the Blended-Wing-Body configuration

Fuselage Structure + Payload + Engine Mass	11,590 kg
Fuel Mass	20,000 kg
Vehicle Total Wing Structure Mass	1,865 kg
Vehicle Gross Take-off Mass	33,455 kg

Trim of the vehicle

The vehicle is trimmed for equal lift and weight, and zero pitching moment about its center of gravity at level flight. A concentrated thrust is applied in the fuselage longitudinal direction to balance the drag force (see Fig. 5.6 for the location and orientation of the thrust). The trim results are shown in Fig. 5.7.

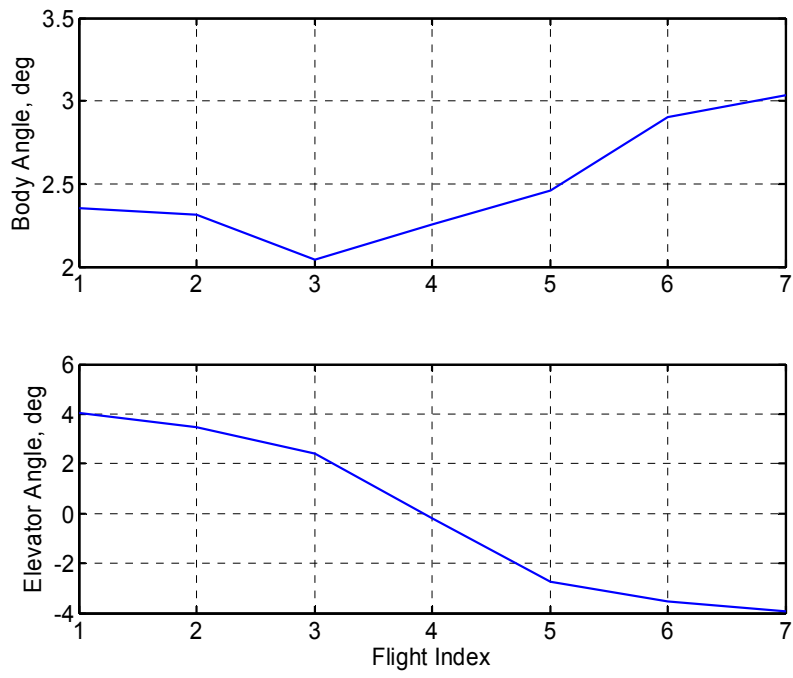


Figure 5.7: Trim results for the Blended-Wing-Body configuration

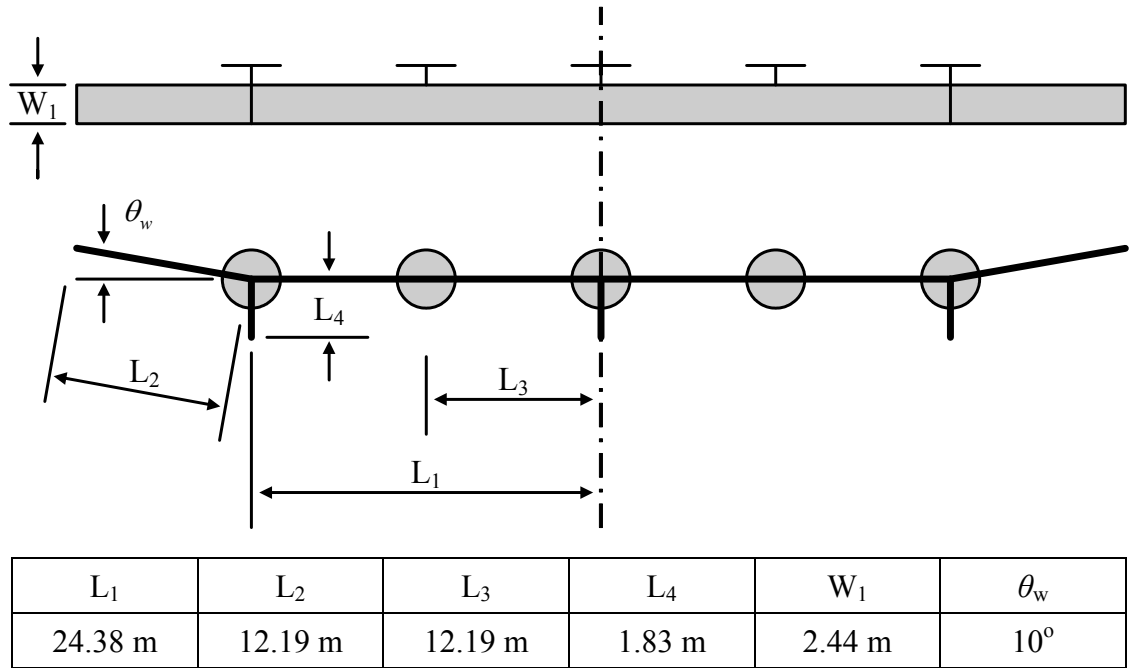


Figure 5.8: Baseline Flying-Wing configuration (after Ref. [51])

5.2.4 Flying-Wing Configuration

Figure 5.8 shows the geometry of the Flying-Wing vehicle after Ref. [51]. It has a span of 72.8 m and a constant chord length of 2.44 m. The outboard one-third wing semi-span has a dihedral angle of 10° . Wing cross-sectional properties can be found in Table 5.8. As indicated in Fig. 5.8, there are five propulsive units and three pods, which are located at middle span and $2/3$ of semi span at each side, respectively. The side ones have a mass of 22.70 kg each, and the center one has a mass of 27.23 kg. The payload is applied on the center pod, ranging from 0 kg (light) to 227 kg (heavy).

Table 5.8: Cross-sectional properties of the Flying-Wing configuration (after Ref. [51])

Elastic (Reference) Axis	25% chord
Center of Gravity	25% chord
Stiffness Properties:	
Torsional Rigidity	$1.65 \times 10^5 \text{ N}\cdot\text{m}^2$
Bending Rigidity (Flatwise)	$1.03 \times 10^6 \text{ N}\cdot\text{m}^2$
Bending Rigidity (Chordwise)	$1.24 \times 10^7 \text{ N}\cdot\text{m}^2$
Inertia Properties:	
Mass per Unit Length	8.93 kg/m
Mass Moment of Inertia I_{xx} (Torsional)	4.15 kg·m
Mass Moment of Inertia I_{yy} (Flatwise Bend)	0.69 kg·m
Mass Moment of Inertia I_{zz} (Flatwise Bend)	3.46 kg·m
Aerodynamic Coefficients for Wings (about 25% chord):	
$c_{l\alpha}$	2π
$c_{l\delta}$	1
c_{d0}	0.01
c_{m0}	0.025
$c_{m\delta}$	-0.25
Aerodynamic Coefficients for Pods (about 25% chord):	
$c_{l\alpha}$	5
c_{d0}	0.02
c_{m0}	0

Trim of the vehicle

With the flight speed of 12.2 m/s at sea level, the Flying-Wing vehicle is trimmed for equivalent lift and weight, equivalent thrust and drag, and zero pitching moment about the c.g. point of the aircraft. Flap-like control surfaces along the trailing edge and the engine thrusts are used as trim inputs. The payload is varied so that the vehicle mass is varied from “light” to “heavy,” as defined above. The trim results are shown in Fig. 5.9 and Table 5.9, and the deformations at trim conditions of light and heavy models are graphically represented in Figs. 5.10 and 5.11. The results indicate that the static characteristics of the Flying-Wing model used here is very similar to the one in Ref. [51].

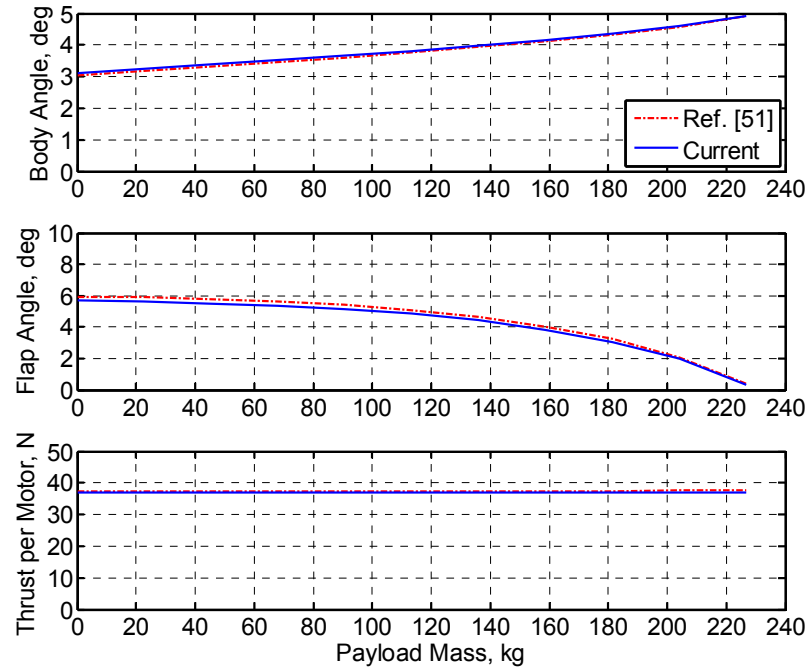


Figure 5.9: Trim results for the Flying-Wing configuration

Table 5.9: Trim results for light and heavy models of the Flying-Wing configuration

	Body Angle	Flap Angle	Thrust per Motor
Light Model	3.11°	5.68°	37.11 N
Heavy Model	4.92°	0.34°	37.02 N

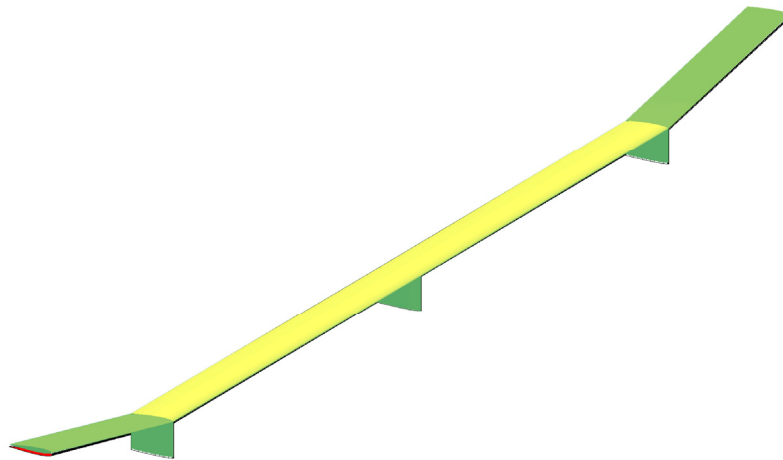


Figure 5.10: Trimmed light model with respect to undeformed shape – nearly identical
($U=12.2$ m/s, at sea level)

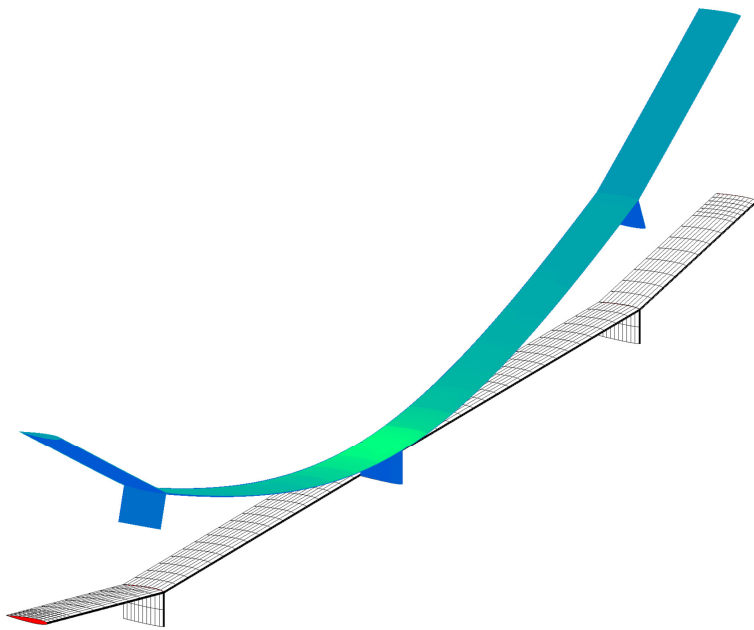


Figure 5.11: Trimmed heavy model with respect to undeformed shape ($U=12.2$ m/s, at sea level)

5.3 Static Stability

The static instability here refers to the loss of elastic stability. For the particular Joined-Wing configuration baseline design considered here, the front and aft wings form a tilted plane, which brings the aft wings under compressive loading conditions when the wings are generating lift. Due to the compressive loads, their elastic response can be a sizing limitation for the vehicle, as shown in Fig. 5.12. Note that the large deformation associated with the buckling of aft wings is naturally modeled in UM/NAST through the nonlinear structural analysis.

To study the effects of the flexibility from different members of the aircraft on the loss of elastic stability of the wings, Models 2 to 5 are brought to steady state at level flight (at sea level). Then, their flight speeds are varied from the nominal flight speed, which is 61.21 m/s, until there is a sudden drop in the lift generation capacity.

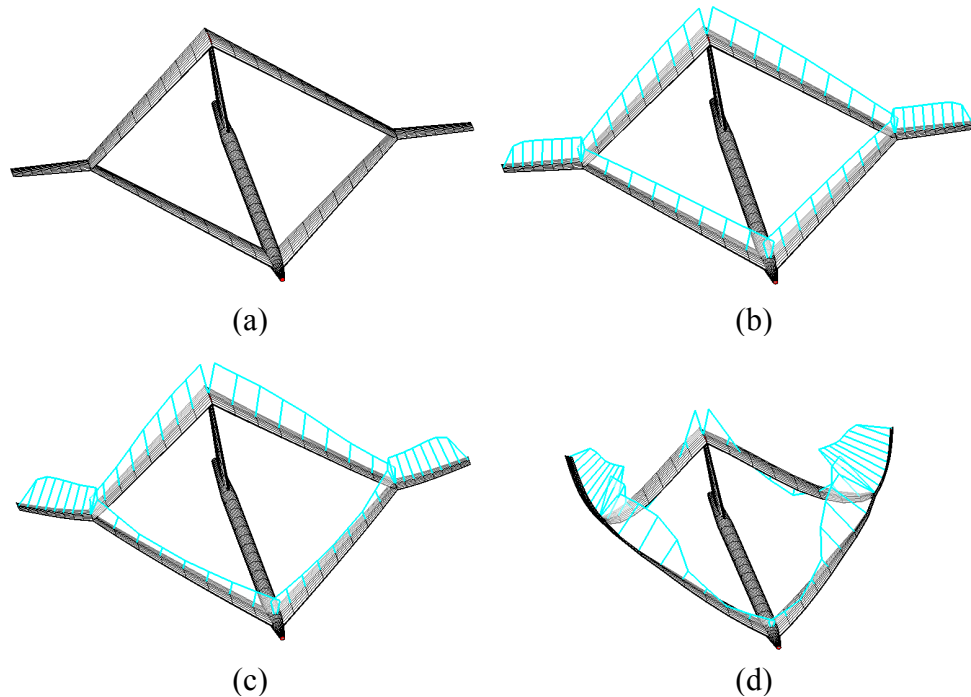


Figure 5.12: Lift distribution on the vehicle as the critical speed is approached, (a) undeformed; (b) $U=61.21$ m/s; (c) $U = 80$ m/s; (d) $U = 81.1$ m/s (sea level, fully fueled, no rigid body degrees of freedom)

The instability happens when the load factor reaches approximately 1.5 to 1.6, with the deformation of the aft wing increases dramatically, bringing the whole wing system close to collapse. The wing shape and deflections of the modified fully flexible model (Model 5) are plotted for varying load factor in Figs. 5.13 and 5.14. The corresponding change of tip positions is plotted versus the variation of flight speed (Fig. 5.15) and load factor (Fig. 5.16). The sudden reduction of the aft wing stiffness results in large bending deflection of the overall wing structure, and consequent drop in the overall lift (represented by the reduction in load factor as shown in Figs. 5.15 and 5.16). This level of wing displacement causes high composite ply strains and stresses, to the point of ply failure (Distributions of ply thickness of wing and vertical tail members are listed in Appdix C). Strain components dependence on the load factor is shown in Figs. 5.17 to 5.19.

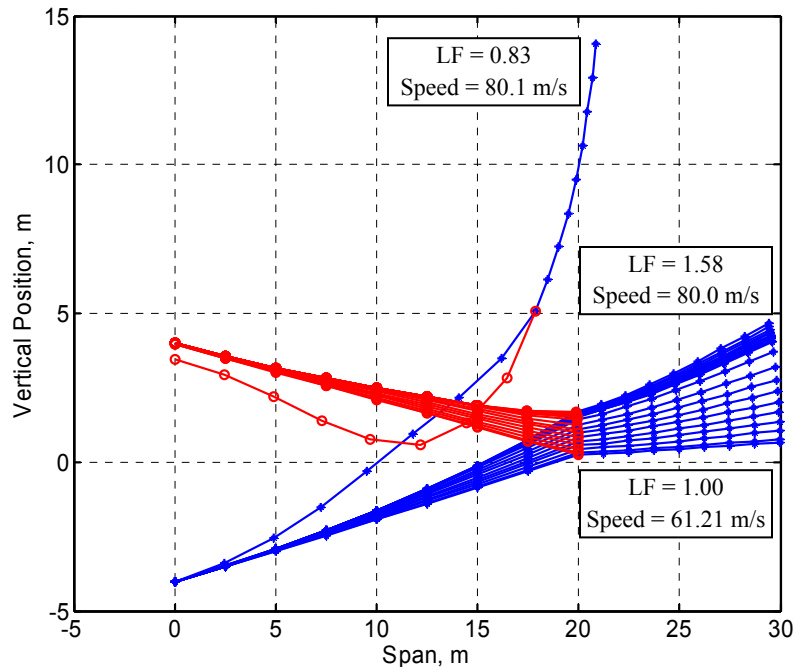


Figure 5.13: Wing shape for varying load factors (Model 5, level flight at sea level)

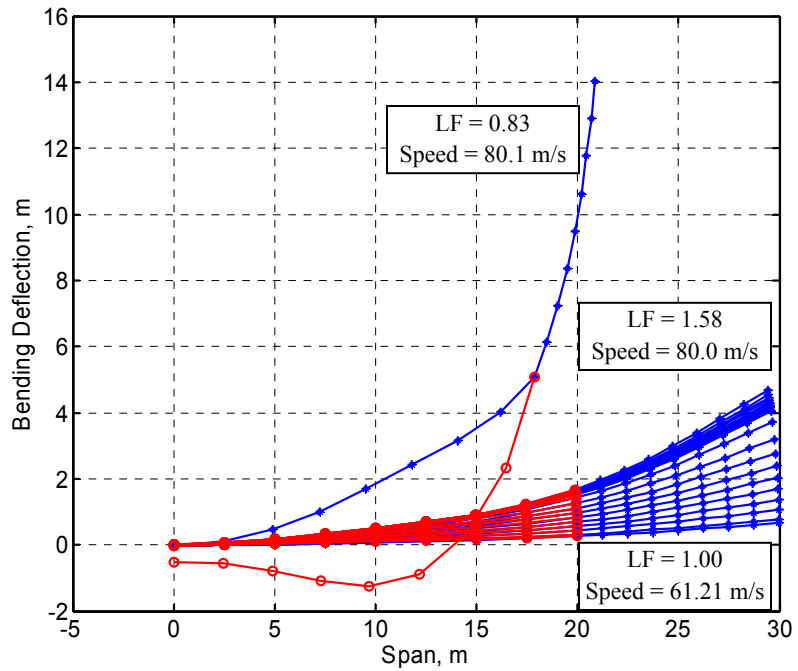


Figure 5.14: Wing bending deflections for varying load factors (Model 5, level flight at sea level)

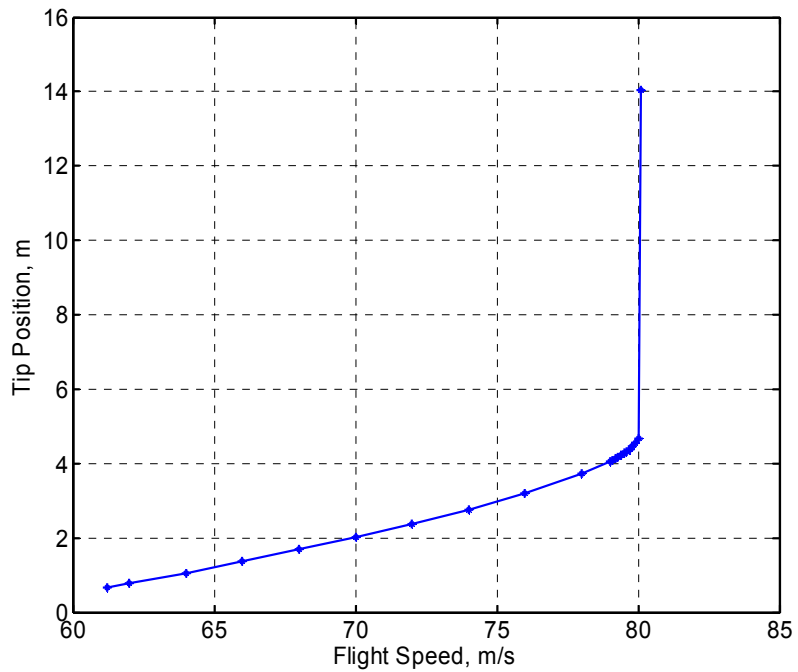


Figure 5.15: Changes in tip deflection as function of the flight speed of the vehicle (Model 5, level flight at sea level)

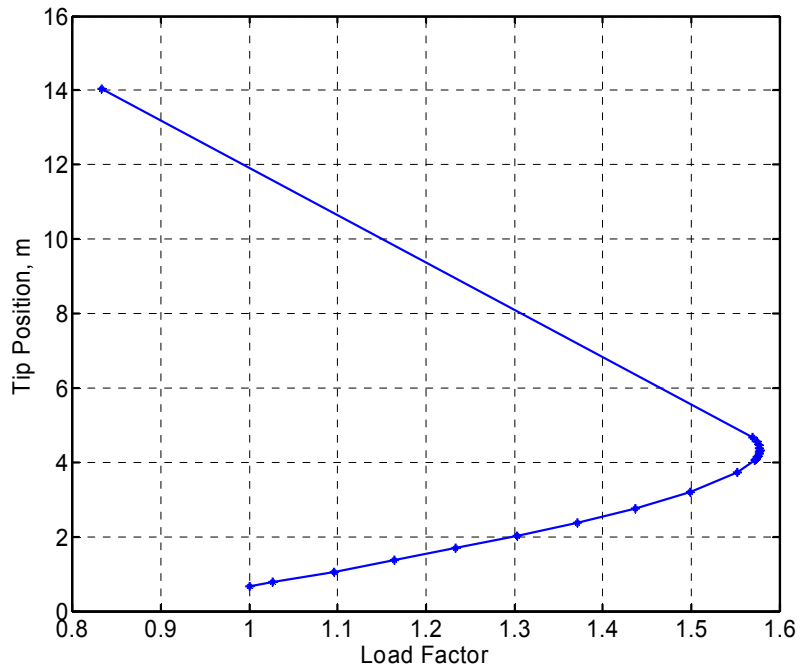


Figure 5.16: Changes in tip deflection as function of the lift generation capability (load factor) of the vehicle (Model 5, level flight at sea level)

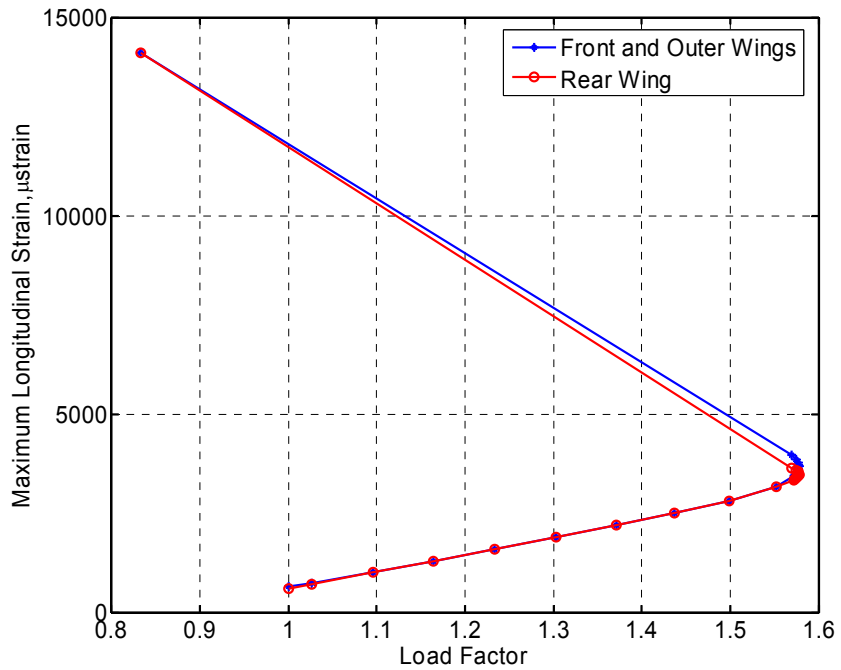


Figure 5.17: Nonlinear growth of maximum longitudinal strain due to loss of stiffness on the aft wing with increasing load factor (Model 5, level flight at sea level)

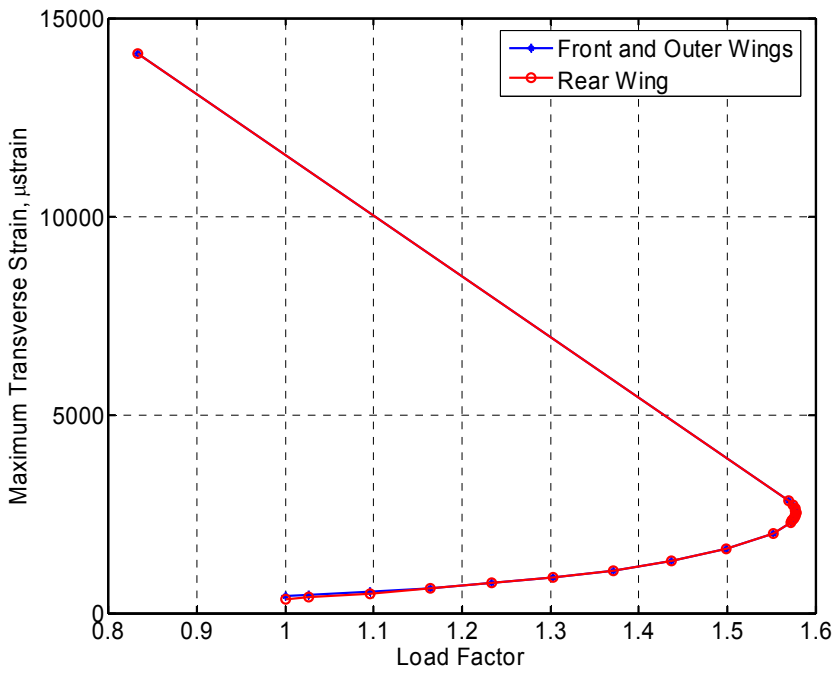


Figure 5.18: Nonlinear growth of maximum transverse strain due to loss of stiffness on the aft wing with increasing load factor (Model 5, level flight at sea level)

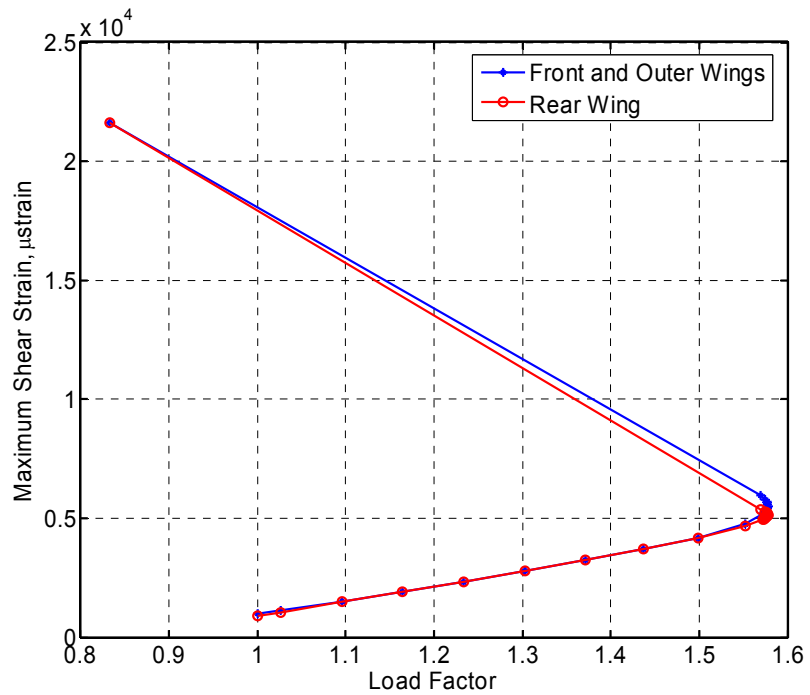


Figure 5.19: Nonlinear growth of maximum shear strain due to loss of stiffness on the aft wing with increasing load factor (Model 5, level flight at sea level)

The onset of this “buckling-like” instability can be observed when the wings demonstrate large deformations, which resulted from the loss of the effective bending stiffness when the wings are compressively loaded. As shown in Fig. 5.12, the effective lift generated on the wings is significantly reduced due to the large wing deformation, which corresponds to a reduction in load factors. The critical speed at which the vehicle loses its elastic stability may vary due to different levels of flexibility of the vehicle (Table 5.6). The plot of load factors as function of flight speed for different models is shown in Fig. 5.20. The model with a flexible vertical tail has the highest critical speed, whereas the one with a flexible fuselage has the lowest critical speed. If one looks closer to the modes of deformation (“unstable mode”), they show a complex interaction between the vertical bending of the fuselage (particularly at the front wing connecting region) and the in-plane bending of the tail. These induce a change in the overall aerodynamic loading of the different wing segments, influencing the compressive load applied to the aft wing.

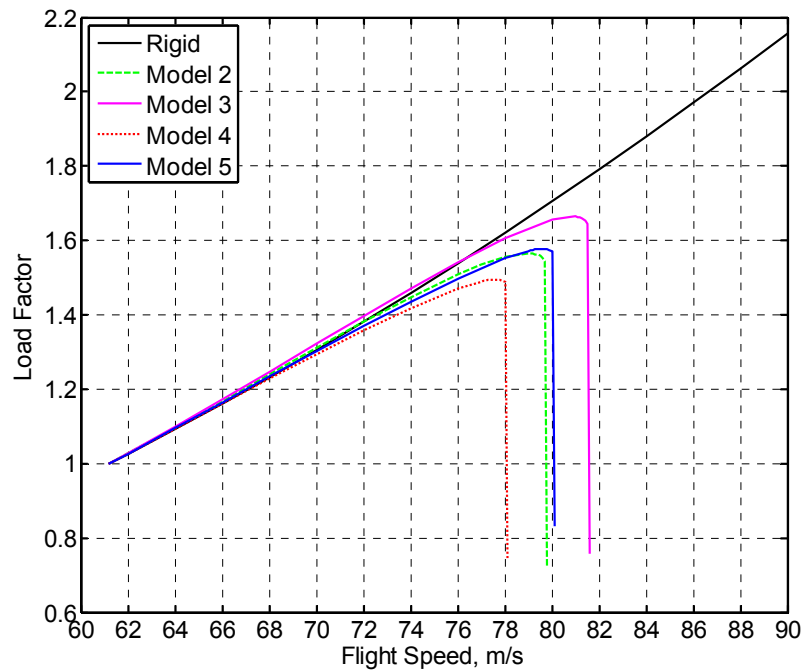


Figure 5.20: Load fact with respect to flight speeds for different models of the Joined-Wing configuration (level flight at sea level)

5.4 Dynamic Stability

The dynamic stability (flutter boundary) is an important design constraint and performance indicator of an aircraft. For the particular Joined-Wing configuration studied here, the static instability described above always happens before the flutter speed can be reached. Therefore, only the flutter boundaries of Single-Wing and Blended-Wing-Body configurations are studied here.

As a tailless vehicle, the Flying-Wing configuration features different flight dynamic characteristics from the conventional aircraft with tails. This dissertation will discuss the variation of phugoid and short-period modes with the change of vehicle deformations due to increased payloads.

5.4.1 Flutter Boundary of Constrained Vehicle: Single-Wing

The calculated flutter speeds with constrained rigid body motions are plotted in Fig. 5.21 for Single-Wing configurations. The induced flexibility of the fuselage slightly reduces the flutter speed, especially at the flight indices at high altitudes (see Fig. 5.1). However, this effect is very small. The reduction of the flutter speed due to the induced flexibility of the tails should be considered carefully. In the studies, overall system stability is evaluated, which includes both the wings and the tails. Since the relative elastic coupling between the wing and tail is weak (*i.e.*, relatively rigid fuselage), one would not expect any significant influence of the tail on the flutter characteristics of the wing. This explains why there is nearly no change in the flutter speed when the tail is set from rigid to flexible (From Model 1 to 2 and from Model 4 to 5). However, if the stiffness of the tail is further reduced (*e.g.*, 12% of the nominal stiffness), there will be a significant decrease of the tail flutter speed, which ended up lower than that of the wing, as seen in Fig. 5.21 (Model 3). The flutter of the tail can also be observed from the unstable modes. Figures 5.22 and 5.23 show the flutter modes of Model 3, which has a fluttering tail. But the flutter of Model 5 comes from the wings as indicated in Figs. 5.24 and 5.25.

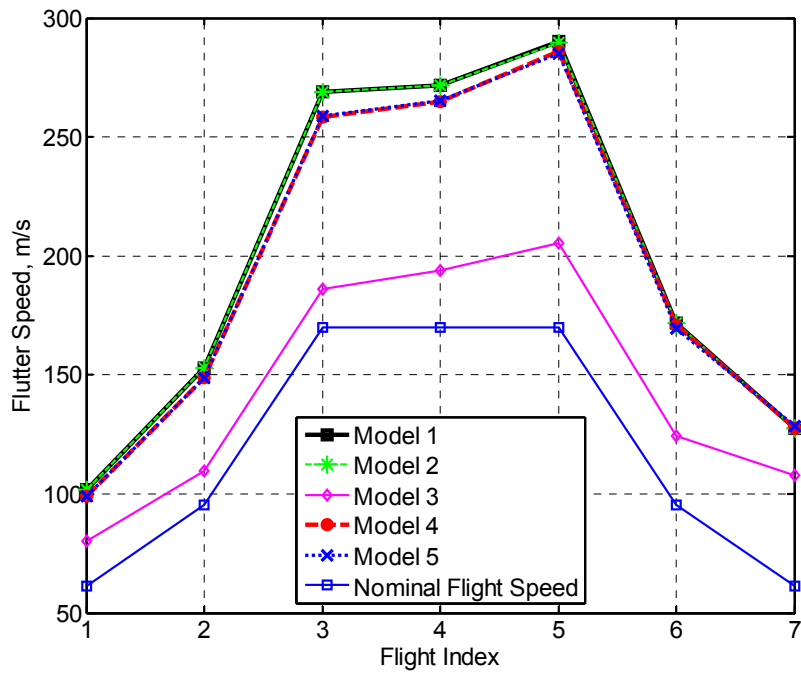


Figure 5.21: Nonlinear flutter speed at each flight index for different models of the Single-Wing configuration (no rigid body motions, no retrim)

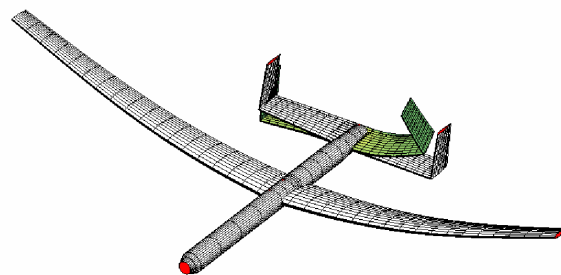


Figure 5.22: Anti-symmetric flutter mode of Single-Wing configuration (Model 3, Index 2)

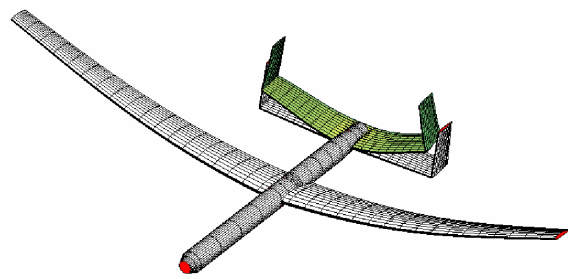


Figure 5.23: Symmetric flutter mode of Single-Wing configuration (Model 3, Index 3)

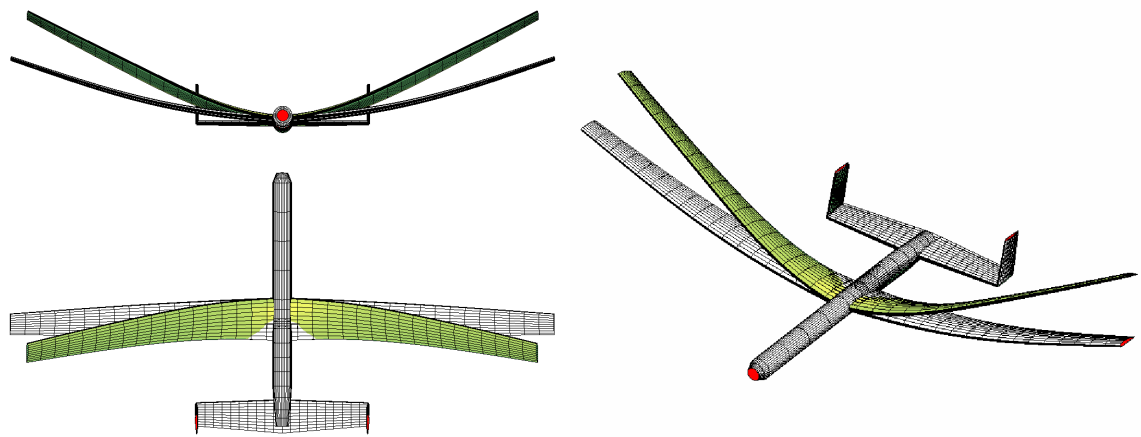


Figure 5.24: Symmetric flutter mode of Single-Wing configuration (Model 5, Index 3)

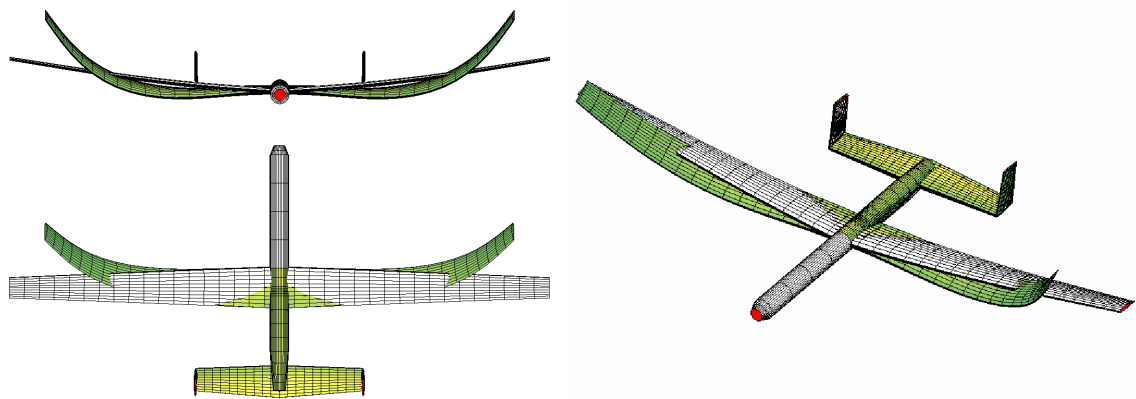


Figure 5.25: Symmetric flutter mode of Single-Wing configuration (Model 5, Index 5)

5.4.2 Flutter Boundary of Free Flight Vehicle: Single-Wing

In the previous section, the rigid body degrees of freedom are constrained when searching for the flutter boundary, which results in the flutter of elastic members only. As the wing oscillations could be coupled with the rigid body motion of the entire vehicle, the flutter boundary in free-flight condition may differ from that of a constrained vehicle. Since the induced flexibility of the different vehicle members has very limited impact on the flutter boundary of the constrained vehicle, only Model 5 – the fully flexible Single-Wing configuration is studied in this section. The results are plotted in Fig. 5.26, including the flutter results with rigid body motions constrained for comparison.

The first observation that can be made from Fig. 5.26 is that the flutter speed in free-flight vehicle may be significantly different from the one with constraints on rigid body motions, especially at the flight indices at high altitudes. At index 3, the nominal flight condition is already unstable due to the inertia of relatively large amount of fuel, which indicates a redesign of this vehicle is required.

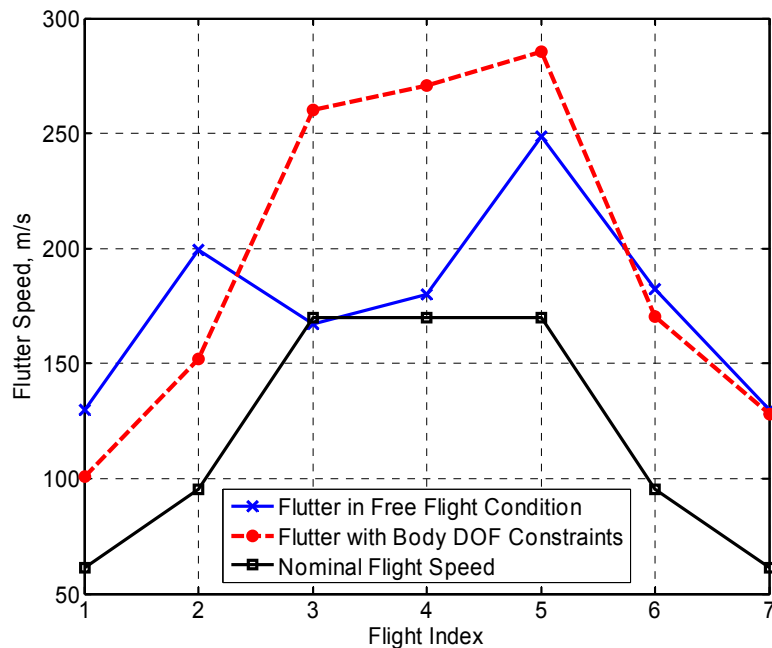


Figure 5.26: Flutter speed of Single-Wing configuration with constrained rigid body DOF and in free flight condition (Model 5, no retrim)

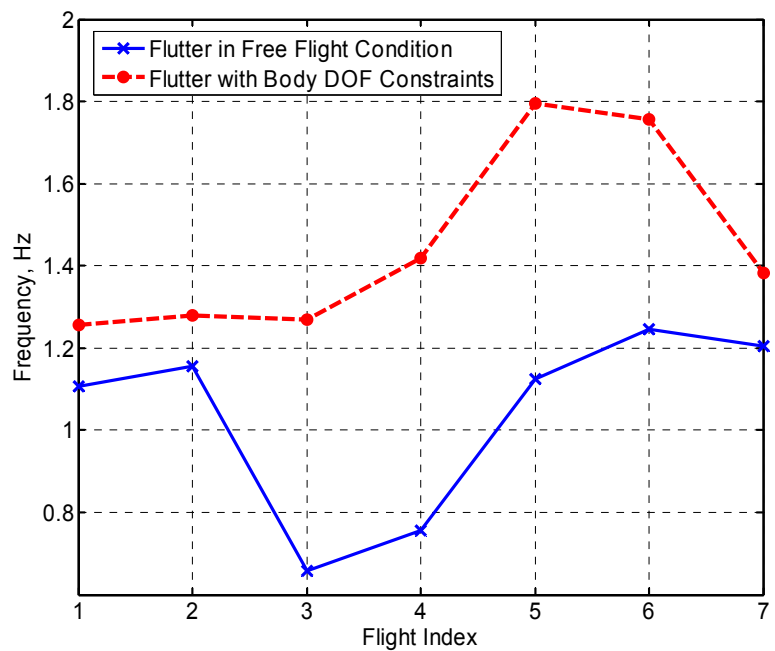


Figure 5.27: Frequency of flutter modes of Single-Wing configuration with constrained rigid body DOF and in free flight condition (Model 5, no retrim)

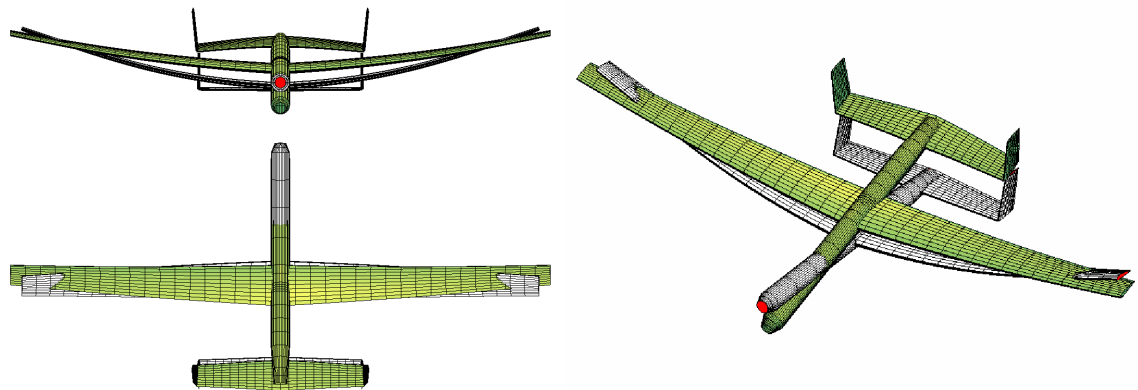


Figure 5.28: Flutter mode of Single-Wing configuration in free flight condition (Model 5, Index 3, no retrim)

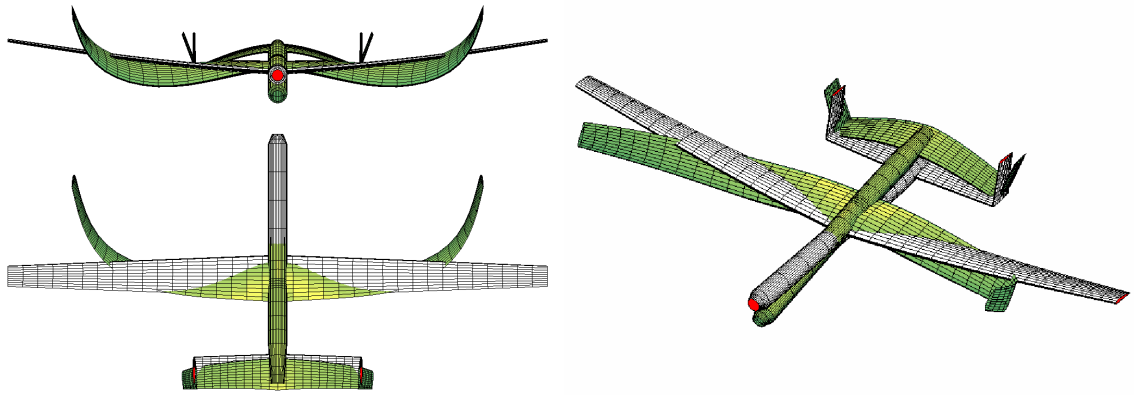


Figure 5.29: Flutter mode of Single-Wing configuration in free flight condition (Model 5, Index 7, no retrim)

5.4.3 Flutter Boundary of Free Flight Vehicle: Blended-Wing-Body

This section investigates the difference between flutter instabilities with and without rigid body motions for the Blended-Wing-Body configuration. The analysis is carried out at flight index 5, which has a nominal flight speed of 170 m/s. According to the analysis (see Fig. 5.30), the nominal vehicle would have its flutter boundary at 205 m/s (constrained) and 156 m/s (unconstrained). Therefore, the vehicle is not stable in terms of the unconstrained flutter, although the wing system itself is (when the rigid body motions are not considered). Changes to the wing stiffness (out-of-plane bending, in-plane bending and twist) could be imposed, such that the flutter boundary in free flight condition is higher than the nominal speed.

Figures 5.30 and 5.31 show the change of flutter boundary and frequency with increased out-of-plane bending stiffness of the vehicle. Flutter in free flight condition and with constrained rigid body DOFs are compared in each plot. As one may find, both of the flutter boundaries are increased as the structure is stiffened in terms of the out-of-plane bending. This is the case since out-of-plane bending participates in the flutter modes of both cases, as indicated in Figs. 5.32 and 5.33. When the out-of-plane bending stiffness is increased to 1.7 times that of the original design, the vehicle is stable in free flight. Another observation that can be made is that the free flight flutter speed is more sensitive to the change in the out-of-plane bending stiffness than the constrained one.

The in-plane bending stiffness, however, has nearly no impact on the free flight flutter, as indicated in Figs. 5.34 and 5.35. This is because in-plane bending does not participate in the flutter modes. There is a discontinuity in the flutter with constraints, when the stiffness is slightly knocked down from the nominal design. This comes from the impact of another mode that has a very similar frequency. The impact does not exist when the wing is further softened or stiffened.

Wing twist also participates in the unstable modes. Therefore, the change of torsional stiffness affects the flutter boundaries for both of the cases, as shown in Figs. 5.36 and 5.37. An increase of torsional stiffness is more effective than out-of-plane bending stiffness for increasing the vehicle's free flight flutter. Moreover, the free flight flutter mode is changed when the torsional stiffness is over twice that of the original one. The unstable body motion switches from symmetric plunging-pitch to anti-symmetric roll motion.

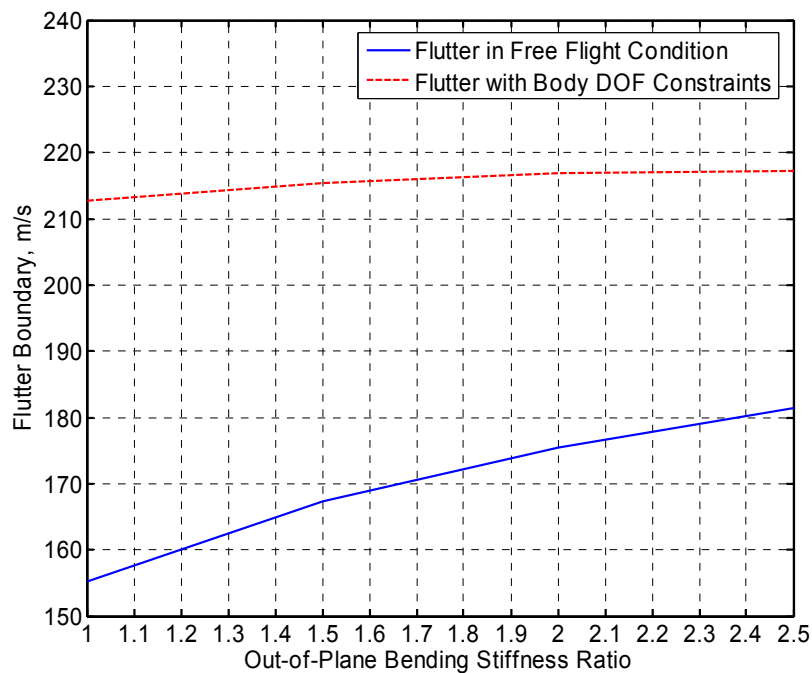


Figure 5.30: Change of flutter boundaries of the Blended-Wing-Body configuration with respect to out-of-plane bending stiffness

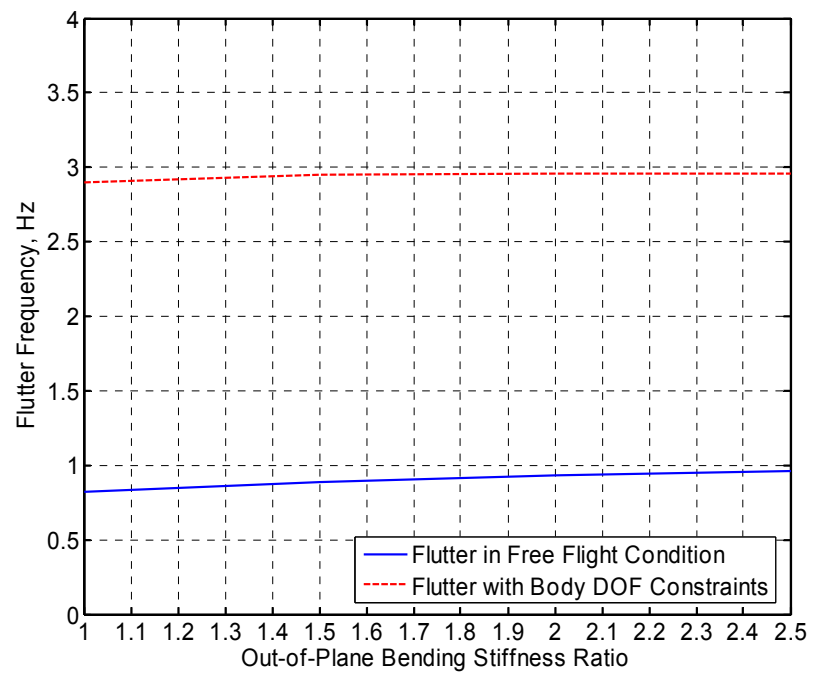


Figure 5.31: Change of flutter frequency of the Blended-Wing-Body configuration with respect to out-of-plane bending stiffness

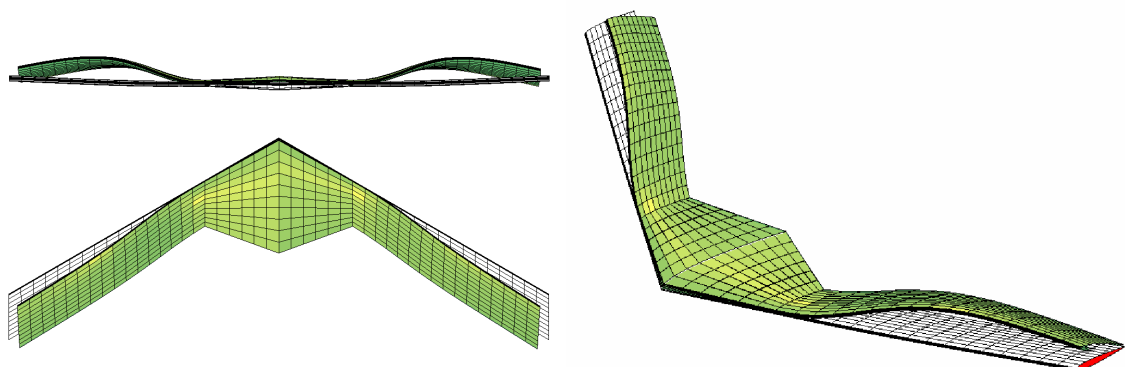


Figure 5.32: Flutter mode shape of the nominal Blended-Wing-Body configuration with all rigid body motions constrained

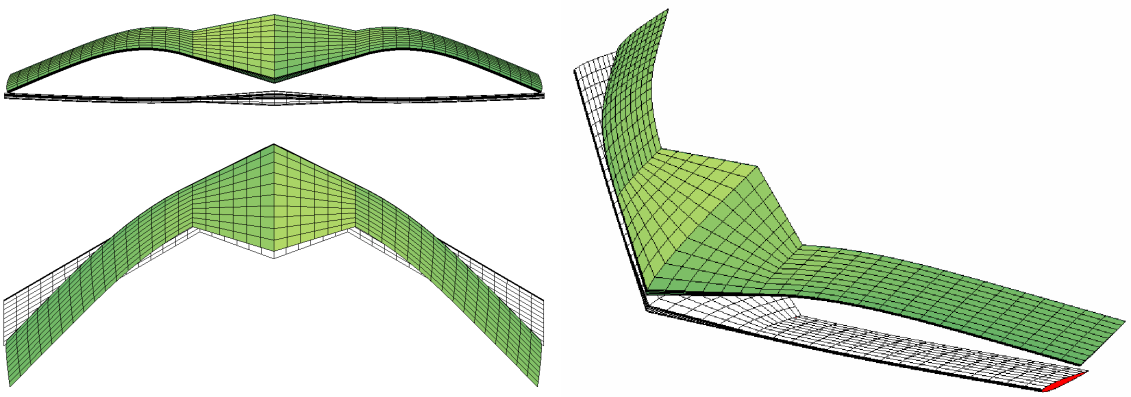


Figure 5.33: Flutter mode shape of the nominal Blended-Wing-Body configuration in free flight condition

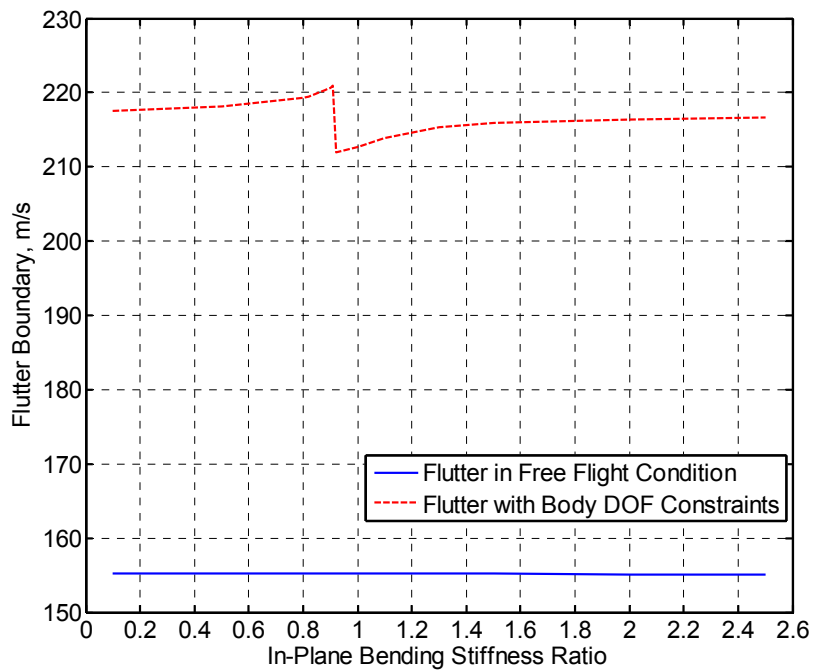


Figure 5.34: Change of flutter boundaries of the Blended-Wing-Body configuration with respect to in-plane bending stiffness

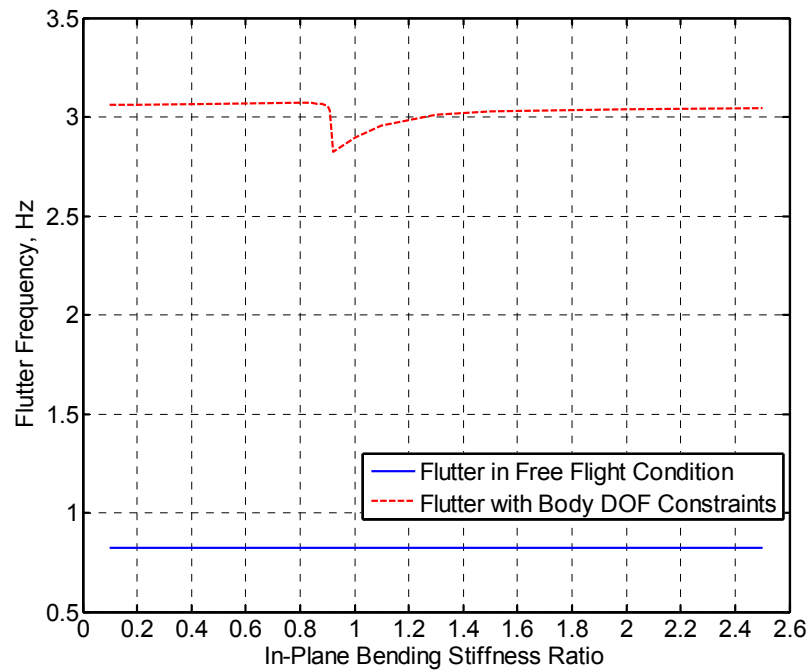


Figure 5.35: Change of flutter frequency of the Blended-Wing-Body configuration with respect to in-plane bending stiffness

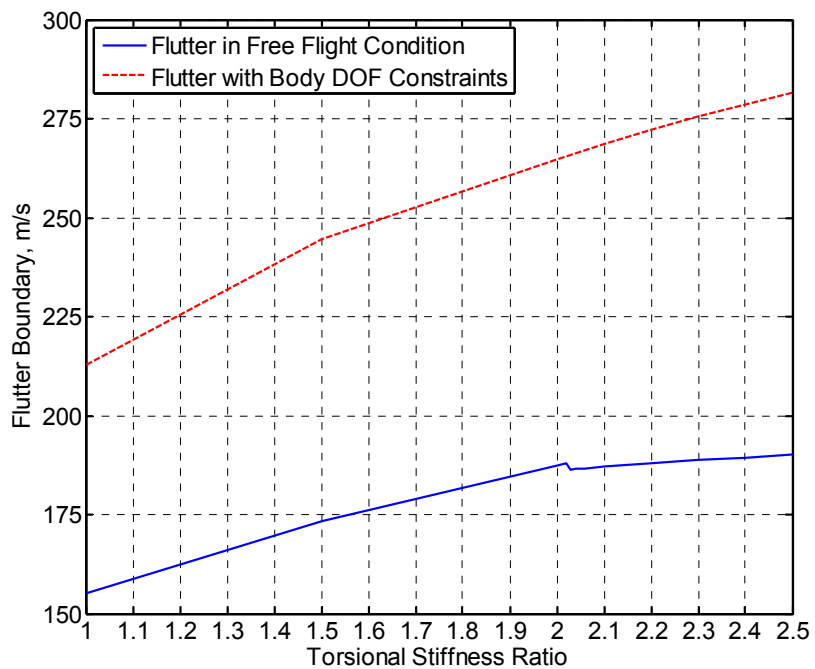


Figure 5.36: Change of flutter boundaries of the Blended-Wing-Body configuration with respect to torsional stiffness

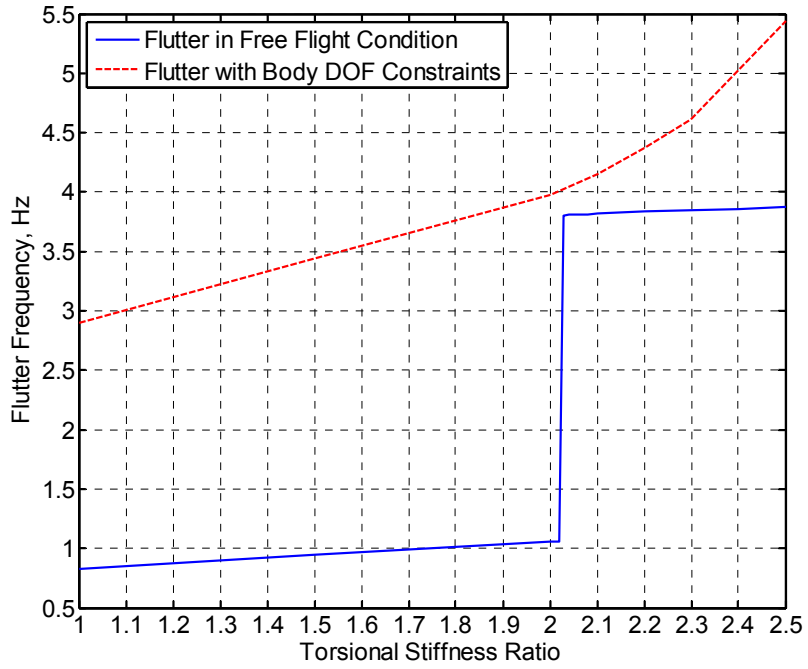


Figure 5.37: Change of flutter frequency of the Blended-Wing-Body configuration with respect to torsional stiffness

5.4.4 Flight Stability: Flying-Wing

To assess the flight stability of the Flying-Wing configuration, a linearization of the aeroelastic equations of motion at each trimmed condition is performed. Table 5.10 summarizes the results for the two extreme loading conditions: light and heavy, including the results given in Ref. [51]. Significant differences are present for both phugoid and short period modes. The latter is never oscillatory in the present model. Figure 5.38 shows the phugoid mode of the vehicle from light to heavy configuration. With the increase of payload, the frequency of the phugoid mode grows, while the damping decreases. At 152 kg payload, the damping crosses the imaginary axis, which indicates the phugoid mode loses stability. Qualitatively the result is the same as reported in Ref. [51]. The quantitative differences are mainly attributed to differences in the inertia distribution on the two models, since the steady aerodynamic loads are virtually the same between Ref. [51] and the present work.

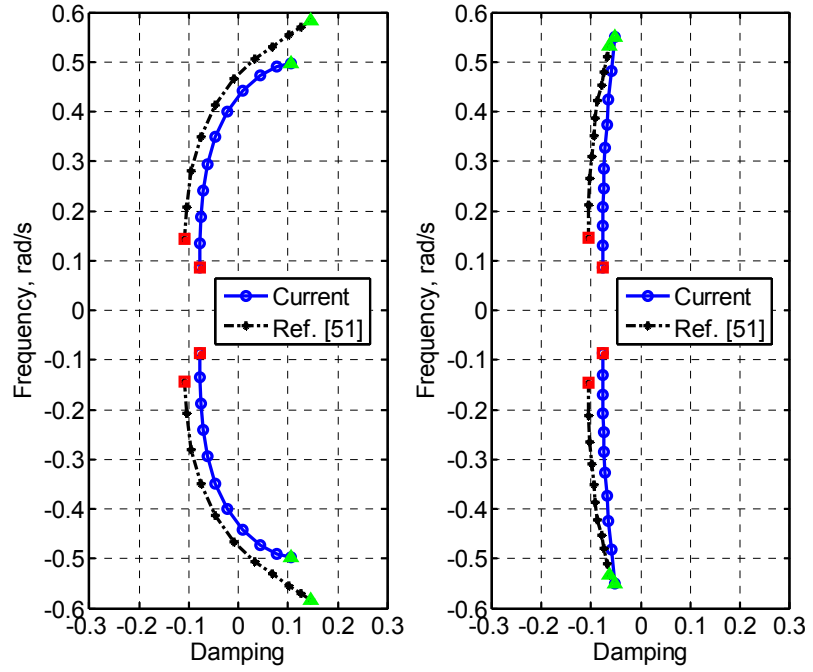


Figure 5.38: Root locus for phugoid mode of the Flying-Wing configuration (left: flexible vehicle, right: rigid vehicle)

Table 5.10: Phugoid and short-period modes for light and heavy models

		Flexible		Rigid	
Modes		Phugoid	Short-Period	Phugoid	Short-Period
Light	Ref. [51]	-0.108±0.142 <i>i</i>	-2.74±1.76 <i>i</i>	-0.106±0.146 <i>i</i>	-2.82±1.82 <i>i</i>
	Current	-0.0771±0.0858 <i>i</i>	-11.7/-8.28	-0.0758±0.0853 <i>i</i>	-11.7/-8.54
Heavy	Ref. [51]	+0.147±0.586 <i>i</i>	-	-0.0613±0.535 <i>i</i>	-3.05±1.63 <i>i</i>
	Current	+0.107±0.498 <i>i</i>	-7.53/-0.91	-0.0525±0.551 <i>i</i>	-9.31/-6.13

5.5 Roll Response

The ability to roll large span aircraft is expected to be reduced by the flexibility of the wings. According to military standards for a large land based transport type aircraft, the vehicle should have the capability to achieve a 30° roll angle within 3.0 seconds. It is of interests to explore the impact of all aircraft member's flexibility on its roll maneuver behavior. In this section, the roll response of Single-Wing and Joined-Wing configura-

tions is studied. The analysis takes place at flight index 5 (see Fig. 5.1). The flight condition is 16.7 km altitude, and 170 m/s. The trimmed body angle of attack is -1.11° for the Single-Wing and -2.73° for the Joined-Wing configuration, respectively. These angles, however, may vary for the models with different level of member flexibility. To achieve the roll motion, anti-symmetric aileron deflection is employed. Figure 5.39 shows the control input for the roll maneuver. The ailerons used in the Single-Wing configuration are built at the tip of the wings, spanning from 77.8% to 100% of its length, where as the ailerons in the Joined-Wing configuration are built at the outer wings, spanning from 25% to 75% of its length.

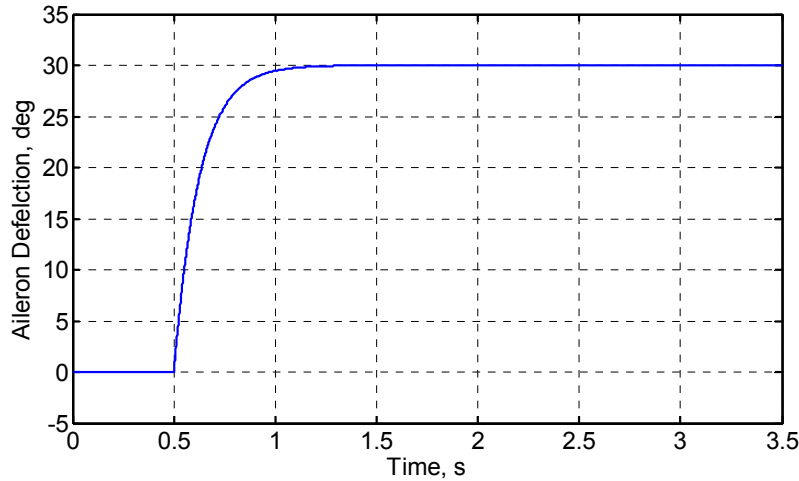


Figure 5.39: Aileron deflection for the Joined-Wing and Single-Wing configurations

5.5.1 Linearized and Fully Nonlinear Approaches

As a comparison, both linearized and nonlinear approaches are applied (Ref. [28]) here. In the linearized approach, the aircraft is first brought to its nonlinear steady state. The flexible members are permitted to have small dynamic deflections about the nonlinear steady state. This approach has the advantage of being computationally efficient, a desirable property on preliminary studies. On the other hand in the nonlinear approach, the deformed shape of the aircraft is updated at each time step, and all the aerodynamic loads are calculated according to the updated deformed shapes. Although more time consuming, this presents the most accurate representation of the maneuver.

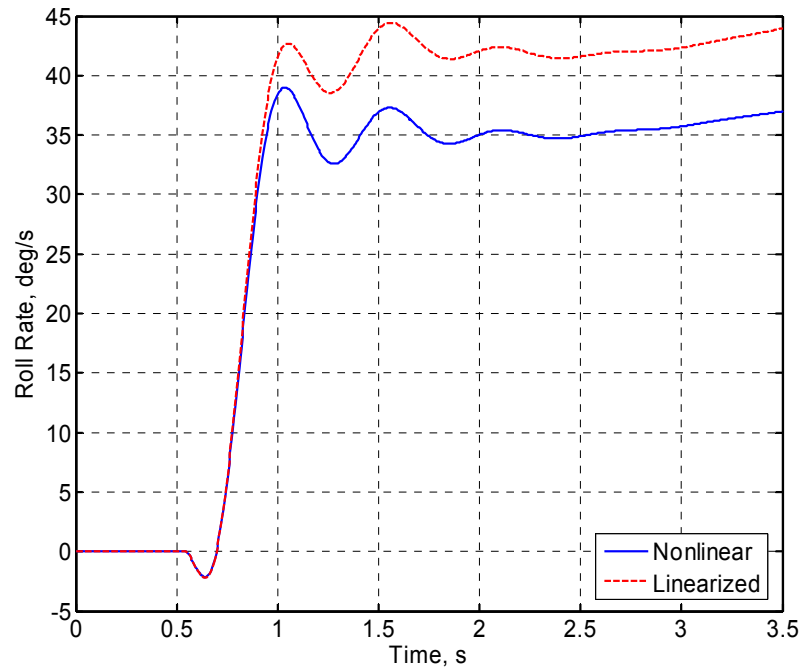


Figure 5.40: Comparison of nonlinear and linearized roll rate of the Single-Wing configuration (Model 5)

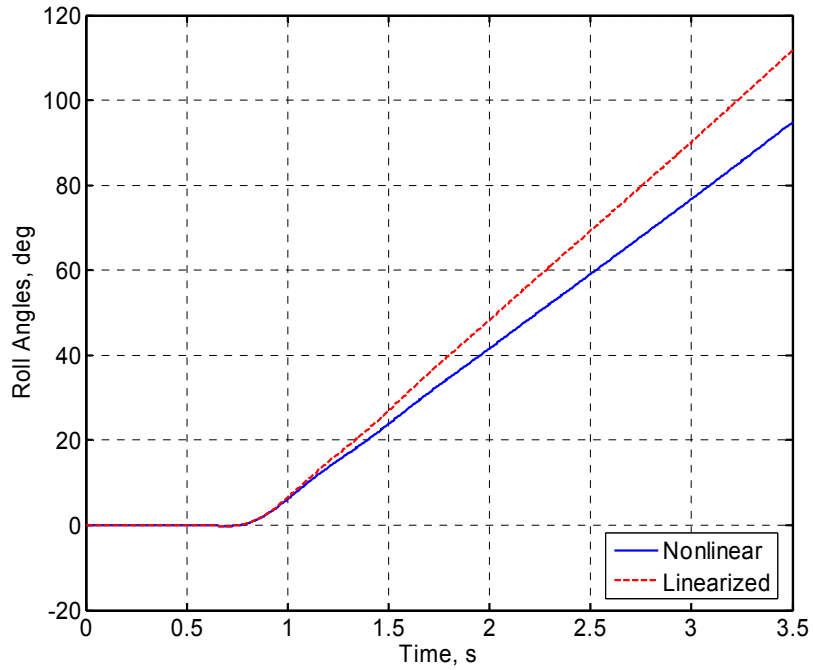


Figure 5.41: Comparison of nonlinear and linearized roll angle of the Single-Wing configuration (Model 5)

Figures 5.40 and 5.41 show the comparison of the roll simulation results from linearized and nonlinear approaches for the fully flexible model (model 5) of the Single-Wing configuration. From the plots, one can see that there is over 18% difference in the steady state roll rate. This reflects at the different roll angle values at a given instant of time. However, this may not be an issue for shallow angle roll maneuvers, where the difference between the two models is very small.

5.5.2 Roll Response of Single-Wing Models

Figures 5.42 to 5.45 show the roll response of different models of the Single-Wing configuration. As it can be seen from the results, the flexibility of the fuselage and the tails does not play an important role in the roll response of this aircraft.

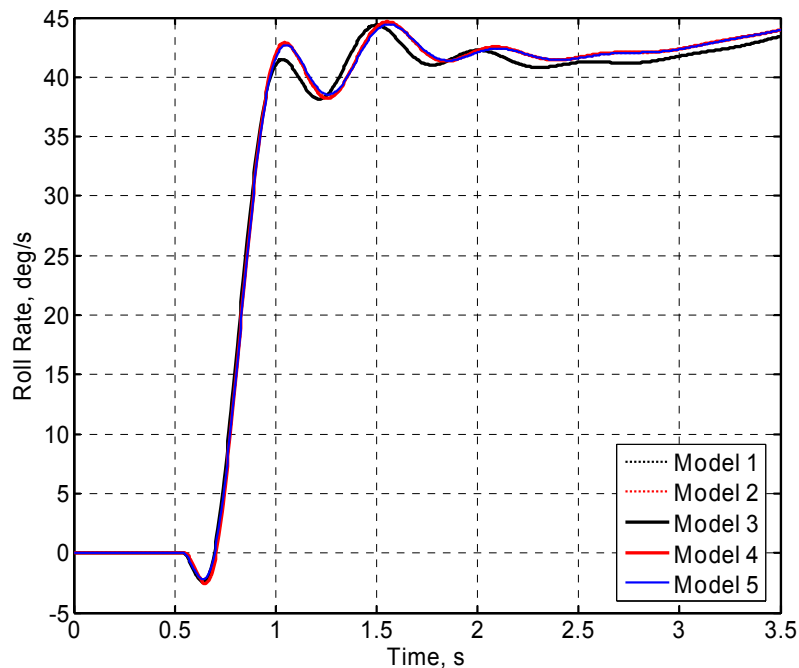


Figure 5.42: Linearized roll rate for the Single-Wing configurations

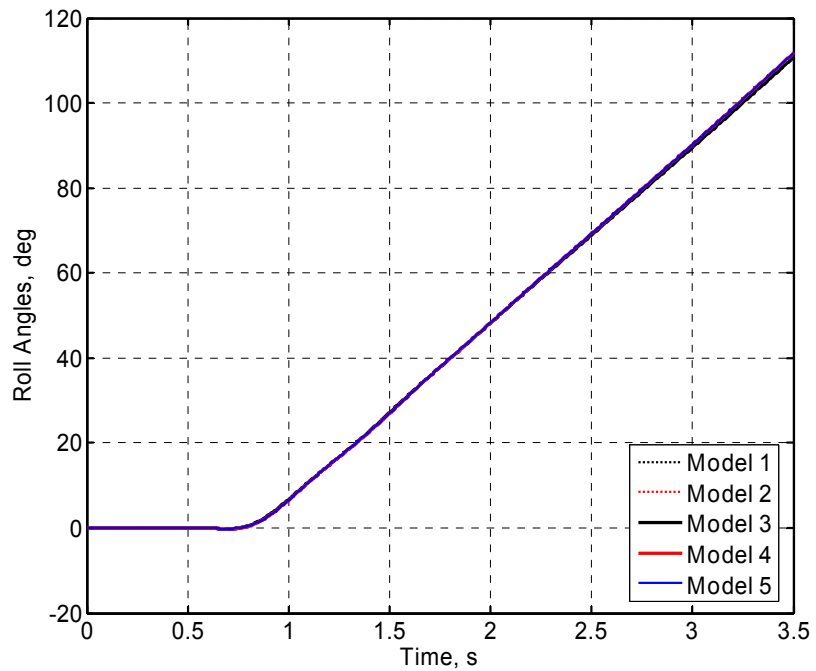


Figure 5.43: Linearized roll angle for the Single-Wing configurations

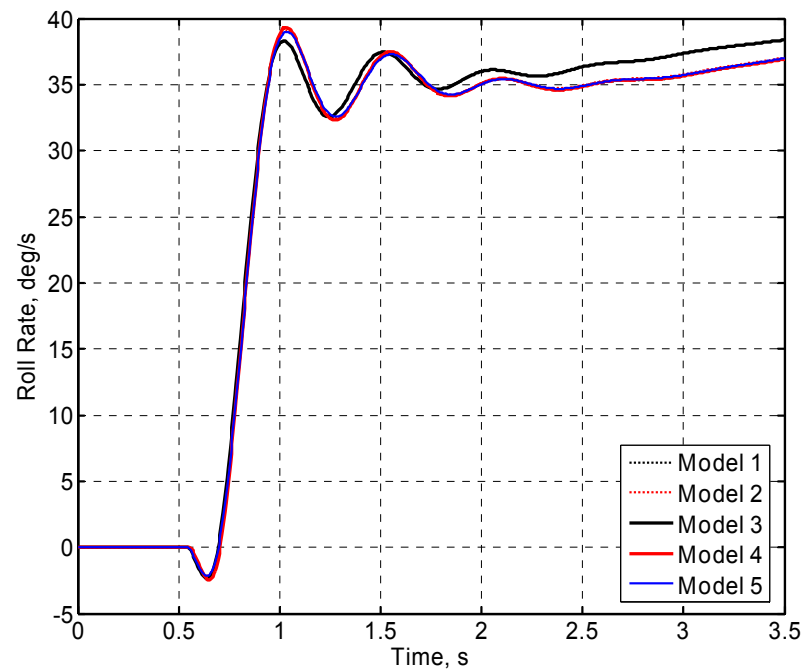


Figure 5.44: Nonlinear roll rate for the Single-Wing configurations

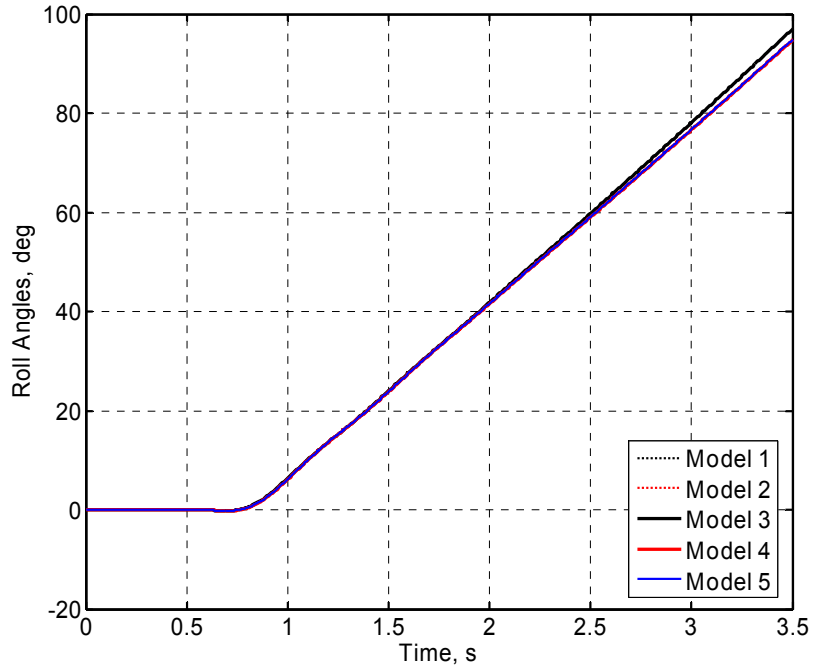


Figure 5.45: Nonlinear roll angle for the Single-Wing configurations

5.5.3 Roll Response of Joined-Wing Models

Figures 5.46 to 5.49 show the roll response of different models of the Joined-Wing configuration. For this configuration, there is a significant difference between the linearized and fully nonlinear approaches for roll analysis, particularly for the terminal roll rate. Moreover, as it can be seen from Figs. 5.46 and 5.48, the additional vehicle flexibility brings more complexity to the roll response as it starts developing. Oscillations in the roll rate response can also be observed with time, due to the induced flexibility of the fuselage and vertical tail. Finally, the maximum roll angle that the vehicle can reach is noticeably lower than that of the semi-rigid model (see Figs. 5.47 and 5.49).

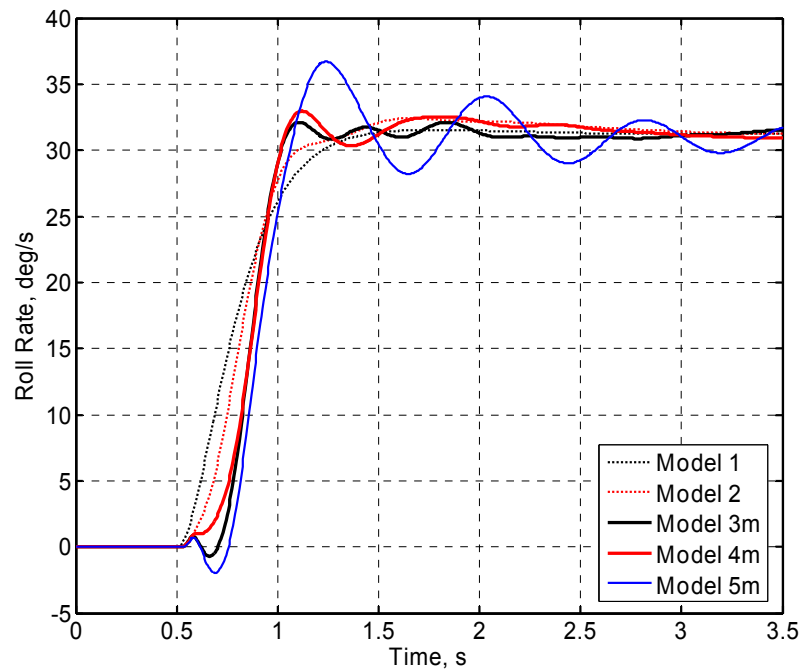


Figure 5.46: Linearized roll rate for the Joined-Wing configurations

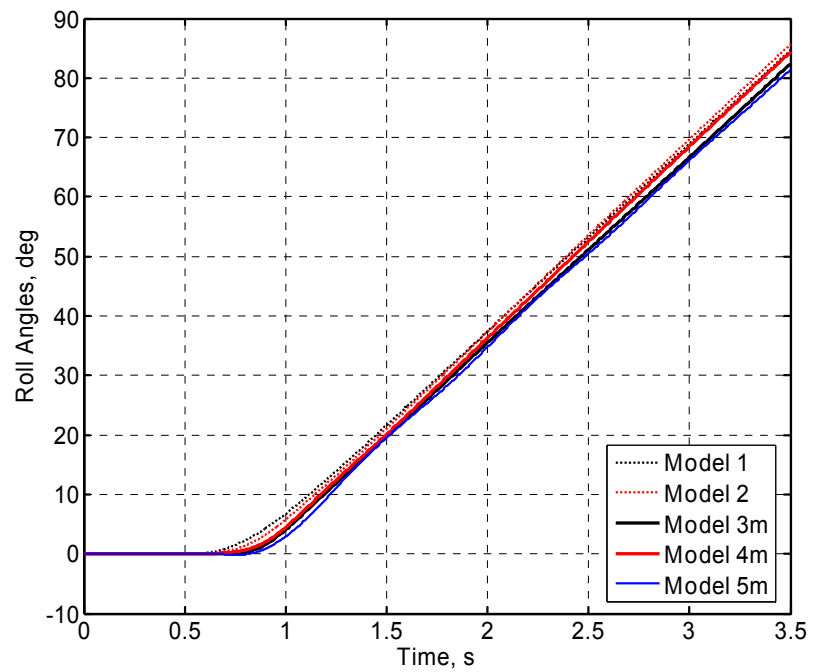


Figure 5.47: Linearized roll angle for the Joined-Wing configurations

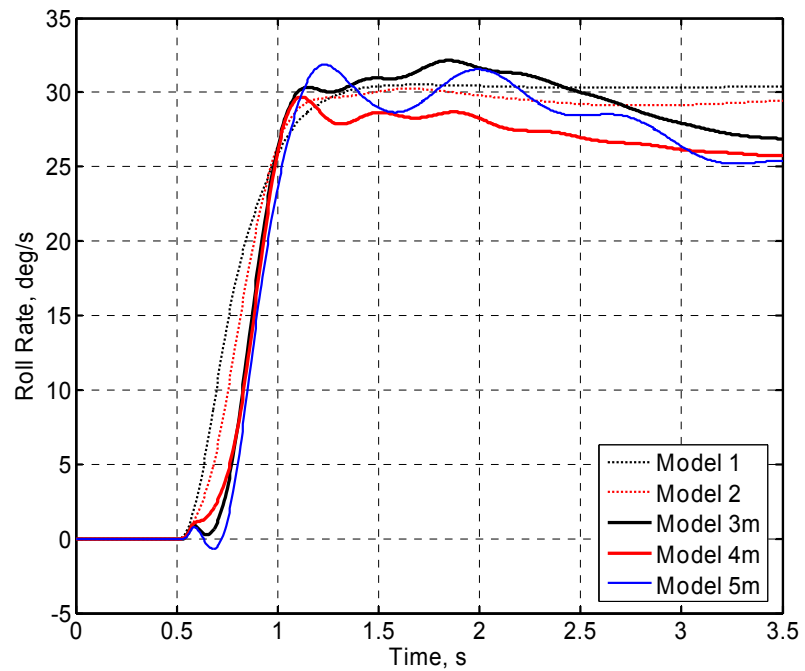


Figure 5.48: Nonlinear roll rate for the Joined-Wing configurations

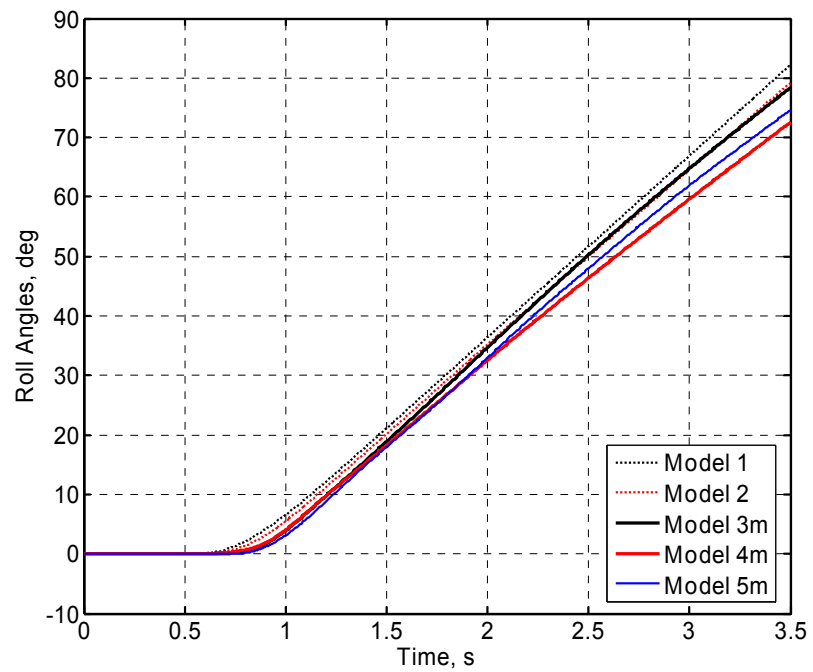


Figure 5.49: Nonlinear roll angle for the Joined-Wing configurations

5.6 Flight Response with Flap Perturbation

As indicated by the stability analysis, the Flying-Wing configuration has an unstable phugoid mode when fully loaded. Therefore, it is necessary to further understand its time domain behavior. This model is initially flying at trimmed level condition. Perturbation is introduced by a commanded flap angle change: between 1 and 2 seconds, the flap angle is linearly ramped up to 5° , and it is linearly ramped back to its trimmed angle between 2 and 3 seconds, as shown in Fig. 5.50. A similar simulation has been carried out in Ref. [51], and the results are presented for comparison.

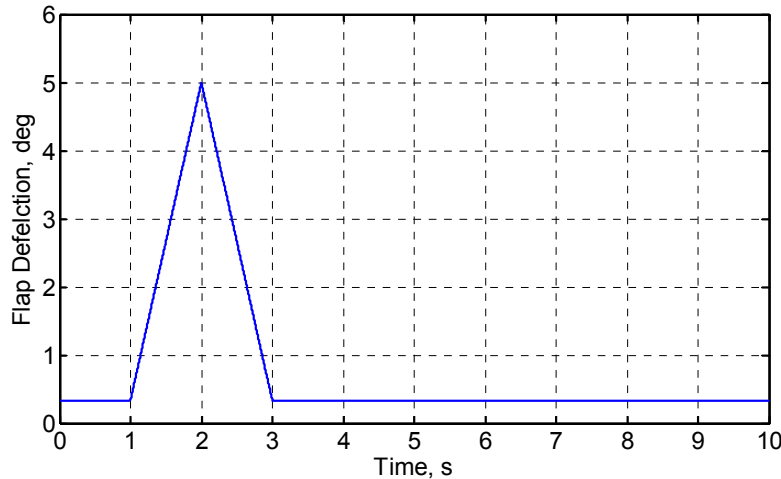


Figure 5.50: Flap deflection for the Flying-Wing configuration

As described in Chapter II, there are two different stall models used in the simulations. For Stall Model 1, the lift coefficient, c_l , is kept constant and equal to c_{lmax} once the angle of attack goes beyond the stall angle, and the moment coefficient (c_{m0}) remains the same as before stall. Stall Model 2 is similar to Stall Model 1 with the only difference that now the moment coefficient is dropped from 0.025 to -0.02.

Figures 5.51 through 5.55 show the Flying-Wing response for the first 80 seconds of flight after the flap was disturbed. Figures 5.51 and 5.52 show the variation of airspeed and altitude of the vehicle, including the two stall models, no stall effects, and the results presented in Ref. [51] for similar perturbation. As one can see, the damping (and

frequency to a lesser extent) is different between the models used in Ref. [51] and in the present study, as already discussed. Ref. [51] does not present any stall effects. From those two figures, the exchange between kinetic energy and potential energy of the vehicle is seen through the out-of-phase variation between air speed and altitude. The unstable phugoid mode makes the oscillations grow with time for the heavy vehicle configuration.

As shown in Fig. 5.53, the mid-span location (root) angle of attack reaches stall angle within a few cycles. From Fig. 5.53, one may also see the difference of the angle of attack with and without stall effects. While this shows stall at the mid-span section of the Flying-Wing happening around 60 s, the wing tip starts experiencing stall about 0.5 s earlier. Among the things that can be observed for this series of results is that at certain points a higher angle of attack is obtained with stall effects on than with stall effects off. This is due to the difference between aerodynamic loads before and after stall. Once the stall angle is approached, the fixed level of aerodynamic lift load results in insufficient force to balance the vehicle weight, in contrast to a continuous linear increase of lift with static angle of attack when stall is off. Therefore, the altitude of the vehicle reduces with increased vertical velocity (Fig. 5.55), leading to instantaneous higher angles of attack. However, the lift reduces the descent rate and the angle of attack falls back to be smaller than the stall angle. This cycle repeats and an oscillation in body vertical velocity can be observed. For the simulation with Stall Model 2, the sudden reduction in aerodynamic moment when stall angle is reached accentuates this behavior. The corresponding change in body velocities is larger than the one with Stall Model 1. Since the actual stall characteristics of an airfoil will depend on the specific vehicle application (not defined in this work) and that qualitatively the two stall models studied here give similar results, only Stall Model 2 is applied in the studies to follow.

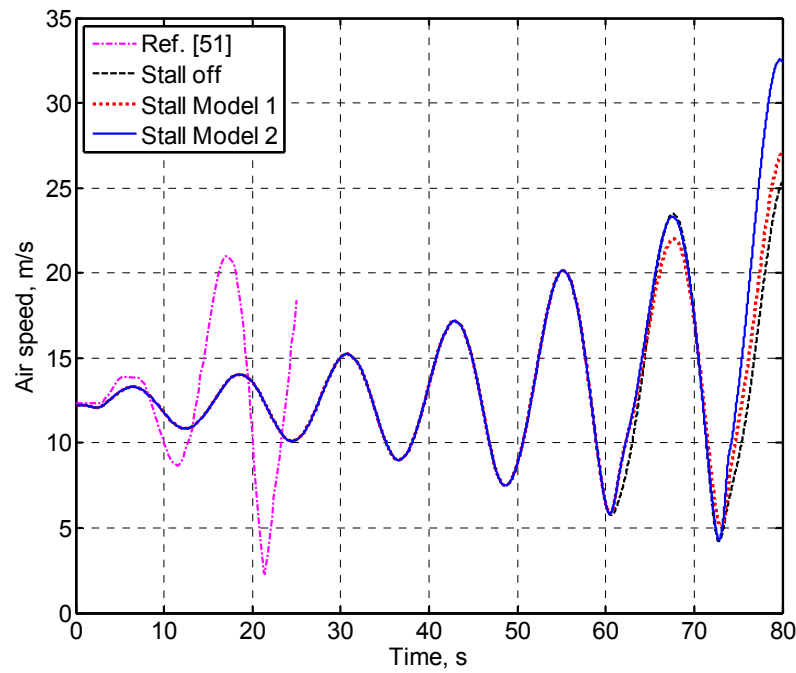


Figure 5.51: Stall effects on the airspeed of flight with initial flap angle perturbation

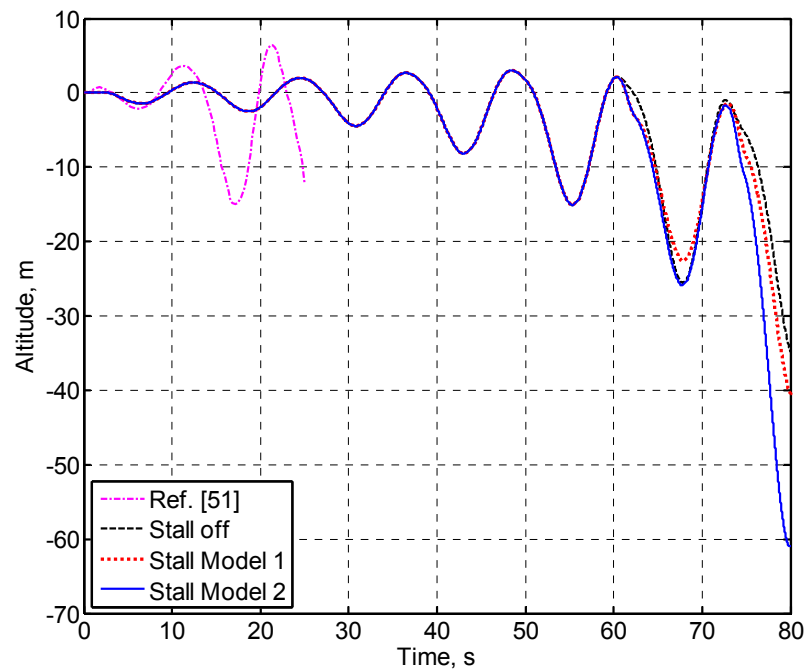


Figure 5.52: Stall effects on the altitude of flight with initial flap angle perturbation

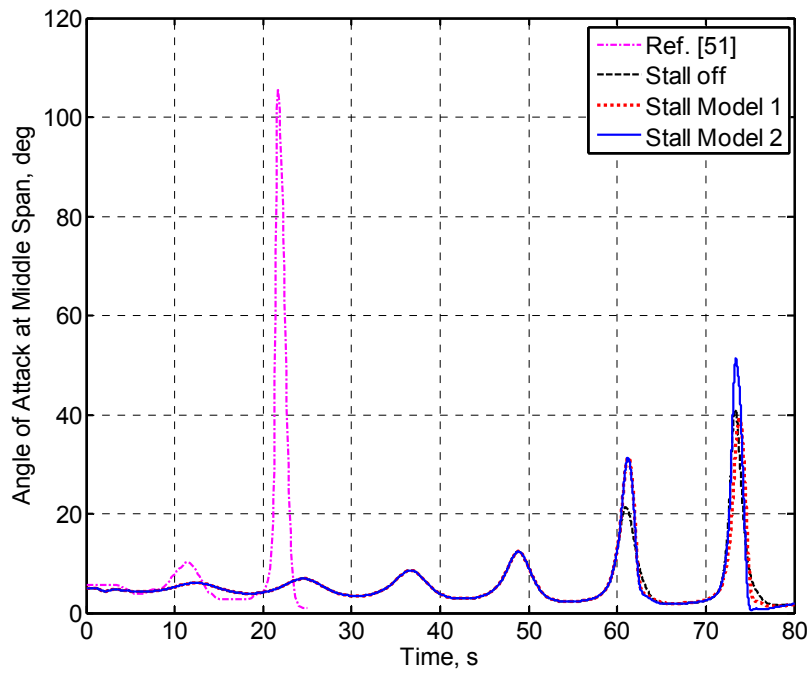


Figure 5.53: Stall effects on the angle of attack of flight with initial flap angle perturbation

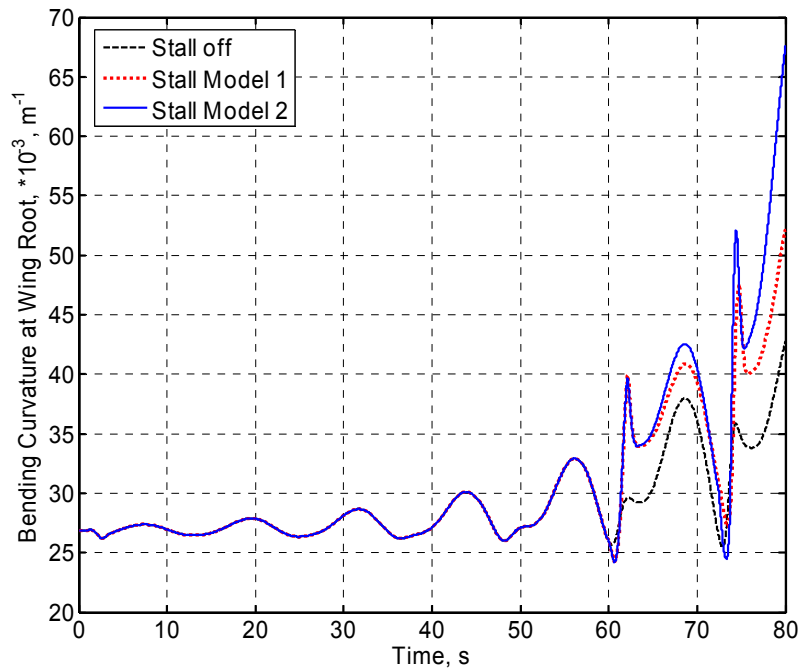


Figure 5.54: Bending curvature at the mid span location of flight with initial flap angle perturbation

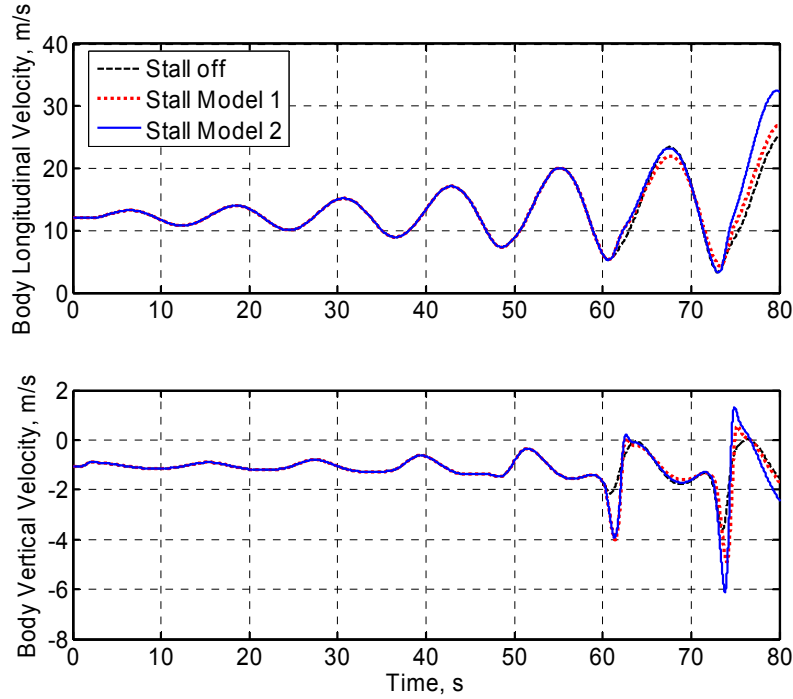


Figure 5.55: Variation of body velocities with initial flap angle perturbation

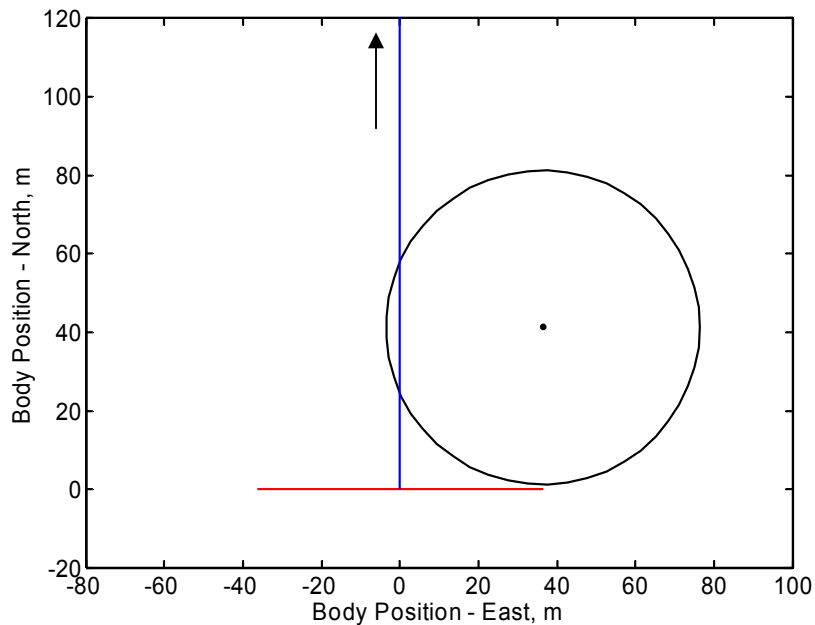


Figure 5.56: Initial vehicle position with respect to the gust region and intended flight path if in calm air

5.7 Gust Response

As discussed above, the Flying-Wing configuration studied here in its heavy configuration shows very large deformations under level flight. This large deformation leads to flight dynamic instability and may compromise the vehicle's structural integrity under gust excitation. As an example, the mishap of the Helios prototype vehicle also demonstrated the importance of knowing the gust response of this type of vehicle.

5.7.1 Effects of Different Gust Durations

To better understand the vehicle response under gust conditions, the discrete gust model described in Chapter II is used. The maximum gust amplitude at the center of the gust region, A_c , is 10 m/s. The spatial distribution within the gust region is given by Eqs. (2.106) and (2.107) with the following coefficients: $r_0 = 40$ m, $n_N = 2$, $n_E = 1$, and the gust duration, t_g , can be 2, 4, or 8 seconds. Figure 5.56 shows the initial vehicle position ($t = 0$ s) with respect the gust profile and its intended flight path if in calm air. The right wing of the vehicle begins to touch the gust region after 0.1 s.

Using the Stall Model 2 when the stall angle is reached, the aerodynamic lift force stops increasing with the angle of attack, and the constant component of the aerodynamic pitching moment is reversed, which makes the airfoil pitch down. Figures 5.57 to 5.59 show the body positions of the vehicle with gust perturbations for the three different gust durations. The first observation from these plots is that the vehicle is flying away from the gust center after it penetrates the gust region (up to 3.5 s). The gust may increase the local plunging motion velocity (in Eq. 2.101 or 2.103), which results in increased local lift forces. Since the gust distribution on the vehicle is not symmetric, roll and yaw moments about vehicle's c.g. point are generated, which leads to roll and yaw motions. For the initial stages when the vehicle penetrates the gust region (before 2.0 s), the lateral deviation is not increased with the increase of the gust duration (Fig. 5.58, bottom). This is because the longer gust duration introduces a smaller loading gradient on the wing, leading to smaller trajectory deviations at the beginning. However, the longer exposure will supply more energy to the motion and the deviation from the original (within calm

air) trajectory will surpass the ones from shorter gust durations. The flight path, however, may change its direction due to different gust durations, as one can observe from Fig. 5.58. For the cases with 4-s and 8-s gusts, the flight path heads back to the gust side after 6 to 7 seconds, while the 2-s gust case demonstrates unchanged deviation direction. This is due to the oscillation of the wings after the gust perturbation ceases. For the 4-s and 8-s cases, the right wings bend down when the gust effects disappear, which leads to a downward local plunging motion velocity (in Eq. 2.101 or 2.103). Therefore, the local lift forces and moments on the right wing become lower than the left one, resulting in a positive yaw moments about the c.g. of the vehicle. On the other hand, the 2-s gust applies relatively little energy to the wings, such that the downward motion of the right wing does not generate enough yaw moment to overcome the ongoing vehicle motion. Moreover, the vehicle motion of the 8-s case is more complicated, since the oscillation of the right wing may lead to another change of the yaw direction after 15 seconds. After all, it is also noticeable that the amplitude of the plunging motion is increased with time, as shown in Fig. 5.59. This is the result of the vehicle's phugoid mode being unstable.

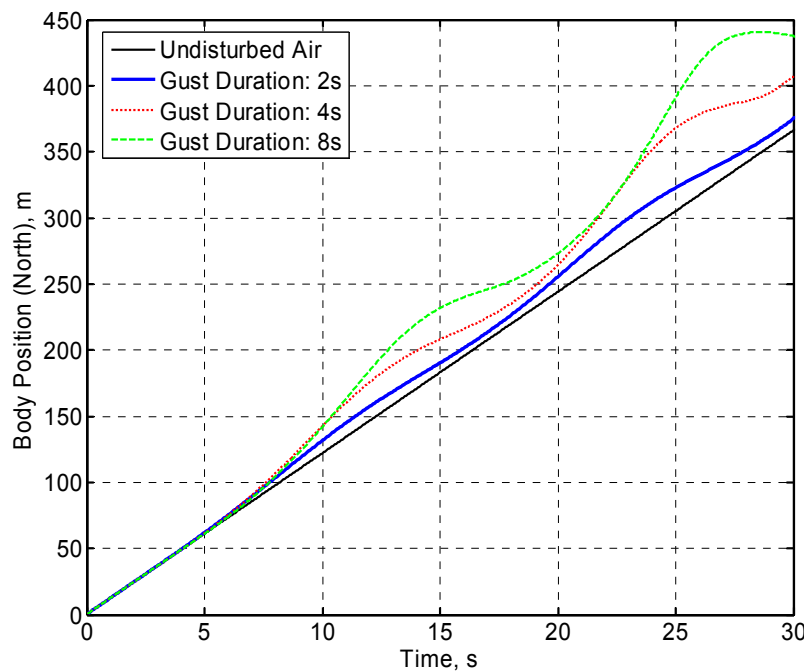


Figure 5.57: Effects of gust duration on body position – North

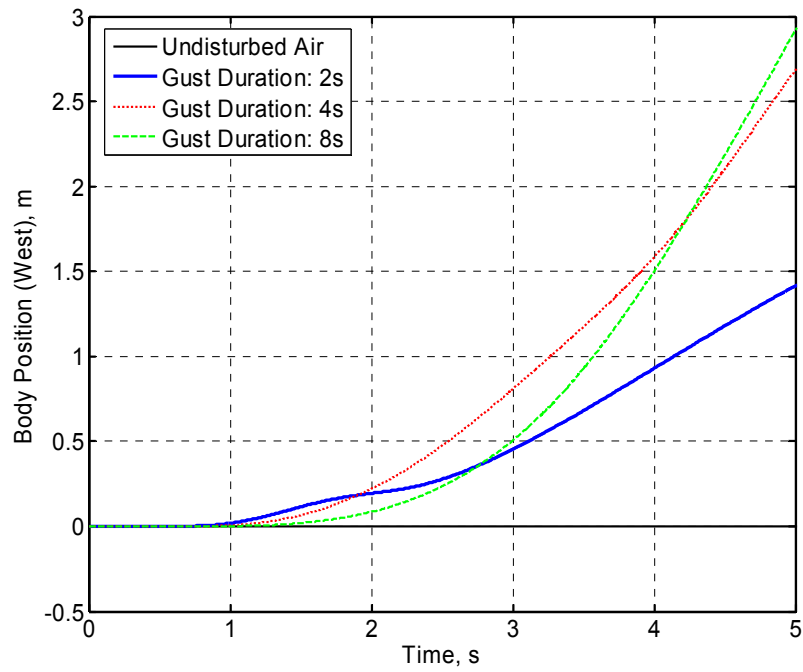
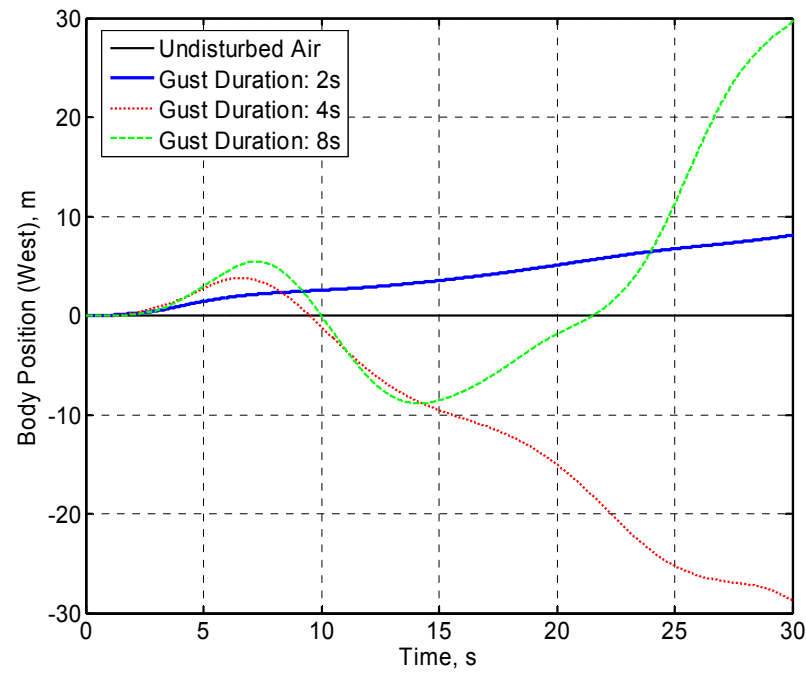


Figure 5.58: Effects of gust duration on body position – West (zoomed for initial times at the bottom)

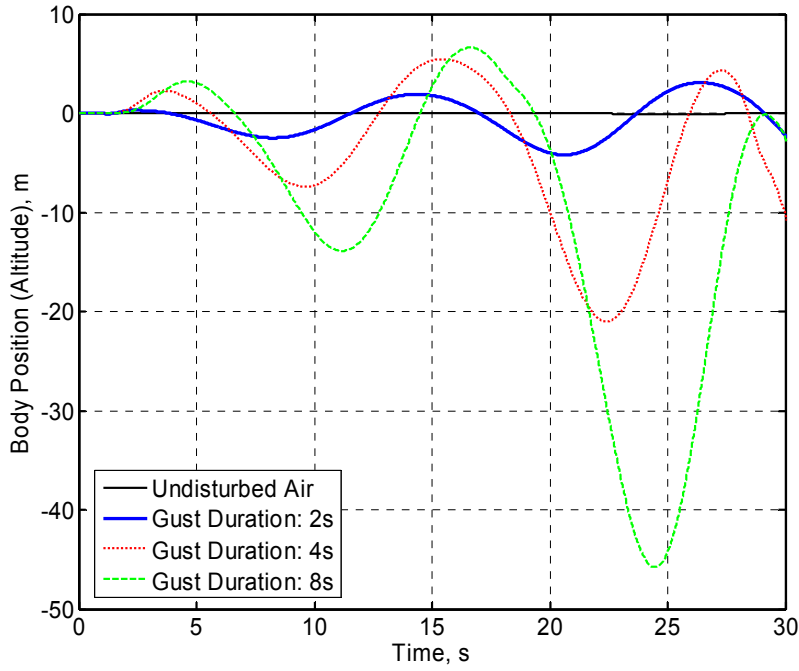


Figure 5.59: Effects of gust duration on body position – Altitude

Figures 5.60 to 5.62 describe the change in the Euler angles of the body as the vehicle goes through the gust perturbation. The variation of the yaw angle has a similar tendency to the body positions. If one looks at the details of the yaw angle at early stages of flight (Fig. 5.60, bottom), it is evident that initially the vehicle yaws away from the gust center, but subsequently, it yaws back into the gust. This is believed to be associated with adverse yaw due to decrease in lift on the right wing. It can also be seen from Fig. 5.61 that the pitching angle oscillates with increased amplitude, which indicates again a longitudinal unstable configuration. As for the roll angle, the 2-s gust duration is short enough that it tends to recover to its undisturbed value within the time window showed in Fig. 5.62. This is expected for a damped roll oscillation, since the lift distributions on the vehicle should return to its original one after the gust effects disappear. However, this symmetry of lift distribution cannot be seen for the 8-s gust. The local angles of attack at the two tips are still different and the amplitude of the motion seems to still be growing. Longer simulation times would be required for the long duration gust cases.

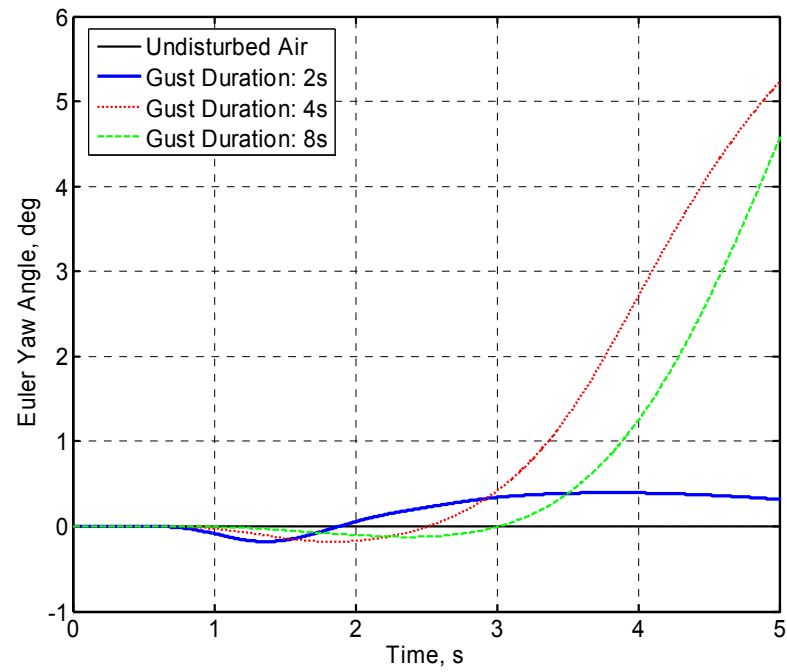
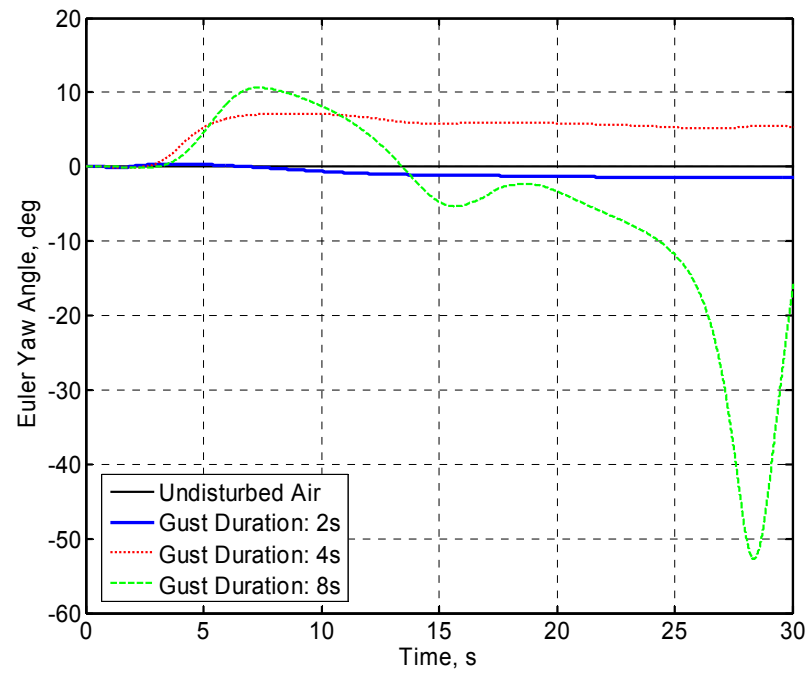


Figure 5.60: Effects of gust duration on Euler angle – Yaw (zoomed for initial times at the bottom)

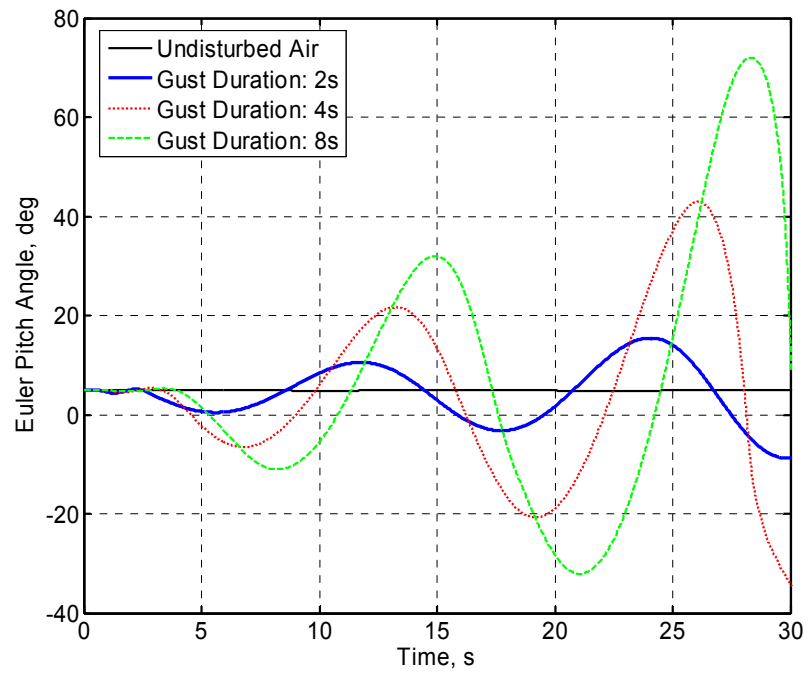


Figure 5.61: Effects of gust duration on Euler angle – Pitch

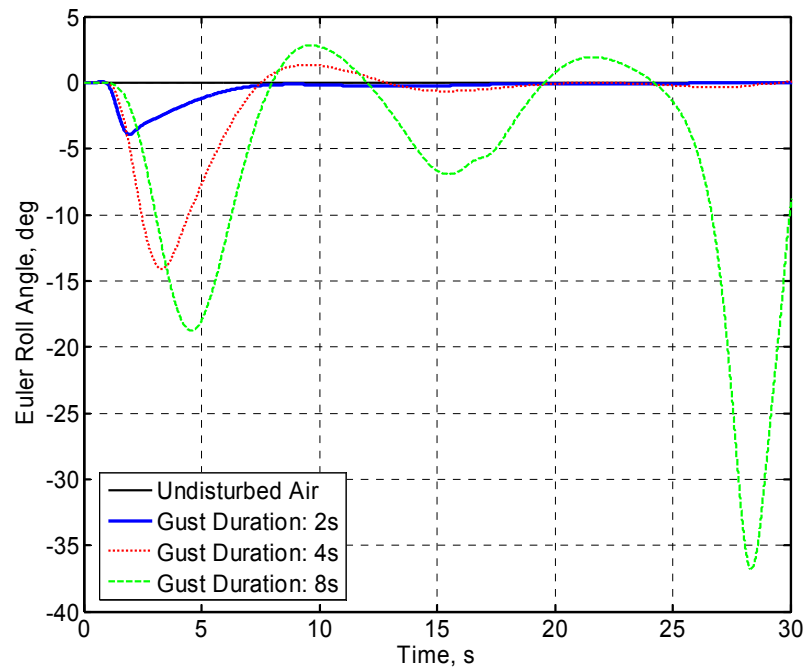


Figure 5.62: Effects of gust duration on Euler angle – Roll

One more observation that can be made is on the wing deformation. Figure 5.63 compares the wing root bending curvature for the three cases. As seen, the vehicle experience large deformation after 25 seconds, especially for the 8-s gust case. Figure 5.64 exemplifies the deformation of the vehicle at the end of 30 s, with 8-s gust. Significant difference can be observed between the deformations at 30 s and the trimmed steady state. The vehicle cannot maintain its trimmed state any more. This scenario resembles the Helios prototype vehicle mishap after its disturbance encounter.

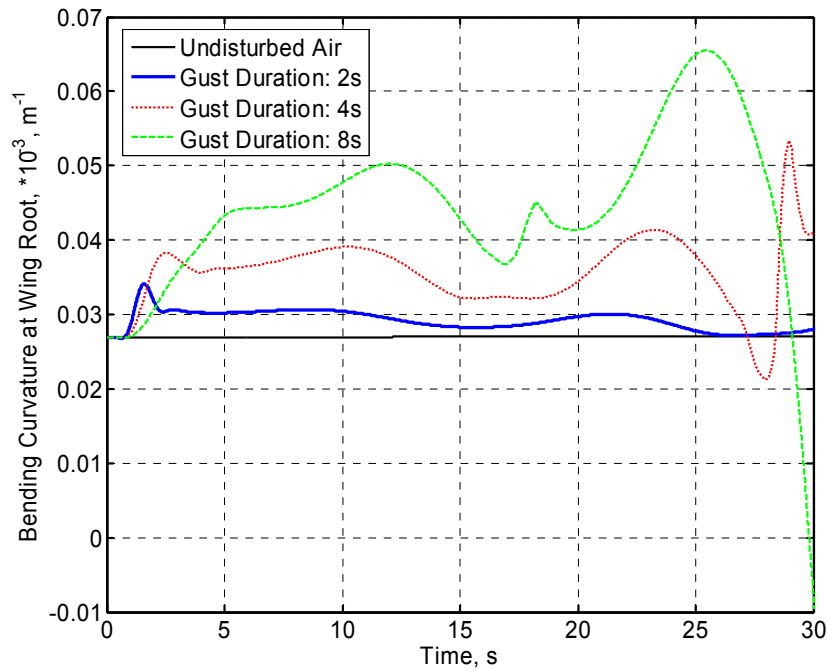


Figure 5.63: Effects of gust duration on bending curvature at the mid span location

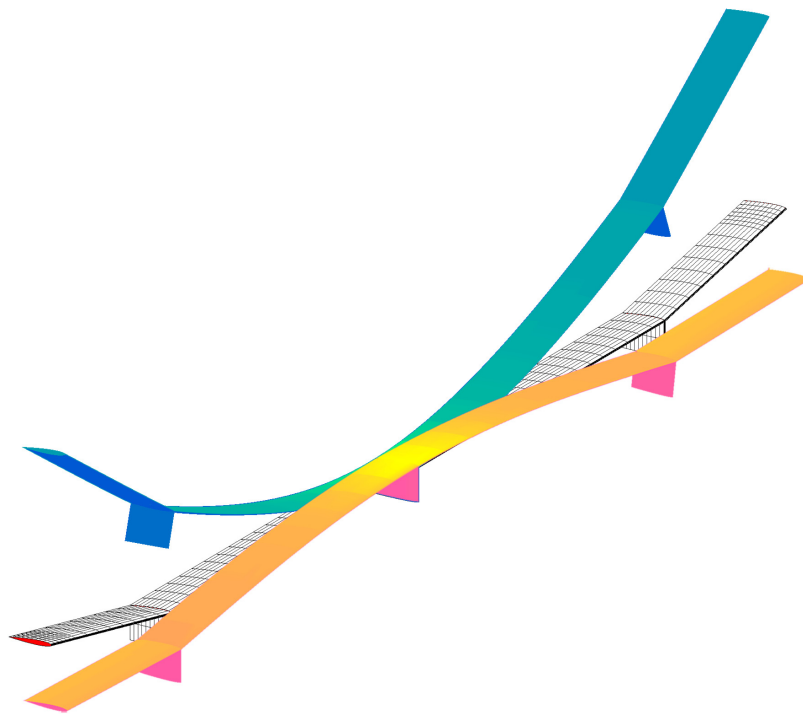


Figure 5.64: Vehicle deformation at 30 seconds with 8-s gust (golden: 30s with 8-s gust; green: trimmed steady state; frame: undefomed)

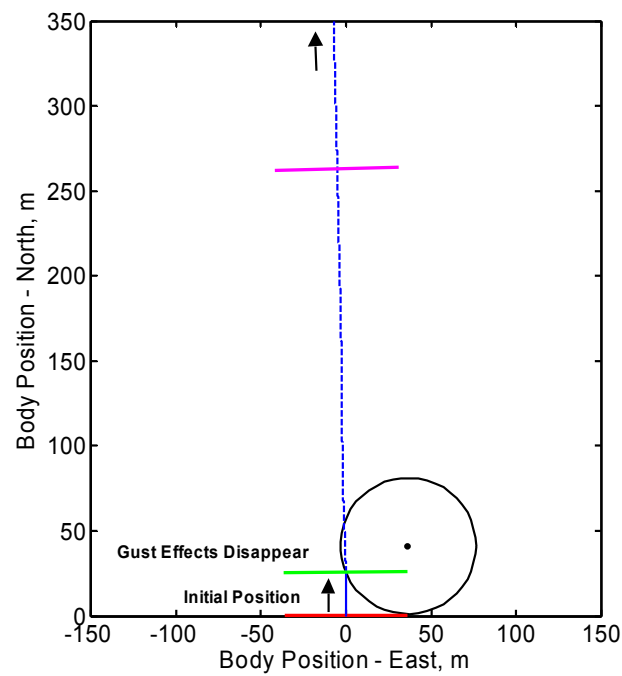


Figure 5.65: Flight path of the Flying-Wing with 2-s gust duration

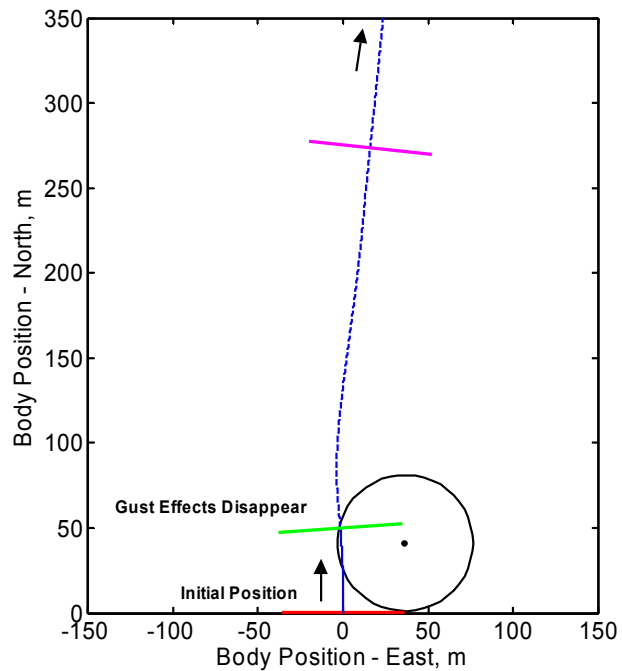


Figure 5.66: Flight path of the Flying-Wing with 4-s gust duration

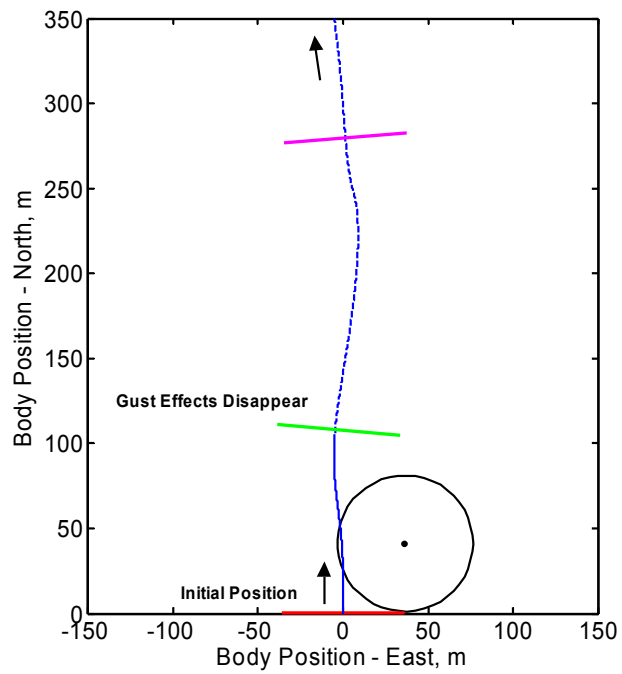


Figure 5.67: Flight path of the Flying-Wing with 8-s gust duration

Figures 5.65 to 5.67 show the flight path for the three different gust durations from a top view. For all cases, the initial position of the vehicle is represented at the bottom center position ($t = 0$ s). Since the gust cases have different durations, their ending point is also indicated in the figures by an appropriate label (“Gust Effects Disappear”). For the simulated cases here, the gust ending time spans a range of vehicle positions within the gust region. The upper line normal to the trajectory (after gust effects disappear is shown with a dashed line) indicates the vehicle position at 20 seconds. From here, one can see the different positions and orientations of the vehicle when it flies in the calm air after gust effects disappear.

5.7.2 Effects of Stall

Another interesting observation can be made when examining the results after 25 seconds. The response does not follow the same tendency as that before then. This is because at approximately 25 seconds the different wing stations exceed the stall angle of attack, changing the vehicle response. The effects of stall on the vehicle can be assessed by turning off the stall effects and comparing the results with and without stall effects. Keeping only the 10-m/s center amplitude and 4-s duration gust case, results are presented for vehicle responses considering stall on and off. With stall effects turned on, the aerodynamic loads on the airfoil are not continuous before and after the moment of stall (see Figs. 5.68 and 5.69). The discontinuity results in reductions in loads and the corresponding mid span bending curvature, as shown in Fig. 5.70. Although there is a sudden drop in lift at around 28 s, the transient loads excite the vehicle to large deformations and eventually large root strains. The configuration has an unstable phugoid mode that exacerbates the transient response and reaches higher bending curvatures levels. The impact of stall on vehicle response is illustrated in Figs. 5.71 to 5.76. The difference after 28 seconds can be clearly seen from those plots, where stall leads to an increase in plunging motion (Fig. 5.73) and pitching angle (Fig. 5.75). Therefore, stall effects can have a significant impact on the trajectory and attitude predictions.

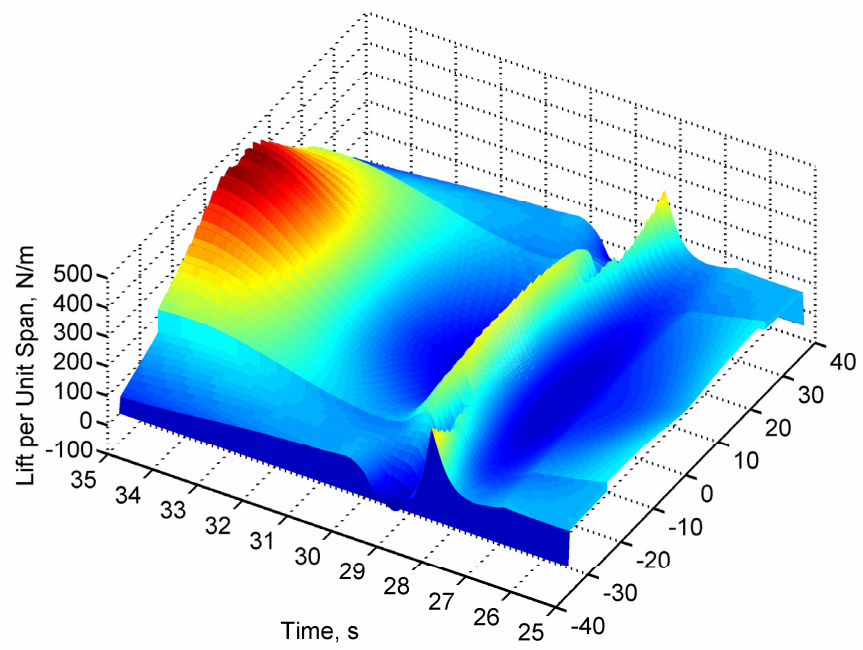


Figure 5.68: Lift distribution on the wings from 25 to 35 seconds with stall effects

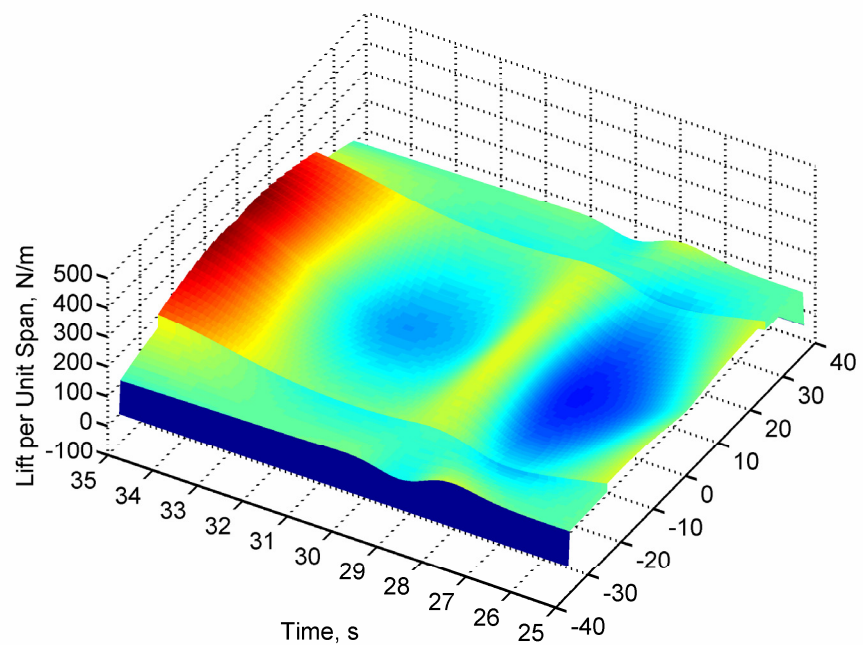


Figure 5.69: Lift distribution on the wings from 25 to 35 seconds without stall effects

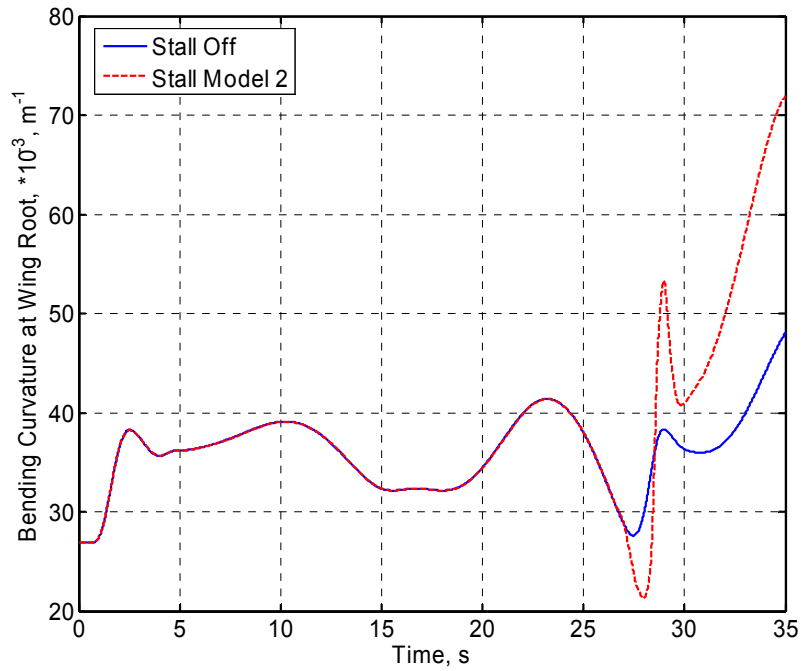


Figure 5.70: Stall effects on bending curvature at the mid span location when vehicle is subjected to 10-m/s center amplitude and 4-s duration gust

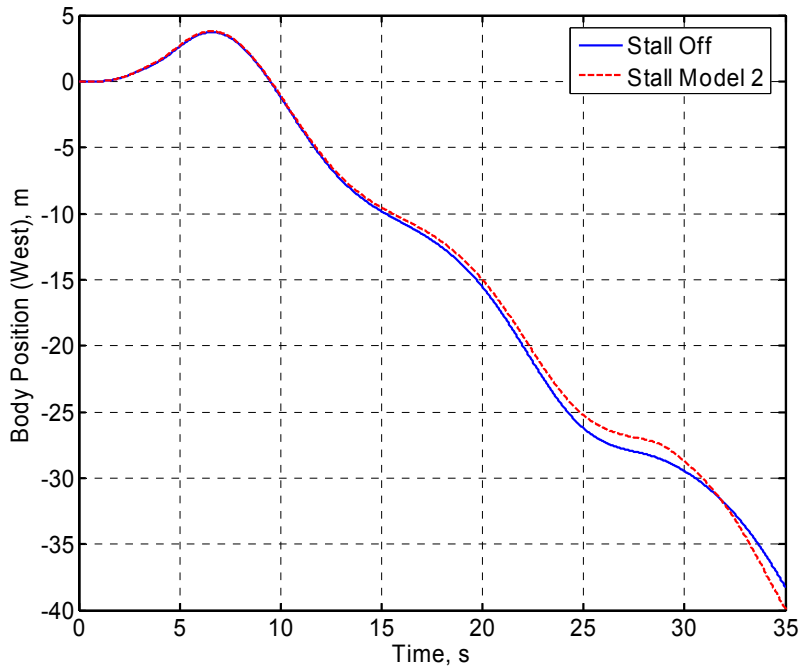


Figure 5.71: Stall effects on body position (west) when vehicle is subjected to 10-m/s center amplitude and 4-s duration gust

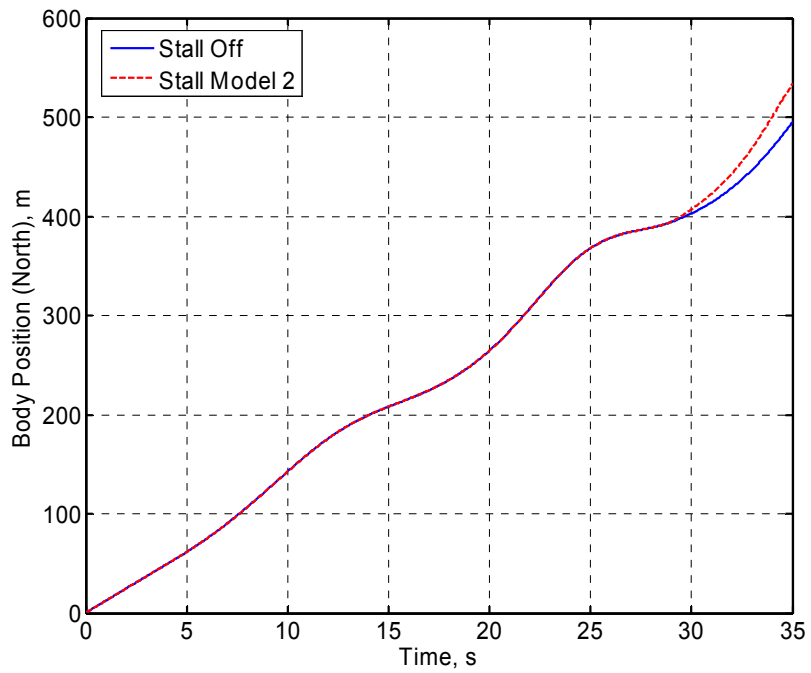


Figure 5.72: Stall effects on body position (north) when vehicle is subjected to 10-m/s center amplitude and 4-s duration gust

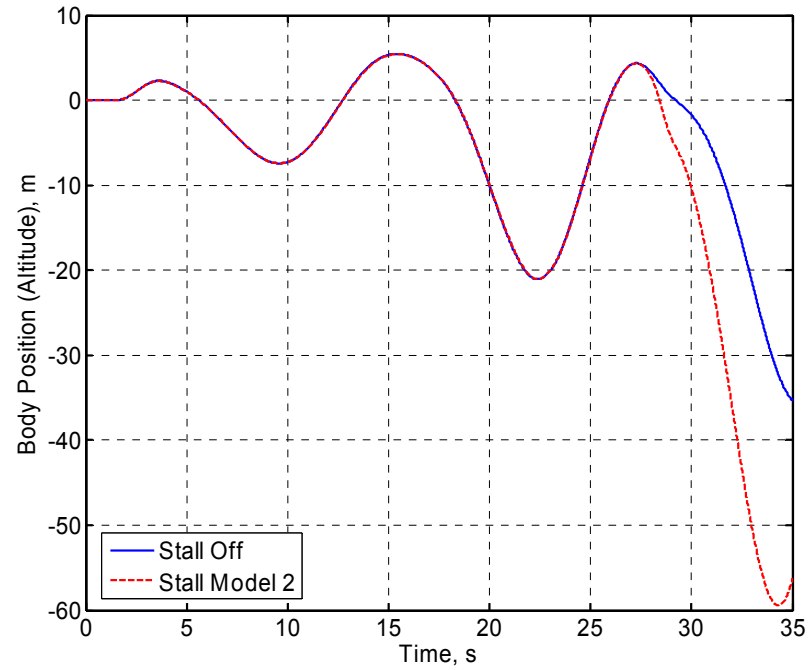


Figure 5.73: Stall effects on body position (altitude) when vehicle is subjected to 10-m/s center amplitude and 4-s duration gust

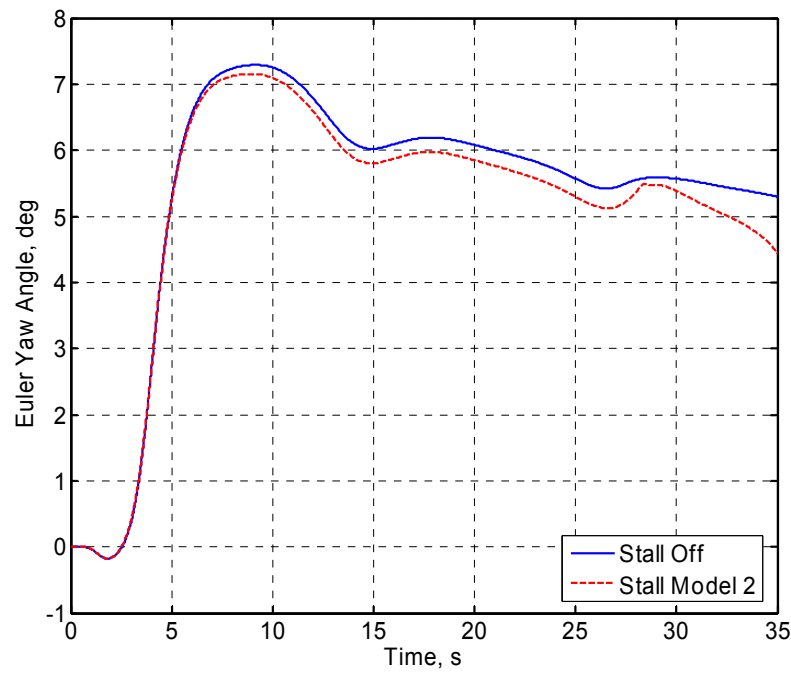


Figure 5.74: Stall effects on body Euler angle (yaw) when vehicle is subjected to 10-m/s center amplitude and 4-s duration gust

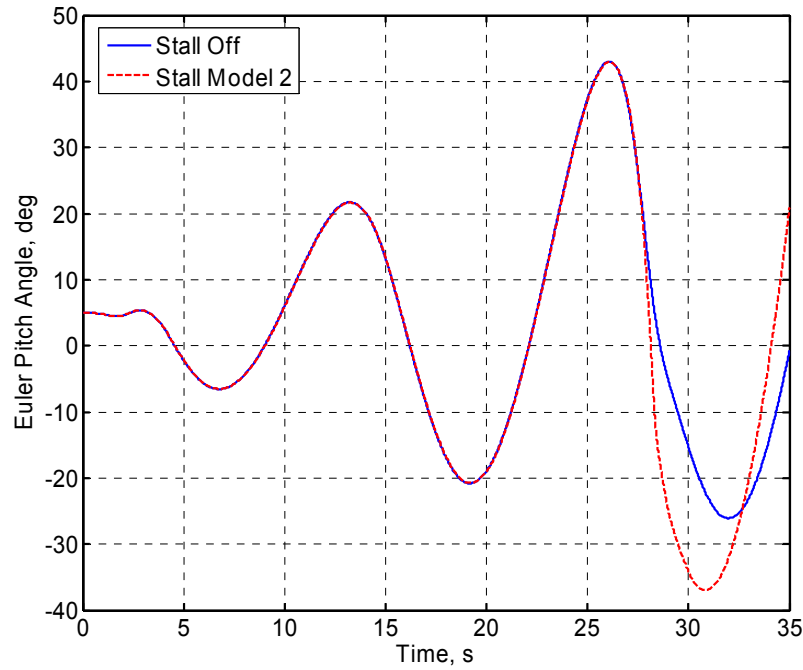


Figure 5.75: Stall effects on body Euler angle (pitch) when vehicle is subjected to 10-m/s center amplitude and 4-s duration gust

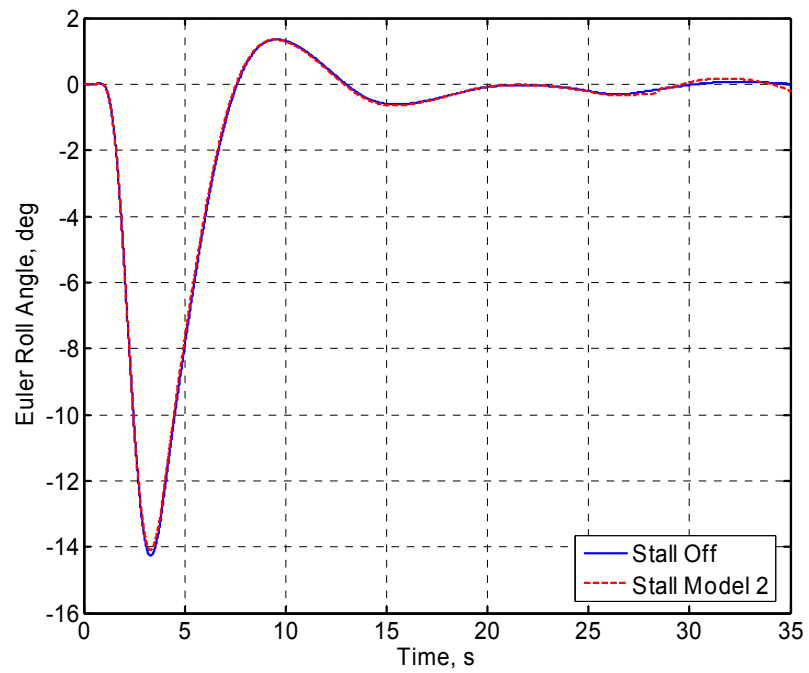


Figure 5.76: Stall effects on body Euler angle (roll) when vehicle is subjected to 10-m/s center amplitude and 4-s duration gust

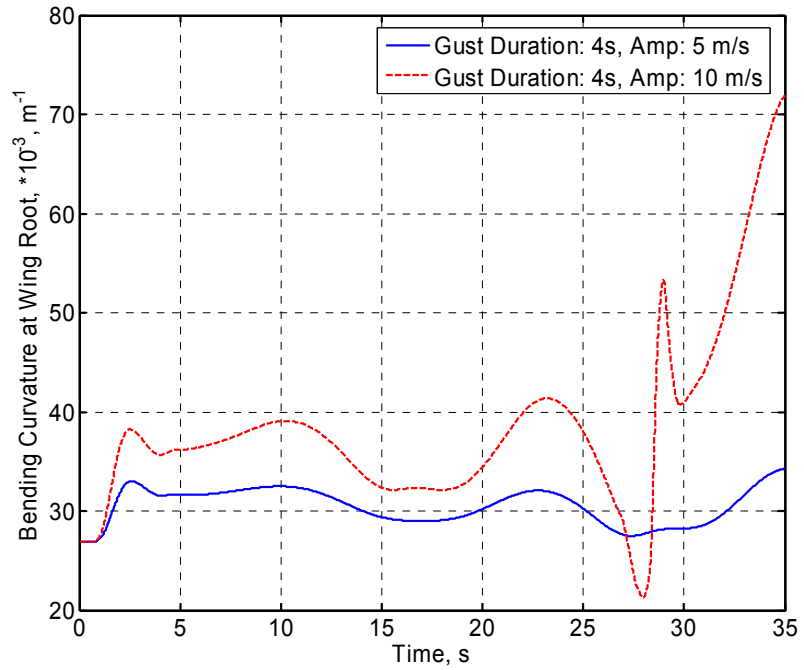


Figure 5.77: Effects of gust amplitude on bending curvature at the mid span location

5.7.3 Effects of Gust Amplitudes

Different gust amplitudes will have different effects on the vehicle response. In the present study, a similar gust perturbation with maximum center amplitude of 5 m/s is applied and the results are compared with the 10 m/s as used previously. Note that both gust scenarios have the same duration of 4 seconds. Figure 5.77 presents the comparison of bending curvature at the vehicle mid span station. It shows that the two cases have similar responses before 25 seconds, although with values directly proportional to the gust magnitude. However, the bending curvature of the 5-m/s gust response shows a more regular pattern up to 35 seconds, while the 10-m/s gust response shows an increase in bending curvature after an initial sudden reduction right after 25 seconds. This variation is related with stall effects as discussed previously. However, the absence of the sudden reduction in the 5-m/s gust case does not mean there will not be any stall happening. Since the phugoid mode of the vehicle is unstable, reinforced by the responses shown in Figs. 5.80 and 5.82, the angle of attack will eventually grow to reach stall and a similar outcome to the 10-m/s gust response is anticipated.

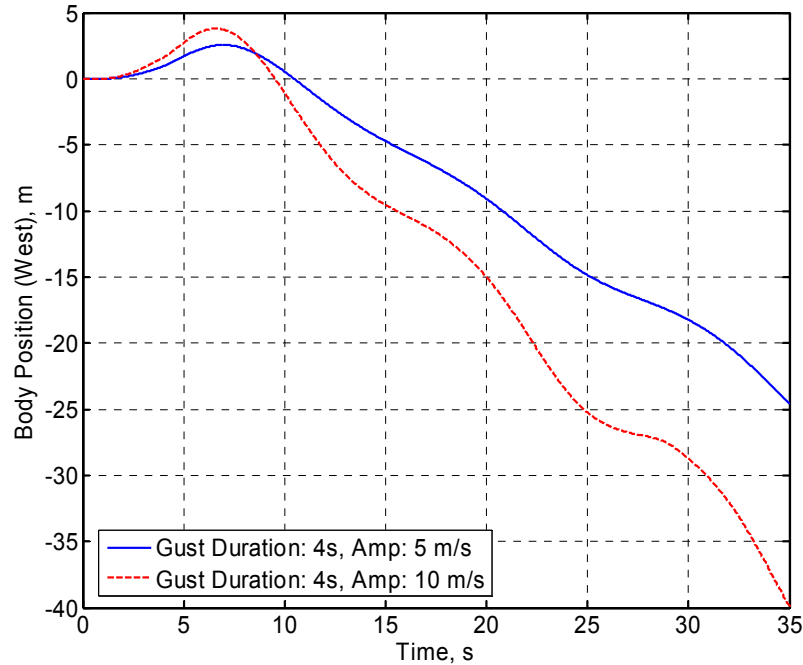
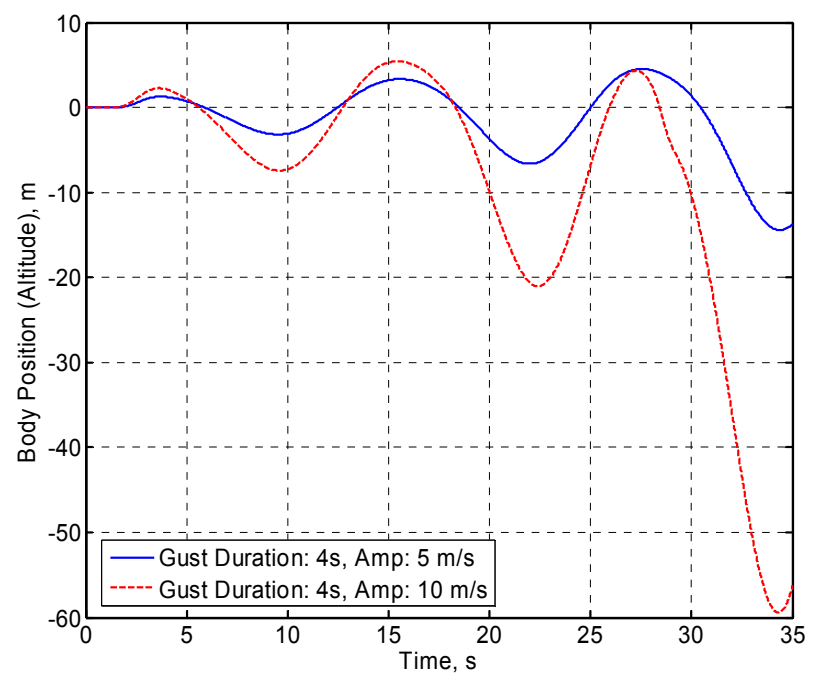
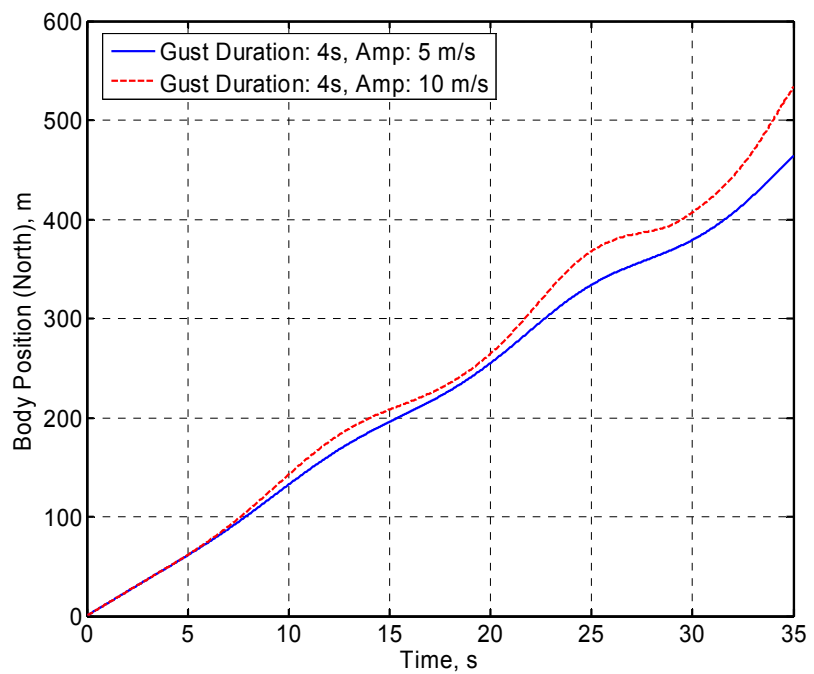


Figure 5.78: Effects of gust amplitude on body position (West)



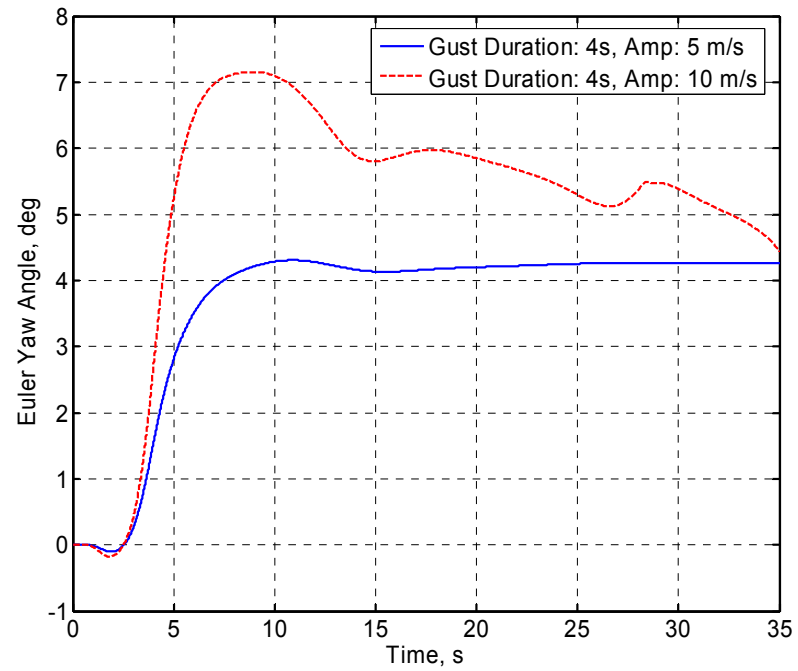


Figure 5.81: Effects of gust amplitude on body Euler angle (Yaw)

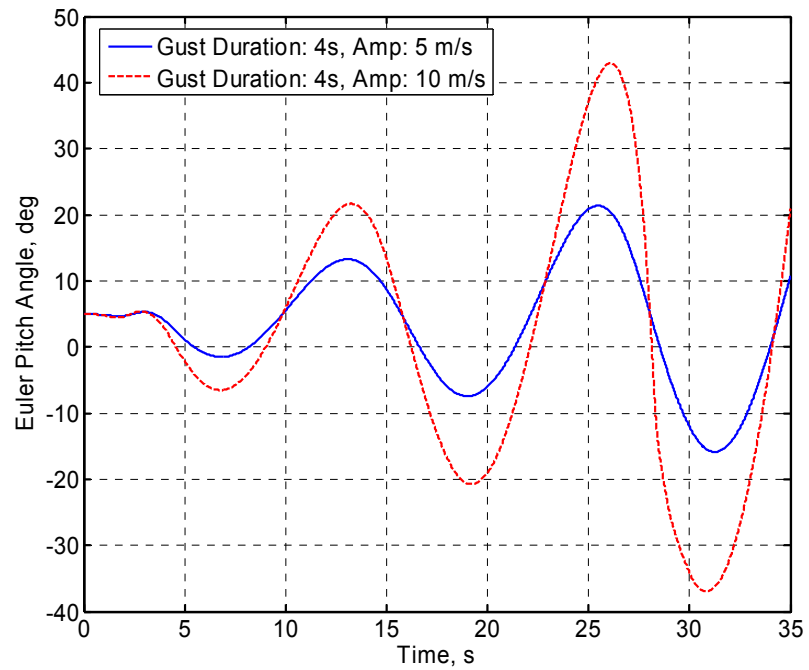


Figure 5.82: Effects of gust amplitude on body Euler angle (Pitch)

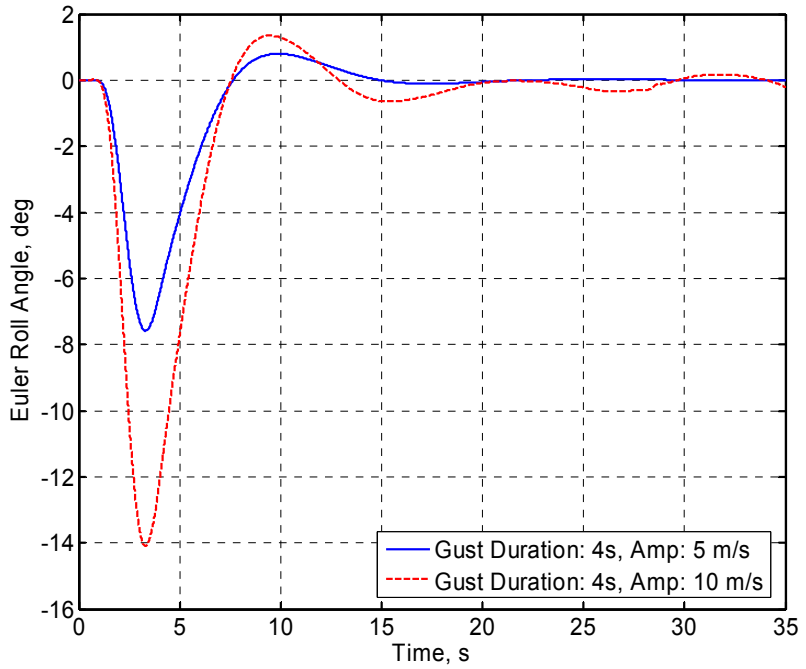


Figure 5.83: Effects of gust amplitude on body Euler angle (Roll)

5.7.4 Effects of Skin Wrinkling

In this section, the effects of skin wrinkling on the gust response are investigated. From preliminary simulations, the region most likely to reach higher curvature is located at the mid span (wing root). Post-wrinkling torsional stiffness reductions are selected as 20% (TSR 1) and 40% (TSR 2) of the original one for this study. As discussed before, the threshold point between the two torsional stiffness states is determined by the corresponding flat bending curvature. The critical flat bending curvature is postulated to be 0.02955 m^{-1} (CFBC 1), which is 10% higher than the bending curvature of the fully-loaded vehicle at level flight in calm air. Gust disturbance with 5-m/s center amplitude and 4-s duration is used.

The bending and twist curvatures at the wing root are compared in Figs 5.84 and 5.85, respectively. As one can see from the plots, the torsional stiffness changes accordingly when the threshold point of the bending curvature is reached, which results in the jump (up and down) of the twist curvature.

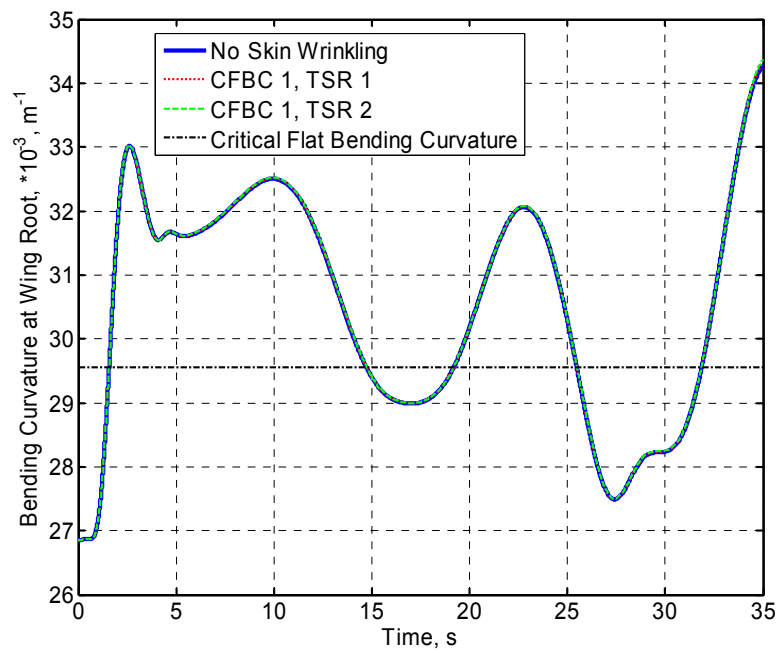


Figure 5.84: Effects of skin wrinkling on bending curvature at wing root when vehicle is subjected to 5-m/s center amplitude and 4-s duration gust

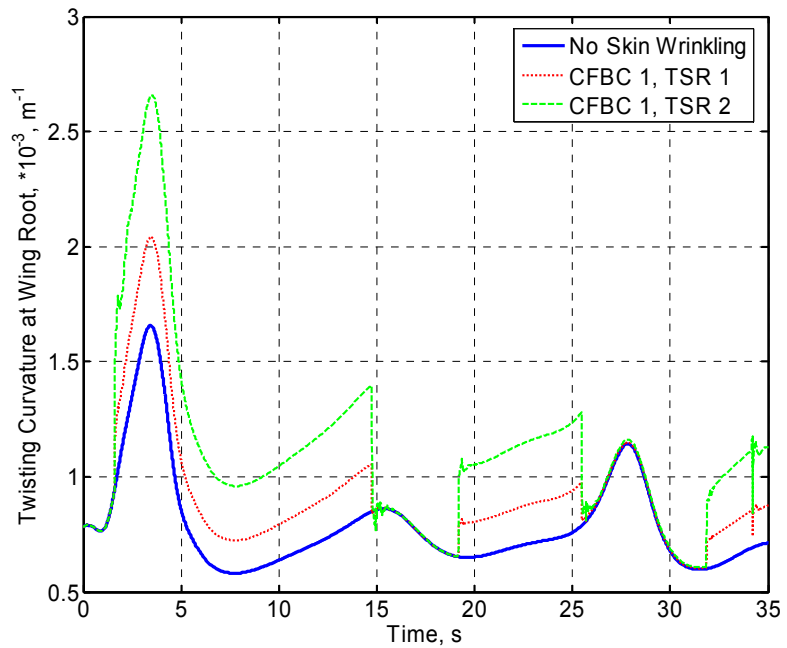


Figure 5.85: Effects of skin wrinkling on twist curvature at wing root when vehicle is subjected to 5-m/s center amplitude and 4-s duration gust

Figures 5.86 to 5.88 show some of the vehicle responses subject to wing skin wrinkling. Skin wrinkling mainly affects the lateral motion and the yaw angle of the body. If the torsional stiffness reduces to 60% of nominal value when skin wrinkles, the difference of lateral displacement at the end of 35 seconds is about 2.38 m, which is about 9.71% of the lateral displacement when skin wrinkling is not considered. The corresponding difference in yaw angle is about 0.33° , which is approximately 7.71% of the yaw angle when skin wrinkling is not considered. For the other responses, the effects of skin wrinkling are very small.

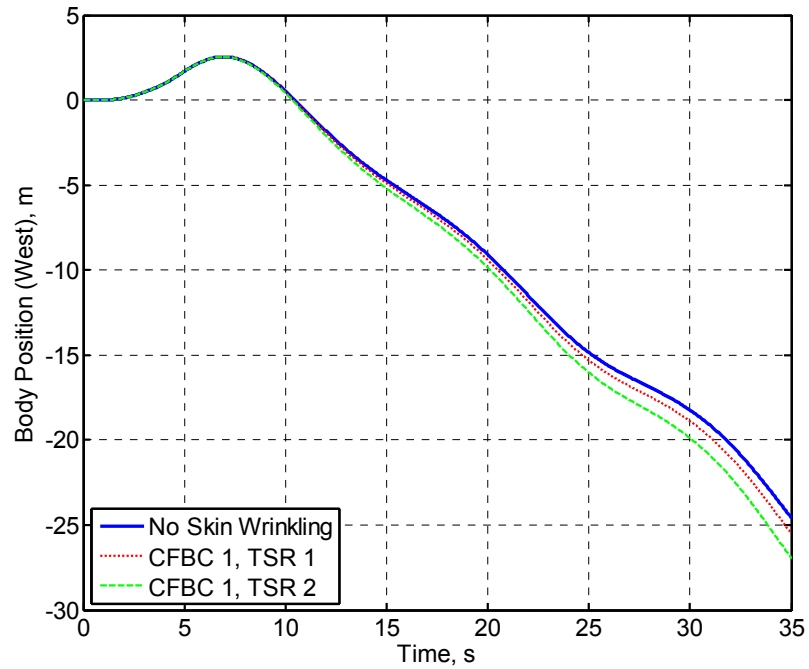


Figure 5.86: Effects of skin wrinkling on body position (west) when vehicle is subjected to 5-m/s center amplitude and 4-s duration gust

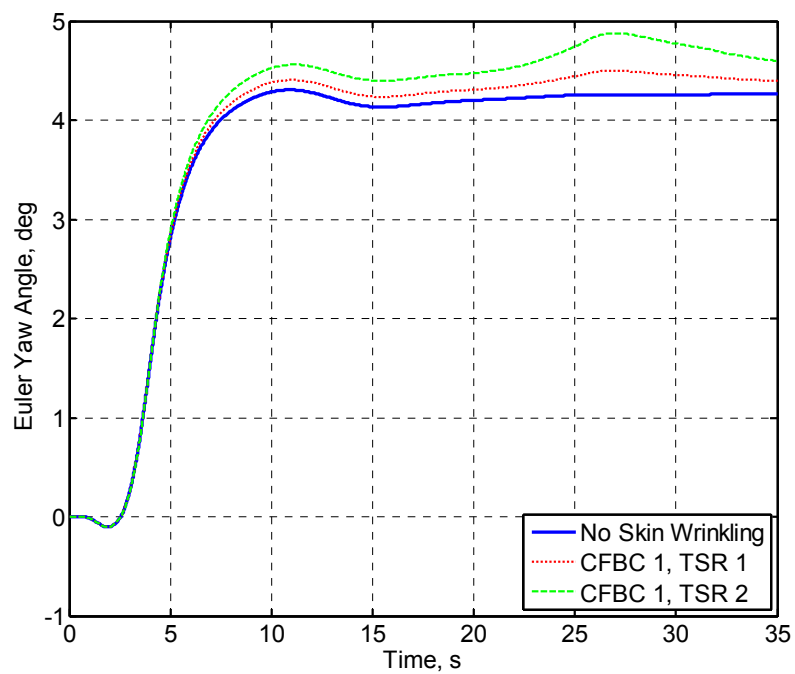


Figure 5.87: Effects of skin wrinkling on body Euler angle (yaw) when vehicle is subjected to 5-m/s center amplitude and 4-s duration gust

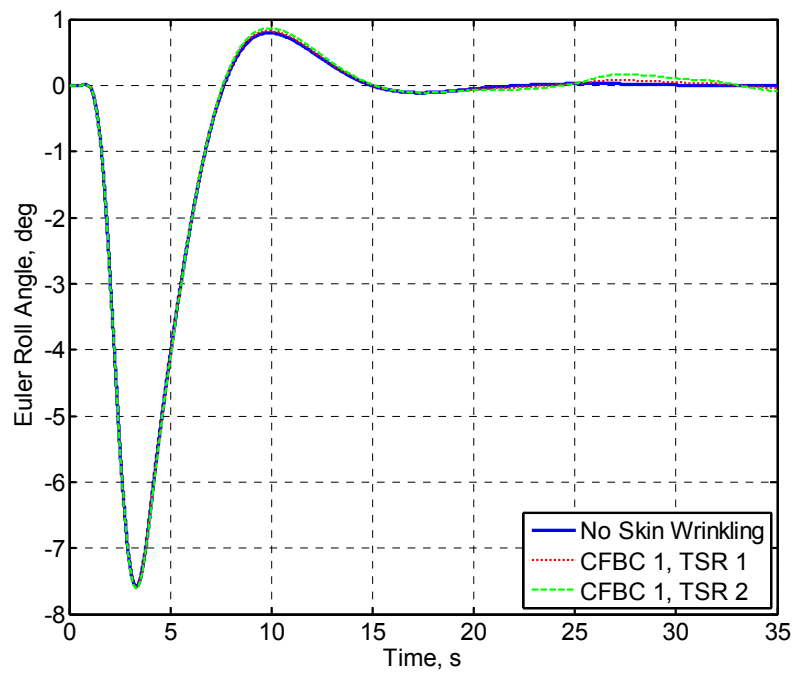


Figure 5.88: Effects of skin wrinkling on body Euler angle (roll) when vehicle is subjected to 5-m/s center amplitude and 4-s duration gust

CHAPTER VI

Conclusions and Recommendations

This chapter first summarizes the main accomplishments of this dissertation. Conclusions are then presented from results of the numerical analysis. Finally, some recommendations for future studies and improvements are made.

6.1 Summary of the Theoretical Formulation Developments

The main objective of this work was to model and analyze the coupled nonlinear aeroelasticity and flight dynamics of complete flexible aircraft. Four highly flexible aircraft configurations were studied in the current work, three of which originated from the ISR SensorCraft concepts, while the last one was a Helios-like highly flexible Flying-Wing. A geometrically nonlinear, strain-based formulation, which can capture the large deformations of slender structures, was used for the structural modeling. Previous to this study, other researchers modeled the wings and horizontal tails of an aircraft as flexible components, while the fuselage and vertical tails were treated as rigid bodies. To explore the potential effects of flexibility from different members on aircraft stability and performance, modeling of fully flexible vehicles becomes necessary. In the structural analysis, split beam systems are required as long as all vehicle members are model as slender beams. A split beam system consists of multiple beam members with some of them extended from others. The new modeling capability was achieved by introducing new kinematic relationships.

Among the configurations analyzed in this dissertation, the Joined-Wing configuration is the most unconventional one, since the front and aft wings join each other at a common point. The modeling of the joint is critical for the Joined-Wing configuration, yet it needs some special treatment due to the nature of the strain-based formulation that is used for structural modeling. The Lagrange Multiplier Method was used to model the relative nodal displacement constraints. With the same approach, absolute nodal displacement constraints can also be accurately modeled. The latter is generally not important for the modeling of aircraft. However, it completes the beam modeling capability. With the Lagrange Multiplier Method implemented, the differential equations of motion were augmented with a set of algebraic equations.

There are many other nonlinear aspects that should be considered when modeling and analyzing the flexible aircraft. This dissertation addressed some of them that influence the aeroelastic characteristics of the configurations analyzed in the current study. Formulations for nonlinear follower loads and bilinear torsional stiffness were developed and implemented.

Gust perturbation has been recognized as a crucial loading case for the highly flexible Helios-like Flying-Wing aircraft. To study the gust responses, a formulation of temporal- and spatial-distributed discrete gust model was seamlessly incorporated into the time simulation scheme. The implementation is general to enables the formulation to accommodate future gust models in time-domain analysis.

For the highly flexible vehicles, their slender members may have very low natural frequencies, whose deformations may couple with the rigid body motion of the vehicle. Therefore, the necessity of flutter analysis with rigid body motions (free flight), in addition to the constrained flutter only, was emphasized. Such a flutter analysis was developed based upon the coupled nonlinear aeroelastic and flight dynamic equations. To determine the flutter boundary, these nonlinear equations were linearized about each steady state, and the eigenvalues of the state-space form of those linearized equations were evaluated. With the same formulation, analyses of the constrained flutter and dynamic flight stability of an aircraft can be performed, by constraining different rigid-body degrees of freedom.

All these theoretical improvements were numerically implemented in the University of Michigan's Nonlinear Aeroelastic Simulation Toolbox (UM/NAST).

6.2 Conclusion from Numerical Studies

Numerical analyses were conducted on four highly flexible aircraft models: Single-Wing, Joined-Wing, Blended-Wing-Body, and Flying-Wing configurations.

In regard to the unique problem of loss of bending stiffness in the aft wing of the particular Joined-Wing configuration studied here, preliminary results indicated that the added flexible fuselage decreased the critical speed, while adding the flexibility of the vertical tail increased it. Since the different models were only trimmed for straight level flight, the other load factor points may represent a very different solution in terms of vehicle c.g. forces and moments. Further studies would be necessary to better understand the implications of the flexibility of the fuselage and vertical tail on the static instability of the vehicle.

The induced flexibility of the fuselage and tails of the Single-Wing configuration did not significantly modify the wing flutter, unless the tail fluttered first, which occurred when the tail was very flexible. Therefore, it is necessary to comprehensively consider the component flexibility when analyzing the stability boundary of highly flexible vehicles.

The flutter boundaries in free-flight and with constrained rigid-body motions were both studied. Due to the flexibility, the oscillations of long slender wings couple with the vehicle rigid-body motions. This results in different flutter boundaries between constrained and unconstrained vehicles. According to the current study, the relative magnitude of these two boundaries could change at different altitudes. Therefore, wind tunnel flutter studies may have limited usefulness if free flight is not reproduced.

Parametric studies were performed to explore the variation characteristics of the both flutter boundaries with respect to the change in wing stiffness. For the particular Blended-Wing-Body configuration studied here, the unstable mode shape for free flight

flutter was a coupled plunging and pitching of the rigid body and the first out-of-plane bending and torsion of the wings. Therefore, changes of wing out-of-plane bending and torsional stiffness had a significant impact on the flutter boundary in free flight. On the other hand, the in-plane bending stiffness had negligible effects on the flutter in free flight, while it impacted significantly the flutter with constrained rigid body motions.

The Joined-Wing configuration was more susceptible to the induced flexibility of the fuselage and tail in terms of roll performance. For this type of vehicles with wing and tail members structurally coupled, the flexibility brings significant oscillations to the roll responses and reduces roll angles. As expected, the induced flexibility of the fuselage and tails of the Single-Wing configuration had very limited impact on its roll performance due to the weak structural coupling.

A detailed study was conducted of the dynamic response of a highly flexible Flying-Wing configuration previously presented in the literature. Effects of gust, stall, and wing skin wrinkling were evaluated for this particular numerical example.

The sample vehicle was trimmed at different payload conditions. Linear stability analysis was performed by solving the linearized system of equations at trimmed conditions. From it, the phugoid mode eventually became unstable with the increased payload. The short period mode was purely real for the range of payloads considered. Fully nonlinear time-marching simulation was performed with an initial flap perturbation from trim condition. The unstable phugoid mode was clearly excited, which compromises the performance and integrity of the vehicle.

Vehicle response to gust was analyzed for different gust amplitudes and duration. As expected, flight path, vehicle attitude, and structural motion were impacted by the presence of gust. The disturbed flight path could deviate from the gust center. However, the after-gust responses may develop differently with different initial gust durations, especially the flight path and yaw angles.

Furthermore, the gust perturbation may excite the phugoid mode of the vehicle. In case the phugoid mode is unstable (*e.g.*, the Flying-Wing configuration studied here with full payload), this may result in uncontrollable diverged vehicle motions when the gust

perturbation is finite. The large plunging and pitching motions of the vehicle with corresponding large elastic deformations also resulted in high instantaneous angles of attack on some stations along the wing, which resulting in local stall. The effects of stall had a significant impact on transient responses of the wing and can alter the vehicle flight behavior. Finally, the skin wrinkling associated with the wing torsional stiffness showed to mainly affect the motions of the vehicle in the lateral direction. For the other responses, the effects of skin wrinkling were small based on the parameters chosen for the numerical study.

6.3 Key Contributions of this Dissertation

The key contributions of this dissertation can be summarized as follows.

1.) Complete kinematic relationships of the strain-based beam formulation were developed such that split beam systems can be modeled with the formulation in addition to single beam systems that were implemented in previous work. With the new kinematic relationships, fully flexible aircraft were structurally modeled as an assemblage of slender beams.

2.) The absolute and relative nodal displacement constraints were introduced in this strain-based formulation through the Lagrange Multiplier Method. The formulation of relative constraints was applied for the modeling of the Joined-Wing configuration with front and aft wings meeting each other. The motions of a fully flexible vehicle with additional nodal displacement constraints were then governed by a set of differential-algebraic equations.

3.) Skin wrinkling effects were modeled through bilinear stiffness representation. This issue is dependent on the wing construction technique and was motivated by the Helios prototype construction.

4.) A frequency-domain stability analysis formulation with nonlinear coupled rigid body and elastic degrees of freedom was developed and implemented based on the

linearized system equations. This provides a very effective computational way of determining the (nonlinear) flutter boundary.

5.) With the fully flexible models, the impact of flexibility of fuselage and vertical tail on aircraft stability and roll performance could be assessed.

In order to achieve these key contributions, other modeling enhancement was made to the current formulation, including the implementation of a temporal- and spatial-distributed discrete gust model, the modeling of follower forces for engine thrust, and different simplified stall models.

6.4 Recommendations for Future Work

The current numerical framework may be used for conducting fundamental modeling and analysis of HALE aircraft. Efforts can be made to develop a design optimization framework, which may facilitate the design process. In case gradient-based optimization schemes are used, analytical solutions for the sensitivities of the aeroelastic and flight dynamic responses with respect to design variables would be required.

Another improvement is about propulsion modeling. In the current work, engine thrust forces are modeled as static loads. No dynamic effects are considered, such as the gyroscopic effects. This would allow modeling the rotating propellers during vehicle deformation.

The aerodynamic formulation should be improved. In the current formulation, there is no consideration of the interference between the lifting surfaces, such as the front and aft wings and/or tail. However, it can have significant impact on vehicle trim and other performance. Also, the currently implemented aerodynamic theory is only valid for flight within subsonic range. The Prandtl-Glauert correction is used to account for compressibility effects. Modeling at high subsonic range, with the consideration of local transonic effects may be useful for certain applications. Furthermore, the current aerodynamics only includes simplified stall models. To understand the actual airfoil stall

characteristics, a more complete stall model that accounts for different Reynolds numbers may be required.

Since the gust response is a major concern for highly flexible aircraft, the gust model should be further developed. The current work only applies discrete gust models for time simulations. An improvement can be made by implementing, for example, the Dryden gust models. Furthermore, a stochastic gust model for analysis can be used, instead of a discrete one. This may be completed by using frequency-domain random analysis. Gusts can be introduced into the system by using Power Spectrum Density (PSD) functions, instead of time domain amplitudes.

Finally, further improvements could be made on the numerical analysis environment – UM/NAST. Although the integration scheme of the nonlinear equations of motion was not a focus of this dissertation, limitations there were observed. The numerical integration schemes available in UM/NAST were introduced in Refs. [15] and [79] – Trapezoid (explicit) method and Modified Generalized- α (implicit) method. The first one is computationally inexpensive, but cannot provide any control of residuals during the integration, which can lead to unbounded numerical errors for long time simulations. The latter one may control the integration error within a user defined tolerance, which provides good numerical stability for long-term simulations. However, this method is computationally expensive. In regard to the implicit method, one may want to increase the size of time steps to reduce the overall simulation time. However, this may increase the sub-iterations required for convergence within each time step, resulting in a longer computational time. Furthermore, for a specific nonlinear time simulation, the system may demonstrate different levels of nonlinearity at different time intervals. Due to the above reasons, a constant time step may not be suitable for the whole time range of integration. An effective way is to develop an algorithm that may determine the time step according to the current nonlinearity. The predefined time step can therefore be modified accordingly, such that the computational accuracy and efficiency are both satisfied. Moreover, the combination of explicit and implicit methods could be another solution to improve computational efficiency while keeping the accuracy. The implicit method can

be used to replace the explicit one at the time step when the integration tends to lose its stability, such as when large-scale state changes happen.

APPENDICES

APPENDIX A

Derivatives of Aerodynamic Loads

The derivatives of aerodynamic forces and moments with respect to the variables are important prerequisite of linearizing the system equations of motion, and further stability analysis. Previous implementation^[15, 79] was not complete and showed some discrepancies with the derivatives calculated based on the finite difference method, especially the derivatives with respect to body velocity and wing strain. The discrepancies impacted the prediction of vehicles flutter boundary in free flight condition. The complete expressions for these derivatives are shown below.

A.1 Rotation of Aerodynamic Forces and Moments

The aerodynamic loads in the local aerodynamic frame (a_l) are given in Eq. (2.101) and repeated as Eq. (A.1)

$$\begin{aligned}
 L &= \pi\rho b^2 (-\ddot{z} + \dot{y}\dot{\alpha} - d\ddot{\alpha}) + 2\pi\rho b\dot{y}^2 \left[-\frac{\dot{z}}{\dot{y}} + \left(\frac{1}{2}b - d \right) \frac{\dot{\alpha}}{\dot{y}} - \frac{\lambda_0}{\dot{y}} \right] + 2\pi\rho b c_l \dot{y}^2 \delta \\
 M &= 2\pi\rho b^2 \left(-\frac{1}{2}\dot{y}\dot{z} - \frac{1}{2}d\dot{y}\dot{\alpha} - \frac{1}{2}\dot{y}\lambda_0 - \frac{1}{16}b^2\ddot{\alpha} \right) + 2\pi\rho b^2 c_4 \dot{y}^2 \delta \\
 D &= -2\pi\rho b \left(\dot{z}^2 + d^2\dot{\alpha}^2 + \lambda_0^2 + 2d\dot{\alpha}\dot{z} + 2\lambda_0\dot{z} + 2d\dot{\alpha}\lambda_0 \right) \\
 &\quad - 2\pi\rho b \left[c_l \dot{y}\dot{z}\delta + (dc_l + bg_2)\dot{y}\dot{\alpha}\delta + c_l \dot{y}\lambda_0\delta + \frac{1}{2}bg_2\ddot{z}\delta + \left(\frac{1}{2}bdg_2 - \frac{1}{4}b^2g_3 \right) \ddot{\alpha}\delta \right]
 \end{aligned} \tag{A.1}$$

where the airfoil motion variables are resolved in the frame aligned with the zero lift line (a_0).

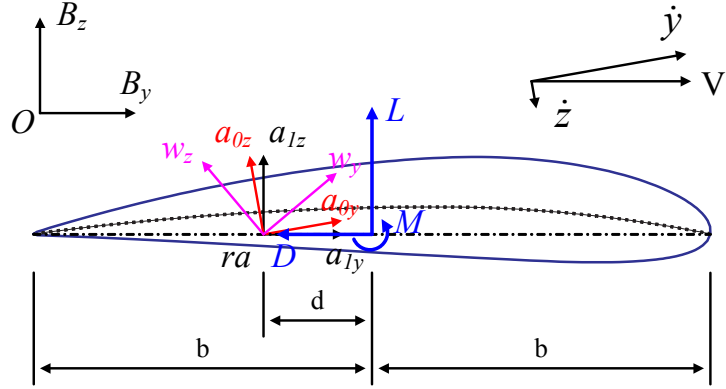


Figure A.1: Rotation of aerodynamic loads

The aerodynamic loads obtained in the local aerodynamic frame are rotated into the body frame (B), since the equations of motion are resolved in this frame. The rotation is completed as follows

$$\begin{aligned} F^{aero} &= C^{Ba_l} \begin{bmatrix} 0 \\ D \\ L \end{bmatrix} = C^{Ba_0} C^{a_0 a_l} \begin{bmatrix} 0 \\ D \\ L \end{bmatrix} = C^{Bw} C^{wa_0} C^{a_0 a_l} \begin{bmatrix} 0 \\ D \\ L \end{bmatrix} \\ M^{aero} &= C^{Ba_l} \begin{bmatrix} M_x \\ 0 \\ 0 \end{bmatrix} = C^{Ba_0} C^{a_0 a_l} \begin{bmatrix} M_x \\ 0 \\ 0 \end{bmatrix} = C^{Bw} C^{wa_0} C^{a_0 a_l} \begin{bmatrix} M_x \\ 0 \\ 0 \end{bmatrix} \end{aligned} \quad (\text{A.2})$$

where

$$M_x = M + dL \quad (\text{A.3})$$

In the above equations, $C^{a_0 a_l}$ is the rotation matrix from the local aerodynamic frame (a_l) to zero lift line (a_0), which is a function of \dot{y} and \dot{z} . It is given by

$$C^{a_0 a_l} = \begin{bmatrix} 1 & 0 & 0 \\ 0 & \cos \tilde{\alpha} & -\sin \tilde{\alpha} \\ 0 & \sin \tilde{\alpha} & \cos \tilde{\alpha} \end{bmatrix} \quad (\text{A.4})$$

where

$$\tilde{\alpha} = \tan^{-1}\left(-\frac{\dot{z}}{\dot{y}}\right) \quad (\text{A.5})$$

C^{wao} is the rotation matrix from the zero lift line to the wing (beam) reference frame (w), which is constant upon the vehicle initialization. C^{Bw} is the rotation matrix from the wing (beam) reference frame to the body frame (B), which is a function of strain, ε ,

$$C^{Bw} \equiv \begin{bmatrix} | & | & | \\ w_x(\varepsilon) & w_y(\varepsilon) & w_z(\varepsilon) \\ | & | & | \end{bmatrix} \quad (\text{A.6})$$

where w_x , w_y , and w_z are base vectors of the wing (beam) reference frame, resolved in the body frame.

The derivation of aerodynamic derivatives will basically follow the same process as described above, *i.e.*, the derivative will be first derived in the local aerodynamic frame, which is then rotated into the body frame.

A.2 Derivatives in the Local Aerodynamic Frame

The first step is to take derivatives of aerodynamic loads with respect to the airfoil motion variables ($\ddot{z}, \ddot{\alpha}, \dot{y}, \dot{z}, \dot{\alpha}$), which are given in Eqs. (A.7) to (A.9). Note that the inflow state λ_0 is an independent variable, and the derivatives with respect to it can be found in Ref. [79].

$$\begin{aligned}
\frac{\partial L}{\partial \ddot{z}} &= -\pi \rho b^2 \\
\frac{\partial L}{\partial \ddot{\alpha}} &= -\pi \rho b^2 d \\
\frac{\partial L}{\partial \dot{y}} &= -2\pi \rho b [\dot{z} - (b-d)\dot{\alpha} + \lambda_0 - 2c_1 \dot{y} \delta - c_2 \delta] \\
\frac{\partial L}{\partial \dot{z}} &= -2\pi \rho b \dot{y} \\
\frac{\partial L}{\partial \dot{\alpha}} &= 2\pi \rho b (b-d) \dot{y}
\end{aligned} \tag{A.7}$$

$$\begin{aligned}
\frac{\partial M_x}{\partial \ddot{z}} &= d \frac{\partial L}{\partial \ddot{z}} \\
\frac{\partial M_x}{\partial \ddot{\alpha}} &= d \frac{\partial L}{\partial \ddot{\alpha}} - \frac{1}{8} \pi \rho b^4 \\
\frac{\partial M_x}{\partial \dot{y}} &= d \frac{\partial L}{\partial \dot{y}} - 2\pi \rho b^2 \left(\frac{1}{2} \dot{z} + \frac{1}{2} d \dot{\alpha} + \frac{1}{2} \lambda_0 - 2c_4 \dot{y} \delta - c_5 \delta \right) \\
\frac{\partial M_x}{\partial \dot{z}} &= d \frac{\partial L}{\partial \dot{z}} - \pi \rho b^2 \dot{y} \\
\frac{\partial M_x}{\partial \dot{\alpha}} &= d \frac{\partial L}{\partial \dot{\alpha}} - \pi \rho b^2 d \dot{y}
\end{aligned} \tag{A.8}$$

$$\begin{aligned}
\frac{\partial D}{\partial \ddot{z}} &= -\pi \rho b^2 g_2 \delta \\
\frac{\partial D}{\partial \ddot{\alpha}} &= -\pi \rho b^2 \left(dg_2 - \frac{1}{2} bg_3 \right) \delta \\
\frac{\partial D}{\partial \dot{y}} &= -2\pi \rho b [c_1 \delta \dot{z} + (dc_1 + bg_2) \delta \dot{\alpha} + c_1 \delta \lambda_0] \\
\frac{\partial D}{\partial \dot{z}} &= -2\pi \rho b (2\dot{z} + 2d\dot{\alpha} + 2\lambda_0 + c_1 \delta \dot{y}) \\
\frac{\partial D}{\partial \dot{\alpha}} &= -2\pi \rho b [2d\dot{z} + 2d^2 \dot{\alpha} + 2d\lambda_0 + (dc_1 + bg_2) \delta \dot{y}]
\end{aligned} \tag{A.9}$$

where the definitions of c_i and g_i can be found in Ref. [79].

The relationships between airfoil motion variables ($\ddot{z}, \ddot{\alpha}, \dot{y}, \dot{z}, \dot{\alpha}$) and the independent variables ($\varepsilon, \dot{\varepsilon}, \ddot{\varepsilon}, \beta, \dot{\beta}$) need to be determined next. The linear and angular velocities resolved in the local aerodynamic frame are given as

$$\begin{bmatrix} \dot{x} \\ \dot{y} \\ \dot{z} \end{bmatrix} = \left(C^{wa_0} \right)^T \left(C^{Bw} \right)^T \left(U_{\infty} + J_{pe} \dot{\varepsilon} + J_{pb} \beta + w_{gust} \right)$$

$$\dot{\alpha} = e_l^T \left(C^{wa_0} \right)^T \left(C^{Bw} \right)^T \left(J_{\theta e} \dot{\varepsilon} + J_{\theta b} \beta \right) \quad (\text{A.10})$$

where U_{∞} is the free stream velocity. w_{gust} is the gust perturbation. J_{pe} , J_{pb} , $J_{\theta e}$, and $J_{\theta b}$ are the structural Jacobians, which have been correctly evaluated in Ref. [79]. e_l represents the unit vector along local x axis. Neglecting the time derivatives of structural Jacobians in the above equations, the linear and angular accelerations can be obtained as

$$\begin{bmatrix} \ddot{x} \\ \ddot{y} \\ \ddot{z} \end{bmatrix} = \left(C^{wa_0} \right)^T \left(C^{Bw} \right)^T \left(J_{pe} \ddot{\varepsilon} + J_{pb} \dot{\beta} \right)$$

$$\ddot{\alpha} = e_l^T \left(C^{wa_0} \right)^T \left(C^{Bw} \right)^T \left(J_{\theta e} \ddot{\varepsilon} + J_{\theta b} \dot{\beta} \right) \quad (\text{A.11})$$

The derivative of the rotation matrix C^{Bw} is given as

$$\frac{dC^{Bw}}{d\varepsilon} = \begin{bmatrix} | & | & | \\ \frac{dw_x}{d\varepsilon} & \frac{dw_y}{d\varepsilon} & \frac{dw_z}{d\varepsilon} \\ | & | & | \end{bmatrix} \quad (\text{A.12})$$

where $\frac{dw_x}{d\varepsilon}$, $\frac{dw_y}{d\varepsilon}$, and $\frac{dw_z}{d\varepsilon}$ are basic variables that may be obtained at each nonlinear steady state, according to the kinematics solver.

Partial derivatives of motion variables with respect to the strain (ε) are obtained by differentiating Eqs. (A.10) and (A.11).

$$\begin{bmatrix} \frac{\partial \dot{x}}{\partial \varepsilon} \\ \frac{\partial \dot{y}}{\partial \varepsilon} \\ \frac{\partial \dot{z}}{\partial \varepsilon} \end{bmatrix} = \left(C^{wa_0} \right)^T \frac{d(C^{Bw})^T}{d\varepsilon} (U_\infty + J_{pe} \dot{\varepsilon} + J_{pb} \beta + w_{gust})$$

$$\frac{\partial \dot{\alpha}}{\partial \varepsilon} = e_l^T \left(C^{wa_0} \right)^T \frac{d(C^{Bw})^T}{d\varepsilon} (J_{\theta e} \dot{\varepsilon} + J_{\theta b} \beta)$$
(A.13)

$$\begin{bmatrix} \frac{\partial \ddot{x}}{\partial \varepsilon} \\ \frac{\partial \ddot{y}}{\partial \varepsilon} \\ \frac{\partial \ddot{z}}{\partial \varepsilon} \end{bmatrix} = \left(C^{wa_0} \right)^T \frac{d(C^{Bw})^T}{d\varepsilon} (J_{pe} \ddot{\varepsilon} + J_{pb} \dot{\beta})$$

$$\frac{\partial \ddot{\alpha}}{\partial \varepsilon} = e_l^T \left(C^{wa_0} \right)^T \frac{d(C^{Bw})^T}{d\varepsilon} (J_{\theta e} \ddot{\varepsilon} + J_{\theta b} \dot{\beta})$$
(A.14)

Following the same method as the above, one may obtain the derivatives with respect to strain rate ($\dot{\varepsilon}$), strain acceleration ($\ddot{\varepsilon}$), body velocity (β), and body acceleration ($\dot{\beta}$), which are listed as Eqs. (A.15) to (A.22).

$$\begin{bmatrix} \frac{\partial \dot{x}}{\partial \dot{\varepsilon}} \\ \frac{\partial \dot{y}}{\partial \dot{\varepsilon}} \\ \frac{\partial \dot{z}}{\partial \dot{\varepsilon}} \end{bmatrix} = \left(C^{wa_0} \right)^T (C^{Bw})^T J_{pe}, \quad \frac{\partial \dot{\alpha}}{\partial \dot{\varepsilon}} = e_l^T \left(C^{wa_0} \right)^T (C^{Bw})^T J_{\theta e}$$
(A.15)

$$\begin{bmatrix} \frac{\partial \ddot{x}}{\partial \dot{\varepsilon}} & \frac{\partial \ddot{y}}{\partial \dot{\varepsilon}} & \frac{\partial \ddot{z}}{\partial \dot{\varepsilon}} \end{bmatrix} = [0 \quad 0 \quad 0], \quad \frac{\partial \ddot{\alpha}}{\partial \dot{\varepsilon}} = 0$$
(A.16)

$$\begin{bmatrix} \frac{\partial \dot{x}}{\partial \ddot{\varepsilon}} & \frac{\partial \dot{y}}{\partial \ddot{\varepsilon}} & \frac{\partial \dot{z}}{\partial \ddot{\varepsilon}} \end{bmatrix} = [0 \quad 0 \quad 0], \quad \frac{\partial \dot{\alpha}}{\partial \ddot{\varepsilon}} = 0$$
(A.17)

$$\begin{bmatrix} \frac{\partial \ddot{x}}{\partial \ddot{\varepsilon}} \\ \frac{\partial \ddot{y}}{\partial \ddot{\varepsilon}} \\ \frac{\partial \ddot{z}}{\partial \ddot{\varepsilon}} \end{bmatrix} = \left(C^{wa_0} \right)^T \left(C^{Bw} \right)^T J_{p\varepsilon}, \quad \frac{\partial \ddot{\alpha}}{\partial \ddot{\varepsilon}} = e_l^T \left(C^{wa_0} \right)^T \left(C^{Bw} \right)^T J_{\theta\varepsilon} \quad (\text{A.18})$$

$$\begin{bmatrix} \frac{\partial \dot{x}}{\partial \beta} \\ \frac{\partial \dot{y}}{\partial \beta} \\ \frac{\partial \dot{z}}{\partial \beta} \end{bmatrix} = \left(C^{wa_0} \right)^T \left(C^{Bw} \right)^T J_{pb}, \quad \frac{\partial \dot{\alpha}}{\partial \beta} = e_l^T \left(C^{wa_0} \right)^T \left(C^{Bw} \right)^T J_{\theta b} \quad (\text{A.19})$$

$$\begin{bmatrix} \frac{\partial \ddot{x}}{\partial \beta} & \frac{\partial \ddot{y}}{\partial \beta} & \frac{\partial \ddot{z}}{\partial \beta} \end{bmatrix} = [0 \ 0 \ 0], \quad \frac{\partial \ddot{\alpha}}{\partial \beta} = 0 \quad (\text{A.20})$$

$$\begin{bmatrix} \frac{\partial \dot{x}}{\partial \dot{\beta}} & \frac{\partial \dot{y}}{\partial \dot{\beta}} & \frac{\partial \dot{z}}{\partial \dot{\beta}} \end{bmatrix} = [0 \ 0 \ 0], \quad \frac{\partial \dot{\alpha}}{\partial \dot{\beta}} = 0 \quad (\text{A.21})$$

$$\begin{bmatrix} \frac{\partial \ddot{x}}{\partial \dot{\beta}} \\ \frac{\partial \ddot{y}}{\partial \dot{\beta}} \\ \frac{\partial \ddot{z}}{\partial \dot{\beta}} \end{bmatrix} = \left(C^{wa_0} \right)^T \left(C^{Bw} \right)^T J_{pb}, \quad \frac{\partial \ddot{\alpha}}{\partial \dot{\beta}} = e_l^T \left(C^{wa_0} \right)^T \left(C^{Bw} \right)^T J_{\theta b} \quad (\text{A.22})$$

With above partial derivatives, the derivatives of aerodynamic loads within the local aerodynamic frames, with respect to the independent variables can be completed as

$$\begin{aligned} \frac{\partial L}{\partial \varepsilon} &= \frac{\partial L}{\partial \ddot{z}} \frac{\partial \ddot{z}}{\partial \varepsilon} + \frac{\partial L}{\partial \ddot{\alpha}} \frac{\partial \ddot{\alpha}}{\partial \varepsilon} + \frac{\partial L}{\partial \dot{y}} \frac{\partial \dot{y}}{\partial \varepsilon} + \frac{\partial L}{\partial \dot{z}} \frac{\partial \dot{z}}{\partial \varepsilon} + \frac{\partial L}{\partial \dot{\alpha}} \frac{\partial \dot{\alpha}}{\partial \varepsilon} \\ \frac{\partial M_x}{\partial \varepsilon} &= \frac{\partial M_x}{\partial \ddot{z}} \frac{\partial \ddot{z}}{\partial \varepsilon} + \frac{\partial M_x}{\partial \ddot{\alpha}} \frac{\partial \ddot{\alpha}}{\partial \varepsilon} + \frac{\partial M_x}{\partial \dot{y}} \frac{\partial \dot{y}}{\partial \varepsilon} + \frac{\partial M_x}{\partial \dot{z}} \frac{\partial \dot{z}}{\partial \varepsilon} + \frac{\partial M_x}{\partial \dot{\alpha}} \frac{\partial \dot{\alpha}}{\partial \varepsilon} \\ \frac{\partial D}{\partial \varepsilon} &= \frac{\partial D}{\partial \ddot{z}} \frac{\partial \ddot{z}}{\partial \varepsilon} + \frac{\partial D}{\partial \ddot{\alpha}} \frac{\partial \ddot{\alpha}}{\partial \varepsilon} + \frac{\partial D}{\partial \dot{y}} \frac{\partial \dot{y}}{\partial \varepsilon} + \frac{\partial D}{\partial \dot{z}} \frac{\partial \dot{z}}{\partial \varepsilon} + \frac{\partial D}{\partial \dot{\alpha}} \frac{\partial \dot{\alpha}}{\partial \varepsilon} \end{aligned} \quad (\text{A.23})$$

$$\begin{aligned}\frac{\partial C^{a_0 a_I}}{\partial \dot{z}} &= \frac{dC^{a_0 a_I}}{d\tilde{\alpha}} \frac{\partial \tilde{\alpha}}{\partial \dot{z}} = \begin{bmatrix} 0 & 0 & 0 \\ 0 & -\sin \tilde{\alpha} & -\cos \tilde{\alpha} \\ 0 & \cos \tilde{\alpha} & -\sin \tilde{\alpha} \end{bmatrix} \left(-\frac{\dot{y}}{\dot{y}^2 + \dot{z}^2} \right) \\ \frac{\partial C^{a_0 a_I}}{\partial \dot{y}} &= \frac{dC^{a_0 a_I}}{d\tilde{\alpha}} \frac{\partial \tilde{\alpha}}{\partial \dot{y}} = \begin{bmatrix} 0 & 0 & 0 \\ 0 & -\sin \tilde{\alpha} & -\cos \tilde{\alpha} \\ 0 & \cos \tilde{\alpha} & -\sin \tilde{\alpha} \end{bmatrix} \left(\frac{\dot{z}}{\dot{y}^2 + \dot{z}^2} \right)\end{aligned}\quad (\text{A.28})$$

which can be further completed as the derivatives with respect to the independent variables $(\varepsilon, \dot{\varepsilon}, \ddot{\varepsilon}, \beta, \dot{\beta})$. This process is omitted here, since it is no more than another chain derivative.

Finally, the complete aerodynamic derivatives in the body frame can be written as Eqs. (A.29) to (A.33).

$$\begin{aligned}\frac{\partial F^{aero}}{\partial \varepsilon} &= \frac{dC^{Bw}}{d\varepsilon} C^{wa_0} C^{a_0 a_I} \begin{bmatrix} 0 \\ D \\ L \end{bmatrix} + C^{Bw} C^{wa_0} \frac{\partial C^{a_0 a_I}}{\partial \varepsilon} \begin{bmatrix} 0 \\ D \\ L \end{bmatrix} + C^{Bw} C^{wa_0} C^{a_0 a_I} \frac{\partial}{\partial \varepsilon} \begin{bmatrix} 0 \\ D \\ L \end{bmatrix} \\ \frac{\partial M^{aero}}{\partial \varepsilon} &= \frac{dC^{Bw}}{d\varepsilon} C^{wa_0} C^{a_0 a_I} \begin{bmatrix} M_x \\ 0 \\ 0 \end{bmatrix} + C^{Bw} C^{wa_0} \frac{\partial C^{a_0 a_I}}{\partial \varepsilon} \begin{bmatrix} M_x \\ 0 \\ 0 \end{bmatrix} + C^{Bw} C^{wa_0} C^{a_0 a_I} \frac{\partial}{\partial \varepsilon} \begin{bmatrix} M_x \\ 0 \\ 0 \end{bmatrix}\end{aligned}\quad (\text{A.29})$$

$$\begin{aligned}\frac{\partial F^{aero}}{\partial \dot{\varepsilon}} &= C^{Bw} C^{wa_0} \frac{\partial C^{a_0 a_I}}{\partial \dot{\varepsilon}} \begin{bmatrix} 0 \\ D \\ L \end{bmatrix} + C^{Bw} C^{wa_0} C^{a_0 a_I} \frac{\partial}{\partial \dot{\varepsilon}} \begin{bmatrix} 0 \\ D \\ L \end{bmatrix} \\ \frac{\partial M^{aero}}{\partial \dot{\varepsilon}} &= C^{Bw} C^{wa_0} \frac{\partial C^{a_0 a_I}}{\partial \dot{\varepsilon}} \begin{bmatrix} M_x \\ 0 \\ 0 \end{bmatrix} + C^{Bw} C^{wa_0} C^{a_0 a_I} \frac{\partial}{\partial \dot{\varepsilon}} \begin{bmatrix} M_x \\ 0 \\ 0 \end{bmatrix}\end{aligned}\quad (\text{A.30})$$

$$\begin{aligned}\frac{\partial F^{aero}}{\partial \ddot{\varepsilon}} &= C^{Bw} C^{wa_0} C^{a_0 a_I} \frac{\partial}{\partial \ddot{\varepsilon}} \begin{bmatrix} 0 \\ D \\ L \end{bmatrix} \\ \frac{\partial M^{aero}}{\partial \ddot{\varepsilon}} &= C^{Bw} C^{wa_0} C^{a_0 a_I} \frac{\partial}{\partial \ddot{\varepsilon}} \begin{bmatrix} M_x \\ 0 \\ 0 \end{bmatrix}\end{aligned}\quad (\text{A.31})$$

$$\frac{\partial F^{aero}}{\partial \beta} = C^{Bw} C^{wa_0} \frac{\partial C^{a_0 a_I}}{\partial \beta} \begin{bmatrix} 0 \\ D \\ L \end{bmatrix} + C^{Bw} C^{wa_0} C^{a_0 a_I} \frac{\partial}{\partial \beta} \begin{bmatrix} 0 \\ D \\ L \end{bmatrix} \quad (\text{A.32})$$

$$\frac{\partial M^{aero}}{\partial \beta} = C^{Bw} C^{wa_0} \frac{\partial C^{a_0 a_I}}{\partial \beta} \begin{bmatrix} M_x \\ 0 \\ 0 \end{bmatrix} + C^{Bw} C^{wa_0} C^{a_0 a_I} \frac{\partial}{\partial \beta} \begin{bmatrix} M_x \\ 0 \\ 0 \end{bmatrix}$$

$$\frac{\partial F^{aero}}{\partial \dot{\beta}} = C^{Bw} C^{wa_0} C^{a_0 a_I} \frac{\partial}{\partial \dot{\beta}} \begin{bmatrix} 0 \\ D \\ L \end{bmatrix} \quad (\text{A.33})$$

$$\frac{\partial M^{aero}}{\partial \dot{\beta}} = C^{Bw} C^{wa_0} C^{a_0 a_I} \frac{\partial}{\partial \dot{\beta}} \begin{bmatrix} M_x \\ 0 \\ 0 \end{bmatrix}$$

A.4 Block Diagrams Showing Aerodynamic Derivative Relationships

The flowing block diagrams are intended to give images of how the aerodynamic derivative chain is formed.

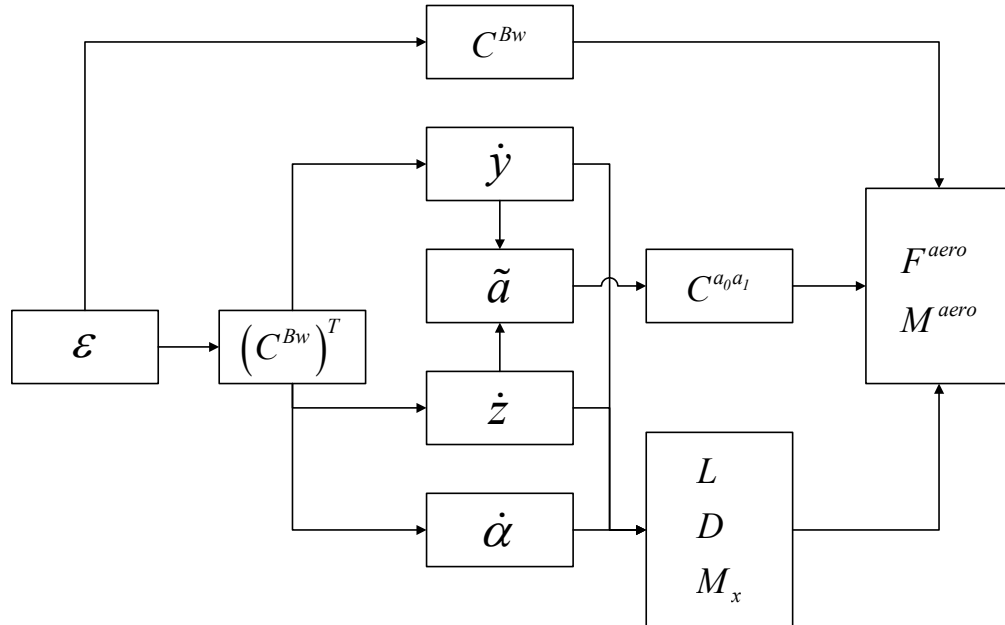


Figure A.2: Relation between strain and aerodynamic loads

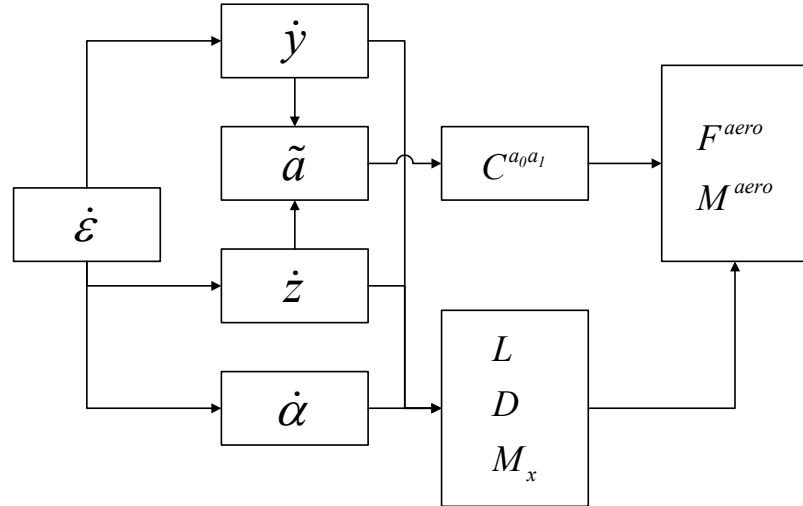


Figure A.3: Relation between strain rate and aerodynamic loads

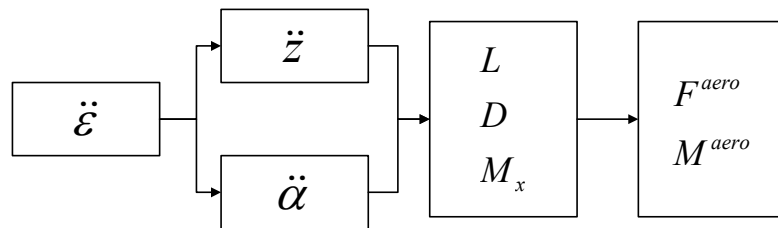


Figure A.4: Relation between strain acceleration and aerodynamic loads

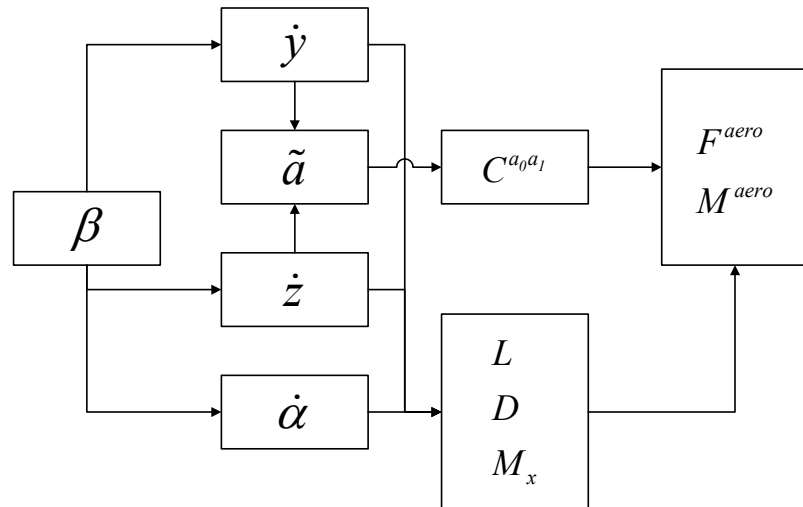


Figure A.5: Relation between body velocity and aerodynamic loads

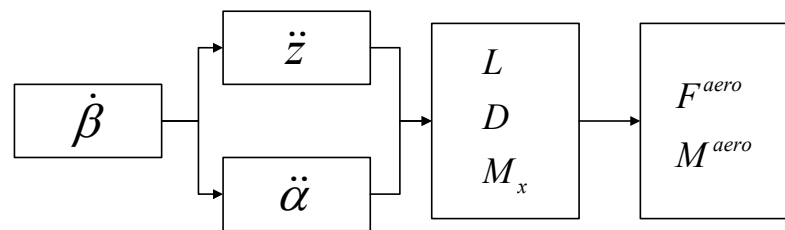


Figure A.6: Relation between body acceleration and aerodynamic loads

APPENDIX B

Linearization of System Equations of Motion

According to the current approach, stability analysis is taken with the linearized equations about a nonlinear steady state. Due to its complexity, this appendix is dedicated to introduce the process of linearization of the nonlinear system equations.

B.1 Generic Nonlinear Equation

Take a generic nonlinear function

$$y(x) = f(x)g(x) \quad (\text{B.1})$$

Let $x = x_0$, the equation can be written as

$$y(x_0) = f(x_0)g(x_0) \quad (\text{B.2})$$

With a small perturbation Δx about x_0 , the equation becomes

$$y(x_0 + \Delta x) = f(x_0 + \Delta x)g(x_0 + \Delta x) \quad (\text{B.3})$$

The right hand side of the above equation can be written as a Taylor expansion

$$y(x_0) + \Delta y(\Delta x) = \left[f(x_0) + \frac{df}{dx} \Big|_{x_0} \Delta x + \text{H.O.T.} \right] \left[g(x_0) + \frac{dg}{dx} \Big|_{x_0} \Delta x + \text{H.O.T.} \right] \quad (\text{B.4})$$

With the high-order terms neglected, Eq. (B.4) becomes

$$y(x_0) + \Delta y(\Delta x) = f(x_0)g(x_0) + f(x_0)\frac{dg}{dx}\Big|_{x_0} \Delta x + g(x_0)\frac{df}{dx}\Big|_{x_0} \Delta x \quad (\text{B.5})$$

Eq. (B.5) minus Eq. (B.2), it yields the linearized equation

$$\Delta y(\Delta x) = f(x_0)\frac{dg}{dx}\Big|_{x_0} \Delta x + g(x_0)\frac{df}{dx}\Big|_{x_0} \Delta x \quad (\text{B.6})$$

Finally, the delta sign can be removed from Eq. (B.6), which becomes

$$y(x) = f(x_0)\frac{dg}{dx}\Big|_{x_0} x + g(x_0)\frac{df}{dx}\Big|_{x_0} x \quad (\text{B.7})$$

B.2 Nonlinear Aeroelastic Equations of Motion

The coupled nonlinear aeroelastic and flight dynamic system equations of motion without nodal displacement constraints are given as Eq. (2.109), and are repeated here as Eq. (B.8). Note that the terms of control surface deflection angles in the aerodynamic load formulations are not included, since the current target is to build a formulation for stability analysis, without considering the effects of control surfaces.

$$\begin{aligned} & M_{FF}(\varepsilon)\ddot{\varepsilon} + M_{FB}(\varepsilon)\dot{\beta} + C_{FF}(\dot{\varepsilon}, \varepsilon, \beta)\dot{\varepsilon} + C_{FB}(\dot{\varepsilon}, \varepsilon, \beta)\beta + K_{FF}\varepsilon \\ &= R_F^{aero}(\ddot{\varepsilon}, \dot{\varepsilon}, \varepsilon, \dot{\beta}, \beta, \lambda) + R_F^{grav}(\zeta) \\ & M_{BF}(\varepsilon)\ddot{\varepsilon} + M_{BB}(\varepsilon)\dot{\beta} + C_{BF}(\dot{\varepsilon}, \varepsilon, \beta)\dot{\varepsilon} + C_{BB}(\dot{\varepsilon}, \varepsilon, \beta)\beta \\ &= R_B^{aero}(\ddot{\varepsilon}, \dot{\varepsilon}, \varepsilon, \dot{\beta}, \beta, \lambda) + R_B^{grav}(\zeta) \end{aligned} \quad (\text{B.8})$$

$$\dot{\zeta} = -\frac{1}{2}\Omega_\zeta(\beta)\zeta$$

$$\dot{P}_B = \begin{bmatrix} C^{GB}(\zeta) & 0 \end{bmatrix} \beta$$

$$\dot{\lambda} = F_1 \begin{bmatrix} \ddot{\varepsilon} \\ \dot{\beta} \end{bmatrix} + F_2 \begin{bmatrix} \dot{\varepsilon} \\ \beta \end{bmatrix} + F_3 \lambda$$

where

$$\begin{bmatrix} R_F^{aero} \\ R_B^{aero} \end{bmatrix} = \begin{bmatrix} J_{p\varepsilon}^T \\ J_{pb}^T \end{bmatrix} B_F F^{aero} + \begin{bmatrix} J_{\theta\varepsilon}^T \\ J_{\theta b}^T \end{bmatrix} B_M M^{aero} \quad (\text{B.9})$$

R_F^{aero} and R_B^{aero} are the flexible and rigid body components of generalized aerodynamic loads, respectively. F^{aero} and M^{aero} are nodal aerodynamic loads. R_F^{grav} and R_B^{grav} are the flexible and rigid body components of generalized gravity force, respectively. The gravity force is transferred from the global frame (G) to the body frame (B). The rotation matrix between the two frames (C^{GB}) is a function of quaternions (ζ).

Before the linearization is performed, some clarifications should be made. The state that the equations will be linearized about is $x_0 = [\ddot{\varepsilon}_0, \dot{\varepsilon}_0, \varepsilon_0, \dot{\beta}_0, \beta_0, \lambda_0, \zeta_0, P_{B0}]$. If one looks at the equations of the generalized mass matrices and load vectors (Eq. 2.60), they contain the contribution from structural Jacobians ($J_{h\varepsilon}, J_{hb}, J_{p\varepsilon}, J_{pb}, J_{\theta\varepsilon}, J_{\theta b}$). These Jacobians are functions of strains (ε). However, it is assumed that they are constant when the system is perturbed. This assumption holds for small perturbations to the system. The advantage of this assumption is to simplify the linearization process, since the generalized matrices are no longer functions of any state variables. After all, the generalized stiffness matrix is independent from the state variables, yet the generalized damping matrices are functions of strain rates ($\dot{\varepsilon}$) and body velocities (β), according to the equations. In the inflow equation, F_1 , F_2 , and F_3 are also assumed to be constants.

Linearization is performed about the state, x_0 . Each of the five equations from Eq. (B.8) is written with the perturbation as follows. Note that the operator $[\cdot]_{x_0}$ denotes the matrix is evaluated at the state of x_0 .

$$\begin{aligned}
& M_{FF} (\ddot{\varepsilon}_0 + \Delta \ddot{\varepsilon}) + M_{FB} (\dot{\beta}_0 + \Delta \dot{\beta}) \\
& + \left(C_{FF} \Big|_{x_0} + \frac{\partial C_{FF}}{\partial \dot{\varepsilon}} \Big|_{x_0} \Delta \dot{\varepsilon} + \frac{\partial C_{FF}}{\partial \beta} \Big|_{x_0} \Delta \beta \right) (\dot{\varepsilon}_0 + \Delta \dot{\varepsilon}) \\
& + \left(C_{FB} \Big|_{x_0} + \frac{\partial C_{FB}}{\partial \dot{\varepsilon}} \Big|_{x_0} \Delta \dot{\varepsilon} + \frac{\partial C_{FB}}{\partial \beta} \Big|_{x_0} \Delta \beta \right) (\beta_0 + \Delta \beta) \\
& + K_{FF} (\varepsilon_0 + \Delta \varepsilon) \\
& = R_F^{aero} \Big|_{x_0} + \frac{\partial R_F^{aero}}{\partial \ddot{\varepsilon}} \Big|_{x_0} \Delta \ddot{\varepsilon} + \frac{\partial R_F^{aero}}{\partial \dot{\varepsilon}} \Big|_{x_0} \Delta \dot{\varepsilon} + \frac{\partial R_F^{aero}}{\partial \varepsilon} \Big|_{x_0} \Delta \varepsilon + \frac{\partial R_F^{aero}}{\partial \dot{\beta}} \Big|_{x_0} \Delta \dot{\beta} + \frac{\partial R_F^{aero}}{\partial \beta} \Big|_{x_0} \Delta \beta \\
& + \frac{\partial R_F^{aero}}{\partial \lambda} \Big|_{x_0} \Delta \lambda + R_F^{grav} \Big|_{x_0} + \frac{\partial R_F^{grav}}{\partial \zeta} \Big|_{x_0} \Delta \zeta
\end{aligned} \tag{B.10}$$

$$\begin{aligned}
& M_{BF} (\ddot{\varepsilon}_0 + \Delta \ddot{\varepsilon}) + M_{BB} (\dot{\beta}_0 + \Delta \dot{\beta}) \\
& + \left(C_{BF} \Big|_{x_0} + \frac{\partial C_{BF}}{\partial \dot{\varepsilon}} \Big|_{x_0} \Delta \dot{\varepsilon} + \frac{\partial C_{BF}}{\partial \beta} \Big|_{x_0} \Delta \beta \right) (\dot{\varepsilon}_0 + \Delta \dot{\varepsilon}) \\
& + \left(C_{BB} \Big|_{x_0} + \frac{\partial C_{BB}}{\partial \dot{\varepsilon}} \Big|_{x_0} \Delta \dot{\varepsilon} + \frac{\partial C_{BB}}{\partial \beta} \Big|_{x_0} \Delta \beta \right) (\beta_0 + \Delta \beta) \\
& = R_B^{aero} \Big|_{x_0} + \frac{\partial R_B^{aero}}{\partial \ddot{\varepsilon}} \Big|_{x_0} \Delta \ddot{\varepsilon} + \frac{\partial R_B^{aero}}{\partial \dot{\varepsilon}} \Big|_{x_0} \Delta \dot{\varepsilon} + \frac{\partial R_B^{aero}}{\partial \varepsilon} \Big|_{x_0} \Delta \varepsilon + \frac{\partial R_B^{aero}}{\partial \dot{\beta}} \Big|_{x_0} \Delta \dot{\beta} + \frac{\partial R_B^{aero}}{\partial \beta} \Big|_{x_0} \Delta \beta \\
& + \frac{\partial R_B^{aero}}{\partial \lambda} \Big|_{x_0} \Delta \lambda + R_B^{grav} \Big|_{x_0} + \frac{\partial R_B^{grav}}{\partial \zeta} \Big|_{x_0} \Delta \zeta
\end{aligned} \tag{B.11}$$

$$\dot{\zeta}_0 + \Delta \dot{\zeta} = -\frac{1}{2} \left(\Omega_\zeta \Big|_{x_0} + \frac{d\Omega_\zeta}{d\beta} \Big|_{x_0} \Delta \beta \right) (\zeta_0 + \Delta \zeta) \tag{B.12}$$

$$\dot{P}_{B0} + \Delta \dot{P}_B = \left[\left(C^{GB} \Big|_{x_0} + \frac{dC^{GB}}{d\zeta} \Big|_{x_0} \right) \quad 0 \right] (\beta_0 + \Delta \beta) \tag{B.13}$$

$$\dot{\lambda}_0 + \Delta \dot{\lambda} = F_1 \begin{bmatrix} \ddot{\varepsilon}_0 + \Delta \ddot{\varepsilon} \\ \dot{\beta}_0 + \Delta \dot{\beta} \end{bmatrix} + F_2 \begin{bmatrix} \dot{\varepsilon}_0 + \Delta \dot{\varepsilon} \\ \beta_0 + \Delta \beta \end{bmatrix} + F_3 (\lambda_0 + \Delta \lambda) \tag{B.14}$$

Following the approach introduced above, Eqs. (B.10) to (B.14) can be organized as

$$\begin{aligned}
& M_{FF} \ddot{\varepsilon} + M_{FB} \dot{\beta} \\
& + \left(C_{FF} + \frac{\partial C_{FF}}{\partial \dot{\varepsilon}} \Big|_{\dot{\varepsilon}_0} \dot{\varepsilon}_0 + \frac{\partial C_{FB}}{\partial \dot{\varepsilon}} \Big|_{\dot{\varepsilon}_0} \beta_0 \right) \dot{\varepsilon} + \left(C_{FB} + \frac{\partial C_{FF}}{\partial \beta} \Big|_{\beta_0} \dot{\varepsilon}_0 + \frac{\partial C_{FB}}{\partial \beta} \Big|_{\beta_0} \beta_0 \right) \beta \\
& + K_{FF} \varepsilon \\
& = \frac{\partial R_F^{aero}}{\partial \ddot{\varepsilon}} \Big|_{\ddot{\varepsilon}_0} \ddot{\varepsilon} + \frac{\partial R_F^{aero}}{\partial \dot{\varepsilon}} \Big|_{\dot{\varepsilon}_0} \dot{\varepsilon} + \frac{\partial R_F^{aero}}{\partial \varepsilon} \Big|_{\varepsilon_0} \varepsilon \\
& + \frac{\partial R_F^{aero}}{\partial \dot{\beta}} \Big|_{\dot{\beta}_0} \dot{\beta} + \frac{\partial R_F^{aero}}{\partial \beta} \Big|_{\beta_0} \beta + \frac{\partial R_F^{aero}}{\partial \lambda} \Big|_{\lambda_0} \lambda + \frac{\partial R_F^{grav}}{\partial \zeta} \Big|_{\zeta_0} \zeta
\end{aligned} \tag{B.15}$$

$$\begin{aligned}
& M_{BF} \ddot{\varepsilon} + M_{BB} \dot{\beta} \\
& + \left(C_{BF} + \frac{\partial C_{BF}}{\partial \dot{\varepsilon}} \Big|_{\dot{\varepsilon}_0} \dot{\varepsilon}_0 + \frac{\partial C_{BB}}{\partial \dot{\varepsilon}} \Big|_{\dot{\varepsilon}_0} \beta_0 \right) \dot{\varepsilon} + \left(C_{BB} + \frac{\partial C_{BF}}{\partial \beta} \Big|_{\beta_0} \dot{\varepsilon}_0 + \frac{\partial C_{BB}}{\partial \beta} \Big|_{\beta_0} \beta_0 \right) \beta \\
& = \frac{\partial R_B^{aero}}{\partial \ddot{\varepsilon}} \Big|_{\ddot{\varepsilon}_0} \ddot{\varepsilon} + \frac{\partial R_B^{aero}}{\partial \dot{\varepsilon}} \Big|_{\dot{\varepsilon}_0} \dot{\varepsilon} + \frac{\partial R_B^{aero}}{\partial \varepsilon} \Big|_{\varepsilon_0} \varepsilon \\
& + \frac{\partial R_B^{aero}}{\partial \dot{\beta}} \Big|_{\dot{\beta}_0} \dot{\beta} + \frac{\partial R_B^{aero}}{\partial \beta} \Big|_{\beta_0} \beta + \frac{\partial R_B^{aero}}{\partial \lambda} \Big|_{\lambda_0} \lambda + \frac{\partial R_B^{grav}}{\partial \zeta} \Big|_{\zeta_0} \zeta
\end{aligned} \tag{B.16}$$

$$\dot{\zeta} = -\frac{1}{2} \Omega_\zeta \Big|_{\beta_0} \zeta - \frac{1}{2} \left(\frac{d\Omega_\zeta}{d\beta} \Big|_{\beta_0} \beta \right) \zeta_0 \tag{B.17}$$

$$\dot{P}_B = \begin{bmatrix} C^{GB} \Big|_{\zeta_0} & 0 \end{bmatrix} \beta + \begin{bmatrix} \left(\frac{dC^{GB}}{d\zeta} \Big|_{\zeta_0} \zeta \right) & 0 \end{bmatrix} \beta_0 \tag{B.18}$$

$$\dot{\lambda} = F_1 \begin{bmatrix} \ddot{\varepsilon} \\ \dot{\beta} \end{bmatrix} + F_2 \begin{bmatrix} \dot{\varepsilon} \\ \beta \end{bmatrix} + F_3 \lambda \tag{B.19}$$

Therefore, the linearized system equations are simplified as Eq. (B.20)

$$\begin{aligned}
& M_{FF} \ddot{\varepsilon} + M_{FB} \dot{\beta} + (C_{FF} + C_{FF/\dot{\varepsilon}_0} \dot{\varepsilon}_0 + C_{FB/\dot{\varepsilon}_0} \beta_0) \dot{\varepsilon} + (C_{FB} + C_{FF/\beta_0} \dot{\varepsilon}_0 + C_{FB/\beta_0} \beta_0) \beta \\
& + K_{FF} \varepsilon \\
& = R_{F/\ddot{\varepsilon}_0}^{aero} \ddot{\varepsilon} + R_{F/\dot{\varepsilon}_0}^{aero} \dot{\varepsilon} + R_{F/\dot{\beta}_0}^{aero} \varepsilon + R_{F/\dot{\beta}_0}^{aero} \dot{\beta} + R_{F/\lambda_0}^{aero} \lambda + R_{F/\zeta_0}^{grav} \zeta \\
& M_{BF} \ddot{\varepsilon} + M_{BB} \dot{\beta} + (C_{BF} + C_{BF/\dot{\varepsilon}_0} \dot{\varepsilon}_0 + C_{BB/\dot{\varepsilon}_0} \beta_0) \dot{\varepsilon} + (C_{BB} + C_{BF/\beta_0} \dot{\varepsilon}_0 + C_{BB/\beta_0} \beta_0) \beta \\
& = R_{B/\ddot{\varepsilon}_0}^{aero} \ddot{\varepsilon} + R_{B/\dot{\varepsilon}_0}^{aero} \dot{\varepsilon} + R_{B/\dot{\beta}_0}^{aero} \varepsilon + R_{B/\dot{\beta}_0}^{aero} \dot{\beta} + R_{B/\lambda_0}^{aero} \lambda + R_{B/\zeta_0}^{grav} \zeta \\
& \dot{\zeta} = -\frac{1}{2} \Omega_\zeta \zeta - \frac{1}{2} (\Omega_{\zeta/\beta_0} \beta) \zeta_0 \\
& \dot{P}_B = [C^{GB} \quad 0] \beta + [(C_{/\zeta_0}^{GB} \zeta) \quad 0] \beta_0 \\
& \dot{\lambda} = F_1 \begin{bmatrix} \ddot{\varepsilon} \\ \dot{\beta} \end{bmatrix} + F_2 \begin{bmatrix} \dot{\varepsilon} \\ \beta \end{bmatrix} + F_3 \lambda
\end{aligned} \tag{B.20}$$

where $(\cdot)_{/z_0}$ denotes $\left. \frac{d(\cdot)}{dz} \right|_{z_0}$ or $\left. \frac{\partial(\cdot)}{\partial z} \right|_{z_0}$ for different variables.

To obtain the state-space form equations, the terms on the right hand side of Eq. (B.20) are moved to the left, and the terms with the same variables are grouped together, which becomes

$$\begin{aligned}
& (M_{FF} - R_{F/\dot{\varepsilon}_0}^{aero}) \ddot{\varepsilon} + (M_{FB} - R_{F/\dot{\beta}_0}^{aero}) \dot{\beta} + (C_{FF} + C_{FF/\dot{\varepsilon}_0} \dot{\varepsilon}_0 + C_{FB/\dot{\varepsilon}_0} \beta_0 - R_{F/\dot{\varepsilon}_0}^{aero}) \dot{\varepsilon} \\
& + (C_{FB} + C_{FF/\beta_0} \dot{\varepsilon}_0 + C_{FB/\beta_0} \beta_0 - R_{F/\beta_0}^{aero}) \beta + (K_{FF} - R_{F/\varepsilon_0}^{aero}) \varepsilon - R_{F/\lambda_0}^{aero} \lambda - R_{F/\zeta_0}^{grav} \zeta \\
& = 0 \\
& (M_{BF} - R_{B/\ddot{\varepsilon}_0}^{aero}) \ddot{\varepsilon} + (M_{BB} - R_{B/\dot{\beta}_0}^{aero}) \dot{\beta} + (C_{BF} + C_{BF/\dot{\varepsilon}_0} \dot{\varepsilon}_0 + C_{BB/\dot{\varepsilon}_0} \beta_0 - R_{B/\dot{\varepsilon}_0}^{aero}) \dot{\varepsilon} \\
& + (C_{BB} + C_{BF/\beta_0} \dot{\varepsilon}_0 + C_{BB/\beta_0} \beta_0 - R_{B/\beta_0}^{aero}) \beta - R_{B/\lambda_0}^{aero} \lambda - R_{B/\zeta_0}^{grav} \zeta \\
& = 0 \\
& \dot{\zeta} + \frac{1}{2} \Omega_\zeta \zeta + \frac{1}{2} (\Omega_{\zeta/\beta_0} \beta) \zeta_0 = 0 \\
& \dot{P}_B - [C^{GB} \quad 0] \beta - [(C_{/\zeta_0}^{GB} \zeta) \quad 0] \beta_0 = 0 \\
& \dot{\lambda} - F_1 \begin{bmatrix} \ddot{\varepsilon} \\ \dot{\beta} \end{bmatrix} - F_2 \begin{bmatrix} \dot{\varepsilon} \\ \beta \end{bmatrix} - F_3 \lambda = 0
\end{aligned} \tag{B.21}$$

According to Eq. (B.9), the derivatives of the generalized aerodynamic loads can be expanded, which are given in Eq. (B.22). Again, one should note that all the derivatives

and matrices are evaluated at the state of x_0 , and the notation is omitted from the equations from now on for simplicity.

$$\begin{aligned}
\frac{\partial R_F^{aero}}{\partial \ddot{\varepsilon}} &= J_{pe}^T B_F \frac{\partial F^{aero}}{\partial \ddot{\varepsilon}} + J_{\theta e}^T B_M \frac{\partial M^{aero}}{\partial \ddot{\varepsilon}}, & \frac{\partial R_F^{aero}}{\partial \dot{\beta}} &= J_{pe}^T B_F \frac{\partial F^{aero}}{\partial \dot{\beta}} + J_{\theta e}^T B_M \frac{\partial M^{aero}}{\partial \dot{\beta}} \\
\frac{\partial R_F^{aero}}{\partial \dot{\varepsilon}} &= J_{pe}^T B_F \frac{\partial F^{aero}}{\partial \dot{\varepsilon}} + J_{\theta e}^T B_M \frac{\partial M^{aero}}{\partial \dot{\varepsilon}}, & \frac{\partial R_F^{aero}}{\partial \beta} &= J_{pe}^T B_F \frac{\partial F^{aero}}{\partial \beta} + J_{\theta e}^T B_M \frac{\partial M^{aero}}{\partial \beta} \\
\frac{\partial R_F^{aero}}{\partial \varepsilon} &= J_{pe}^T B_F \frac{\partial F^{aero}}{\partial \varepsilon} + J_{\theta e}^T B_M \frac{\partial M^{aero}}{\partial \varepsilon}, & & \\
\frac{\partial R_B^{aero}}{\partial \ddot{\varepsilon}} &= J_{pb}^T B_F \frac{\partial F^{aero}}{\partial \ddot{\varepsilon}} + J_{\theta b}^T B_M \frac{\partial M^{aero}}{\partial \ddot{\varepsilon}}, & \frac{\partial R_B^{aero}}{\partial \dot{\beta}} &= J_{pb}^T B_F \frac{\partial F^{aero}}{\partial \dot{\beta}} + J_{\theta b}^T B_M \frac{\partial M^{aero}}{\partial \dot{\beta}} \\
\frac{\partial R_B^{aero}}{\partial \dot{\varepsilon}} &= J_{pb}^T B_F \frac{\partial F^{aero}}{\partial \dot{\varepsilon}} + J_{\theta b}^T B_M \frac{\partial M^{aero}}{\partial \dot{\varepsilon}}, & \frac{\partial R_B^{aero}}{\partial \beta} &= J_{pb}^T B_F \frac{\partial F^{aero}}{\partial \beta} + J_{\theta b}^T B_M \frac{\partial M^{aero}}{\partial \beta}
\end{aligned} \tag{B.22}$$

Therefore, Eq. (B.21) can be written as:

$$\begin{aligned}
\bar{M}_{FF} \ddot{\varepsilon} + \bar{M}_{FB} \dot{\beta} + \bar{C}_{FF} \dot{\varepsilon} + \bar{C}_{FB} \beta + \bar{K}_{FF} \varepsilon - R_{F/\lambda_0}^{aero} \lambda - R_{F/\zeta_0}^{grav} \zeta &= 0 \\
\bar{M}_{BF} \ddot{\varepsilon} + \bar{M}_{BB} \dot{\beta} + \bar{C}_{BF} \dot{\varepsilon} + \bar{C}_{BB} \beta - R_{B/\lambda_0}^{aero} \lambda - R_{B/\zeta_0}^{grav} \zeta &= 0 \\
\dot{\zeta} + \frac{1}{2} \Omega_\zeta \zeta + \frac{1}{2} (\Omega_{\zeta/\beta_0} \beta) \zeta_0 &= 0 \\
\dot{P}_B - \begin{bmatrix} C^{GB} & 0 \end{bmatrix} \beta - \begin{bmatrix} (C_{/\zeta_0}^{GB} \zeta) & 0 \end{bmatrix} \beta_0 &= 0 \\
\dot{\lambda} - F_1 \begin{bmatrix} \ddot{\varepsilon} \\ \dot{\beta} \end{bmatrix} - F_2 \begin{bmatrix} \dot{\varepsilon} \\ \beta \end{bmatrix} - F_3 \lambda &= 0
\end{aligned} \tag{B.23}$$

where

$$\begin{aligned}
\bar{M}_{FF} &= M_{FF} - J_{pe}^T B_F \frac{\partial F^{aero}}{\partial \ddot{\varepsilon}} - J_{\theta e}^T B_M \frac{\partial M^{aero}}{\partial \ddot{\varepsilon}} \\
\bar{M}_{FB} &= M_{FB} - J_{pe}^T B_F \frac{\partial F^{aero}}{\partial \dot{\beta}} + J_{\theta e}^T B_M \frac{\partial M^{aero}}{\partial \dot{\beta}} \\
\bar{C}_{FF} &= C_{FF} + \frac{\partial C_{FF}}{\partial \dot{\varepsilon}} \dot{\varepsilon}_0 + \frac{\partial C_{FB}}{\partial \dot{\varepsilon}} \beta_0 - J_{pe}^T B_F \frac{\partial F^{aero}}{\partial \dot{\varepsilon}} - J_{\theta e}^T B_M \frac{\partial M^{aero}}{\partial \dot{\varepsilon}} \\
\bar{C}_{FB} &= C_{FB} + \frac{\partial C_{FF}}{\partial \beta} \dot{\varepsilon}_0 + \frac{\partial C_{FB}}{\partial \beta} \beta_0 - J_{pe}^T B_F \frac{\partial F^{aero}}{\partial \beta} - J_{\theta e}^T B_M \frac{\partial M^{aero}}{\partial \beta} \\
\bar{K}_{FF} &= K_{FF} - J_{pe}^T B_F \frac{\partial F^{aero}}{\partial \varepsilon} - J_{\theta e}^T B_M \frac{\partial M^{aero}}{\partial \varepsilon}
\end{aligned} \tag{B.24}$$

and

$$\begin{aligned}
\bar{M}_{BF} &= M_{BF} - J_{pb}^T B_F \frac{\partial F^{aero}}{\partial \ddot{\varepsilon}} - J_{\theta b}^T B_M \frac{\partial M^{aero}}{\partial \ddot{\varepsilon}} \\
\bar{M}_{BB} &= M_{BB} - J_{pb}^T B_F \frac{\partial F^{aero}}{\partial \dot{\beta}} - J_{\theta b}^T B_M \frac{\partial M^{aero}}{\partial \dot{\beta}} \\
\bar{C}_{BF} &= C_{BF} + \frac{\partial C_{BF}}{\partial \dot{\varepsilon}} \dot{\varepsilon}_0 + \frac{\partial C_{BB}}{\partial \dot{\varepsilon}} \beta_0 - J_{pb}^T B_F \frac{\partial F^{aero}}{\partial \dot{\varepsilon}} - J_{\theta b}^T B_M \frac{\partial M^{aero}}{\partial \dot{\varepsilon}} \\
\bar{C}_{BB} &= C_{BB} + \frac{\partial C_{BF}}{\partial \dot{\beta}} \dot{\varepsilon}_0 + \frac{\partial C_{BB}}{\partial \dot{\beta}} \beta_0 - J_{pb}^T B_F \frac{\partial F^{aero}}{\partial \dot{\beta}} - J_{\theta b}^T B_M \frac{\partial M^{aero}}{\partial \dot{\beta}}
\end{aligned} \tag{B.25}$$

Finally, Eq. (B.23) can be put into state space form

$$\begin{aligned}
[\dot{\varepsilon} \quad \ddot{\varepsilon} \quad \dot{\beta} \quad \dot{\zeta} \quad \dot{P}_B \quad \dot{\lambda}]^T &= Q_l^{-1} Q_2 [\varepsilon \quad \dot{\varepsilon} \quad \beta \quad \zeta \quad P_B \quad \lambda]^T \\
&= A [\varepsilon \quad \dot{\varepsilon} \quad \beta \quad \zeta \quad P_B \quad \lambda]^T
\end{aligned} \tag{B.26}$$

where

$$Q_l = \begin{bmatrix} I & 0 & 0 & 0 & 0 & 0 \\ 0 & \bar{M}_{FF} & \bar{M}_{FB} & 0 & 0 & 0 \\ 0 & \bar{M}_{BF} & \bar{M}_{BB} & 0 & 0 & 0 \\ 0 & 0 & 0 & I & 0 & 0 \\ 0 & 0 & 0 & 0 & I & 0 \\ 0 & -F_{IF} & -F_{IB} & 0 & 0 & I \end{bmatrix} \tag{B.27}$$

$$Q_2 = \begin{bmatrix} 0 & I & 0 & 0 & 0 & 0 \\ -\bar{K}_{FF} & -\bar{C}_{FF} & -\bar{C}_{FB} & R_{F/\zeta_0}^{grav} & 0 & R_{F/\lambda_0}^{aero} \\ 0 & -\bar{C}_{BF} & -\bar{C}_{BB} & R_{B/\zeta_0}^{grav} & 0 & R_{B/\lambda_0}^{aero} \\ 0 & 0 & -\frac{1}{2}\Omega_{\zeta/\beta_0}\zeta_0 & -\frac{1}{2}\Omega_\zeta & 0 & 0 \\ 0 & 0 & [C^{GB} \quad 0] & [C_{/\zeta_0}^{GB} \quad 0]\beta_0 & 0 & 0 \\ 0 & F_{2F} & F_{2B} & 0 & 0 & F_3 \end{bmatrix}$$

APPENDIX C

Properties of the Numerical Models

This appendix provides the detailed definitions of Single-Wing, Joined-Wing, and Blended-Wing-Body configurations. The nomenclatures used, as well as the units corresponding to the numerical values, are defined as follows.

K11 (N·m)	Extensional stiffness
K12 (N·m)	Extension-twist coupling stiffness
K13 (N·m)	Extension-flatwise bending coupling stiffness
K14 (N·m)	Extension-chordwise bending coupling stiffness
K22 (N·m ²)	Torsional stiffness
K23 (N·m ²)	Twist-flatwise bending coupling stiffness
K24 (N·m ²)	Twist-chordwise bending coupling stiffness
K33 (N·m ²)	Flatwise bending stiffness
K34 (N·m ²)	Flatwise bending-chordwise bending coupling stiffness
K44 (N·m ²)	Chordwise bending stiffness
mass (kg/m)	Mass per unit length
Ixx (kg·m ² /m)	x-axis rotational inertia per unit length
Ixy (kg·m ² /m)	x-axis to y-axis coupling rotational inertia per unit length
Ixz (kg·m ² /m)	x-axis to z-axis coupling rotational inertia per unit length
Iyy (kg·m ² /m)	y-axis rotational inertia per unit length
Iyz (kg·m ² /m)	y-axis to z-axis coupling rotational inertia per unit length
Izz (kg·m ² /m)	z-axis rotational inertia per unit length

xle (m)	Distance of airfoil tip from reference axis, local x direction
yle (m)	Distance of airfoil tip from reference axis, local y direction

C.1 Single-Wing Configuration

For the Single-Wing configuration, the member and group definitions are shown in Fig. C.1. Cross-sectional stiffness and inertia distributions of each member are listed as follows.

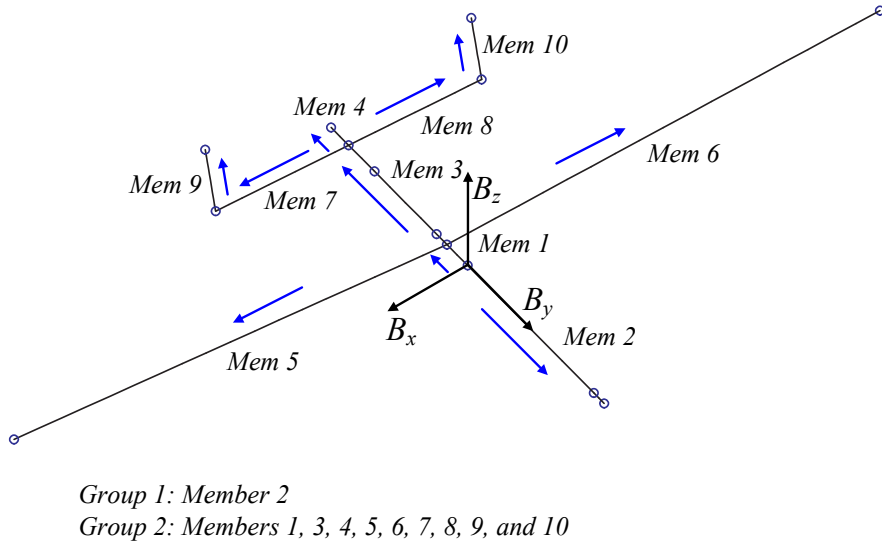


Figure C.1: Member and group definitions for the Single-Wing configuration (arrows indicate the kinematics marching direction and element progression as presented below)

<u>Member 1</u>	3.7253e-009
K11	K14
1.1541e+009	-4.0679e-014
K12	K22
0	4.4005e+008
K13	K23
	0

K24		0.5000 0.5000
0	yle	
K33		0 0
5.7287e+008		<u>Member 2</u>
K34		K11 * 1.0e+009
-1.2107e-008		1.1541
K44		1.1541
		0.9233
5.7328e+008		K12
mass		0
		0
44.1556 44.1556		0
Ixx		K13 * 1.0e-008
43.8515 43.8515		0.3725
Ixy		0.3725
		-0.3725
0 0		K14 * 1.0e-007
Ixz		-0.0000
		-0.0000
0 0		0.5960
Iyy		K22 * 1.0e+008
21.9180 21.9180		4.4005
Iyz * 1.0e-015		4.4005
		2.2531
-0.4025 -0.4025		K23
Izz		0
		0
21.9335 21.9335		0
xle		K24

0	Iyy
0	
0	21.9180 21.9180
	21.9180 21.9180
K33 * 1.0e+008	21.9180 11.2220
5.7287	Iyz * 1.0e-015
5.7287	
2.9331	-0.4025 -0.4025
	-0.4025 -0.4025
K34 * 1.0e-007	-0.4025 -0.1180
-0.1211	Izz
-0.1211	
-0.0838	21.9335 21.9335
	21.9335 21.9335
K44 * 1.0e+008	21.9335 11.2299
5.7328	xle
5.7328	
2.9352	0.5000 0.5000
	0.5000 0.5000
mass	0.5000 0.5000
44.1556 44.1556	yle
44.1556 44.1556	
44.1556 35.3245	0 0
	0 0
Ixx	0 0
43.8515 43.8515	<u>Member 3</u>
43.8515 43.8515	
43.8515 22.4519	K11 * 1.0e+009
Ixy	1.1541
0 0	1.1541
0 0	1.1541
0 0	1.1541
	1.0639
Ixz	K12
0 0	0
0 0	0
0 0	0

0	5.7287
0	5.7287
K13 * 1.0e-007	5.7287
	4.4882
0.0373	K34 * 1.0e-007
0.0373	
0.0373	-0.1211
0.0373	-0.1211
0.1676	-0.1211
	-0.1211
K14 * 1.0e-007	-0.1490
-0.0000	K44 * 1.0e+008
-0.0000	
-0.0000	5.7328
-0.0000	5.7328
0.5960	5.7328
	5.7328
K22 * 1.0e+008	4.4914
4.4005	mass
4.4005	
4.4005	44.1556 44.1556
4.4005	44.1556 44.1556
3.4476	44.1556 44.1556
	44.1556 44.1556
K23	44.1556 40.7060
0	Ixx
0	
0	43.8515 43.8515
0	43.8515 43.8515
0	43.8515 43.8515
	43.8515 43.8515
K24	43.8515 34.3558
0	Ixy
0	
0	0 0
0	0 0
0	0 0
	0 0
K33 * 1.0e+008	0 0
5.7287	Ixz

0	0	<u>Member 4</u>
0	0	
0	0	K11
0	0	
0	0	9.1967e+008
Iyy		K12
21.9180	21.9180	0
21.9180	21.9180	
21.9180	21.9180	K13
21.9180	21.9180	
21.9180	17.1718	1.1176e-008
Iyz * 1.0e-014		K14
-0.0402	-0.0402	2.9802e-008
-0.0402	-0.0402	
-0.0402	-0.0402	K22
-0.0402	-0.0402	
-0.0402	-0.1006	2.2268e+008
Izz		K23
21.9335	21.9335	0
21.9335	21.9335	
21.9335	21.9335	K24
21.9335	21.9335	
21.9335	17.1840	0
xle		K33
0.5000	0.5000	2.8989e+008
0.5000	0.5000	
0.5000	0.5000	K34
0.5000	0.5000	
0.5000	0.5000	-7.9162e-009
yle		K44
0	0	2.9009e+008
0	0	
0	0	mass
0	0	
0	0	37.2563 35.1865

Ixx		K12
26.3406	22.1899	0
		0
Ixy		0
		0
0	0	0
		0
Ixz		0
		0
0	0	0
Iyy		K13 * 1.0e+006
13.1657	11.0910	-1.6465
Iyz * 1.0e-015		-1.2569
-0.2637	-0.2533	-0.9630
Izz		-0.7620
13.1749	11.0988	-0.5907
		-0.4525
xle		-0.3567
yle		-0.2754
0	0	-0.2074
<u>Members 5 and 6</u>		K14 * 1.0e+006
0.5000	0.5000	5.1014
		3.8944
K11 * 1.0e+009		2.9838
		2.3610
1.5957		1.8302
1.0738		1.4019
0.8772		1.1052
0.7433		0.8534
0.6201		0.6427
0.5143		K22 * 1.0e+008
0.4419		1.1325
0.3750		0.7082
0.3134		0.5089
		0.3760
		0.2708
		0.1916
		0.1386

0.0974	-0.3972
0.0661	-0.2873
	-0.2019
K23	-0.1370
0	K44 * 1.0e+009
0	
0	2.4921
0	1.2539
0	0.9011
0	0.6658
0	0.4795
0	0.3393
0	0.2454
0	0.1724
K24	0.1170
0	mass
0	
0	138.2394 134.3141
0	112.2792 108.8991
0	91.9036 88.9596
0	78.0512 75.3798
0	65.2892 62.8904
0	54.3050 52.1515
0	46.8336 44.8164
	39.9074 38.0265
	33.5264 31.7818
K33 * 1.0e+007	
9.4176	Ixx
6.4306	
4.6212	237.3384 217.6894
3.4146	171.4953 156.4685
2.4593	123.9789 112.4420
1.7401	92.2326 83.0827
1.2586	66.9509 59.8391
0.8843	47.8037 42.3393
0.6001	34.9467 30.6228
	24.8690 21.5158
	17.1395 14.6007
K34 * 1.0e+007	
-2.0425	Ixy
-1.4681	
-1.0550	0 0
-0.7795	0 0
-0.5614	0 0

0	0		165.2505	150.7708
0	0		119.4643	108.3476
0	0		88.8740	80.0573
0	0		64.5129	57.6601
0	0		46.0630	40.7975
0	0		33.6741	29.5077
		Ixz	23.9635	20.7324
			16.5153	14.0690
0	0	xle		
0	0		0.4869	0.4869
0	0		0.4869	0.4869
0	0		0.4869	0.4869
0	0		0.4869	0.4869
0	0		0.4869	0.4869
0	0		0.4869	0.4869
0	0		0.4869	0.4869
0	0		0.4869	0.4869
		Iyy	0.4869	0.4869
8.6424	7.9269	yle		
6.2448	5.6976		0.0282	0.0282
4.5146	4.0945		0.0282	0.0282
3.3586	3.0254		0.0282	0.0282
2.4379	2.1790		0.0282	0.0282
1.7407	1.5417		0.0282	0.0282
1.2725	1.1151		0.0282	0.0282
0.9056	0.7835		0.0282	0.0282
0.6241	0.5317		0.0282	0.0282
		Iyz	0.0282	0.0282
-1.8744	-1.7192	<i>Members 7 and 8</i>		
-1.3544	-1.2357			
-0.9791	-0.8880	K11 * 1.0e+008		
-0.7284	-0.6561			
-0.5287	-0.4726		6.7153	
-0.3775	-0.3344		5.9849	
-0.2760	-0.2418		5.2961	
-0.1964	-0.1699		4.6488	
-0.1354	-0.1153		4.0430	
		Izz	K12	
228.6960	209.7624		0	

0	
0	1.4750
0	1.1570
0	0.8933
0	0.6773
K13	0.5030
-0.0201	K34
-0.0168	
-0.0139	-0.0101
-0.0113	-0.0079
-0.0091	-0.0061
	-0.0046
K14 * 1.0e+008	-0.0034
4.3530	K44 * 1.0e+008
3.6396	
3.0083	9.1263
2.4542	7.1586
1.9723	5.5269
	4.1906
K22 * 1.0e+007	3.1120
1.9024	mass
1.4922	
1.1521	22.1434 21.4791
0.8735	19.7740 19.1430
0.6487	17.5376 16.9397
	15.4339 14.8693
K23	13.4632 12.9317
0	Ixx
0	
0	32.5006 29.6624
0	25.6447 23.2669
0	19.9334 17.9635
	15.2318 13.6205
K24	11.4136 10.1146
0	Ixy
0	
0	0 0
0	0 0
0	0 0
	0 0
K33 * 1.0e+007	0 0

		0	0
Ixz		0	0
			<i>Members 9 and 10</i>
	0	0	
	0	0	K11 * 1.0e+008
	0	0	
	0	0	4.7571
			4.3501
Iyy			3.9609
			3.5896
	0.5169	0.4718	3.2360
	0.4079	0.3701	
	0.3170	0.2857	K12
	0.2423	0.2166	
	0.1815	0.1609	0
			0
Iyz * 1.0e-009			0
			0
	-0.3530	-0.3222	
	-0.2786	-0.2527	0
	-0.2165	-0.1951	
	-0.1655	-0.1479	K13
	-0.1240	-0.1099	
			-0.0101
			-0.0089
Izz			-0.0078
			-0.0068
	31.9837	29.1906	-0.0058
	25.2369	22.8969	
	19.6164	17.6778	K14 * 1.0e+008
	14.9896	13.4038	
	11.2321	9.9538	
xle			2.1844
			1.9228
	0.3000	0.3000	
	0.3000	0.3000	1.6827
	0.3000	0.3000	
	0.3000	0.3000	1.4633
	0.3000	0.3000	
	0.3000	0.3000	1.2635
yle			
			K22 * 1.0e+006
	0	0	
	0	0	
	0	0	6.7628
			5.7300
			4.8196
			4.0216
	0	0	
	0	0	3.3262
			K23

0		Ixx
0		
0	11.1477	10.5447
0	9.4656	8.9344
0	7.9801	7.5148
K24	6.6754	6.2705
	5.5363	5.1863
0		Ixy
0		
0	0	0
0	0	0
0	0	0
0	0	0
K33 * 1.0e+006	0	0
5.2435		Ixz
4.4427		
3.7369	0	0
3.1181	0	0
2.5790	0	0
K34	0	0
-0.0036		Iyy
-0.0030		
-0.0026	0.1773	0.1677
-0.0021	0.1506	0.1421
-0.0018	0.1269	0.1195
K44 * 1.0e+008	0.1062	0.0997
	0.0881	0.0825
3.2443		Iyz * 1.0e-009
2.7488		
2.3121	-0.1211	-0.1145
1.9292	-0.1028	-0.0970
1.5957	-0.0867	-0.0816
mass	-0.0725	-0.0681
	-0.0601	-0.0563
15.5004	15.2157	Izz
14.1844	13.9140	
12.9254	12.6692	10.9704
11.7233	11.4813	10.3769
10.5782	10.3505	9.3150
		8.7923
		7.8532
		7.3953

6.5692	6.1707	
5.4482	5.1038	
		yle
xle		
		0 0
		0 0
0.3000	0.3000	0 0
0.3000	0.3000	0 0
0.3000	0.3000	0 0
0.3000	0.3000	0 0
0.3000	0.3000	0 0

C.2 Joined-Wing Configuration

For the Joined-Wing configuration, the member and group definitions are shown in Fig. C.2. Cross-sectional stiffness and inertia distributions of each member are listed as follows.

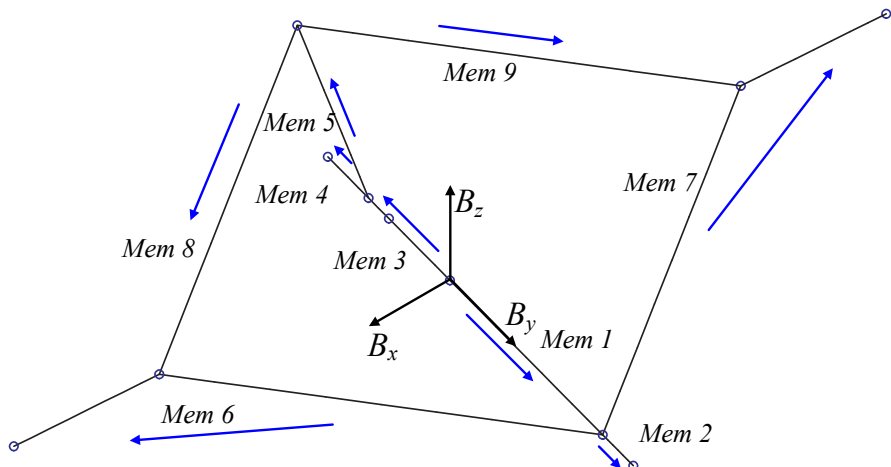


Figure C.2: Member and group definitions for the Joined-Wing configuration (arrows indicate the kinematics marching direction and element progression as presented below)

Member 1

K11 * 1.0e+009	1.1542
	1.1542
	1.1542

1.1542	0
1.1542	0
	0
K12	0
0	K33 * 1.0e+008
0	
0	5.7292
0	5.7292
0	5.7292
0	5.7292
K13 * 1.0e-008	5.7292
0.3725	K34 * 1.0e-007
0.3725	
0.3725	-0.1490
0.3725	-0.1211
-0.3725	-0.1211
K14 * 1.0e-010	-0.1211
-0.1602	K44 * 1.0e+008
-0.1602	
-0.1602	5.7328
-0.1602	5.7328
-0.1602	5.7328
K22 * 1.0e+008	5.7328
4.4005	mass
4.4005	
4.4005	44.1611 44.1611
4.4005	44.1611 44.1611
4.4005	44.1611 44.1611
K23	44.1611 44.1611
0	Ixx
0	
0	43.8533 43.8533
0	43.8533 43.8533
0	43.8533 43.8533
K24	43.8533 43.8533
0	Ixy

0 0	yle
0 0	
0 0	0 0
0 0	0 0
0 0	0 0
Ixz	0 0
0 0	<u>Member 2</u>
0 0	
0 0	K11 * 1.0e+009
0 0	
0 0	1.0213
Iyy	0.7555
	0.4896
21.9198 21.9198	K12
21.9198 21.9198	
21.9198 21.9198	0
21.9198 21.9198	0
21.9198 21.9198	0
Iyz * 1.0e-015	K13 * 1.0e-008
-0.4025 0.4857	
-0.0694 -0.0625	0
-0.0625 -0.4025	0.4657
-0.0625 -0.0625	-0.0466
-0.4302 0.0416	K14 * 1.0e-006
Izz	0.1192
	-0.0298
21.9335 21.9335	0.0074
21.9335 21.9335	
21.9335 21.9335	K22 * 1.0e+008
21.9335 21.9335	
21.9335 21.9335	3.0485
xle	1.2338
	0.3358
0.5000 0.5000	K23
0.5000 0.5000	
0.5000 0.5000	0
0.5000 0.5000	0
0.5000 0.5000	0

K24	0 0 0 0
	0 Iyy
	0 21.9198 15.1852
	0 9.9941 6.1456
K33 * 1.0e+008	0 3.4388 1.6728
	3.9690 Iyz * 1.0e-015
	1.6063
	0.4372 -0.4025 -0.5274
	-0.0035 0.0694
K34 * 1.0e-008	-0.1041 -0.0763
	-0.8382 Izz
	-0.4424
	-0.1455 21.9335 15.1947
	10.0003 6.1494
K44 * 1.0e+008	3.4410 1.6739
	3.9714 xle
	1.6073
	0.4375 0.5000 0.5000
mass	0.5000 0.5000
	44.1611 39.0752 yle
	33.9893 28.9035
	23.8176 18.7317 0 0
Ixx	0 0
	43.8533 30.3799 <u>Member 3</u>
	19.9945 12.2951
	6.8798 3.3467 K11 * 1.0e+009
Ixy	1.1542
	0 0 1.1542
	0 0 1.0581
	0 0 K12
Ixz	0
	0 0 0

		5.7328
K13 * 1.0e-008		4.4157
	0.3725	mass
	0.3725	
	-0.1863	44.1611 44.1611
		44.1611 44.1611
K14 * 1.0e-010		44.1611 40.4810
	-0.1602	Ixx
	-0.1602	
	-0.1346	43.8533 43.8533
		43.8533 43.8533
K22 * 1.0e+008		43.8533 33.7782
	4.4005	Ixy
	4.4005	
	3.3895	0 0
		0 0
K23		0 0
	0	Ixz
	0	
	0	0 0
		0 0
K24		0 0
	0	Iyy
	0	
	0	21.9198 21.9198
		21.9198 21.9198
K33 * 1.0e+008		21.9198 16.8838
	5.7292	Iyz * 1.0e-015
	5.7292	
	4.4129	-0.4025 -0.4025
		-0.4025 -0.4025
K34 * 1.0e-007		-0.4025 0.0625
	-0.1211	Izz
	-0.1211	
	-0.1211	21.9335 21.9335
		21.9335 21.9335
K44 * 1.0e+008		21.9335 16.8943
	5.7328	xle

			0
0.5000	0.5000		
0.5000	0.5000		K33 * 1.0e+008
0.5000	0.5000		
yle			2.4170
			1.1372
0	0		K34 * 1.0e-008
0	0		
0	0		-0.7451
			-0.2328
<u>Member 4</u>			
			K44 * 1.0e+008
K11	* 1.0e+008		
			2.4185
8.6568			1.1379
6.7331			
		mass	
K12			36.8009 33.1208
0			29.4408 25.7607
0			
		Ixx	
K13	* 1.0e-008		
			25.3780 18.5006
0.8382			12.9936 8.7047
0			
		Ixy	
K14	* 1.0e-007		
			0 0
-0.2981			0 0
-0.0001			
		Ixz	
K22	* 1.0e+008		
			0 0
1.8565			0 0
0.8735			
		Iyy	
K23			
			12.6851 9.2474
0			6.4948 4.3510
0			
		Iyz	* 1.0e-015
K24			
			-0.1353 -0.3504
0			-0.2186 -0.2377

		K22 * 1.0e+007
Izz		6.1299
12.6930	9.2532	3.6193
6.4988	4.3537	1.9721
		0.9633
xle		
		K23
0.5000	0.5000	
0.5000	0.5000	0
		0
yle		0
		0
0	0	
0	0	
		K24
<u>Member 5</u>		0
		0
K11 * 1.0e+009		0
		0
1.3043		
0.9996		K33 * 1.0e+007
0.7353		
0.5115		7.7978
		4.5627
K12		2.4569
		1.1808
0		
0		K34
0		
0		0.0011
K13 * 1.0e-003		0.0007
		0.0004
		0.0002
-0.9295		
-0.8941		K44 * 1.0e+009
-0.7892		
-0.6380		3.2797
		1.9192
K14 * 1.0e+007		1.0336
		0.4969
-7.6634		
-5.1273		mass
-3.2233		
-1.8608		77.1956 72.6121
		59.9062 55.8699

44.8057	41.3168		
31.8943	28.9526	0.5000	0.5000
Ixx		0.5000	0.5000
		0.5000	0.5000
230.2534	191.6265		
138.8188	112.6078	yle	
77.7695	60.9800		
39.4859	29.5369	0	0
		0	0
Ixy		0	0
		0	0
0	0		
0	0	<u>Members 6 and 7</u>	
0	0		
0	0	K11 * 1.0e+008	
Ixz		9.1669	
		6.0901	
0	0	4.5106	
0	0	3.0346	
0	0	4.4895	
0	0	2.1177	
Iyy		1.3144	
		0.4888	
5.2780	4.3926	K12	
3.1815	2.5808		
1.7819	1.3972	0	
0.9044	0.6765	0	
		0	
Iyz * 1.0e-008		0	
		0	
0.1015	0.0844	0	
0.0620	0.0503	0	
0.0354	0.0277	0	
0.0184	0.0138		
Izz		K13 * 1.0e+005	
		8.0030	
224.9753	187.2339	4.3333	
135.6374	110.0270	2.9405	
75.9876	59.5828	2.1794	
38.5815	28.8604	1.6480	
xle		0.8064	
		0.4660	

0.1332		K33 * 1.0e+007
K14 * 1.0e+006		3.0482
-2.6163		1.5938
-1.4197		0.8979
-0.9621		0.4390
-0.7090		0.5122
-0.5440		0.2421
-0.2669		0.1303
-0.1543		0.0363
-0.0441		K34 * 1.0e+006
K22 * 1.0e+007		-6.6316
2.0160		-3.4670
1.1300		-1.9533
0.6122		-0.9554
0.2277		-1.1137
0.4239		-0.5541
0.1911		-0.2981
0.1028		-0.0789
0.0313		K44 * 1.0e+008
K23		7.8754
0		4.1221
0		2.3209
0		1.1305
0		1.3280
0		0.4629
0		0.2491
0		0.0942
0	mass	
K24		51.4542 48.6978
0		35.4362 33.3101
0		26.0408 24.2653
0		15.9677 14.7071
0		27.1772 26.3279
0		15.7799 15.2539
0		9.8186 9.4679
0		3.0391 2.9222
0	Ixx	

52.7151	44.6888	-0.1313	-0.1062
29.0450	24.1243	-0.0597	-0.0467
16.4957	13.3464	-0.0727	-0.0661
7.4420	5.8149	-0.0371	-0.0336
9.1974	8.3618	-0.0201	-0.0181
4.7035	4.2486	-0.0054	-0.0048
2.5494	2.2859		
0.6804	0.6049	I _{zz}	

I _{xy}	50.7811	43.0492
	27.9814	23.2409
0 0	15.8910	12.8572
0 0	7.1672	5.6002
0 0	8.8621	8.0570
0 0	4.5322	4.0939
0 0	2.4566	2.2026
0 0	0.6556	0.5828
0 0		xle

I _{xz}	0.4869	0.4869
	0.4869	0.4869
0 0	0.4869	0.4869
0 0	0.4869	0.4869
0 0	0.4869	0.4869
0 0	0.4869	0.4869
0 0	0.4869	0.4869
0 0	0.4869	0.4869
0 0	0.4869	0.4869
0 0		yle

I _{yy}	0.0282	0.0282
	0.0282	0.0282
1.9341 1.6396	0.0282	0.0282
1.0635 0.8834	0.0282	0.0282
0.6047 0.4892	0.0282	0.0282
0.2749 0.2148	0.0282	0.0282
0.3353 0.3048	0.0282	0.0282
0.1713 0.1547	0.0282	0.0282
0.0928 0.0832	0.0282	0.0282
0.0248 0.0220		<u>Members 8 and 9</u>

I _{yz}	K11 * 1.0e+008	
-0.4199 -0.3560	9.1669	
-0.2308 -0.1917	6.0901	

4.5106	
3.0346	
K12	
0	3.0482
0	1.5938
0	0.8979
0	0.4390
0	
0	K34 * 1.0e+006
0	
0	-6.6316
0	-3.4670
K13 * 1.0e+005	-1.9533
	-0.9554
8.0030	
4.3333	K44 * 1.0e+008
2.9405	
2.1794	7.8754
K14 * 1.0e+006	4.1221
	2.3209
	1.1305
-2.6163	
-1.4197	mass
-0.9621	
-0.7090	51.4542 48.6978
K22 * 1.0e+007	35.4362 33.3101
	26.0408 24.2653
	15.9677 14.7071
2.0160	
1.1300	Ixx
0.6122	
0.2277	52.7151 44.6888
K23	29.0450 24.1243
	16.4957 13.3464
	7.4420 5.8149
0	
0	Ixy
0	
0	0 0
0	0 0
K24	0 0
	0 0
0	
0	Ixz
0	
0	0 0
0	0 0
K33 * 1.0e+007	0 0

0	0		27.9814	23.2409
Iyy			15.8910	12.8572
			7.1672	5.6002
		xle		
1.9341	1.6396			
1.0635	0.8834			
0.6047	0.4892		0.4869	0.4869
0.2749	0.2148		0.4869	0.4869
Iyz			0.4869	0.4869
-0.4199	-0.3560	yle		
-0.2308	-0.1917			
-0.1313	-0.1062		0.0282	0.0282
-0.0597	-0.0467		0.0282	0.0282
Izz			0.0282	0.0282
50.7811	43.0492			

The wing and vertical tail structures of the Joined-Wing configuration are built with composite materials. For the layups of their cross-sections, the top and bottom skins have ply groups composed of [0/+45/-45/0] and the web with ply group of [0₄]. Every ply is made of S-glass, whose material properties are listed in Table C.1.

Table C.1: Material properties of S-glass

Density (kg/m ³)	1855
Q ₁₁ (GPa)	48.0
Q ₁₂ (GPa)	3.5
Q ₂₂ (GPa)	12.2
Q ₆₆ (GPa)	3.6

Note: 1 – fiber direction; 2 – transverse to fiber; 6 – shear

The distributions of skin ply thickness for each element within vertical tail and wing members are listed as follows. The web thickness is four times the thickness of a 0-degree ply group at a given element.

<u>Member 5</u>	0.5715
	0.4572
0° ply (mm)	0.2286
	0.8001
0.9144	0.5143
0.8001	0.3429
0.6858	0.1143
0.5715	-45° ply (mm)
+45° ply (mm)	0.6858
	0.5715
0.6858	0.4572
0.6096	0.2286
0.5334	0.8001
0.4572	0.5143
-45° ply (mm)	0.3429
	0.1143
0.6858	0° ply (mm)
0.6096	1.0859
0.5334	0.8001
0.4572	0.6858
0° ply (mm)	0.5715
0.9144	0.8573
0.8001	0.5143
0.6858	0.3429
0.5715	0.1143

Members 6 and 7

0° ply (mm)	0° ply (mm)
1.0859	1.0859
0.8001	0.8001
0.6858	0.6858
0.5715	0.5715
0.8573	+45° ply (mm)
0.5143	0.6858
0.3429	0.5715
0.1143	0.4572
+45° ply (mm)	0.2286
	0.6858

Members 8 and 9

-45° ply (mm)	0° ply (mm)
0.6858	1.0859
0.5715	0.8001
0.4572	0.6858
0.2286	0.5715

C.3 Blended-Wing-Body Configuration

For the Blended-Wing-Body configuration, the member and group definitions are shown in Fig. C.3. Cross-sectional stiffness and inertia distributions of each member are listed as follows.

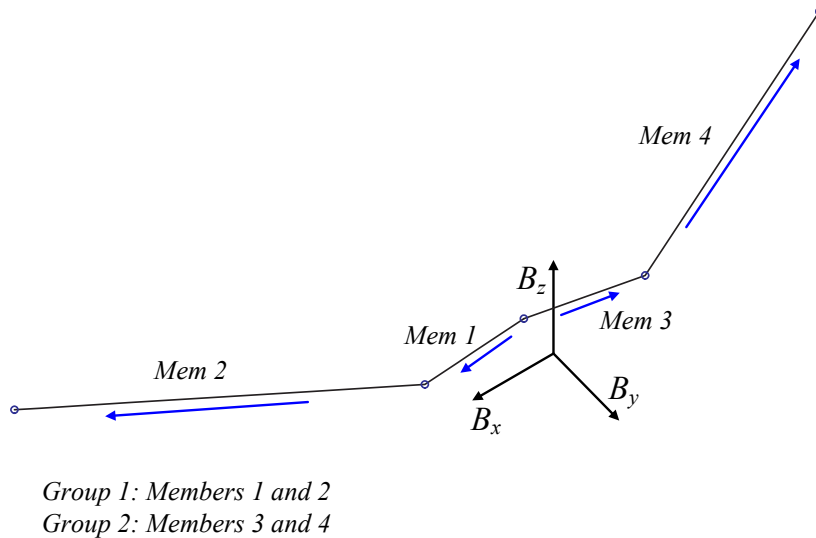


Figure C.3: Member and group definitions for the Blended-Wing-Body configuration (arrows indicate the kinematics marching direction and element progression as presented below)

Members 1 and 3 3.6052

K11 * 1.0e+009 K12

3.6052	0
3.6052	0

0		4.7339
		0.7608
K13		0.2002
0	Mass * 1.0e+003	
0		
0	2.1291 0.1284	
	0.1284 0.1100	
K14	0.1100 0.2833	
0	Ixx * 1.0e+004	
0		
0	1.7143 0.1836	
	0.1836 0.0615	
K22 * 1.0e+010	0.0615 0.0368	
1.2045	Ixy	
0.2946		
0.1692	0 0	
	0 0	
K23	0 0	
0	Ixz	
0		
0	0 0	
	0 0	
K24	0 0	
0	Iyy * 1.0e+003	
0		
0	3.2704 0.3163	
	0.3163 0.1102	
K33 * 1.0e+009	0.1102 0.0621	
1.1912	Iyz	
1.5814		
1.2682	0 0	
	0 0	
K34	0 0	
0	Izz * 1.0e+004	
0		
0	9.6466 0.7405	
	0.7405 0.3043	
K44 * 1.0e+011	0.3043 0.1839	

xle		K14
0.6438	0.5812	
0.5812	0.5186	0
0.5186	0.4560	0
		0
yle		0
		0
0	0	0
0	0	0
0	0	0
<u>Members 2 and 4</u>		K22 * 1.0e+007
K11 * 1.0e+009		2.7121
		1.8673
4.2337		2.1494
3.5060		2.4857
4.2642		3.0821
4.6061		2.2660
4.0449		1.4219
3.1126		0.4598
2.5944		
1.2258		K23
K12		0
		0
0		0
0		0
0		0
0		0
0		0
0		0
0		0
0		0
0		K24
K13		0
		0
0		0
0		0
0		0
0		0
0		0
0		0
0		0
0		K33 * 1.0e+007

2.1368		2.1323	2.5825
1.8020		2.5825	5.0712
1.6673		5.0712	5.7635
1.9142		5.3848	2.5099
2.5942		2.5099	1.9261
3.0938		1.9261	1.6731
3.1902		1.6731	0.0000
1.1530		Ixy	
K34		0	0
0		0	0
0		0	0
0		0	0
0		0	0
0		0	0
0		0	0
0		0	0
0		Ixz	
K44 * 1.0e+009		0	0
0.4726		0	0
0.4092		0	0
0.9685		0	0
1.1418		0	0
0.7080		0	0
0.3870		0	0
0.3260		Iyy	
0.2989		0	0
mass		0.2349	0.2245
49.4267	37.4048	0.2245	0.1855
37.4048	45.1907	0.1855	0.1894
45.1907	48.0717	0.1894	0.2439
48.0717	50.9219	0.2439	0.3161
50.9219	38.1495	0.3161	0.3578
38.1495	32.2195	0.3578	0.2510
32.2195	19.8132	0.2510	0.0000
19.8132	0.0000	Iyz	
Ixx		0	0
2.5825	2.1323	0	0

0	0		0.4560	0.4560
0	0		0.4560	0.4560
0	0		0.4560	0.4560
0	0		0.4560	0.4560
0	0		0.4560	0.4560
		Izz	0.4560	0.4560
2.3475	1.9078		yle	
1.9078	2.3970			
2.3970	4.8818		0	0
4.8818	5.5196		0	0
5.1409	2.1938		0	0
2.1938	1.5683		0	0
1.5683	1.4221		0	0
1.4221	0.0000		0	0
		xle	0	0
0.4560	0.4560			

BIBLIOGRAPHY

BIBLIOGRAPHY

- [1] Tilmann, C. P., P. M. Flick, C. A. Martin and M. H. Love. "High-Altitude Long Endurance Technologies for SensorCraft." RTO Paper MP-104-P-26, *RTO AVT Symposium on Novel and Emerging Vehicle and Vehicle Technology Concepts*, Brussels, Belgium, Apr., 2003.
- [2] Noll, T. E., J. M. Brown, M. E. Perez-Davis, S. D. Ishmael, G. C. Tiffany and M. Gaier. "Investigation of the Helios Prototype Aircraft Mishap. Volume 1, Mishap Report." NASA Report. Jan., 2004.
- [3] Friedmann, P. P. "Renaissance of Aeroelasticity and Its Future." *Journal of Aircraft*, Vol. 36, No. 1, Jan.-Feb., 1999, pp. 105-121.
- [4] Livne, E. and T. A. Weisshaar. "Aeroelasticity of Nonconventional Airplane Configurations - Past and Future." *Journal of Aircraft*, Vol. 40, No. 6, Nov.-Dec., 2003, pp. 1047-1065.
- [5] Livne, E. "Future of Airplane Aeroelasticity." *Journal of Aircraft*, Vol. 40, No. 6, Nov.-Dec., 2003, pp. 1066-1092.
- [6] Dowell, E., J. Edwards and T. Strganac. "Nonlinear Aeroelasticity." *44th AIAA/ASME/ASCE/AHS Structures, Structural Dynamics, and Materials Conference*, Norfolk, VA, Apr. 7-10, 2003.
- [7] van Shoor, M. C., S. H. Zerweck and A. H. von Flotow. "Aeroelastic Stability and Control of a Highly Flexible Aircraft." AIAA-89-1187-CP, Proceedings of *30th AIAA / ASME / ASCE / AHS / ASC Structures, Structural Dynamics and Materials Conference*, Mobile, AL, Apr. 3-5, 1989.
- [8] Drela, M. "Integrated Simulation Model for Preliminary Aerodynamic, Structural, and Control-Law Design of Aircraft." AIAA-99-1394, Proceedings of *40th AIAA / ASME / ASCE / AHS / ASC Structures, Structural Dynamics, and Materials Conference and Exhibit*, St. Louis, MO, Apr. 12-15, 1999.

- [9] Patil, M. J., D. H. Hodges and C. E. S. Cesnik. "Nonlinear Aeroelasticity and Flight Dynamics of High-Altitude Long Endurance Aircraft." *Journal of Aircraft*, Vol. 38, No. 1, Jan. - Feb., 2001, pp. 88-94.
- [10] Patil, M. J., D. H. Hodges and C. E. S. Cesnik. "Nonlinear Aeroelastic Analysis of Complete Aircraft in Subsonic Flow." *Journal of Aircraft*, Vol. 37, No. 5, Sep. - Oct., 2000, pp. 753-760.
- [11] Hodges, D. H. and E. H. Dowell. "Nonlinear Equations of Motion for Elastic Bending and Torsion of Twisted Non-uniform Blades." NASA TN D-7818, 1974.
- [12] Hodges, D. H. and R. A. Ormiston. "Stability of Elastic Bending and Torsion of Uniform Cantilever Rotor Blades in Hover with Variable Structural Coupling." NASA TN D08192.
- [13] Hodges, D. H. "Finite Rotation and Nonlinear Beam Kinematics." *Vertica*, Vol. 11, No. 1/2, 1987, pp. 297-307.
- [14] Chang, C.-S., D. H. Hodges and M. J. Patil. "Flight Dynamics of Highly Flexible Aircraft." *Journal of Aircraft*, Vol. 45, No. 2, Mar.-Apr., 2008, pp. 538-545.
- [15] Shearer, C. M. *Coupled Nonlinear Flight Dynamics, Aeroelasticity, and Control of Very Flexible Aircraft*. Ph.D. Dissertation, The University of Michigan, Ann Arbor, MI, Aug., 2006.
- [16] Wolkovitch, J. "The Joined Wing: An Overview." *Journal of Aircraft*, Vol. 23, No. 3, 1996, pp. 161-178.
- [17] Livne, E. "Aeroelasticity of Joined-Wing Airplane configurations: Past Work and Future Challenges - a Survey." AIAA-2001-1370, *42nd AIAA / ASME / ASCE / AHS Structures, Structural Dynamics, and Materials Conference*, Seattle, WA, Apr. 16-19, 2001.
- [18] Lin, H.-H., J. Jhou and R. Stearman. "Influence of Joint Fixity on the Aeroelastic Characteristics of a Joined Wing Structure." AIAA-90-0980-CP, Proceedings of *31st AIAA / ASME / ASCE / AHS / ASC Structures, Structural Dynamics and Materials Conference*, Long Beach, CA, Apr. 2-4, 1990, pp. 1442-1454.
- [19] Samuels, M. F. "Structural Weight Comparison of a Joined Wing and a Conventional Wing." *Journal of Aircraft*, Vol. 19, No. 6, Jun., 1982, pp. 485-491.
- [20] Gallman, J. W. and I. M. Kroo. "Structural Optimization for Joined-Wing Synthesis." *Journal of Aircraft*, Vol. 33, No. 1, Jan. - Feb., 1996, pp. 214-223.

- [21] Miura, H., A. T. Shyu and J. Wolkovitch. "Parameter Weight Evaluation of Joined Wing by Structural Optimization." *Journal of Aircraft*, Vol. 25, No. 12, 1988, pp. 1142-1149.
- [22] Blair, M. and R. Canfield. "A Joined-Wing Structural Weight Modeling Study." AIAA-2002-1337, *43rd AIAA / ASME / ASCE / AHS / ASC Structures, Structural Dynamics, and Materials Conference*, Denver, CO, Apr. 22-25, 2002.
- [23] Kroo, I. M., J. W. Gallman and S. C. Smith. "Aerodynamic and Structural Studies of Joined-Wing Aircraft." *Journal of Aircraft*, Vol. 28, No. 1, 1991, pp. 74-81.
- [24] Gallman, J. W. and S. C. Smith. "Optimization of Joined Wing Aircraft." *Journal of Aircraft*, Vol. 30, No. 6, Nov. - Dec., 1993, pp. 897-965.
- [25] Roberts Jr., R. W., R. A. Canfield and M. Blair. "Sensor-Craft Structural Optimization and Analytical Certification." AIAA-2003-1458, *44th AIAA / ASME / ASCE / AHS Structures, Structural Dynamics, and Materials Conference*, Norfolk, VA, Apr. 7-10, 2003.
- [26] Rasmussen, C. C., R. A. Canfield and M. Blair. "Optimization Process for Configuration of Flexible Joined-wing." AIAA-2004-4330, *10th AIAA / ISSMO Multidisciplinary Analysis and Optimization Conference*, Albany, NY, Aug. 30 - Sep. 1, 2004.
- [27] Reich, G. W., D. Raveh and P. S. Zink. "Application of Active Aeroelastic Wing Technology to a Joined-Wing Sensorcraft." AIAA-2002-1633, *43rd AIAA / ASME / ASCE / AHS / ASC Structures, Structural Dynamics, and Materials Conference*, Denver, CO, Apr. 22-25, 2002.
- [28] Cesnik, C. E. S. and E. L. Brown. "Active Wing Warping Control of a Joined-Wing Airplane Configuration." AIAA-2003-1715, *44th AIAA / ASME / ASCE / AHS / ASC Structures, Structural Dynamics, and Materials Conference*, Norfolk, VA, Apr. 7-10, 2003.
- [29] Cesnik, C. E. S. and W. Su. "Nonlinear Aeroelastic Modeling and Analysis of Fully Flexible Aircraft." AIAA-2005-2169, *46th AIAA / ASME / ASCE / AHS / ASC Structures, Structural Dynamics, and Materials Conference*, Austin, TX, Apr. 18-21, 2005.
- [30] Demasi, L. and E. Livne. "Exploratory Studies of Joined Wing Aeroelasticity." AIAA-2005-2172, *46th AIAA / ASME / ASCE / AHS / ASC Structures, Structural Dynamics, and Materials Conference*, Austin, TX, Apr. 18-21, 2005.
- [31] Demasi, L. and E. Livne. "The Structural Order Reduction Challenge in the Case of Geometrically Nonlinear Joined-Wing Configurations." AIAA-2007-2052,

48th AIAA / ASME / ASCE / AHS / ASC Structures, Structural Dynamics, and Materials Conference, Honolulu, HI, Apr. 23-26, 2007.

- [32] Demasi, L. and E. Livne. "Dynamic Aeroelasticity Coupling Full Order Geometrically Nonlinear Structures and Full Order Linear Unsteady Aerodynamics - The Joined Wing Case." AIAA-2008-1818, *49th AIAA / ASME / ASCE / AHS / ASC Structures, Structural Dynamics, and Materials Conference*, Schaumburg, IL, Apr. 7-10, 2008.
- [33] Weisshaar, T. A. and D. Lee. "Aeroelastic Tailoring of Joined-Wing Configurations." AIAA-2002-1207, *43rd AIAA / ASME / ASCE / AHS / ASC Structures, Structural Dynamics, and Materials Conference*, Denver, CO, Apr. 22-25, 2002.
- [34] Lee, D.-H. *Aeroelastic Tailoring and Structural Optimization of Joined-Wing Configurations*. Ph. D. Dissertation, Perdue University, West Lafayette, IN, Jul., 2002.
- [35] Begin, L. "The Northrop Flying Wing Prototypes." AIAA-1983-1047, *Proceedings of Aircraft Prototype and Technology Demonstrator Symposium*, Dayton, OH, Mar. 23 - 24, 1983, pp. 135-144.
- [36] Liebeck, R. H., M. A. Page and B. K. Rawdon. "Blended-Wing-Body Subsonic Commercial Transport." AIAA-98-0438, *36th Aerospace Sciences Meeting & Exhibit*, Reno, NV, Jan. 12-15, 1998.
- [37] Weisshaar, T. A. and H. Ashley. "Static Aeroelasticity and the Flying Wing." AIAA-1973-397, *14th AIAA / ASME / SAE Structures, Structural Dynamics, and Materials Conference*, Williamsburg, VA, Mar. 20-22, 1973.
- [38] Fremaux, C. M., D. M. Vairo and R. D. Whipple. "Effect of Geometry, Static Stability, and Mass Distribution on the Tumbling Characteristics of Generic Flying-Wing Models." AIAA-1993-3615-CP, 1993.
- [39] Esteban, S. "Static and Dynamic Analysis of an Unconventional Plane: Flying Wing." *AIAA Atmospheric Flight Mechanics Conference and Exhibit*, Montreal, Canada, Aug. 6-9, 2001.
- [40] Mialon, B., T. Fol and C. Bonnaud. "Aerodynamic Optimization of Subsonic Flying Wing Configurations." *20th AIAA Applied Aerodynamics Conference*, St. Louis, MO, Jun. 24-26, 2002.
- [41] Sevant, N. E., M. I. G. Bloor and M. J. Wilson. "Aerodynamic Design of a Flying Wing Using Response Surface Methodology." *Journal of Aircraft*, Vol. 37, No. 4, Jul. - Aug., 2000, pp. 562-569.

- [42] Love, M. H., P. S. Zink, P. A. Wieselmann and H. Youngren. "Body Freedom Flutter of High Aspect Ratio Flying Wings." AIAA-2005-1947, *46th AIAA / ASME / ASCE / AHS Structures, Structural Dynamics, and Materials Conference*, Austin, TX, Apr. 18-21, 2005.
- [43] Liebeck, R. H. "Blended Wing Body Design Challenges." *AIAA/ICAS International Air and Space Symposium and Exposition: The Next 100 Years*, Dayton, OH, Jul. 14-17, 2003.
- [44] Mukhopadhyay, V. "Nonlinear Blended-Wing-Body (BWB) Fuselage Structural Design for Weight Reduction." AIAA-2005-2349, *46th AIAA / ASME / ASCE / AHS / ASC Structures, Structural Dynamics, and Materials Conference*, Austin, TX, Apr. 18-21, 2005.
- [45] Wakayama, S. "Multidisciplinary Design Optimization of the Blended-Wing-Body." AIAA-1998-4938, *7th AIAA / USAF / NASA / ISSMO Symposium on Multidisciplinary Analysis and Optimization*, St. Louis, MO, Sep. 2-4, 1998.
- [46] Wakayama, S. "Blended-Wing-Body Optimization Problem Setup." AIAA-2000-4740, *8th AIAA / USAF / NASA / ISSMO Symposium on Multidisciplinary Analysis and Optimization*, Long Beach, CA, Sep. 6-8, 2000.
- [47] Wakayama, S. and I. Kroo. "The Challenge and Promise of Blended-Wing-Body Optimization." AIAA-1998-4736, *7th AIAA / USAF / NASA / ISSMO Symposium on Multidisciplinary Analysis and Optimization*, St. Louis, MO, Sep. 2-4, 1998.
- [48] Ko, A., L. T. Leifsson, W. H. Mason, J. A. Schetz, B. Grossman and R. T. Haftka. "MDO of a Blended-Wing-Body Transport Aircraft with Distributed Propulsion." AIAA-2003-6732, *AIAA's 3rd Annual Aviation Technology, Integration, and Operations (ATIO) Tech*, Denver, CO, Nov. 17-19, 2003.
- [49] Beran, P. S., J. Y. Hur, R. D. Snyder, D. Strong, D. Bryson and T. Strganac. "Static Nonlinear Aeroelastic Analysis of a Blended Wing Body." AIAA-2005-1994, *46th AIAA / ASME / ASCE / AHS / ASC Structures, Structural Dynamics, and Materials Conference*, Austin, TX, Apr. 18-21, 2005.
- [50] Lockyer, A. J., A. Drake, J. Bartley-Cho, E. Vartio, D. Solomon and T. Shimko. "High Lift over Drag Active (HiLDA) Wing." AFRL-VA-WP-TR-2005-3066. Apr., 2005.
- [51] Patil, M. J. and D. H. Hodges. "Flight Dynamics of Highly Flexible Flying Wings." *International Forum on Aeroelasticity and Structural Dynamics, 2005*, Munich, Germany, Jun. 28 - Jul. 1, 2005.

- [52] Su, W. and C. E. S. Cesnik. "Dynamic Response of Highly Flexible Flying Wings." AIAA-2006-1636, *47th AIAA / ASME / ASCE / AHS / ASC Structures, Structural Dynamics, and Materials Conference*, Newport, RI, May 1-4, 2006.
- [53] Patil, M. J. and D. J. Taylor. "Gust Response of Highly Flexible Aircraft." AIAA-2006-1638, *47th AIAA / ASME / ASCE / AHS / ASC Structures, Structural Dynamics, and Materials Conference*, Newport, RI, May 1-4 2006.
- [54] Patil, M. J. "Nonlinear Gust Response of Highly Flexible Aircraft." AIAA-2007-2103, *48th AIAA / ASME / ASCE / AHS / ASC Structures, Structural Dynamics, and Materials Conference*, Honolulu, HI, Apr. 23-26, 2007.
- [55] Wang, Z., P. C. Chen, D. D. Liu, D. T. Mook and M. J. Patil. "Time Domain Nonlinear Aeroelastic Analysis for HALE Wings." AIAA-2006-1640, *47th AIAA / ASME / ASCE / AHS / ASC Structures, Structural Dynamics, and Materials Conference*, Newport, RI, May 1-4, 2006.
- [56] Hoblit, F. M. *Gust Loads on Aircraft: Concepts and Applications*. AIAA Education Series, Washington, DC: American Institute of Aeronautics and Astronautics, Inc., 1988, pp. 29-46.
- [57] Chen, P. C. "Nonhomogeneous State-Space Approach for Discrete Gust Analysis of Open-Loop / Closed-Loop Aeroelastic Systems." AIAA-2002-1715, *43rd AIAA / ASME / ASCE / AHS / ASC Structures, Structural Dynamics, and Materials Conference*, Denver, CO, Apr. 22-25, 2002.
- [58] Lee, Y.-N. and C. E. Lan. "Analysis of Random Gust Responses with Nonlinear Unsteady Aerodynamics." *AIAA Journal*, Vol. 38, No. 8, Aug., 2000, pp. 1305-1312.
- [59] Hodges, D. H., A. R. Atilgan, C. E. S. Cesnik and M. V. Fulton. "On a Simplified Strain Energy Function for Geometrically Nonlinear Behavior of Anisotropic Beams." *Composites Engineering*, Vol. 2, No. 5-7, 1992.
- [60] Cesnik, C. E. S., D. H. Hodges and V. G. Sutyrin. "Cross-Sectional Analysis of Composite Beams Including large Initial Twist and Curvature Effects." *AIAA Journal*, Vol. 34, No. 9, 1996.
- [61] Popescu, B., D. H. Hodges and C. E. S. Cesnik. "Obliqueness Effects in Asymptotic Cross-Sectional Analysis of Composite Beams." *Computers and Structures*, Vol. 76, No. 4, 2000, pp. 533-543.
- [62] Cesnik, C. E. S., V. G. Sutyrin and D. H. Hodges. "Refined Theory of Composite Beams: 'The Role of Short-Wavelength Extrapolation'." *International Journal of Solids and Structures*, Vol. 33, No. 10, 1996.

- [63] Popescu, B. and D. H. Hodges. "On Asymptotic Correct Timoshenko-like Anisotropic Beam Theory." *International Journal of Solids and Structures*, Vol. 37, No. 3, 2000, pp. 535-558.
- [64] Yu, W., D. H. Hodges and C. E. S. Cesnik. "On Timoshenko-like Modeling of Initially Curved and Twisted Composite Beams." *International Journal of Solids and Structures*, Vol. 39, No. 19, 2002, pp. 5101-5121.
- [65] Cesnik, C. E. S. and S.-J. Shin. "On the Modeling of Active Helicopter Blades." *International Journal of Solids and Structures*, Vol. 38, No. 10-13, 2001, pp. 1765-1789.
- [66] Cesnik, C. E. S. and M. Ortega-Morales. "Active Beam Cross-Sectional Modeling." *Journal of Intelligent Material Systems and Structures*, Vol. 12, No. 7, 2001, pp. 483-496.
- [67] Cesnik, C. E. S. and R. Palacios. "Modeling Piezocomposite Actuators Embedded in Slender Structures." *44th AIAA/ASME/ASCE/AHS Structures, Structural Dynamics, and Materials Conference*, Norfolk, VA, Apr. 7-10, 2003.
- [68] Cesnik, C. E. S. and D. H. Hodges. "VABS: A New Concept for Composite Rotor Blade Cross-Sectional Modeling." *Journal of the American Helicopter Society*, Vol. 42, No. 1, 1997, pp. 27-38.
- [69] MSC.Software. *MSC.Nastran 2004 Quick reference Guide - Volume 1*. Santa Ana, CA: MSC.Software Corporation, 2003.
- [70] Hodges, D. H. "A Mixed Variational Formulation Based on Exact Intrinsic Equations for Dynamics of Moving Beams." *Journal of Solids and Structures*, Vol. 26, 1990, pp. 1253-1273.
- [71] Shang, X. *Aeroelastic Stability of Composite Hingeless Rotors with Finite-state Unsteady Aerodynamics*. PhD Dissertation, Georgia Institute of Technology, Atlanta, GA, 1995.
- [72] Cheng, T. *Structural Dynamics Modeling of Helicopter Blades for Computational Aeroelasticity*. Master's Thesis, Massachusetts Institute of Technology, Cambridge, MA, 2002.
- [73] Bauchau, O. A. and T. Joo. "Computational Schemes for Non-linear Elastodynamics." *International Journal for Numerical Methods in Engineering*, Vol. 45, 1999, pp. 693-713.
- [74] Palacios, R. and C. E. S. Cesnik. "Reduced Structural Modeling of Integrally-Strained Slender Wings." *45th AIAA/ASME/ASCE/AHS Structures, Structural Dynamics, and Materials Conference*, Palm Springs, CA, Apr. 19-22, 2004.

- [75] Palacios, R. and C. E. S. Cesnik. "Static Nonlinear Aeroelasticity of Flexible Slender Wings in Compressible Flow." AIAA-2005-1945, *46th AIAA / ASME / ASCE / AHS / ASC Structures, Structural Dynamics, and Materials Conference*, Austin, TX, Apr. 18-21, 2005.
- [76] Palacios, R. *Asymptotic Models of Integrally-Strained Slender Structures for High-Fidelity Nonlinear Aeroelastic Analysis*. Ph. D. Dissertation, The University of Michigan, Ann Arbor, MI, Dec., 2004.
- [77] Palacios, R. and C. E. S. Cesnik. "Geometrically Nonlinear Theory of Composite Beams with Deformable Cross Sections." *AIAA Journal*, Vol. 46, No. 2, Feb., 2008, pp. 439-450.
- [78] Cesnik, C. E. S. and E. L. Brown. "Modeling of High Aspect Ratio Active Flexible Wings for Roll Control." *43rd AIAA / ASME / ASCE / AHS / ASC Structures, Structural Dynamics, and Materials Conference*, Denver, CO, Apr. 22-25, 2002.
- [79] Brown, E. L. *Integrated Strain Actuation In Aircraft With Highly Flexible Composite Wings*. Ph.D. Dissertation, Massachusetts Institute of Technology, Cambridge, MA, Feb., 2003.
- [80] Peters, D. A. and M. J. Johnson. "Finite-State Airloads for Deformable Airfoils on Fixed and Rotating Wings." *Proceedings of Symposium on Aeroelasticity and Fluid/Structure Interaction/Proceedings of the Winter Annual Meeting*, Fairfield, NJ, 1994, pp. 1-28.
- [81] Peters, D. A. and W. Cao. "Finite State Induced Flow Models Part I: Two-Dimensional Thin Airfoil." *Journal of Aircraft*, Vol. 32, No. 2, Mar. - Apr., 1995, pp. 313-322.
- [82] Cesnik, C. E. S. and W. Su. "Nonlinear Aeroelastic Behavior of Fully Flexible Slender Vehicles." *International Forum on Aeroelasticity and Structural Dynamics, 2005*, Munich, Germany, Jun. 28 - Jul. 1, 2005.
- [83] Shearer, C. M. and C. E. S. Cesnik. "Nonlinear Flight Dynamics of Very Flexible Aircraft." AIAA-2005-5805, *AIAA Atmospheric Flight Mechanics Conference and Exhibit*, San Francisco, CA, Aug. 15-18, 2005.
- [84] Shearer, C. M. and C. E. S. Cesnik. "Modified Generalized Alpha Method for Integrating Governing Equations of Very Flexible Aircraft." AIAA-2006-1747, *47th AIAA / ASME / ASCE / AHS / ASC Structures, Structural Dynamics, and Materials Conference*, Newport, RI, May 1-4, 2006.

- [85] Hénon, M. "On the Numerical Computation of Poincaré Maps." *Physica D*, Vol. 5, 1982, pp. 412-414.
- [86] Radcliffe, T. O. and C. E. S. Cesnik. "Aeroelastic Response of Multi-Segmented Hinged Wings." AIAA-2001-1371, *42nd AIAA / ASME / ASCE / AHS Structures, Structural Dynamics, and Materials Conference*, Seattle, WA, Apr. 16-19, 2001.
- [87] Stevens, B. L. and F. L. Lewis. *Aircraft Control and Simulation*. New York: John Wiley & Sons, Inc., 1992.
- [88] Patil, M. J. *Nonlinear Aeroelastic Analysis, Flight Dynamics, and Control of a Complete Aircraft*. Ph.D. Dissertation, Georgia Institute of Technology, Atalnta, GA, May, 1999.